THE WEAR AND THERMO-ELASTOHYDRODYNAMIC BEHAVIOR OF THRUST WASHER BEARINGS UNDER NON-AXISYMMETRIC LOADS

A Thesis
Presented to
The Academic Faculty
by

Robert L. Jackson III

In Partial Fulfillment
of the Requirements for the Degree
Doctor of Philosophy in Mechanical Engineering

Advisor: Dr. Itzhak Green

Woodruff School of Mechanical Engineering
Georgia Institute of Technology
April, 2004

THE WEAR AND THERMO-ELASTOHYDRODYNAMIC BEHAVIOR OF THRUST WASHER BEARINGS UNDER NON-AXISYMMETRIC LOADS

Approved By:

Dr. Itzhak Green, Chair

Dr. Wenjing Ye

Dr. Jianmin Qu

Dr. Olivier A. Bauchau

Dr. Q. Jane Wang

April 12, 2004

ACKNOWLEDGEMENTS

Thanks to my advisor, Professor Itzhak Green for helping me along the way through the research and the Doctoral thesis process. I also thank him for believing in me throughout the research, even when things were not going exactly as planned. I am sure he will remain a close friend and mentor throughout my life. Thanks to my committee for all the insight they have given me. Thanks to Hun Kim for providing crucial support and information. Thanks to Rohit Paranjpe for bringing this project to Georgia Tech. I also thank the others out of industry who helped during the course of the research, especially David Zini, Sandra Dutt, Pat Gibson and Pranit Nanavati.

I must also say thanks to the many undergraduate and graduate students I have worked with on the thrust washer bearing and elasto-plastic spherical contact research. They are Dawei Shen, Scott Shipley, Peter Cameron, Andrew Andreassen, Paul Fortson, Travis Iams, Helen Inglis, Fabio Campos, Jake Quicksall, James McClearen, Itti Chusoipin, Chris Barlow, and Michael Joseph. Thanks also to all the graduate students in Tribology and Mechanics of Materials at Georgia Tech who have been great friends and provided technical help on many occasions.

I am also very grateful to General Motors for funding the research with contract E25-Z76 through the Center for Surface Engineering and Tribology.

Thanks to the Georgia Institute of Technology. The institute will forever be a part of who I am since I have spent ten years here for my undergraduate and graduate work. I have seen the campus change as buildings have been torn down and built. I have also seen the sports teams (especially the swim team) have good times and bad times, but I

will always be a loyal fan and supporter through both. I am proud to say that I am a Ramblin' Wreck for Georgia Tech and a 'Helluva' Engineer.

I cannot forget my parents who taught me all the important things in life, and always led me in the right direction. I also thank them for supporting me through all my decisions, both economically and emotionally. They have always been a cornerstone in my life and I don't know if they realize how important they are to me.

Thanks to all my friends, for putting up with me while I was doing this work and for also always being supportive. Special thanks to Alec McGillivray, Alex Chung, Garett Plyler, E. W. Hagerman, Attila Sereg, Brian Horton and Jim Zander. I could not have made it through the hard times without the good times that they provided.

Last but certainly not least, I would like to thank my wife, Kristen, for supporting me through what has been a tough year and through my graduate studies. Everyday I get to spend with her and Cody is a perfect day. This marks a new beginning in our lives that we both are looking forward to.

TABLE OF CONTENTS

LIST OF TABLES

LIST OF FIGURES

NOMENCLATURE

A = area of contact

A_n = nominal contact area

a = contact radius

B = material dependant exponent

C = critical yield stress coefficient

D = contact area factor

d = separation of mean asperity height

E = elastic modulus

e_y = uniaxial yield strain, S_y/E

F = force

f = friction coefficient

G = Gaussion height distribution

G_o = Roeland's equation constant

H = hardness

H_G = hardness geometric limit

h = film thickness, separation of mean surface height

K = hardness factor

k = mean contact pressure factor

m_n = nth moment of the surface profile

N = total number of asperities or rotational speed in the context of the Stribeck curve.

p = fluid pressure

P = contact force or average bearing pressure in the context of the Stribeck curve.

p_o = maximum contact pressure

q = volumetric heat rate

Q = heat rate

R = radius of hemispherical asperity

r = radial distance from axis of symmetry

S_o= Roeland's Equations constant

S_y = yield strength

T = Temperature

U= surface tangential speed

y_s = distance between the mean asperity height and the mean surface height

x, y, z = Cartesian Coordinate System

Z – dynamic viscosity of fluid ($N \cdot s/m^2$)

z = axis of symmetry for single hemisphere

z = height of asperity measured from the mean of asperity heights

δ = average surface roughness

η = area density of asperities

ϕ = flow factor for modified Reynolds Equation

Φ_s = stochastic shear flow factor

μ = dynamic fluid viscosity

μ_∞ = Roeland's Equation dynamic fluid viscosity constant

ω = interference between hemisphere and surface,

ψ = plasticity index

ν = Poisson's ratio

γ = radial displacement in asperity contact, angle of rotation in thrust washer bearing model

σ = standard deviation of surface heights (roughness)

σ_s = standard deviation of asperity heights

Subscripts

1 = surface one

2 = surface two

a = axial

c = critical value at onset of plastic deformation

eff = effective

E = elastic regime

F = fit to current FEM data

o = maximum or original

s = shear

t = hemispherical contact transitional value from elastic to elasto-plastic behavior or in tangential direction

vm = von Mises stress

x = *x direction*

y = y direction

Superscripts

* = normalized by σ, or critical value at initiation of yielding

C = critical yield stress coefficient

′ = equivalent or displaced

¯ = single hemisphere model

SUMMARY

Friction and wear between mechanical components has long been of great interest to engineers and scientists. It is commonly known that excessive wear of components can lead to altered performance and premature failure of machinery. Friction is likely to also affect the efficiency of systems by converting mechanical energy into non-recoverable thermal energy. Hence, it is of great importance that bearings, which are designed to decrease the friction and wear between contacting mechanical components, perform to a level acceptable for their individual application.

The goal of this thesis is to investigate the physical phenomena that distress thrust washer bearings through physical modeling and numerical techniques. The thrust washer bearing under investigation supports non-axisymmetric loads within the planetary gearsets of automatic transmissions and consists of a number of flat-faced washers that are placed between an idle helical gear and its contacting face. Because of the non-axisymmetric loading, the gears and washers are tilted in relation to the carrier, forming a converging and diverging gap. Due to such tilt, there are areas of concentrated contact between the components.

The performance of the thrust washer bearing is governed by a number of physical phenomena which are coupled to each other. These physical phenomena include but are not limited to macro-scale deformations, frictional heat generation, heat transfer, hydrodynamic lubrication, asperity contact, and wear. The hydrodynamic lubrication generates fluid pressures which tend to separate the bearing components. In some cases thermo-elastic instability can occur which will cause the temperature and thermal

expansion of a portion of the bearing to increase monotonically until failure. Thermo-viscous distress also occurs when the fluid temperature rises and the viscosity decreases until the fluid film collapses. While the bearing can operate with low friction and wear for certain loads and speeds, at higher loads and speeds the bearing often distresses and the friction and wear increases significantly.

A quasi steady-state numerical simulation of thrust washer bearings is constructed. For this, the finite element method is used to model the thermo-mechanical deformations. Other numerical schemes are also incorporated to model frictional heat generation, boundary lubrication, asperity contact, and full film lubrication. To simulate surface asperity contact, an extensive finite element study of elasto-plastic hemispherical contact is performed. All of these mechanisms are coupled together and must be solved simultaneously. The resulting set of nonlinear equations is solved using the Newton-Raphson method.

The results of the finite element elasto-plastic hemispherical contact model are normalized such that they are valid for macro contacts (e.g., rolling element bearings) and micro contacts (e.g., asperity contact), although micro-scale surface characteristics such as grain boundaries are not considered. The material is modeled as a homogeneous elastic-perfectly plastic. The numerical results are compared to other existing models of spherical contact, including the fully plastic case and the perfectly elastic case (known as the Hertz contact). This work finds that the fully plastic average contact pressure, or hardness, commonly approximated to be a constant factor of about three times the yield strength, actually varies with the deformed contact geometry, which in turn is dependant upon the material properties (e.g., yield strength, elastic modulus, and Poisson's ratio).

These results are not represented, largely overlooked, or not theoretically explained in previous works. Experimental and analytical results have also been shown to compare well with the current work. The results are fit by empirical formulations for a wide range of interferences (displacements which cause normal contact between the hemisphere and rigid flat) and materials for use in other applications. The elasto-plastic result for a single hemisphere is used to statistically model contact between entire rough surfaces having many asperities. This model is used in the comprehensive numerical model of the thrust washer bearing. Also presented are the finite element predictions of the residual stresses and strains that are formed after an elasto-plastic hemispherical contact is unloaded.

In conjunction with the numerical modeling, an experimental investigation of thrust washer bearing behavior is also performed. A test rig, designed specifically for testing thrust washer bearings, is used to provide a physical model. The test rig allows controlled variation of the operational parameters (speed, load, lubrication flow rate, etc.) that govern the tribological behavior of the washer. The test rig also records pertinent real-time data (frictional torque and temperature) from the bearing.

Although the numerical results do not always predict quantitatively the experimental results, they do show similar qualitative results. The trends of the numerical model results compare well to the experimental results and suggest that at certain loads and speeds hydrodynamic pressure decreases contact and reduces friction. The results show that the thrust washers provide additional hydrodynamic load carrying capacity. Although at high loads, the bearing operates in the boundary lubrication regime (asperity contact). The numerical and experimental results show that asperity contact can cause high temperatures, high friction, severe wear, and subsequent bearing distress.

Bearing distress, marked by a sharp increase in friction, temperature and a sudden collapse in the fluid film, occurs in both the experimental and numerical models. The cause of the sudden and severe bearing distress is due to thermo-viscous distress and thermo-elastic instabilities. These effects of these mechanisms can be lessened by increasing hydrodynamic load carrying capacity, decreasing the 'dry' coefficient of friction, improving the thermal conductivity and by decreasing the load and speed at which the bearing is operated. Although not originally proposed as a topic to be included in this thesis, application of a low friction coating such as PTFE was found to improve thrust washer bearing performance significantly.

CHAPTER 1

INTRODUCTION

1.1 Problem Statement

The goal of this research project is to investigate the physical phenomena that distress a thrust washer bearing system within an automatic transmission. The thrust washer bearing system must bear the load produced by the planets of a helical planetary gear set within the transmission. The thrust washer bearing system consists of one or two flat-faced washers that are placed between a helical gear and its carrier. From this point forward, 'bearing' will refer to the thrust washer bearing system within the test rig, unless specified otherwise.

Previous to this work, the behavior of the thrust washer bearing system and its lubrication in the automatic transmission between gears and their carriers was largely unknown. The problem is that the bearing is distressing at an accelerated rate and from uncertain reasons. When this happens, the planetary gearset locks up and maintenance is required. Experience shows that the failed bearing in the transmission is sometimes completely worn away, thus leaving debris in the transmission fluid. Obviously, this result is undesirable and unacceptable.

Description of Industrial Application

A planetary gearset consists of an outer-ring, a sun gear and usually three or four planet gears which mesh in between (see Figure 1.1). Bearings are located on both sides of each planet gear within the transmission. The gear itself also rides on a number of needles placed between the shaft and the inner bore of the gear. In this study, there are four planet gears in a planetary gearset, so the system includes eight bearings. In each automatic transmission there are two planetary gearsets, and thus eight sets of bearings. So, because of the large number of these bearings, each bearing must be very reliable.

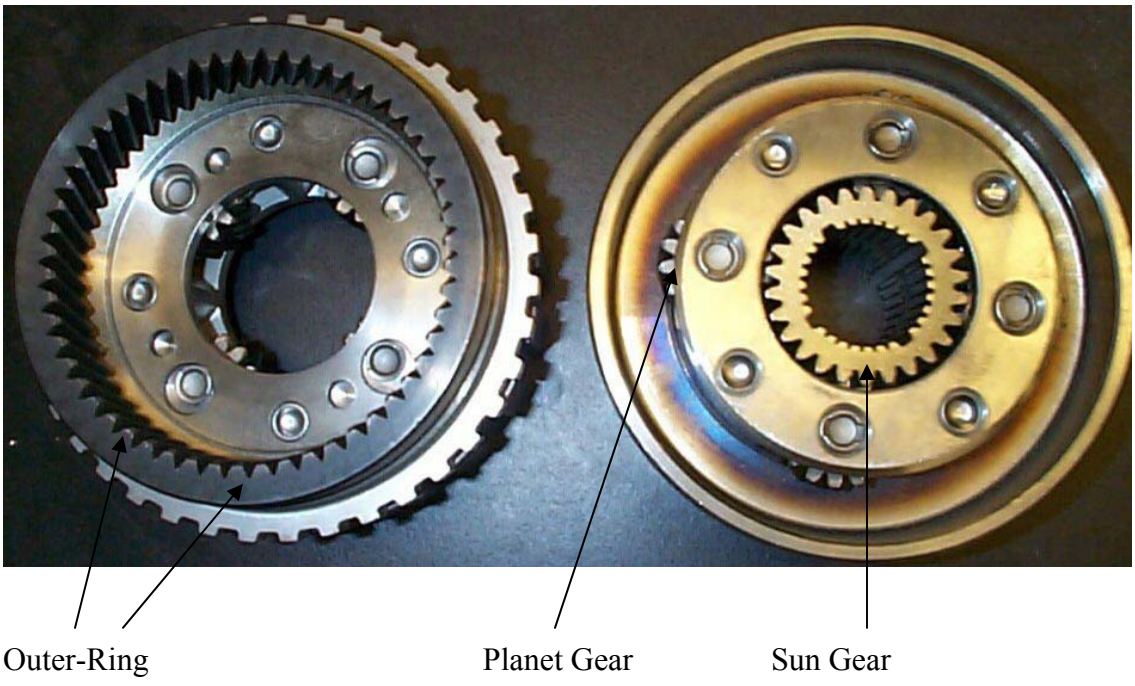

Figure 1.1: Photograph of a used planetary gearset from an automatic transmission.

Due to the helix angle of the helical gears an axial load is produced in addition to the tangential and radial loads (see Figure 1.2). A force analysis of the helical gear is

presented later. Skewing of the needles on which the helical gear rides could be causing additional axial thrust loads (Ulezelski, 1983). According to Ulezelski, these thrust loads are caused when the skewed needles produce a thread effect when rotating. This has been experimentally confirmed by Bair and Winer (1989).

During actual transmission operation, the bearing cycles through various loads and rotational speeds as the transmission shifts from gear to gear. The only data acquired about the performance and life of the bearing are from tests in which the bearing is run through these cycles for long periods of time. Because real time data is not recorded from these tests, the only way to quantify the bearing performance is through the wear of the washer bearing. Thus, little is known about the actual physical and tribological behavior of the bearing.

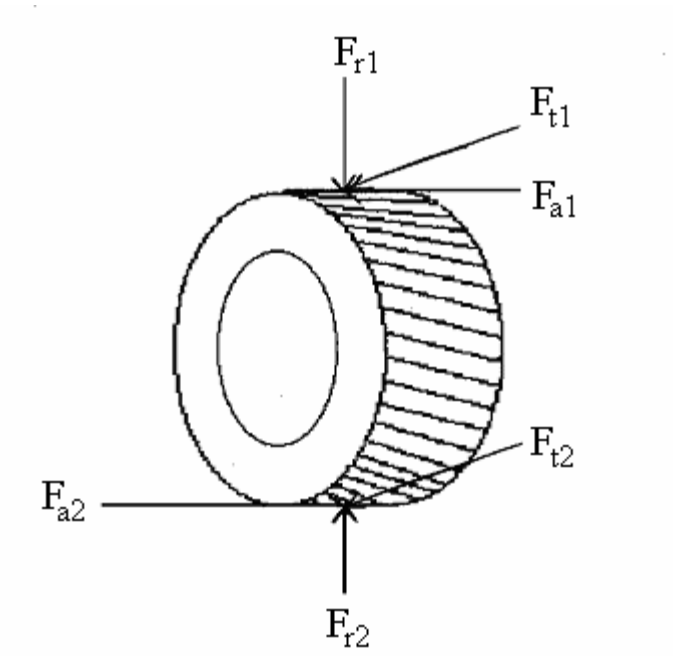

Figure 1.2: A helical planet gear in the transmission and the forces induced on its teeth. For clarity, not all forces are represented (this is not a free-body diagram).

The reason the washer is failing could be that an inadequate amount of lubrication is reaching the washer or that the lubrication there is not being used optimally by the geometry and motion of the washer and surrounding parts. It is believed that the lubrication on and around the washer and gears is a mist produced by the rotation and revolution of the gears and carriers.

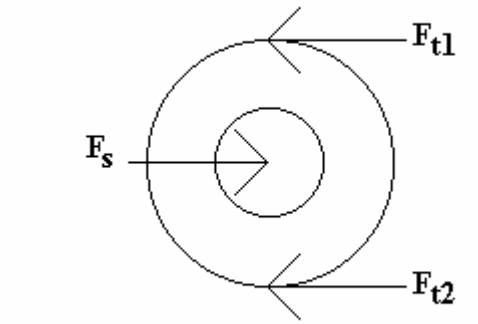

Figure 1.3: Forces on idler gear in the tangential direction and the resulting reaction force.

Force Analysis of Transmission Idler Gear

In the transmission, the helical gear, which the bearing supports, is an idler. If a gear is an idler, then it transmits no torque to the shaft it is riding on. Thus, the moment about the axis of the gear caused by the tangential forces on the gear teeth must sum to zero. The forces present in the radial and tangential directions are then only the forces on the gear teeth and the reaction force of the shaft against the inner bore of the gear. These forces are shown in Figure 1.3, where

$$F_s = F_{t1} + F_{t2} \quad (1.1)$$

$$F_{t1} = F_{t2} \quad (1.2)$$

Since the teeth of the gear are helical, the normal forces (F_{n1},F_{n2}) have axial load components at the contact point. See Figure 1.4 for a depiction of these and how they are induced on the teeth. When φ is the helix angle, these forces are:

$$F_{a1} = F_{t1} \cdot \tan \varphi \quad (1.3)$$

$$F_{a2} = F_{t2} \cdot \tan \varphi \quad (1.4)$$

The axial forces induced by the normal forces on the helical teeth are thus equal because the normal forces are equal. The normal forces also induce equal and opposite radial forces which cancel out. This results in a free body diagram of the axial and radial forces as seen in Figure 1.5. The axial forces cause a moment (M_g) about the center of mass of the gear and perpendicular to the shaft axis. This couple is matched by a counter moment caused by the gear contacting the shaft, a bearing on either side, or a combination of these.

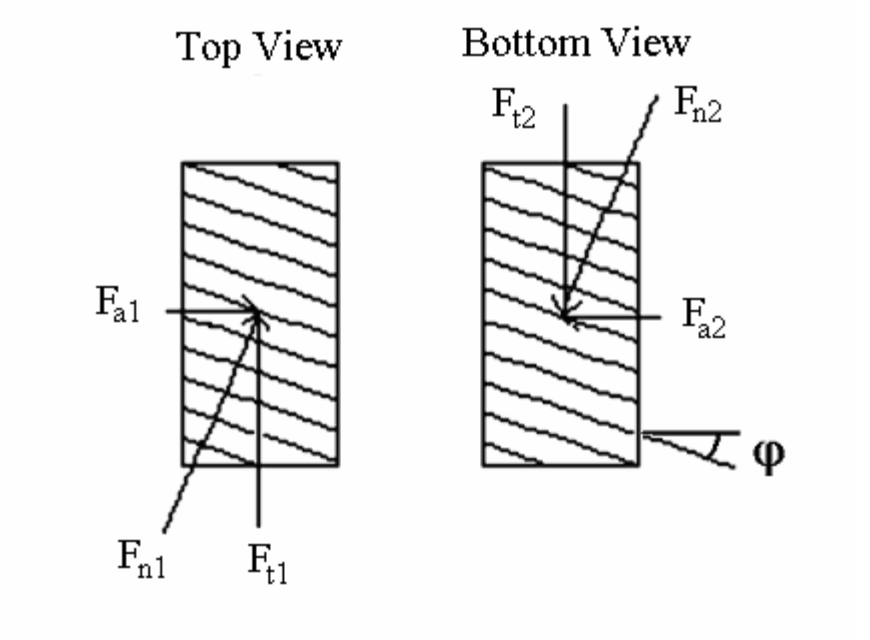

Figure 1.4: View of gear with tangential and helically induced axial forces on idler gear in transmission.

Then according to the free body diagram, the two opposing axial forces cancel, and because they are not collinear, they produce a pure moment (couple). Thus, the gear should center itself between the bearings on either side. However, this cannot be true in the actual transmission, since bearing wear and failure is seen more excessively on one side of the gear than the other. This phenomenon confirms the Ulezelski (1983) report, which suggests that the needles on which the gear rides could skew and cause an additional axial load that is not represented by the above force analysis. Thus, the axial load placed on the thrust washer is induced by a combination of helical gear forces and forces induced by the skewing of the needles.

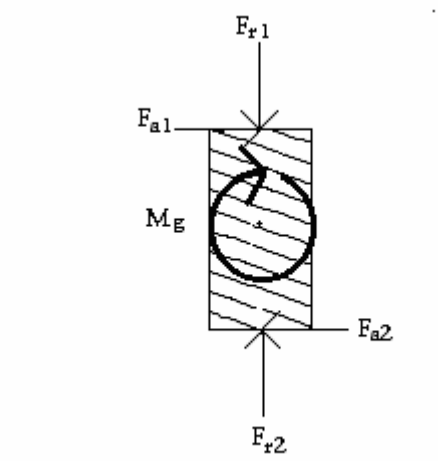

Figure 1.5: Side view of gear that shows forces which induce a moment onto the idler gear.

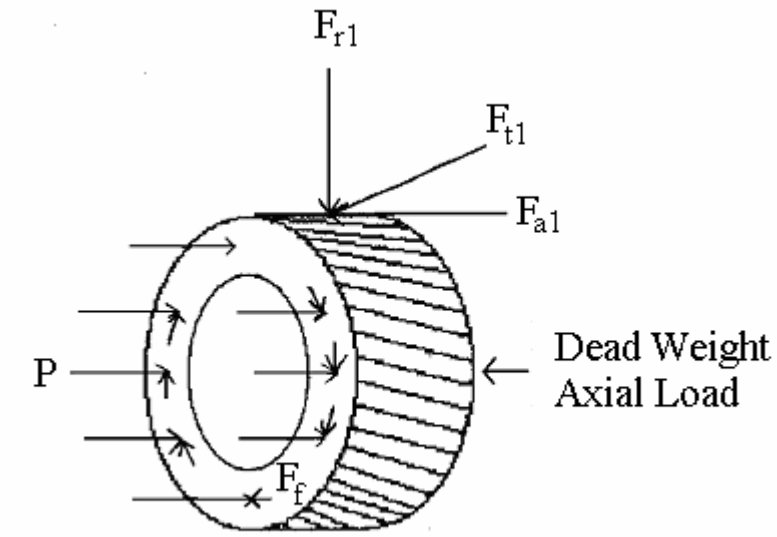

Figure 1.6: A helical planet pinion in the test rig and the forces induced on its teeth. For clarity, not all forces are represented (this is not a free-body diagram).

Even though the skewing of the needles may induce an axial load on the gear in one direction, the moment caused by the helical gear will cause the gear to rotate so that the axial surface of the gear is not parallel to the carrier and bearing. This results in a point contact at the gear, bearing and carrier interfaces. This loading situation is

modified for the numerical and experimental tests so that the bearing may be easily loaded.

In the experimental test rig the gear is not an idler as in the transmission. Instead the gear is loaded axially from dead weight through a lever and pulley system. The resulting situation is depicted in Fig. 1.6. The gear is driven from an adjacent gear and so has a radial, tangential and axial force that is not balanced on the opposite side of the gear like the idler in the transmission. Instead the radial force is taken by the shaft and the axial force from the gear teeth adds to the axial force applied through the dead weight. The tangential force produces a moment that is balanced by the moment caused by the friction on the surface of the bearing. The resulting load is suspected to produce a situation similar to the diagram in Figure 1.7. It is concluded that the pinion loading condition in the test rig is more severe than the actual planet gear loading in the transmission.

1.2 Objective

The purpose of this work is to develop an understanding of the physical phenomena that govern the behavior and life of a thrust washer bearing system. Before this work, there was little or no knowledge of what different physical phenomena affected the bearing or how much they affected it. The behavior of the bearing during operation and whether it showed any possibility of sustaining hydrodynamic forces was also unknown. It is also desirable to identify the physical phenomena that cause the bearing to distress at certain loads and speeds. Thus the objective of this research is to identify and model the physical phenomena which govern bearing behavior.

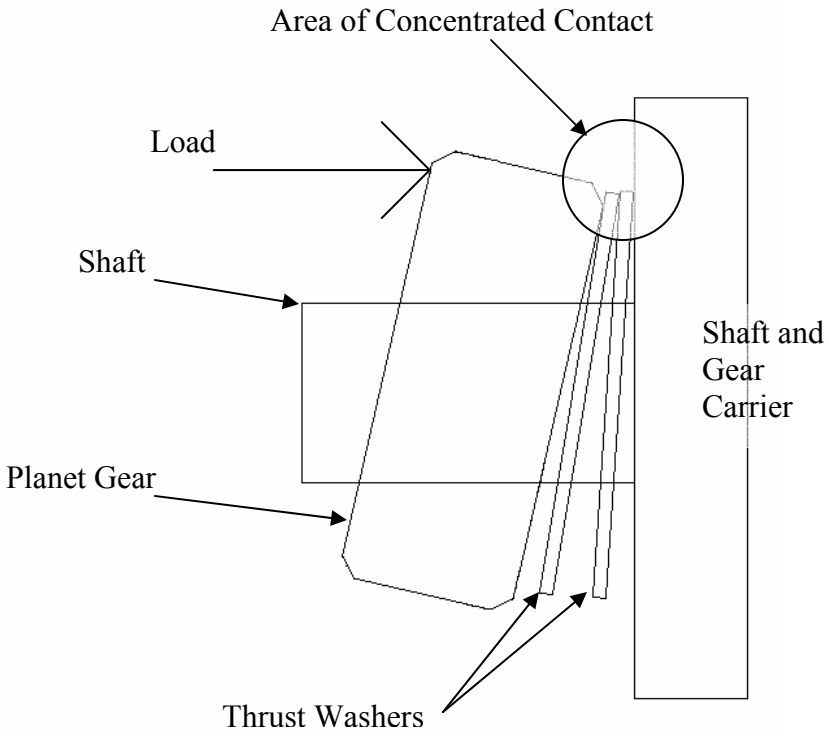

Figure 1.7: Diagram of contact loading conditions of the thrust washer bearing in test rig.

1.3 Current Approach

The thrust washer bearing problem is approached in two ways, through an experimental simulation and through a numerical simulation. Figure 1.7 shows the division of the thrust washer work into its main components.

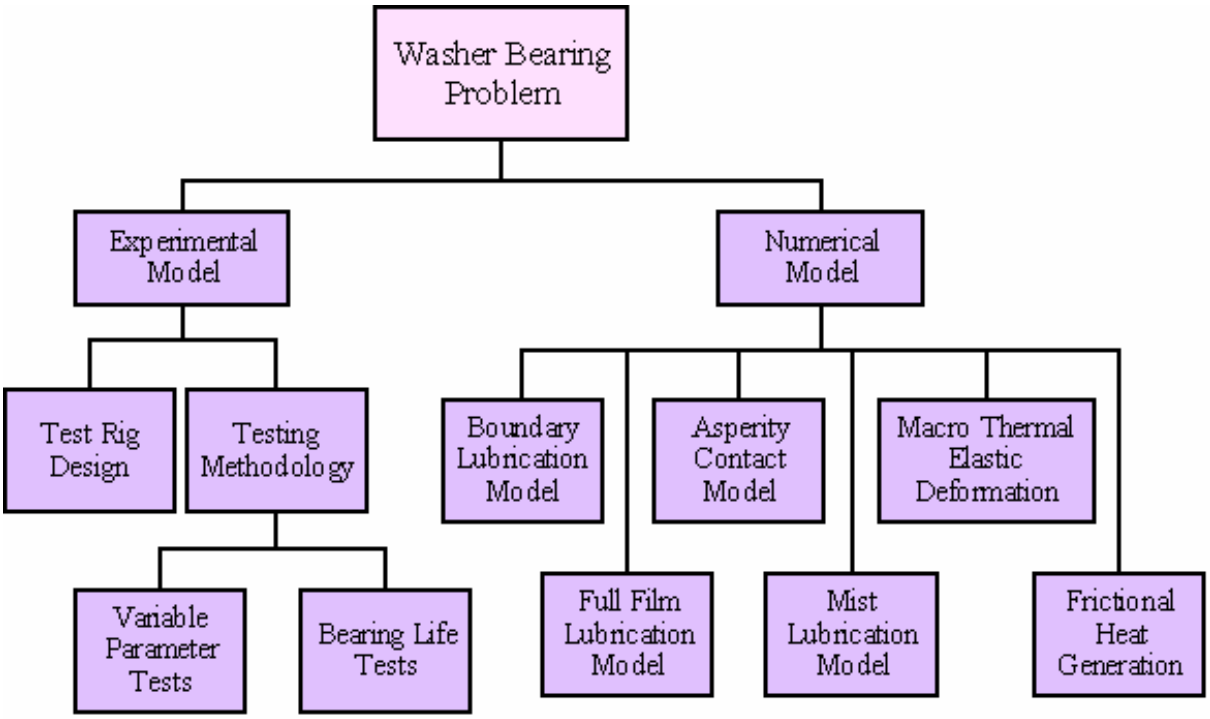

Figure 1.8: Graphic showing the various components which make up the thrust washer bearing investigation.

To gain an understanding of the bearing behavior under non-axisymmetric loading, a test rig was designed to provide a physical model. Figure 1.8 shows a schematic of the test rig in the region where the thrust washer bearings are tested. The test rig allows controlled variation in the operational parameters governing the tribological behavior of the washer. For given washer materials and surface finishes, the parameters that most affect the life of the bearing and its tribological behavior are believed to be thrust or axial load, rotational speed, lubrication supply, lubrication properties, and the geometry of the bearing.

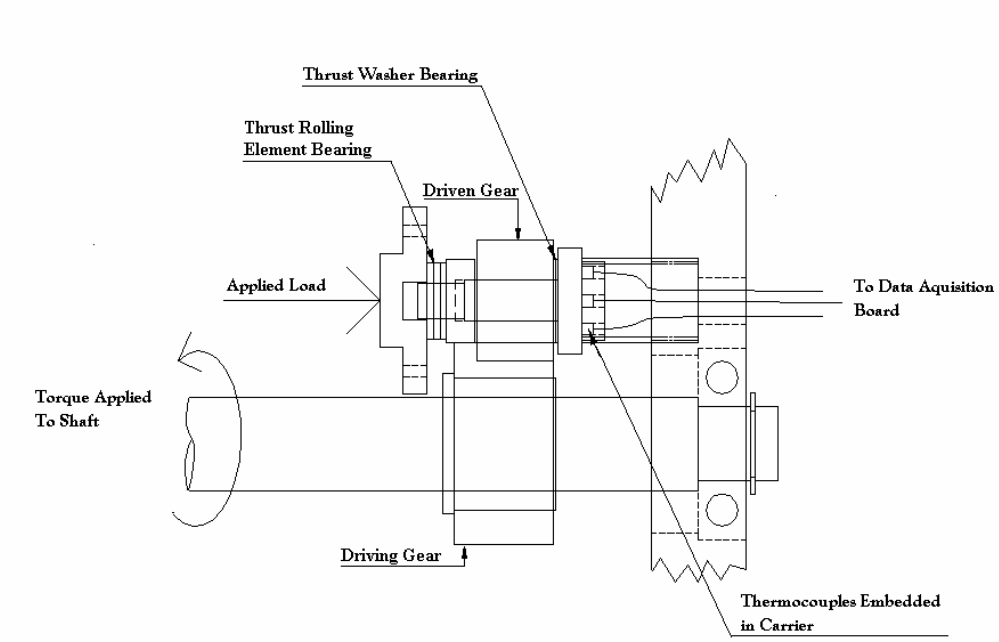

Figure 1.9: Diagram of thrust washer bearing testing configuration within the test rig.

The test rig also records pertinent real-time data from the bearing. The test rig monitors two real-time indicators of bearing behavior: the frictional torque transferred through the bearing and the temperature near the bearing. The frictional torque is recorded from the power output of the motor, since with increasing frictional torque the power needed to run the motor at a constant speed will increase. The temperatures are recorded using thermocouples embedded near the bearing surface.

Tests conducted indicate the possible presence of hydrodynamic and EHD effects at certain rotational speeds and axial load combinations at which the calculated effective coefficient of friction decreases with velocity. In the tested cases, however, a distinctive and sharp increase in the temperatures and in the coefficient of friction occurs at the instant of bearing distress.

In conjunction with the experimental effort a numerical simulation of the thrust

washer system is constructed to provide an analytical model, and a better understanding of the washer thermomechanical and lubrication behavior in order to predict bearing distress. The numerical simulation is also capable of modeling new design concepts to avoid bearing distress. In addition, the various mechanical, thermal, and lubrication models will be solved simultaneously by using an iterative approach as each of the phenomena is coupled to the other. Upon convergence, the coupled models provide a quasi-steady state solution. The interfacial conditions are the conditions between the components, such as fluid pressure and contact force, which are adjusted until they converge to the final solution.

1.4 Significant Contributions

Prior to this work the physical phenomena and mechanisms which govern thrust bearing performance were largely unknown. This work provides a strong foundation for future work in thrust washer bearings and other similar tribological elements. The once shallow thrust washer bearing knowledge base is greatly enhanced by the experimental and numerical findings presented within this work. These findings indicate what the important thermo-mechanical mechanisms are that govern thrust washer bearing behavior. These mechanisms should be addressed when designing and implementing thrust washer bearings. This work links thrust bearing distress to the phenomena of thermo-elastic instability and thermo-viscous distress.

Also a notable contribution to those studying the operation of tribological elements such as bearings and seals is the comprehensive numerical model of thrust washer bearings. The numerical model incorporates a large number of coupled physical

phenomena into one mathematical model which is solved as a set of nonlinear equations. In comparison to other tribological models, there are very few significant assumptions being made that compromise the model's effectiveness. The results show that the model predicts some significant trends that are seen in the experimental work, although it does not always predict the same quantitative results. The final model is to be used as a design tool for future thrust washer designs in industry and to narrow down various possibilities to a feasible design without the need for extensive testing.

Another significant contribution of this work is the in depth characterization of elasto-plastic spherical contact. Although this characterization is used to model elasto-plastic asperity contact in the thrust washer bearing numerical simulation, it is generalized for the use in a variety of applications. These applications include the design of heavily loaded ball bearings, micro-switches and other similar contact geometries. This work also addresses and clarifies the current fundamental understanding of elasto-plastic contact and hardness. The improved understanding the work provides is a benefit to those studying similar contact conditions now and in the future.

CHAPTER 2

LITERATURE REVIEW

2.1 General Literature Review

A number of models and techniques are used in this project to simulate the thrust washer bearing and the mechanisms that affect its behavior. These models and the work which lead to them are discussed below. A section on literature resulting from experimental work on thrust washer bearing and other pertinent work is also presented.

Work concerning flat thrust washer bearings as described earlier is very scarce. There is however, a great deal of information on situations or models which are similar. Although not presented here, mechanical seals are in many ways tribologically similar to thrust washer bearings.

Other research has looked into certain aspects of the bearing behavior, but not the behavior of the system as a whole. For instance, Shamim(1994) investigated the effectiveness of mist lubrication in machinery, and found that it works well in some cases. It is believed that the lubrication on and around the washer and gears is a mist produced by the squirting of fluid and the splashing of the gears.

Brockwell, et al.(1970) investigated experimentally the effect on the number of grooves on the thrust washer bearing. They also confirmed the occurrence of thermal deformations creating the converging gaps needed for hydrodynamic lubrication. The

researchers also used regression to analyze the effect of various parameters in the bearings operation. This regression analysis showed that waviness on the washer surfaces can enhance load carrying capacity.

One of the few other experimental investigations of thrust washers was the work of McClintock(1974). The washers tested only contained a single radial groove, which would make them more comparable to the current washers. McClintock investigated the wear of thrust washers using a variety of lubricant types. Thus, this investigation was less concerned with the bearing behavior and mechanisms governing their behavior than the effect of different lubricants on bearing behavior. The paper does suggest, though, the existence of full film hydrodynamic lubrication at certain loads because of the lack of wear at these loads.

Although investigating a slightly different case of 'flat land bearings,' Heshmat (1987) also investigated experimentally grooved flat land or parallel surface thrust bearings under different loads, speeds and oil temperatures. These results showed that the load carrying capacity of the bearings is independent of bearing size. Burnishing was shown to occur at the center of the space between the grooves. This work also confirmed the hydrodynamic enhancing effect of thermo-elastic expansion Heshmat also interestingly suggested that asperities carry a portion of the load not normally modeled by classical Reynolds hydrodynamic analysis.

In 1958, Cameron and Wood formulated a model of a grooved parallel surface thrust bearing, in which the hydrodynamic lift was created by a converging gap induced by thermal deformations. It is noteworthy, that in this model the temperature across the fluid film was assumed constant.

Over the years, others have performed similar analyses on thrust bearings. One notable analysis was published by Taniguchi and Ettles(1975). In their work they modeled hydrodynamic and thermo-elastic behavior of radially grooved parallel surface thrust washers.

In 1990, Carpino performed an analytical simulation of a flexible thrust washer driven at low speeds. The washer was modeled to carry multiple point loads and to also have grooves. However, due to the staggered loads and resulting deflection, converging gaps form. The converging gaps are sufficient for producing hydrodynamic lift. The mechanics of this case may be similar to the current one, except for a single non-axisymmetric load at much higher speeds.

More recently, Kazama and Yamaguchi(1993) modeled a rotating and tilted hydrostatic thrust bearing, including boundary lubrication affects. In many ways this case is close to the current thrust washer bearing case. The only real differences are that they did not account for macro-deformations and the affects of frictional heating. The Patir and Chang(1978) model, which will be discussed in greater detail later, was used to model the boundary lubrication regime.

Groove geometry and thermal effects on the lubrication of thrust washer bearings were studied by Yu and Sadeghi (2001, 2002). In this study, grooves and thermal deformation are the primary means of providing a converging gap capable of causing

significant hydrodynamic load carrying capacity. In the current study the primary cause for a converging gap to form is the axisymmetric loading condition.

Kucinschi et al. (2003) conduct a thermo-elastohydrodynamic analysis of a grooved thrust washer bearing. The work does not consider asperity contact or boundary lubrication and only models the thrust bearing as having a full film. Also, Kucinschi et al. does not model the washer as a free body. Thus the investigation is the equivalent of a grooved thrust bearing, without any washers. As others have previously found, the study states that the grooves allow for the formation of a converging gap by way of thermal deformations. These groove effects will not be present in the current work, although thermal deformations are included. The current work also models the thrust washers as free bodies..

In addition to these works, there are other works which pertain to specific aspects of thrust washer bearing behavior, such as asperity contact and thermoelastic instability. These works are outlined in the next few sections on these specific topics.

2.2 Thermoelastic Instability and Scuffing

There is a considerable amount of work studying thermal instabilities for various cases, although the thrust washer bearing case has been largely unaddressed until now. Before this work, the cause of severe distress in these bearings was unknown. Now it is believed to be caused by thermoelastic instabilities (TEI) and thermoviscous distress (TVD) in the bearing, which will both be defined in detail in the next few sections.

In practice, the thermoelastic instability (TEI) manifests itself as thermoelastic wear cycles, or severe bearing distress which is marked by a sudden increase in

temperature. These cycles can be explained physically as the following sequence of events. A disturbance in the bearing may cause the bearing to suddenly contact at a point and heat very quickly (see Fig. 2.1). The temperature at this point rises very quickly. This point is called a hot spot. The hot spot can also initiate at the area of concentrated contact of a tilted bearing, as is the case in non-axisymmetrically loaded thrust washer bearing. At the hot spot the temperature increases causing thermal expansion of the material below this point. As mentioned earlier, the thermal expansion can initially enhance hydrodynamic lubrication by creating a converging gap on the surface. However, the viscosity will eventually decrease with temperature rise and the thermo-elastic expansion will continue to cause the hot spot to grow past its point of optimal hydrodynamic geometry.

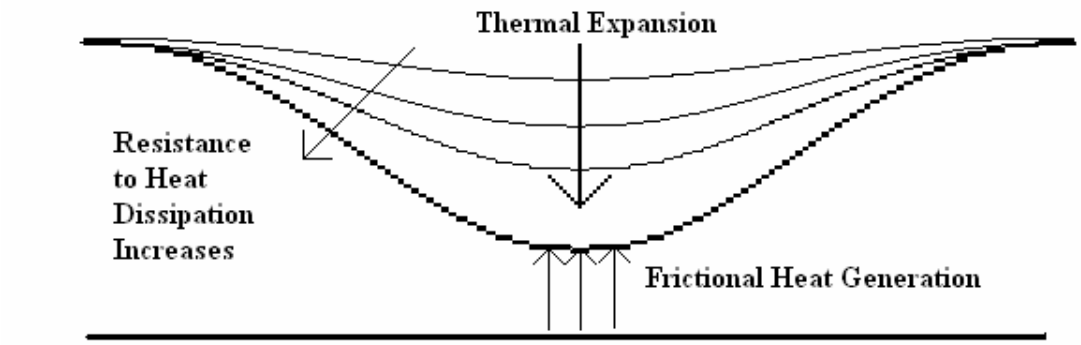

Figure 2.1: Schematic of the progression of a thermoelastic instability.

As the hot spot thermally expands, the contact becomes more localized and the surrounding area slopes down steeply from the tip. This causes the heat generation to become more localized at the tip and for the heat transfer between the surfaces to

decrease around the tip. In addition, the contact will carry more load because it has grown taller than other contacts carrying load. The local temperature of the hot spot in turn increases and expands more, this initiates a vicious and unstable cycle (see Fig. 5.3). In reality, however, the cycle will end due to seizure and wear. The wear which occurs is largely adhesive and falls under the definition of scuffing wear (Williams, 1994).

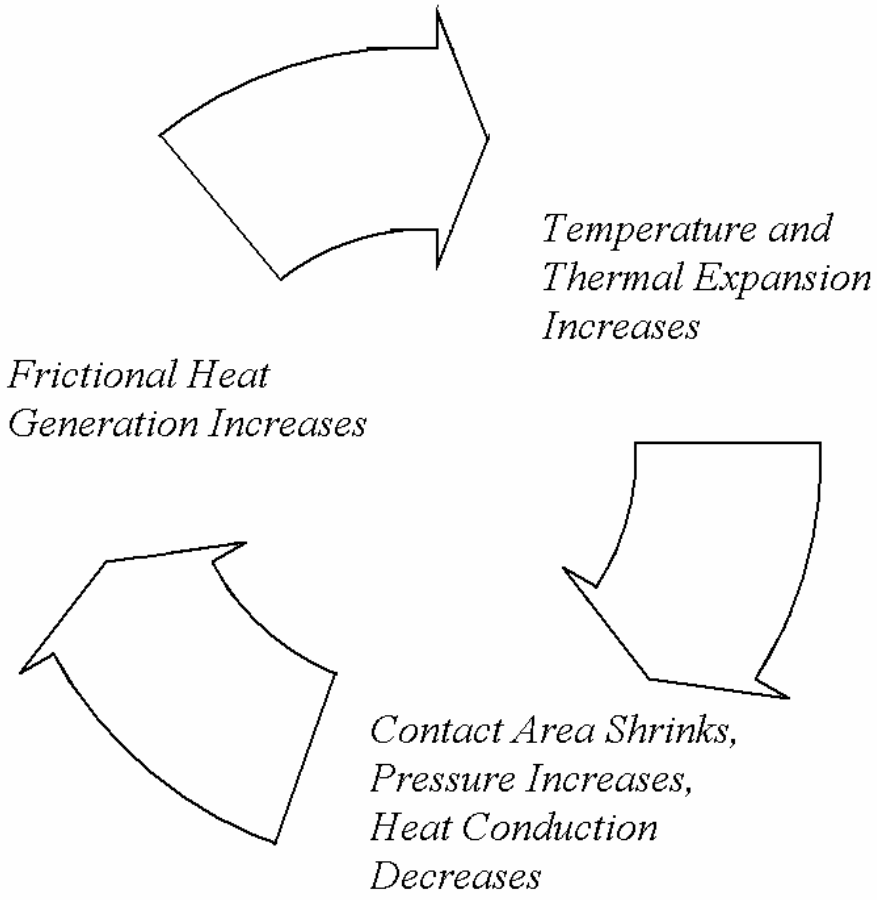

Figure 2.2: Viscous cycle characteristic of a thermoelastic instability.

The wear acts as a dampening effect by causing removal of material in the protruding hot spot. This has multiple effects of 1) decreasing the height of the hot spot and 2)

removing ‘hot’ material and reducing the temperature of the hot spot. Thus, although wear can at times cause detrimental damage to the surface, at other times it damps out TEI. After wear has essentially removed the hot spot, a new hot spot may form at the same location or a new location, and the TEI cycle begins again. When wear dampened TEI occurs cyclic fluctuations in the surface temperature and bulk temperature can occur. Barber (1969) documents this cycle. Similar to the above explanation, he states that the heat generation and expansion is eventually slowed by the wear of material, allowing for other points of TEI to initiate.

Barber (1967) documented the existence of TEI in conforming sliding contacts and gave a theoretical explanation of the phenomena. It appears that it wasn’t until a subsequent work by Barber in 1969 that the TEI term was coined. This work noted that the heat expansion of localized contacts could grow unstable and that wear provided a dampening effect.

Dow and Burton (1972) analytically modeled TEI in the sliding contact between a thin blade or scraper and a half space. This model provides calculations for a predicted critical velocity, identifying the threshold of TEI. In 1973, Dow and Burton expanded their model to consider the effect of wear. They analytically proved that wear rate will dampen the thermoelastic instability by changing the geometry. Increasing wear rates will thus actually stabilize a thermoelastic contact.

Also in 1973, Burton et al. modeled TEI for a seal-like configuration. The model implemented a geometry of two straight blades in contact with each other. The model provides an equation for the critical velocity at the threshold of TEI in this case. This

equation predicts that the critical velocity is inversely proportional to the friction coefficient and the coefficient of thermal expansion.

For the case of lubricated parallel surfaces, Banerjee and Burton (1976) derived a critical speed which defined the threshold of TEI. They modeled the surfaces as a good thermal conductor sliding on a good insulator. Although this may be a reasonable assumption for clutches which usually have layers of metal and a paper-like friction material, it is not a good assumption for thrust washer bearings. Banerjee and Burton's equation for the critical speed that marks the threshold of TEI is

$$U_{crit} = \bar{h}\kappa\sqrt{\frac{K}{\mu\alpha}} \tag{2.1}$$

where $\bar{h}$ is the nominal thickness, κ is the disturbance wave number, K is the thermal conductivity of the 'good' conductor, μ is the fluid viscosity, and α is the thermal expansion coefficient of the 'good' conductor.

In 1976, Lebeck examined the occurrence of TEI in rotating rings in sliding contact (similar to a mechanical face seal). In this work a more realistic geometry is modeled and multiple modes of deformation and instability are considered. Lebeck also considers the effect of wear but not hydrodynamic lubrication. The resulting model shows that stability depends on the material properties and geometry of the contact.

Kennedy et al. (1985) experimentally monitored the phenomena of TEI in mechanical face seals. Isolated contact patches at the peaks of surface waviness were seen to wear and heat considerably more than other areas. These conditions occurred in both seals run dry or well lubricated. Using materials with increasing wear resistance resulted in seal that was more prone to TEI

Johnson et al. (1988) derived a stability threshold for an elliptical EHD contact with rough surfaces. Johnson also correlates this stability threshold to the onset of scuffing failure or distress. The formulation theorizes that for TEI to occur that the heat generated from friction is greater than the heat that can be transferred away through conduction and convection. In 1988, Maksimov also distinguished between the phenomena of TEI and stick-slip sliding, since at times they can both produce periodic behavior.

Anderson and Knapp (1990) qualitatively investigated the scale dependence of different hot spots encountered in automotive applications. The results indicate that TEI can occur on different scales, such as at the asperity level or at the macro-scale due to the same thermoelastic mechanics. Regional or macro-scale hot spots due to uneven loading are characteristic of the current thrust washer bearing, although smaller asperity scale hot spots may initiate larger scale distress. Zagrodzki (1990) modeled the TEI of multiple disk clutch systems. The model suggested that high thermal stresses can arise within the disks during operation.

Lee and Barber (1993) analytically modeled a disk of finite thickness in order to investigate TEI of automotive disk breaks. Lee and Barber (1994) experimentally investigated the TEI of automotive disk brakes using an array of thermocouples. Oscillatory instabilities were recorded, but the instabilities often required adequate time to develop. Brake or contact pressure had no effect on the critical temperature which agrees with theoretical results, although the system temperature will of course increase with higher pressures.

In 1999, Yi et al. studied the effect of geometrical simplifications used in past models has on accuracy. The TEI solution of an actual 3-D disk is compared to the 2-D layer model used by Lee and Barber (1993) and to the 3-D strip or layer. Yi et al. found that although new modes of instability occur with more accurate models, the simplified models still make good predictions for the critical speed. Although these solutions may be adequate for some applications the thrust washer bearing is a much more complicated situation.

In 2000, Yi et al. modeled the TEI of multi-disk systems by numerically solving the eigenvalue problem for the system. They find that the TEI critical speed decreases with the number of disks due to a decrease in the rigidity of the system. These results suggest that in thrust washer bearings, the TEI critical speed will decrease with the number of washers.

Most recently, Jang and Khonsari (2000, 2002, and 2004), considered the effect of boundary lubrication on thermoelastic instability and modeled the growth rate of a thermoelastic instability. Although they do consider these lubrication effects, the model still follows Banerjee and Burton (1976) and assumes the case of a good thermal conductor rubbing against a good insulator. These results clearly indicate though that two surfaces in boundary lubrication have a much lower critical speed than surfaces completely separated by a fluid film.

During the current work, the thrust washer bearing has often reached a point of distress under certain loads and speeds from what is believed to be a thermoelastic instability. This point of distress is marked by a sudden increase in the COF and the bearing temperature. While the bearing is in distress, material is often transferred

between bearing surfaces and/or worn away. Under severe conditions the contacting surfaces can even weld together and cause the test rig to seize. Since this also occurs mostly at high speeds, it fits the definition of scuffing failure and wear as described in Williams (1998). At low speeds wear does occur, but parts rarely weld together. At low speeds the wear is abrasive (wear due to scratching with little or no surface adhesion), while at higher speeds scuffing is thus the wear mode when the bearing is under distress, however, it is not the cause of distress. Bollani (1976) investigated the effect of lubricant additives, geometry, and speed on the occurrence of scuffing. Bollani found that scuffing was less likely to occur at low speeds.

Salomon (1976) provides a simplified map of fluid film failure as a function of speed and load. At low speeds Salomon predicts that the surfaces can operate in the boundary lubrication regime without scuffing occurring. As speed is increased, the surface contact becomes more volatile and scuffing occurs in unison with surface contact. This is probably due to the increase in temperature at higher speeds causing the materials to adhere.

2.3 Boundary Lubrication and Flow in Regions of Asperity Contact

A Stribeck curve is a plot of the coefficient of friction versus the product of the bearing linear speed and viscosity normalized by the average bearing pressure. Using the traditional notation for the Stribeck curve, the equation form of this relation is:

$$f_{eff} = f_{eff}\left(\frac{ZN}{P}\right) \tag{2.2}$$

where: f_{eff} - effective coefficient of friction

Z – dynamic viscosity of fluid ($N \cdot s/m^2$)

N – rotational speed (rev/s)

P – average bearing pressure (N/m^2)

This curve is frequently used to qualitatively identify the transitions from boundary lubrication to mixed lubrication, and to hydrodynamic lubrication (see Fig. 2.3). On the right side of the Stribeck curve the rotational speed and viscosity are high enough to generate enough hydrodynamic lift to overcome the average bearing pressure and separate the surfaces with a thin film of fluid. When a film separates the surfaces, little or no contact occurs between the bumps or asperities on the surfaces. Thus, when a bearing is operating on the right side of the Stribeck curve, the friction and wear are low. However, if the bearing operates under heavier loads, with lower viscosity and lower speed, it will locate on the left side of the Stribeck curve. Moving left on the Stribeck indicates a loss of hydrodynamic lift and so eventually some of the applied load is carried by contact between the surfaces (see Fig. 2.4). This contact occurs at the peaks or asperities of the surface. As more asperities come into contact the friction and wear will increase drastically. The bearing is then in the boundary lubrication regime, where the bearing might benefit from some hydrodynamic lift, but it is not enough to provide a full film of lubrication between the surfaces. It is believed that the thrust washer bearing often operates in a boundary lubrication regime, because the friction and wear between the components is usually higher than what is seen in bearing operating in the full film regime. .

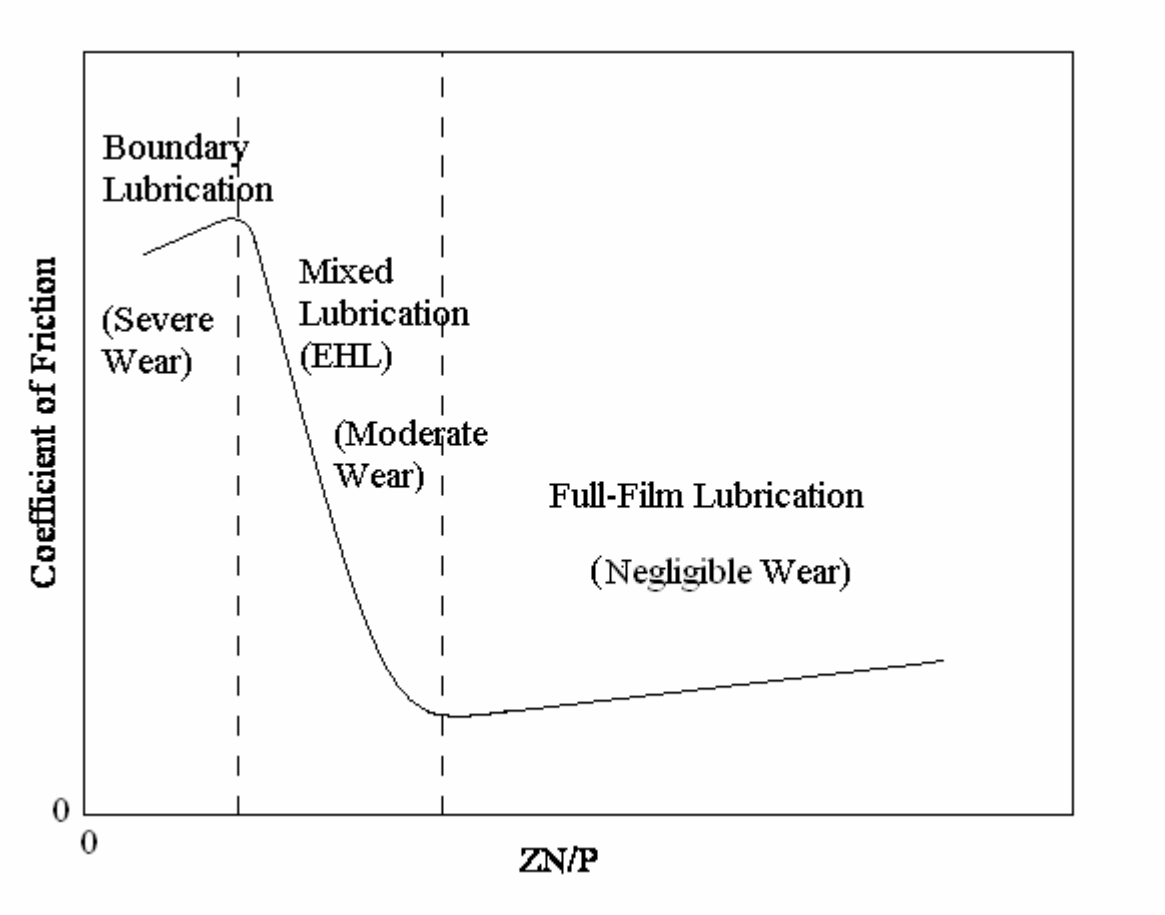

Figure 2.3: Stribeck plot with lubrication regimes marked.

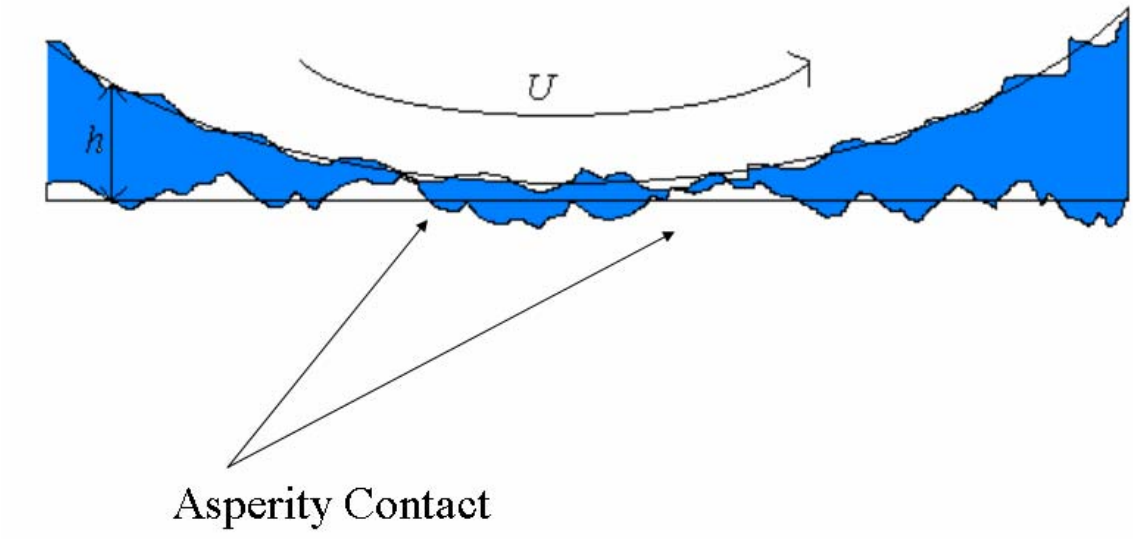

Figure 2.4: Depiction of boundary lubrication between two rough surfaces.

In regions in or near contact where asperities between surfaces come in close proximity, the asperities can influence the lubrication flow (see Fig. 2.4). Here the lubrication regime is known as boundary lubrication, in other words there is only a thin film of lubricant separating the surfaces, and the micro-topography of the surfaces greatly affect the flow of the lubricant.

Patir and Cheng (1978,1979) were the first to formulate these asperity flow effects between two three-dimensional surfaces. These flow effects were taken into account in the form of Flow Factors which were incorporated into a modified form of the Reynolds Equation given by

$$\frac{\partial}{\partial \mathrm{x}}\left(\phi_x \frac{h^3}{12\mu}\frac{\partial p}{\partial x}\right)+\frac{\partial}{\partial y}\left(\phi_y \frac{h^3}{12\mu}\frac{\partial p}{\partial y}\right)=\frac{U_1+U_2}{2}\frac{\partial \bar{h}_T}{\partial x}+\frac{U_1-U_2}{2}\sigma\frac{\partial \phi_s}{\partial x}+\frac{\partial \bar{h}_T}{\partial t} \qquad (2.3)$$

where ϕ_x, ϕ_y, and ϕ_s are flow factors which describe the affect the asperities have on the lubricant flow in different directions. The details of the nomenclature and how Eq. 2.3 is used is discussed in Section 3.1. Patir and Cheng give formulations for the flow factors as functions of surface roughness, asperity orientation (longitudinal or transverse) and film height.

2.4 Thermoviscous Distress

When a fluid film separates two rough surfaces from contacting the friction and heat generation will decrease, thus hindering the occurrence of a TEI. The fluid film separation provided by hydrodynamic lift can be characterized by the Stribeck curve in Figure 2.3. TEI is not likely to occur if the bearing is operating in the full film region to the far right of Stribeck curve. However, if viscosity decreases due to heat generation

and causes the bearing to operate in the boundary lubrication regime on the far left of the Stribeck curve, TEI becomes much more likely.

There are two separate mechanisms which eventually cause distress at high rotational speeds. The first is the TEI which will cause the geometry to change and the temperature to increase drastically. The second is a physical phenomena here labeled as the thermoviscous distress (TVD) which happens when the temperature of the fluid increases and the viscosity decreases, and in turn the hydrodynamic load carrying capacity decreases.

Fohl and Uetz (1976) discuss TVD (although not using the same nomenclature) in their work as a cause of increased wear and seizure. In their experimental work they found that the load required to cause seizure decreases with fluid and surface temperature. They also found that the wear rate will increase with temperature. They cite that these trends are caused by two mechanisms: 1) TVD and 2) a change in material properties with temperature. Czichos (1976) also documents fluid film failure due to an increase in the bulk oil temperature in EHD contacts.

2.5 Elasto-plastic Asperity Contact

One of the earliest models of elastic asperity contact is that of Greenwood and Williamson (1966). This (GW) model uses the solution of the frictionless contact of an elastic hemisphere and a rigid flat plane, otherwise known as the Hertz contact solution (Timoshenko and Goodier, 1951), to stochastically model an entire contacting surface of asperities with a postulated Gaussian height distribution. The GW model assumes that the asperities do not interfere with adjacent asperities and that the bulk material below the asperities does not deform. The Gaussian distribution is often approximated by an exponential distribution to allow for an analytical solution, although Green (2000) has analytically solved the integrals using the complete Gaussian height distribution. Supplementing the GW model, many elasto-plastic asperity models have been devised [Kogut and Etsion (2002), Chang et al. (1987), Zhao et al. (2000)]. Many of these elasto-plastic models make use of the fully plastic truncation model, which is probably incorrectly attributed to Abbott and Firestone (1933), while Greenwood and Tripp derive a very similar model (1971). Although these previous models have proven useful, they contain clear pitfalls which may be detrimental to their validity.

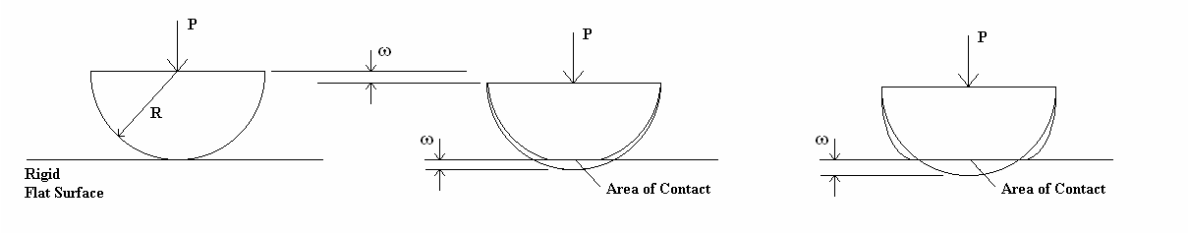

(a) (b) (c)

Figure 2.5: Spherical contact model before contact (a), during mostly elastic deformation (b), and during mostly plastic deformation (c).

The Hertzian solution (Timoshenko and Goodier, 1951) provides closed-form expressions to the deformations and stresses of two spheres in a purely elastic contact. The two spheres may have different radii and different elastic properties. However, the closed-form solutions render an equivalent case where a single elastic sphere, having an equivalent elastic modulus, E', and an equivalent radius, R, is in contact with a rigid flat (see Fig. 2.5, and Eqs. (2.4-2.8) that follow). The interference, ω, can be described as the distance the sphere is displaced normally into the rigid flat. The Hertz solution assumes that the interference is small enough such that the geometry does not change significantly. The solution also approximates the sphere surface as a parabolic curve with an equivalent radius of curvature at its tip. The resulting equations for contact radius and load from the Hertz solution are:

$$\overline{A}_E = \pi R\omega \tag{2.4}$$

$$\overline{P}_E = \frac{4}{3} E'\sqrt{R}(\omega)^{3/2} \tag{2.5}$$

where

$$\frac{1}{E'} = \frac{1-\nu_1^2}{E_1} + \frac{1-\nu_2^2}{E_2} \tag{2.6}$$

$$\frac{1}{R} = \frac{1}{R_1} + \frac{1}{R_2} \tag{2.7}$$

and E_1, ν_1, R_1, E_2, ν_2, R_2, are the elastic properties and radii of sphere 1 and 2, respectively.

Abbott and Firestone (1933) are traditionally credited with the fully-plastic asperity contact model that is described next, however the model does not appear explicitly in their work. The model assumes that under fully plastic conditions the area of contact of an asperity pressed against a rigid flat can be approximately calculated by truncating the asperity tips as the rigid flat translates an interference, ω. For a hemisphere, this approximated fully plastic area is given by:

$$\bar{A}_{AF} = 2\pi R\omega \tag{2.8}$$

Using Eq. (2.8) the contact load of the hemispherical asperity is simply the contact area multiplied by the average contact pressure, which in this case is the hardness, since the contact is assumed to be fully plastic. The approximated fully plastic contact force is thus:

$$\bar{P}_{AF} = 2\pi R\omega H \tag{2.9}$$

From this point forward, Eqs. (2.8) and (2.9) will be referred to as the AF model. Greenwood and Tripp (1971) also independently model fully plastic contact between hemispheres using a similar truncation method.

Chang et al. (1987), (CEB model) approximated elasto-plastic contact by modeling a plastically deformed portion of a hemisphere using volume conservation. The CEB model assumptions are discussed above, namely: (1) that the hemisphere deformation is localized to near its tip, (2) the hemisphere behaves elastically below the critical interference, ω_c, and fully plastically above that value, and (3) the volume of the plastically deformed hemisphere is conserved. Using these assumptions the following approximations for contact area and force in the elastic-plastic range ($\omega/\omega_c>1$) are analytically derived as

$$\overline{A}_{CEB} = \pi R\omega\left(2 - \omega_c / \omega\right) \tag{2.10}$$

$$\overline{P}_{CEB} = \pi R\omega\left(2 - \omega_c / \omega\right)KH \tag{2.11}$$

where K is the hardness factor given by $K = 0.454 + 0.41\,\nu$. Also, the critical interference used in the CEB model, is given by:

$$\omega_c = \left(\frac{\pi KH}{2E'}\right)^2 R \tag{2.12}$$

where the hardness is assumed to be $H=2.8\cdot S_y$. However, the CEB is fundamentally flawed and contains a discontinuity at ω_c.

Zhao et al. (2000) devised an elasto-plastic (ZMC) model, which interpolates between the elastic and fully plastic (AF) models. The ZMC model divides the interference into three segments: (1) elastic (Hertz), (2) elasto-plastic

(using a template) and (3) fully plastic (AF). A template function satisfies continuity of the function and its slope at the two transitions.

The most widely used prediction for the hardness is Tabor's (1951), who calculates it to be approximately three times the yield strength for most cases. More recently, Mesarovic and Fleck (2000) studied the contact of elastic-perfectly plastic spheres using the finite element analysis. They plot $P/(A \cdot S_y)$ as a function of a/R, i.e., the ratio of the average contact pressure to the yield strength versus the radius of the contact (or equivalently the deformation). An interesting trend then emerges, but is not theoretically explained. The current work produces precisely the same trend and gives a thorough physical explanation.

Kogut and Etsion (2002) also performed a FEM analysis of the same case of an elastic-perfectly plastic sphere in contact with a rigid flat. Again in their analysis, the value of H is set to be fixed at $2.8 \cdot S_y$. Notably, the slope of $P/(A \cdot S_y)$ is not zero (it still increases monotonically) at the point where full plasticity is assumed. Their work gives a very detailed analysis of the stress distribution in the contact region, and empirical expressions are provided for the contact area, the contact force, and the average contact pressure. The resulting equations have a discontinuous slope at $\omega^*=6$, and they describe the deformation only up to $\omega^*=110$, at which point full plasticity is assumed. These are given in a piece-wise form:

For $1 \le \omega^* \le 6$

$$\overline{P}^*_{KE} = 1.03\left(\omega^*\right)^{1.425}$$

$$\overline{A}^*_{KE} = 0.93\left(\omega^*\right)^{1.136}$$

$$\left(\frac{\overline{P}}{\overline{A} \cdot S_y}\right)_{KE} = 1.19\left(\omega^*\right)^{0.289} \tag{2.13}$$

For $6 \le \omega^* \le 110$

$$\overline{P}^*_{KE} = 1.40\left(\omega^*\right)^{1.263}$$

$$\overline{A}^*_{KE} = 0.94\left(\omega^*\right)^{1.146}$$

$$\left(\frac{\overline{P}}{\overline{A} \cdot S_y}\right)_{KE} = 1.61\left(\omega^*\right)^{0.117} \tag{2.14}$$

These equations have a discontinuous slope at ω^*=6, and they describe the deformation only up to ω^*=110, at which point full plasticity and the AF model is assumed. At values ω^*<1 the Hertz contact solution is assumed.

The original CEB work calculated the various integrals numerically because of the perceived complexity confederated by the Gaussian distribution. To bypass such cumbersome numerical integrations the Gaussian distribution has commonly been replaced with simplified exponential distribution functions to allow for closed-form solutions (see GW (1966), Etsion and Front (1994), Polycarpou and Etsion (1999), Hess and Soom (1992,1993), Liu et al. (2000). Recently, Green (2002) solved analytically the integrals for the CEB model using the complete Gaussian height distribution. In the current work the uncompromised Gaussian distribution is used, and the integrals are evaluated numerically.

As mentioned above, rough surfaces can be modeled as a collection of individual asperities of various heights. These asperities are then categorized by a few statistical parameters describing the surface. First, the GW model assumes that all asperities have the same radius of curvature, R. Then, the distance between the surfaces can be described in two ways: (1) the distance between the mean of the surface heights, h, and (2) the distance between the mean of the surface asperities or peaks, d. These values are related by

$$h = d + y_s \tag{2.15}$$

The value of y_s is derived by Front [17] and given as:

$$y_s = \frac{0.045944}{\eta R} \tag{2.16}$$

where η is the area density of the asperities.

When the surfaces are pressed together, some of the asperities will interfere a distance ω with the opposing surface. Since the surfaces cannot penetrate each other, ω is also the distance each asperity compresses perpendicular to the surfaces. The interference is defined as:

$$\omega = z - d \tag{2.17}$$

where the height of each asperity is defined by a distance, z, from the mean asperity height. The heights of the asperities are also assumed to have a statistical distribution function, $G(z)$. The nominal contact area, A_n, is the area of the surface upon which the

asperities in contact are scattered. Thus, the number of asperities on the contacting surface can be found by multiplying the nominal surface area by the area density of the asperities:

$$N = \eta A_n \tag{2.18}$$

Then, the total number of asperities in contact is defined as:

$$N_c = \eta A_n \int_d^\infty G(z)dz \tag{2.19}$$

The individual asperity contact area, $\overline{A}$, and force, $\overline{P}$, are functions of each asperity's interference, ω. Thus, the contribution of all asperities of a height z to the total contact area and total contact force can be calculated as:

$$A'(z) = \eta A_n \overline{A}(z-d)G(z) \tag{2.20}$$

$$P'(z) = \eta A_n \overline{P}(z-d)G(z) \tag{2.21}$$

Then, the total area of contact and total contact force between the surfaces is found by simply integrating Eq. (2.20) and Eq. (2.21) over the entire range of asperity contact:

$$A(d) = \eta A_n \int_d^\infty \overline{A}(z-d)G(z)dz \tag{2.22}$$

$$P(d) = \eta A_n \int_d^\infty \overline{P}(z-d)G(z)dz \tag{2.23}$$

The GW model then assumes that the hemispherical asperities deform elastically and are defined by the Hertz elastic solution [18].

Thus far, the models had not taken into account anisotropic rough surfaces, in which the asperities may be elongated. So and Liu(1991) modeled an anisotropic rough surface by treating the asperities as ellipsoids. They concluded that the behavior of anisotropic and isotropic surfaces differ little while they are in the realm of mostly elastic deformation. However, they showed that as deformations become more plastic, the real area of contact of the anisotropic surfaces are less than the equivalently rough isotropic surfaces.

All the above models used the results of single asperities to stochastically model surfaces with many asperities with given surface properties. Another method is to discritize a real surface's topography or to numerically generate surfaces of equivalent surface parameters and then numerically simulate the contact between them. These deterministic models have been created in two-dimensions(Lee and Cheng, 1992), and in three dimensions, elastically(Ren and Lee, 1993) and elasto-plastically(Ren and Lee, 1996). These models require much more computation time and resources than the other models since entire surfaces are being meshed and modeled.

None of the models described have taken into account the traction force caused by sliding friction or the interference between asperities of surfaces moving in parallel to one another. In 2000, Faulkner and Arnell developed an elasto-plastic finite element asperity model which included sliding friction. This was performed by modeling the three-dimensional spherical asperities at various distances apart while still in sliding contact. The data was then statistically used to model an entire surface of asperities, as was done in the GW model. The major problem with this model was that it was

computationally intensive and took many hours to execute (approximately 960 hrs on a Pentium 200MHz PC).

Additionally, the reversed case of a rigid sphere indenting a deformable half-space has been thoroughly investigated experimentally [Tabor (1951), Francis (1976), Oliver and Pharr (1992)] and numerically [Mesarovic and Fleck (2000), Kral et al. (1993, 1995a, 1995b), Streator (2003)]. Work has also been done on the contact of a rigid cylinder contacting and elasto-plastic layered half-space (Tian and Saka, 1991). More generally, various experimental and numerical works have investigated other contacting geometries and hardness tests [Tabor (1951), Oliver and Pharr (1992), Giannakopoulos et al.(1994)]. The two works by Barber et al. (2000) and Liu et al. (1999) provide a more in depth look at past and more recent findings in the field of contact mechanics. Perhaps a most important and relevant work is by Johnson (1968) who experimentally measured the plastic strains between copper cylinders and spheres. Johnson's experimental results compare favorably with the findings of the current work. Despite the extensive body of works, the results, trends and theories presented in the present work, to the authors' knowledge, have not yet been thoroughly documented.

2.6 Mist Lubrication Temperature/Viscosity Model

Within the transmission the lubricant is applied by small holes in the shaft at the center of the planetary gear set. Centrifugal forces cause the fluid in these holes to travel toward the outer radius of the assembly. The fluid thus may interact with gears, rotating

components and other bearings before supplying any washer bearing in the assembly. Thus the lubricant may aerate or gather bubbles within it that are not expelled before it is used to lubricate a washer bearing. These bubbles will affect the behavior and load carrying capacity of the bearing.

Work by Nikolajsen(1999a) formulates an analytical model of aerated oil, which can be used in fluid-film bearing models. The model incorporates the affects of surface tension on the bubbles and the expected decrease in viscosity due to less viscous air being mixed in with the oil. However, as Nikolajsen shows, the viscosity can actually increase with increased aeration of the oil and is caused by the surface tension of the bubbles. Thus, mist or oil aeration can increase the load carrying capacity of a bearing. Where μ_{af} and ρ_{af} are the approximated viscosity and approximated density of the aerated oil, respectively, the resulting formulas of Nikolajsen's model are

$$\rho_{af} = \frac{(1+\eta)(\bar{p}+2\bar{\sigma}/\bar{r})}{(\eta+\bar{p}+2\bar{\sigma}/\bar{r})}\rho_{oil} \tag{2.25}$$

$$\mu_{af} = \mu_1 + \mu_2 \tag{2.26}$$

$$\mu_1 = \frac{\rho_{af}}{\rho_{oil}(1+\eta)} \tag{2.27}$$

$$\mu_2 = \frac{\pi^2 \sigma h_{in}^{3/2} r^2}{\sqrt{2h}\mu_{oil} u d_{in}^3} \tag{2.28}$$

where $\bar{p}$ is the normalized fluid pressure, $\bar{\sigma}$ is the normalized surface tension, η is the mass ratio of air to oil, r is the average bubble radius, u is the relative speed of the surface, d_{in} is the average distance between bubbles, and h is the film thickness. The summed value μ_1 accounts for the decrease in viscosity due to the air bubbles and μ_2 accounts for the increase in viscosity due to the surface tension of the bubbles. The

parameter h_{in} is the maximum film thickness of the bearing, otherwise known as the inlet height. All these values except the bubble radius are known or can be easily approximated. The average bubble radius and mass ratio is not so easily approximated without actually measuring the bubbles in the film, which is very difficult to do.

The one drawback of this model is that it is isothermal and does not consider the affect of temperature on the viscosity. This can be accounted for by substituting in the lubricant viscosity as predicted by the Roeland's equation (1966), which models empirically the effects of temperature on viscosity. This pressure independent form of Roeland's equation is given as

$$log(log\mu + 1.2) = -S_o log(1 + \frac{t_m}{135}) + log(G_o) \tag{2.29}$$

and solving for the viscosity, μ, yields

$$\mu = \mu_\infty 10^{G_o(1+t_m/135)^{-So}} \tag{2.30}$$

where μ_∞=6.31 x 10^{-5} N·s/m^2 and the rest of the variables can be found by fitting the formula to experimentally obtained viscosity values with respect to changing temperatures. Nikolajsen(1999b) used his model to calculate the effect of aerated lubrication on the operation and load support of a journal bearing. As expected, since the viscosity actually increases with bubble density, the load support did as well. This increase in viscosity has been confirmed by a few empirical investigations, but most noteworthy is Hayward(1961), which clearly showed that viscosity increased with bubble density. Of course, if the bubble density is increased until the oil begins to behave more like air, then the viscosity drastically decreases.

In 1994, Shamim conducted an experimental study of the mist lubrication of angular contact ball bearings under an axial thrust and its effect on the bearing life in comparison to sump lubrication. Shamim found that the life of the bearings was actually increased and the effective friction coefficient lowered by the use of mist lubrication over an oil sump. Although this is not a fluid film bearing, it does suggest that mist lubrication can be an effective method of applying lubrication.

2.7 Elastic and Thermal Deformation and the Boundary Element Method

Currently, the most common numerical modeling method in engineering is the finite element method. The finite element method provides a way to model an object and its governing equation (elasticity, energy, etc.) by breaking it up into a finite number of elements. The elements individually approximate the modeled equation within each element and satisfy its local boundary conditions, whether from adjacent elements or an external load. The finite element method is robust and can provide a solution to many engineering problems, although for complex shapes and non-linear models, which must be solved iteratively, the method can be computationally costly. For some applications, the boundary element method can be much more efficient, particularly in thermo-mechanical problems in tribology, where load and heat sources originate at the surface (boundary).

In comparison, the boundary element method (BEM) requires that only the surface of the modeled object be meshed. This in turn, results in a smaller set of equations then would have resulted from a FEM mesh of the object. The BEM essentially numerically integrates the exact linear elastic solution of a given geometry and

material to elements defined on the surface of the object. This integration need only be performed once for a given configuration. Thus the solution can then be used for successive iterations in order to predict the deformations and stresses at the washer surface under whatever boundary pressures, temperatures or other conditions that exist. The derived equations for the BEM, based on a given geometry and prescribed material properties is similar to the FEM and is written as

$$[\mathbf{K}]\{\mathbf{u}\}=\{\mathbf{F}\} \qquad [10]$$

where [**K**] is the resulting stiffness matrix, {**u**} is a vector of the displacements on the surface of the modeled domain and {**F**} is a vector of the traction forces on the surface of the modeled domain. So as far as end formulation is concerned, the only difference between the FEM and BEM is that there are no displacements or tractions, unknown or prescribed, on the inside of the modeled domain. A more lengthy derivation can be found in many textbooks, including the recently published book by Beer(2001).

The first main drawback of the boundary element method is that unlike the banded stiffness matrix of the FEM, the BEM matrix is usually fully populated. Also, the BEM requires more pre-processing calculations. Also, the BEM method does not solve initially for any information on the inside of the object. However, in the current research, and in Tribology in general, the stresses and strains inside an object are not required. These inner values can be solved for in post-processing calculations if needed. In addition, if the material behaves nonlinearly (i.e. elasto-plastically) than the inside of the object must be meshed. Then the BEM loses its advantages. Another problem is that the BEM is not effective at modeling thin objects without requiring a very dense mesh.

CHAPTER 3

ELASTO-PLASTIC CONTACT OF HEMISPHERES AND ROUGH SURFACES

3.1 *Introduction*

It is believed from experience and experimental results that the washer bearing does not always operate under a full film regime. Since the load on the bearing is not axisymmetric it is likely that a portion of the bearing is in the boundary lubrication regime. To model the contact and friction in this area, an elasto-plastic asperity contact model is created. This model predicts the contact pressure on the surface by modeling the contact between asperities on the surfaces.

Since in reality all engineering surfaces are rough to some degree, the modeling of the contact between these rough surfaces is very important. Modeling the contact between rough surfaces leads to an improved understanding of the friction, wear, thermal and electrical conductance between surfaces. When loading presses two rough surfaces together, only the peaks or asperities on the surface will be in contact. Thus, the asperities or peaks of the surfaces often carry very high loads. These high loads will often cause yielding in the surface material and thus purely elastic contact models of rough surfaces are not always adequate.

Section 3.2 presents a finite element study of elasto-plastic hemispherical contact with a rigid flat. The material is modeled as elastic-perfectly plastic. The results are

normalized such that they are valid for macro contacts (e.g., rolling element bearings) and micro contacts (e.g., asperity contact), although micro-scale surface characteristics such as grain boundaries are not considered. In the former, e.g., rolling element bearings, load may be high and the deformations excessive. In the latter, e.g., asperity contact, a model on the micro-scale is of great interest to those investigating friction and wear. In addition, the real area of contact of such asperities will affect the heat and electrical conduction between surfaces. In either scale contact is often modeled as a hemisphere against a rigid flat.

The numerical results are compared to other existing models of spherical contact, including the fully plastic truncation model (often but probably incorrectly attributed to Abbott and Firestone, 1933) and the perfectly elastic case (known as the Hertz contact). This work finds that the fully plastic average contact pressure, or hardness, commonly approximated to be a constant factor of about three times the yield strength, actually varies with the deformed contact geometry, which in turn is dependant upon the material properties (e.g., yield strength). These results are not represented, largely overlooked, or not theoretically explained in previous works. Experimental and analytical results have also been shown to compare well with the current work. The results are fit by empirical formulations for a wide range of interferences (displacements which cause normal contact between the hemisphere and rigid flat) and materials for use in other applications.

In Section 3.3 the elasto-plastic result for a single hemisphere is used to statistically model an entire rough surface of many asperities. The results of the statistical model provide formulations for the average contact pressure as a function of

the distance separating the surfaces. These formulations are implemented in the bearing numerical simulation in Chapter 4.

Section 3.4 also presents the finite element predictions of the residual stresses and strains that are formed after an elasto-plastic hemispherical contact is unloaded. Although these results are not used in the thrust washer bearing numerical simulation, they are important in the study of heavily loaded cyclic bearing contacts, and the condition of rough surfaces after unloaded from elasto-plastic contact. The FEM produces contours for the normalized axial and radial displacements as functions of the removed interference depth and location on the surface of the hemisphere. Contour plots of the von Mises stress and other stress components are also presented to show the formation of the residual stress distribution with increasing plastic deformation. This work shows that high residual von Mises stresses appear in the material pile-up near the edge of the contact area after complete unloading. Values are defined for the minimum normalized interference, that when removed, results in plastic residual stresses. This work also defines an interference at which the maximum residual stress transitions from a location below the contact region and along the axis of symmetry to one near to the surface at the edge of the contact radius (within the pile-up).

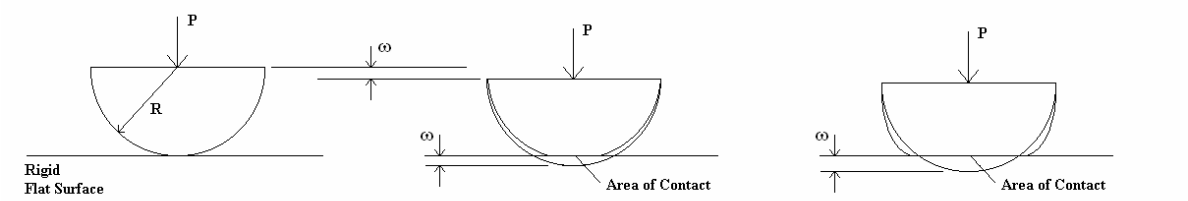

(a) (b) (c)

Figure 3.1: Spherical contact model before contact (a), during mostly elastic deformation (b), and during mostly plastic deformation (c).

3.2 *Finite Element Model of Elasto-Plastic Hemispherical Contact*

This section uses the finite element method to model the case of an elastic-perfectly plastic hemisphere in frictionless contact with a rigid flat (see Fig. 3.1). The von Mises criterion defines the yielding of the material. The resulting numerical data is also fitted by continuous functions that capture deformations all the way from purely elastic to fully plastic conditions. These expressions, that have a relatively low statistical error, may be used in other applications whether they are on macro or micro scales. For example, a statistical model for asperity contact (such as Greenwood and Williamson, 1966) can greatly benefit from such expressions. Section 3.3 implements the single elasto-plastic hemispherical contact model in a statistical representation of rough surfaces in contact

The finite element analysis presented in this work produced different results than the similar Kogut and Etsion (KE) model (2003). The current work accounts for geometry and material effects which are not accounted for in the KE model. Most notable of these effects is that the predicted hardness is not a material constant as suggested by Tabor (1951) and many others; rather hardness changes with the evolving

contact geometry and the material properties as proven in this work. Moreover, the current work uses a mesh that is orders of magnitude finer than that in the KE model which was mandated by mesh convergence. The current work models deformation surpassing $\omega/\omega_c=110$ (the limit of KE), and likewise models five different material strengths, S_y, that showed a markedly different behavior in the transition from elasto-plastic to fully plastic deformation. The formulations derived in the current work are also continuous for the entire range of modeled interferences, whereas the KE model is discontinuous in two separate locations.

3.2.1 Critical Interference

While in the elastic regime, the stresses within the hemisphere increase with P and ω. These stresses eventually cause the material within the hemisphere to yield. The interference at the initial point of yielding is known as the critical interference, ω_c. The current work derives this critical interference analytically using the von Mises yield criterion (VM). The following equations, for the critical interference, contact area and load are all independent of the hardness, which the current work shows not to be constant with respect to S_y. This is a notable improvement compared to previous elasto-plastic contact models [Chang et al. (1987), Zhou (2000) Kogut and Etsion (2003)]. The derivation is given in Appendix A, resulting in:

$$\omega_c = \left(\frac{\pi \cdot C \cdot S_y}{2E'} \right)^2 R \tag{3.1}$$

where C is derived in Appendix A to be

$$C = 1.295\exp(0.736\nu) \tag{3.2}$$

The Poisson's ratio, ν, to be used in Eq. (3.2) is that of the material which yields first. For ν=0.32, as is used in this section, Eq. (3.2) results in C=1.639. While from an engineering perspective the corresponding values given by Eq. (3.2) and Eq. (2.12) are very close, the CEB model is limited to this fixed relationship between the hardness and the yield strength. It should be noted that Eq. (3.2) is not limited by any such assumption. Likewise the CEB model contains a discontinuity at ω_c.

The critical load, P_c, is then calculated from the critical interference, ω_c, by substituting Eq. (3.1) into Eq. (2.5). The resulting critical contact force at initial yielding is thus:

$$P_c = \frac{4}{3}\left(\frac{R}{E'}\right)^2\left(\frac{C}{2}\pi \cdot S_y\right)^3 \tag{3.3}$$

Similarly, the critical contact area is calculated from Eq. (2.4) and is given by:

$$A_c = \pi^3\left(\frac{CS_yR}{2E'}\right)^2 \tag{3.4}$$

These critical values predict analytically the onset of plasticity. These values are, therefore, chosen to normalize the results of all the models. The normalized parameters are:

$$\omega^* = \omega/\omega_c \tag{3.5}$$

$$P^* = P / P_c \tag{3.6}$$

$$A^* = A / A_c \tag{3.7}$$

Normalizing the Hertzian contact area (Eq. (2.4)) and force (Eq. (2.5)), and the AF contact area (Eq. (2.8)) and force (Eq. (2.9)), by the critical values given in Eqs. (3.3) and (3.4), results in the following simplified expressions:

$$A_E^* = \omega^* \tag{3.8}$$

$$P_E^* = \left(\omega^*\right)^{3/2} \tag{3.9}$$

$$A_{AF}^* = 2\omega^* \tag{3.10}$$

$$P_{AF}^* = \frac{3\mathrm{H}}{CS_y}\omega^* \tag{3.11}$$

3.2.2 Finite Element Model

To improve upon the efficiency of computation, an axisymmetric 2-D model is used. The present study utilizes the commercial program ANSYS™, while ABAQUS™ produces the same results. Kogut and Etsion (2003) also use ANSYS™. However, the mesh (see Fig. 3.2) in the current analysis is orders of magnitude more refined, as necessitated by mesh convergence (Reddy, 1993).

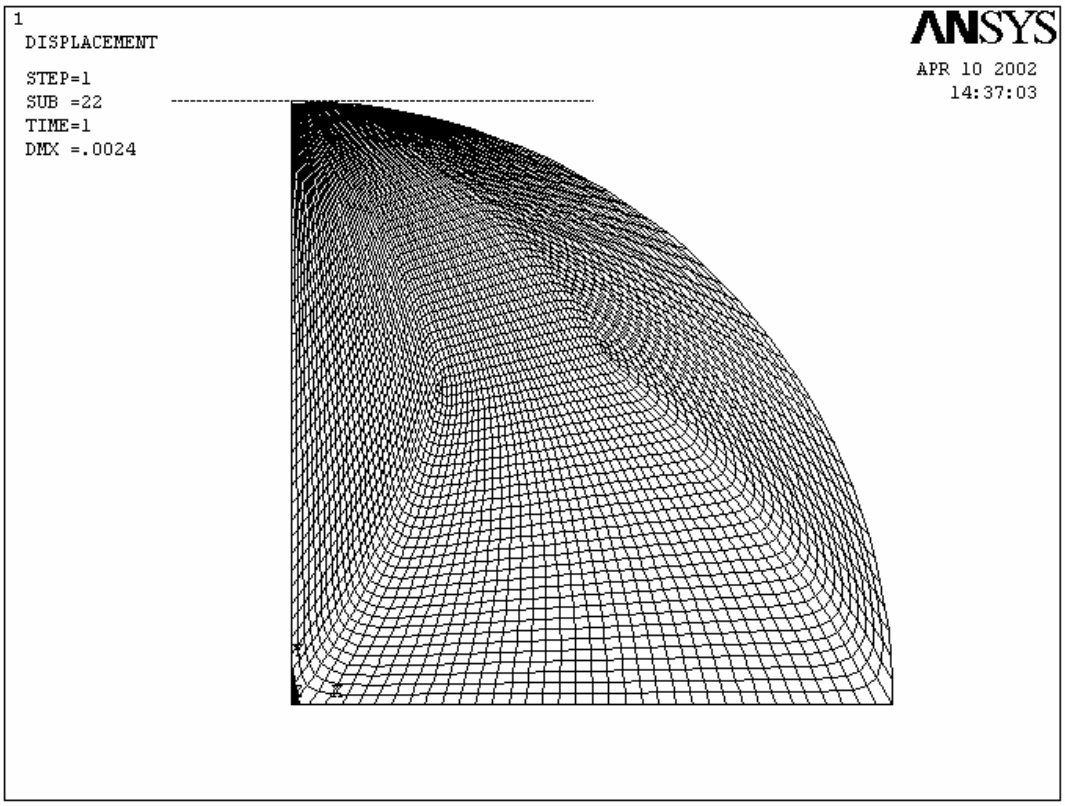

Figure 3.2: Finite element mesh of hemisphere generated by ANSYS™.

The model refines the element mesh near the region of contact to allow the hemisphere's curvature to be captured and accurately simulated during deformation. The model uses quadrilateral, four node elements to mesh the hemisphere, but the results have also been confirmed to yield identical results using a mesh of eight node elements. The resulting ANSYS™ mesh is presented in Fig. 3.2, where ABAQUS™ produces a similar mesh. The quarter-circle mesh represents the axisymmetric hemispherical body, and the straight line represents the rigid plane.

The contact region is meshed by 100 contact elements. These are in essence very stiff springs attached between surface nodes, and they activate only when penetration onset into the rigid flat is detected. This contact region varies in order to fit the expected

area of contact. The contact elements thus apply forces to the nodes of the elements that are in contact.

The contact force acting on the hemisphere is found from the reaction forces on the hemisphere base nodes that retain the desired interference. The radius of the contact area is determined by finding the edge of the contact, or the location of the last activated contact element.

In order to validate the model, mesh convergence must be satisfied. The mesh density was iteratively increased by a factor of two until the contact force and contact area differed by less than one percent between iterations. The resulting mesh consists of at least 11,101 elements, since the number of meshed elements will vary with the expected region of contact. The stiffness of the contact elements was also increased by an order of magnitude in successive iterations until the contact force solution differed by no more than one percent between successive iterations.

In addition to mesh convergence, the model also compares well with the Hertz elastic solution at interferences below the critical interference. The contact force of the model differs from the Hertzian solution by no more than two percent. The contact radius differs by a maximum of 8.1%, but the average error is only 4.4%. When the contact areas are calculated from the radii, the maximum error increases to 17%. The smaller error in the contact force is attributed to overall force balance (static equilibrium) enforced by the FEM packages. However, the contact radius is obtained from a discrete mesh (which has a finite resolution). Moreover, the magnitude of the contact element stiffness also has some effect upon such radii, although not on the overall force balance. Generally, though, the differences are small enough that the FEM solution practically

conforms to the Hertzian solution at interferences below critical (and even slightly above).

There are two ways to simulate the contact problem. The first applies a force to the rigid body and then computes the resulting displacement. The second applies a displacement and then computes the resulting contact force. In both methods, the displacement, stress, and strain in the elastic body can be determined, as well as the contact pressure. In this model the latter approach is used, where the base nodes of the hemisphere are displaced a distance or interference, ω, approaching the rigid flat surface. The radial displacements of the base nodes are restricted. This method is used because the resulting solution converges more rapidly than the former.

The contact problem and the elasto-plastic material property make the analysis highly non-linear and difficult to converge. An iterative scheme is used to solve for the solution, and many load steps are used to enhance solution convergence. Initially, a small interference is set of the total interference and then it is incremented after the load step converges. This continues until a converged solution is found for the desired interference.

3.2.3 Numerical Results and Discussion

The results of the described finite element hemisphere model are presented for a variety of interferences. While the elastic modulus and Poisson's ratio are held constant at 200 GPa and 0.32, respectively, five different material yield strengths are modeled. These are designated Mat.1 through Mat.5 corresponding to their yield strengths which are 0.210 GPa, 0.5608 GPa, 0.9115 GPa, 1.2653 GPa, and 1.619 GPa. The yield strengths

cover a typical range of steel materials used in engineering (Shigley, 1989). The generated numerical data for five steel materials is given in Table 3.1. Once the mesh is generated, computation takes from ten minutes for small interferences to several hours for large interferences on a 2.5 GHz PC. For the weaker materials it is difficult to calculate the results for small normalized interferences because the actual applied interference is very small and requires a very refined mesh within the contact region. Although the results for only five sets material properties are presented here, work has been done to confirm the results for properties modeling materials such as aluminum, bronze, copper, titanium and malleable cast iron.

The dimensionless contact area is normalized by the Hertz solution (Eq. (3.8)) and plotted as functions of ω^* in Fig. 3.3. The data is presented on a log scale to capture the entire range of interferences. While $\omega^* < 1.9$ the finite element model agrees well with the Hertz solution ($A^*/\omega^*=1$). This is likely because the plastic deformations are still relatively small such that the Hertz solution is not dramatically affected. As the hemisphere begins to plastically deform below the surface, the hemisphere weakens and thus does not retain its shape as well as if it were perfectly elastic throughout. Thus the area of contact eventually becomes larger in the elasto-plastic case than in the perfectly elastic case. The FEM model values for the dimensionless contact area continue to increase with interference even past Abbot and Firestone's fully plastic (AF) model (1933) at $A^*/\omega^*=2$. Since the AF model is based on the truncation of the contacting geometries, it does not model the actual deformation of the hemisphere. It seems reasonable then that the FEM solution for contact area could continue past the AF model.

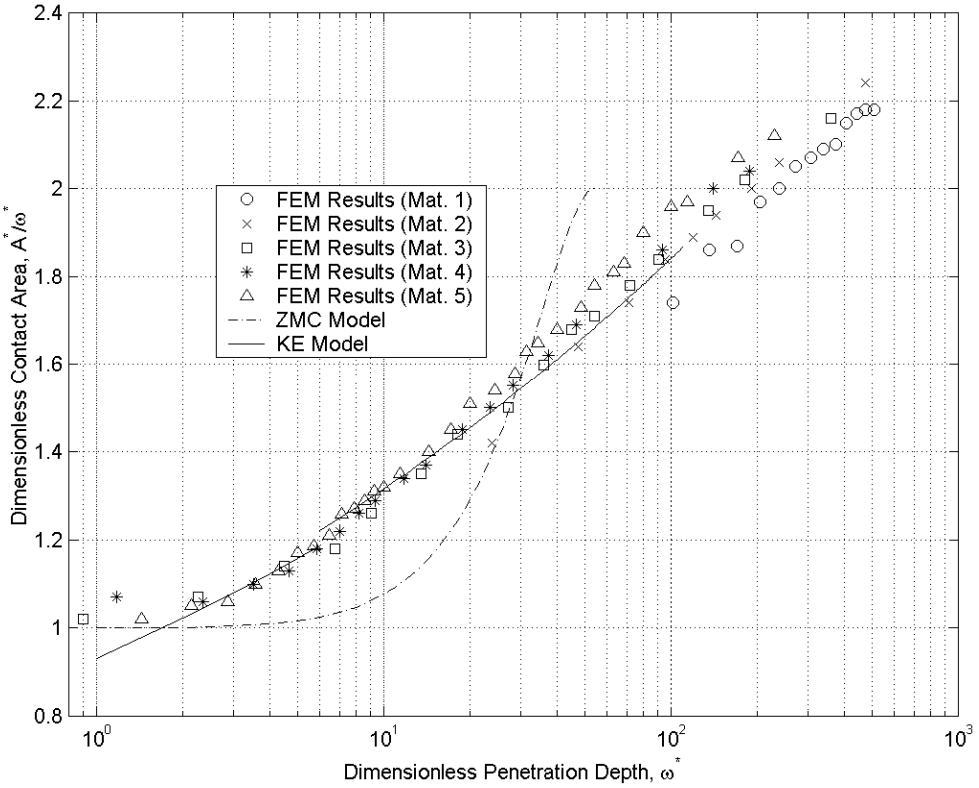

Figure 3.3: FEM predicted contact area.

Overall though, the FEM predicted contact area generally follows the Hertz elastic solution near the critical interference and then increases past the AF model as the interference increases. Later in this work, this trend will be followed by empirical formulations fitted to the data. The FEM results also indicate a material dependence of the normalized contact area. Since the contact area is calculated by counting the number of elements in contact, and there are only a finite number of such elements, there is an inherent error in the data. The scatter in the data can be attributed mostly to this, and to the fact that the FEM is yet a discrete formulation.

For the contact area, all the models follow the same general trend, but they differ in magnitude. The model (ZMC) by Zhou et al. (2000) follows the Hertz elastic solution at low and moderate interferences, but abruptly migrates to the AF model before the current model and the KE model. The KE model and the current empirical model also agree fairly well on average, except at large interferences. The KE model clearly shows a slight discontinuity at ω^*=6 and then terminates at ω^*=110. The KE model does not connect with the Hertz elastic solution at the critical interference depth. Also, the nondimensional KE model is material independent such that its contact area falls between the data of materials 1 and 5 of this work.

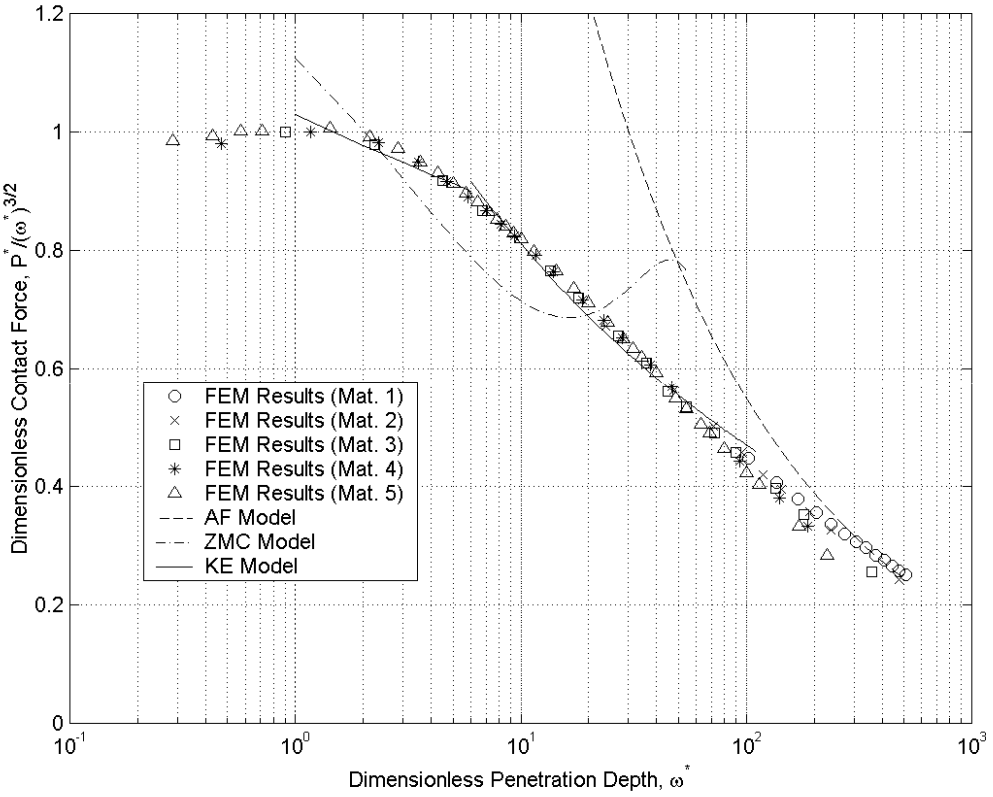

Figure 3.4: FEM predicted contact force.

The dimensionless contact force is normalized by the Hertz solution (Eq. (3.9)) and plotted as a function of ω^* in Fig. 3.4. This plot uses a log scale to capture the entire range of interferences. The normalized contact force $(P^*/(\omega^*)^{3/2})$ calculated from the current model follows precisely the Hertz elastic solution $(P^*/(\omega^*)^{3/2}=1)$ at small interferences. With increasing interference the current model eventually increases toward the AF model. It is interesting to note that the AF model predicts higher loads at small interferences than the Hertzian solution, but eventually crosses over to become the lesser of the two. This is because the AF model assumes a constant pressure distribution, which is equal to the hardness, while the average pressure of the Hertzian solution is initially

lower than the hardness. At higher interferences, the FEM data displays a material dependant behavior.

The non-dimensional contact force trends of all the models are similar; however, the ZMC again crosses to the AF model prematurely. At low interferences, the KE and ZMC models predict a contact force that is greater than the elastic model. This cannot be the case, as the yield strength of the material limits the stiffness of the hemisphere. Again the KE model shows a discontinuity at ω^*=6 and then terminates at ω^*=110. Generally the KE model and the current FEM results are very similar. At about ω^*=50 the KE model crosses over the current model and continues to overestimate the contact force until ω^*=110. The KE and ZMC models also fail to capture the material dependence effects at large interferences.

The average contact pressure to yield strength ratio, $P/(A \cdot S_y)$, is calculated from the data and plotted in Fig. 3.5, alongside the Hertz contact solution. The Firestone and Abbott [9] fully plastic (AF) model is represented by the horizontal line at $P/(A \cdot S_y)$=3. The average contact pressure should approach the hardness of the material as the contact becomes fully plastic. It is widely accepted that the hardness is approximated by $3 \cdot S_y$ (Tabor, 1951). It becomes evident in this plot that this is not always the case. From the data it seems that hardness is not a constant material property. The cause of this trend will be discussed later in greater detail. The work by Mesarovic and Fleck (2000) also confirms this trend, but does not address the trend theoretically.

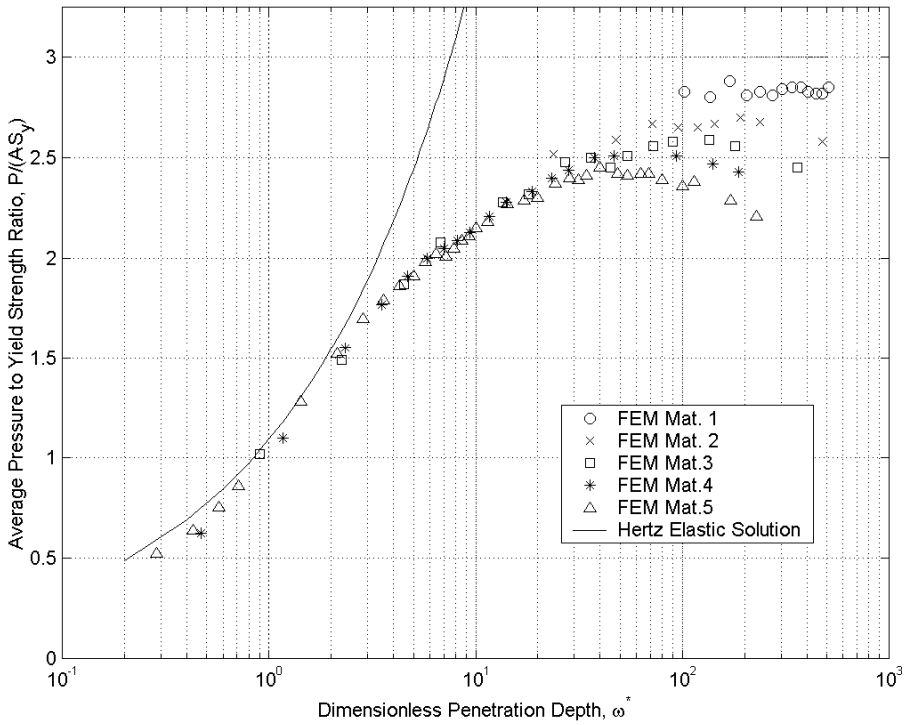

Figure 3.5: Average contact pressure to yield strength ratio.

3.2.4 Empirical Formulation

General empirical approximations of the FEM data are desired for use at any deflection and for any set of material properties. This will help designers in a variety of single contact problems, and it will be readily incorporated into statistical models to model rough surfaces.

As mentioned previously, the FEM solution for the area of contact continues past the AF model with increasing interference. Hence, the leading coefficient in Eq. (3.10) is allowed to vary when equations are fitted to the FEM data. This is reasonable, since the AF model is not an exact solution (it is based on a truncation assumption). Here a power function is used in place of this leading coefficient and is fit to the numerical data.

Figures 3.3-3.5 show that there are two distinct regions in the FEM data; thus a piecewise formulation is used to fit the data. At small interferences the Hertz solution is assumed and at large interferences the power function is fit to the FEM data, resulting in:

For $0 \le \omega^* \le \omega_t^*$

$$\overline{A}_F^* = \omega^* \tag{3.12}$$

For $\omega_t^* \le \omega^*$

$$\overline{A}_F^* = \omega^* \left(\frac{\omega^*}{\omega_t^*} \right)^B \tag{3.13}$$

where

$$B = 0.14 \exp\left(23 \cdot e_y\right) \tag{3.14}$$

$$e_y = \frac{S_y}{E'} \tag{3.15}$$

$$\omega_t^* = 1.9 \tag{3.16}$$

The value ω_t^* represents the transition point from elastically dominant behavior to elasto-plastic behavior. The formulation follows the Hertzian solution (Eq. (3.12)) for $\omega^* < 1.9$. Then it transitions to the elasto-plastic case and eventually continues past the AF model for high values of ω^*. Equation (3.13) is also somewhat dependant on the material properties, according to the definition in Eqs. (3.14-3.15). Statistically, Eq. (3.13) differs from the FEM data for all five materials by an average of 1.3% and a maximum of 4.3%. An equation of the same form as the ZMC model fitted to the FEM data results in an average error of 43.2%. Notably, Eqs. (3.12) and (3.13) are continuous at ω_t^*.

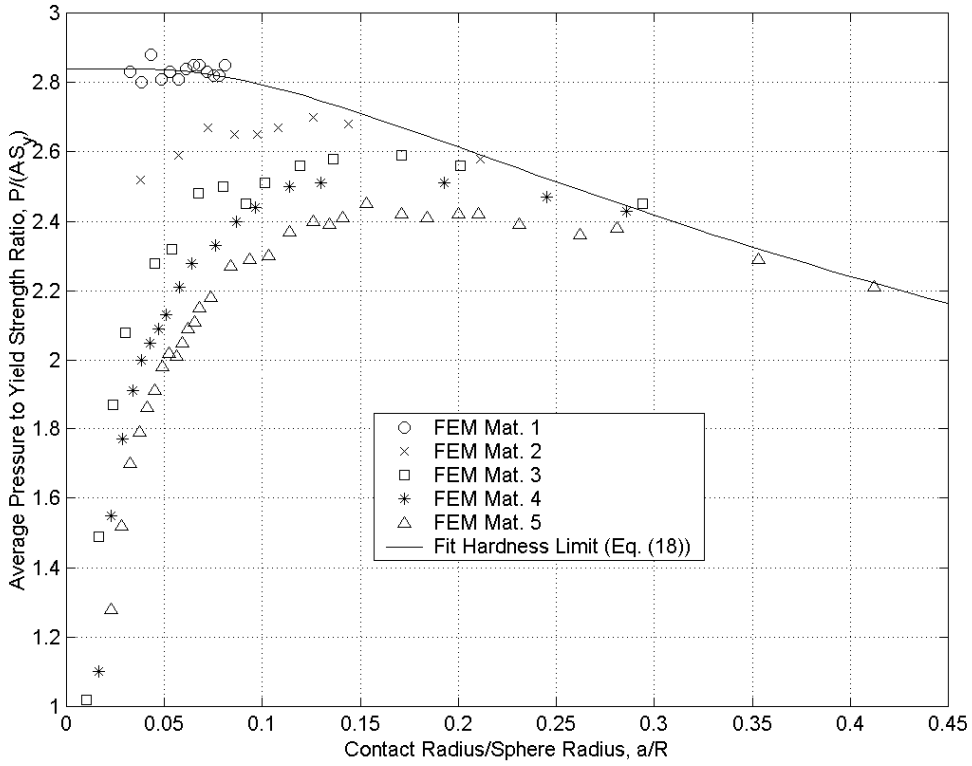

Figure 3.6: Average contact pressure to yield strength ratio.

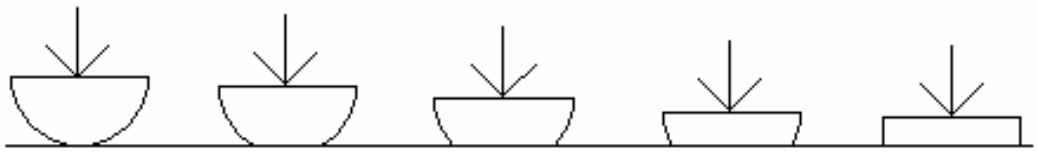

$H_G/S_y \approx 3$ $\quad$ $3 > H_G/S_y > 1$ $\quad$ $H_G/S_y \approx 1$

$a/R = 0^+$ $\quad$ $0 < a/R < 1$ $\quad$ $a/R = 1$

Figure 3.7: Diagram of progression of change in hardness with geometry.

In order to formulate a fit for the FEM contact force, the material dependant trend at high interferences shown in Fig. 3.4 is modeled. To assist in this model, a plot of $P/(A \cdot S_y)$ as a function of a/R in Fig. 3.6 reveals the cause of the material dependency. In this plot a limit appears to emerge for the fully plastic average pressure, commonly referred to as the hardness. Here the hardness appears to change as a function of a/R, or with the evolving geometry of contact. The trend may be explained by the progression schematically shown in Fig. 3.7. As the interference increases and the contact geometry changes, the limiting average pressure to yield strength ratio, H_G/S_y, must change from Tabor's predicted value of three to a theoretical value of one when $a=R$. The contact region when $a=R$ is essentially the case of a deformable blunt rod in contact with a rigid flat whose H_G/S_y value is theoretically one. A Weibull function fitted to the limiting values of H_G results in:

$$\frac{H_G}{S_y} = 2.84\left[1 - \exp\left(-0.82\left(\frac{a}{R}\right)^{-0.7}\right)\right] \tag{3.17}$$

This formulation is plotted alongside the data in Fig. 3.6. Interestingly, as a/R approaches zero, the limiting value of H_G/S_y=2.84 agrees almost precisely with the theoretical value of 2.83 (Williams [27, p.109]). Equation (3.17) is only valid for the range of fitted data, or $(0 < a/R \le 0.412)$. Caution should thus be taken when using this function outside this range. This range is acceptable for many applications, particularly tribological applications where deformations above this range are either unlikely or unacceptable. From the relation $\bar{A} = \pi \cdot a^2$, a is solved for and normalized by R. Then $\bar{A}_c \cdot \bar{A}_F^*$ is substituted for $\bar{A}$. Equation (13) is then substituted for $\bar{A}_F^*$, and Eq. (4) for $\bar{A}_c$, thus yielding:

$$\frac{a}{R}=\frac{\sqrt{\bar{A}_c\cdot\bar{A}_F^*}}{\sqrt{\pi}R}=\sqrt{\frac{\pi^3\left(CS_yR\right)^2\omega^*\left(\frac{\omega^*}{\omega_t^*}\right)^B}{4\pi\left(RE'\right)^2}}=\frac{\pi Ce_y}{2}\left[\omega^*\left(\frac{\omega^*}{\omega_t^*}\right)^B\right]^{\frac{1}{2}} \tag{18}$$

This substitution is valid only when $\omega^* \geq \omega_t^*$. Equation (3.18) can then be substituted into Eq. (3.17) so it may then be rewritten as a function of ω* as follows:

$$\frac{H_G}{S_y}=2.84\left[1-\exp\left(-0.82\left(\frac{\pi Ce_y}{2}\sqrt{\omega^*}\left(\frac{\omega^*}{\omega_t^*}\right)^{\frac{B}{2}}\right)^{-0.7}\right)\right] \tag{3.19}$$

This results in a formulation for H_G as a function of the material properties, E, S_y, and ν (not just upon S_y as suggested by Tabor (1951)).

To formulate an approximation of the contact force as predicted by the FEM results, the AF model for contact force must first be corrected by way of substituting in Eq. (3.17) or Eq. (3.19) into Eq. (3.11), letting H_G replace H, and by allowing the AF contact area to deviate from Eq. (3.10) (see reasoning for Eq. (3.17)). This results in an equation for a corrected fully plastic model. Once again a piecewise solution is fit to the FEM data. At small interferences, the Hertz solution is assumed. The resulting piecewise equation fit to the FEM data is given as:

For $0 \leq \omega^* \leq \omega_t^*$

$$\bar{P}_F^*=\left(\omega^*\right)^{3/2} \tag{3.20}$$

For $\omega_t^* \le \omega^*$

$$\overline{P}_F^* = \left[\exp\left(-\frac{1}{4}\left(\omega^*\right)^{\frac{5}{12}}\right)\right](\omega^*)^{3/2} + \frac{4H_G}{CS_y}\left[1-\exp\left(-\frac{1}{25}\left(\omega^*\right)^{\frac{5}{9}}\right)\right]\omega^* \tag{3.21}$$

where $\omega_t^*=1.9$. This formulation approaches asymptotically the Hertz elastic model at small interferences, and approaches and continues past the AF model at large interferences. Statistically this formulation differs from the FEM data for all five materials by an average error of 0.94% and a maximum of 3.5% when Eq. (3.19) is used for H_G.

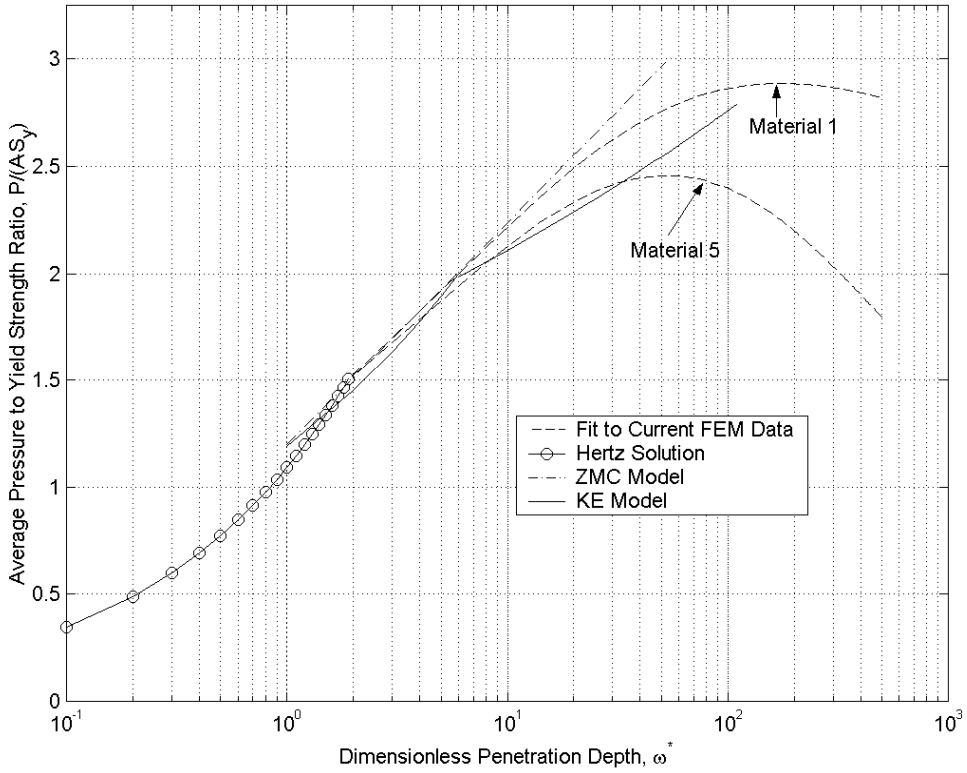

Figure 3.8: Predicted Average Pressure to Yield Strength Ratio for various models.

The average pressure to yield strength ratio, $P/(A \cdot S_y)$, can now be modeled by combining Eqs. (3.12-3.16) and Eqs. (3.20-3.21). Since these equations are normalized by their critical values, the resulting formulation for the average pressure is:

$$\frac{\bar{P}}{\bar{A} \cdot S_y} = \frac{2}{3} C \frac{P_F^*}{A_F^*} \tag{3.22}$$

This ratio is shown in Fig. 3.8 (only the weakest and strongest materials are plotted for clarity). The largest differences between the ZMC and KE models and the current FEM model then appear. It is apparent that the KE and ZMC models do not account for material dependence in the limiting average pressure to yield strength ratio, H_G/Sy. Both ZMC and KE are monotonically increasing and truncated at some point that traditionally is considered to be the "hardness." The ZMC and KE models both estimate the average pressure in the transition from the elastic to the elasto-plastic regime fairly well. It is also apparent that these models do not intersect with the Hertzian solution at $P/(A \cdot S_y)=2 \cdot C/3$. The discontinuity in the slope in the KE model at a value of 6 and in the current model at a value of 1.9 is also clearly evident (see Eqs. (2.15, 2.16) and Eqs. (3.12-3.21)).

3.2.5 Comparison with Experimental Results

Johnson (1968) performed experiments on the elasto-plastic contact of copper cylinders and spheres. During one experiment, he tested the contact of a copper sphere and a comparatively rigid steel surface. These test conditions are comparable to the hemisphere against a rigid flat case modeled in this work. For the highest load tested, the contact has a nearly uniform pressure distribution, thus suggesting it is in the fully plastic regime. At this load, the *a/R* ratio is given as 0.204 and the average pressure as $2.59 \cdot S_y$.

Interestingly, the predicted geometric hardness limit or average pressure for the same *a/R* using Eq. (3.17) is $2.61 \cdot S_y$. In comparison, the KE model, which assumes the AF model at this interference, predicts an average pressure of $2.8 \cdot S_y$.

Johnson provides the contact radius and load in his results, which can also be compared with the predictions of the current formulations (Eqs. (3.12-3.21)) and those of the KE model (Eqs. (2.15)-(2.16)). Table 3.2 presents this comparison. The material properties provided by Johnson were used when available; otherwise values from Johnson (1968) were used. All material properties are given in Table 3.2. Since Johnson does not provide the interference at each load, the predicted pressure is calculated from the experimental contact area using the current formulations and the KE model. Both numerical models compare well with the experimental results and differ by a maximum of just over 10%. However, overall the current model proves to be a more accurate model. In fact, at the largest load the difference is merely 1.7%. These results also indicate that there is a definite need for formulations which can accurately capture elasto-plastic hemispherical contact at large interferences. The experimental results also show again, that the hardness or the fully plastic average pressure varies with deformation and is not constant at $2.8 \cdot S_y$ or $3 \cdot S_y$.

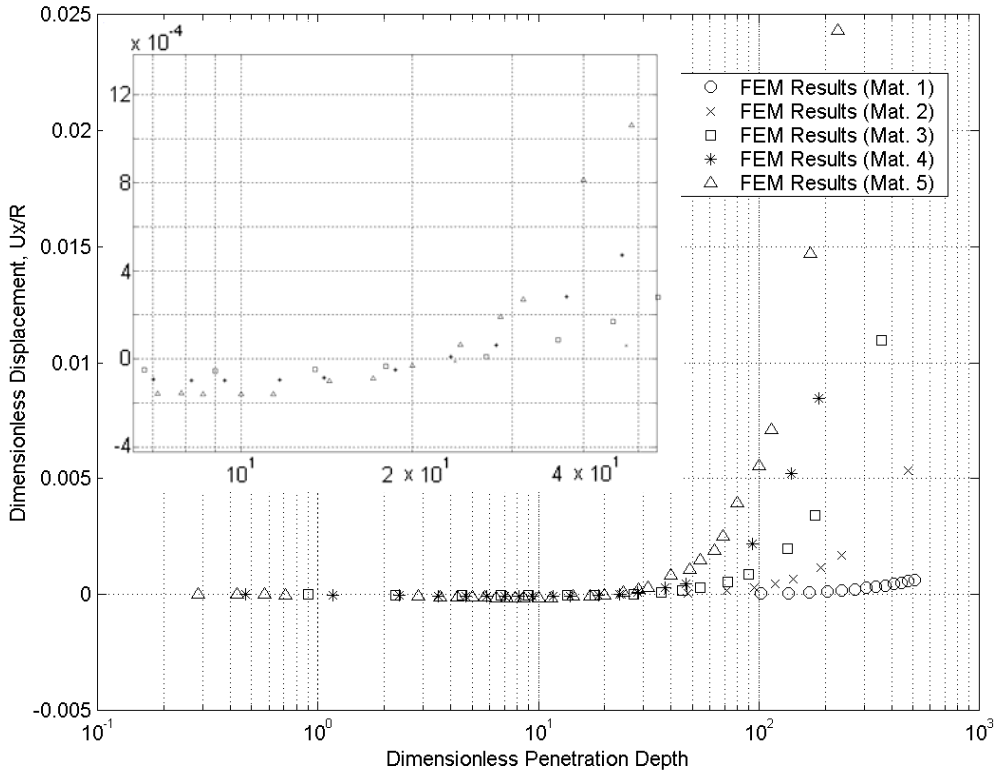

Figure 3.9: Displacement at edge of contact area plotted as a function of penetration depth.

3.2.6 Evolution of Deformation

As long as the deformations are purely elastic, i.e., below the critical interferences, the entire hemisphere will abide by the 3D Hooke's law. Conforming to Poisson's effect the material volume should compress with a compressive contact pressure (as shown schematically in Fig. 3.1b). To investigate this phenomenon Fig. 3.9 shows the radial deformation of the last contact point between the deformed hemisphere and the rigid flat as extracted from the FEM post-processing data. Indeed at relatively small values of ω^* there seems to be a shrinkage in volume (even though that some plastic deformation has already taken place, but overall the elastic deformation of the

entire hemisphere dominates). At values below an approximate value of ω^*=22, the radial displacements are all negative, very small, and are generally strength independent (see inset). In plasticity, however, volume is conserved. As the deformation increases, yielded material flows plastically and is incompressible, making Poisson's ratio effectively equal to 0.5 (Goodier and Hodge, 1958). The FEM results find that beyond ω^*=22 (approximately), the radial deformation of the last contact point displaces positively, i.e., the schematics of the deformation follows the geometry depicted in Fig. 3.1(c). The positive displacement becomes material dependent, which increases with material strength.

3.2.7 Stress Distribution and Evolution

Initially, at small interferences, the hemisphere will deform only elastically. While in the elastic regime, the maximum von Mises stress will always occur beneath the contact surface and within the bulk material. Eventually, as the interference increases and the stresses increase yielding will initiate at the point of maximum von Mises stress.

At interferences just above the critical, the plastically deformed region is small, and confined below the surface by a sizeable region of elastic material (see Fig. 3.10a). It should be noted that because of plotting resolution the region of plastic deformation is smaller then the highest stress region shown in each plot.

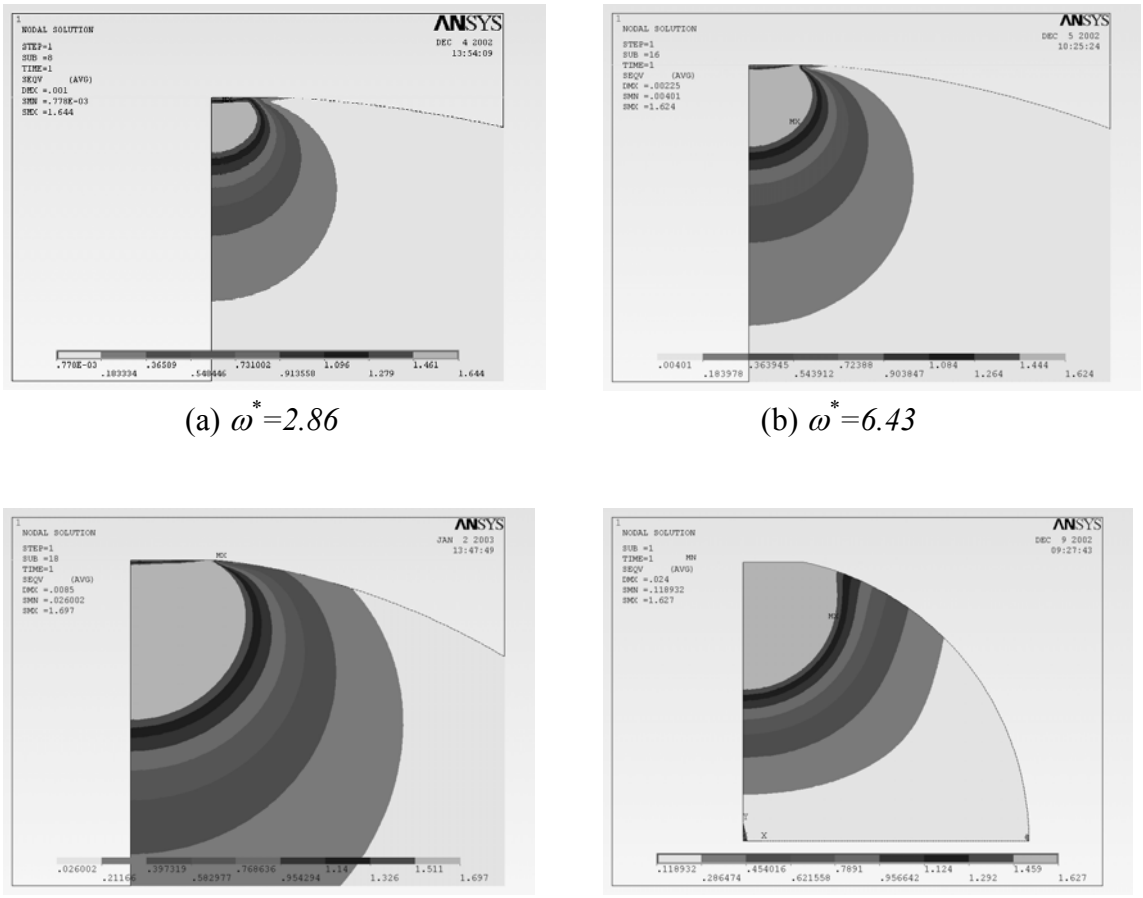

(a) $\omega^*=2.86$ (b) $\omega^*=6.43$

(c) $\omega^*=24.3$ (d) $\omega^*=68.6$

Figure 3.10: Stress plots from ANSYS™, showing the evolution of the stress distribution from (a) elasto-plastic (not yet plastic on surface) to (d) just before fully plastic.

For instance, the highest stress region in Fig. 3.10b has a von Mises stress range between 1.444 GPa and 1.624 GPa, and thus not the entire region in this stress range is at the yield stress of 1.619 GPa. With increasing interference, the plastic region expands until it reaches the surface of the hemisphere (Fig. 3.10b-c). From close inspection of post-processing data, according to the current model, the interference at which the plastically deformed region first reaches the surface is approximately when $\omega_s^* = 9.6$, for

material 5 (this differs from the value $\omega_s^* = 6$ as reported by Kogut and Etsion (2003)). The value of ω_s^* also varies slightly with the material yield strength and the deformed contact geometry for the same reason that the average pressure or hardness vary with strength.

Repeated FEM analyses were performed to search for the interferences of two important cases: (1) when plastic deformation first reaches the contacting surface at the far right end point, and (2) when the contact surface first becomes entirely (fully) plastic. Table 3.3 gives these results. To pinpoint precisely these values much more arduous searches are needed. The search performed here, albeit being intensive, was not as exhaustive and, therefore, the values given here contain some uncertainty (given as the resolution in Table 3.3). Searches were done on the stronger materials excluding material 1 and 2, which have the slowest convergence rates.

After plastic deformation has reached the surface, an elastic volume on the loaded tip of the hemisphere is still maintained (Fig. 3.10c) by the presence of hydrostatic stresses, which suppress yielding according to the von Mises criterion. Eventually this elastic region will turn plastic as well as the interference is increased. Figure 3.10d shows a state of stress just before the fully plastic state is reached on the contact surface. Although an exhaustive analysis of ω_{fp}^* is not performed here, this initial fully plastic interference seems to range between $\omega^*=70$ and $\omega^*=80$, depending on the material yield strength. This range of values is also close to the value of 68 as predicted by the KE model.

Table 3.1: Tabulated Finite Element Results (Radius = 1 μm, E=200 GPa, ν=0.32).

Material	ω^*	A^*	P^*
1	101.91	1.774E+02	4.597E+02
S_y=0.210 GPa	135.88	2.522E+02	6.452E+02
	169.85	3.181E+02	8.376E+02
	203.82	4.017E+02	1.034E+03
	237.79	4.761E+02	1.233E+03
	271.76	5.569E+02	1.434E+03
	305.72	6.313E+02	1.642E+03
	339.69	7.105E+02	1.853E+03
	373.66	7.864E+02	2.048E+03
	407.63	8.766E+02	2.272E+03
	441.60	9.562E+02	2.471E+03
	475.57	1.037E+03	2.674E+03
	509.54	1.109E+03	2.889E+03
2	23.82	3.382E+01	7.815E+01
S_y=0.561 GPa	47.64	7.793E+01	1.848E+02
	71.46	1.242E+02	3.034E+02
	95.28	1.751E+02	4.253E+02
	119.10	2.249E+02	5.453E+02
	142.93	2.768E+02	6.756E+02
	190.57	3.810E+02	9.402E+02
	238.21	4.914E+02	1.204E+03
	476.42	1.065E+03	2.517E+03
3	0.90	9.177E-01	8.585E-01
S_y=0.912 GPa	2.25	2.419E+00	3.308E+00
	4.51	5.135E+00	8.782E+00
	6.76	7.999E+00	1.525E+01
	13.52	1.823E+01	3.811E+01
	18.03	2.592E+01	5.510E+01
	27.05	4.067E+01	9.219E+01
	36.06	5.776E+01	1.320E+02
	45.08	7.577E+01	1.699E+02
	54.09	9.258E+01	2.128E+02
	72.12	1.282E+02	2.998E+02
	90.15	1.662E+02	3.918E+02
	135.23	2.636E+02	6.234E+02
	180.31	3.644E+02	8.531E+02
	360.61	7.804E+02	1.747E+03

Material	ω^*	A^*	P^*
4	0.47	5.468E-01	3.139E-01
S_y=1.265 GPa	1.17	1.255E+00	1.267E+00
	2.34	2.472E+00	3.514E+00
	3.51	3.861E+00	6.236E+00
	4.68	5.308E+00	9.282E+00
	5.85	6.893E+00	1.259E+01
	7.02	8.582E+00	1.612E+01
	8.19	1.034E+01	1.977E+01
	9.36	1.210E+01	2.360E+01
	11.70	1.564E+01	3.168E+01
	14.04	1.923E+01	4.019E+01
	18.72	2.720E+01	5.806E+01
	23.39	3.513E+01	7.718E+01
	28.07	4.354E+01	9.712E+01
	37.43	6.062E+01	1.387E+02
	46.79	7.929E+01	1.822E+02
	93.58	1.742E+02	4.009E+02
	140.4	2.802E+02	6.322E+02
	187.2	3.821E+02	8.506E+02
5	0.29	3.133E-01	1.505E-01
S_y=1.619 GPa	0.43	4.766E-01	2.790E-01
	0.57	6.270E-01	4.324E-01
	0.71	7.691E-01	6.053E-01
	1.43	1.464E+00	1.720E+00
	2.14	2.243E+00	3.111E+00
	2.86	3.024E+00	4.695E+00
	3.57	3.923E+00	6.413E+00
	4.29	4.856E+00	8.263E+00
	5.00	5.844E+00	1.021E+01
	5.72	6.778E+00	1.225E+01
	6.43	7.781E+00	1.438E+01
	7.14	8.995E+00	1.654E+01
	7.86	9.999E+00	1.879E+01
	8.57	1.106E+01	2.111E+01
	9.29	1.217E+01	2.348E+01
	10.00	1.316E+01	2.593E+01
	11.43	1.545E+01	3.089E+01
	14.29	1.996E+01	4.138E+01
	17.15	2.491E+01	5.228E+01
	20.00	3.021E+01	6.367E+01
	24.29	3.743E+01	8.122E+01
	28.58	4.526E+01	9.944E+01
	31.43	5.118E+01	1.119E+02
	34.29	5.655E+01	1.246E+02
	40.01	6.711E+01	1.502E+02
	48.58	8.402E+01	1.861E+02
	54.29	9.648E+01	2.126E+02
	62.87	1.138E+02	2.519E+02
	68.58	1.257E+02	2.785E+02
	80.01	1.521E+02	3.321E+02
	100.0	1.959E+02	4.228E+02
	114.3	2.257E+02	4.923E+02
	171.5	3.556E+02	7.458E+02
	228.6	4.846E+02	9.795E+02

Table 3.2: Comparison of Experimental [12] and Numerical Results.

P^* (EXPERIMENTAL)	A^* (EXPERIMENTAL)	P^* (CURRENT)	% *DIFF.*	P^* (KE)	% *DIFF.*
360.1	159.4	404.3	10.9	400.9	10.2
1230.5	527.4	1306.3	5.8	1331.9[&]	7.6
2401.0	1042.8	2442.6	1.7	2633.3[&]	8.8
Material Properties, Copper: Sy=265.5 kPa E=115 GPa ν=0.34 Steel: E=200 GPa ν=0.33					

[&]The KE model assumes the results of Abbott and Firestone (1933) for fully plastic contact.

Table 3.3: FEM generated interferences for initial yield of surface and the fully plastic regime.

MATERIAL (S_Y/E)	ω^* AT INITIAL SURFACE YIELD	RESOLUTION	ω^* AT INITIAL FULLY PLASTIC	RESOLUTION
0.00456	7.89	+/-1.13	81.13	+/- 9.01
0.00633	9.36	+/- 0.58	81.87	+/- 11.70
0.00810	9.64	+/- 0.36	74.23	+/- 5.71

3.3 Statistical Model of the Elasto-plastic Contact of Rough Surfaces

In this section, the results of a finite element analysis of an elasto-plastic hemisphere in contact with a rigid flat (see Section 3.2) are used to statistically model an entire surface of asperities in contact. The contact between real surfaces with known material and surface properties, such as the elastic modulus, yield strength, and roughness are modeled. The asperity is modeled as an elastic-perfectly plastic material. The model produces predictions for contact area, contact force, and surface separation. The results of this model are compared to other existing models of asperity contact. The models compared are shown to agree in some cases but disagree in others. Significant limitations of the statistical models (including the Greenwood and Williamson model (1966)) are also identified.

The current individual hemispherical contact model (Eqs. 3.12, 3.20 and 3.21) are substituted into Eqs. (2.22 and 2.23). Other individual contact models are also considered, including the CEB model (Eqs. 2.10-11) and the KE model (Eqs. 2.13-14). Equations (2.22 and 2.23) are numerically integrated using Guass-Legendre quadrature.

For substitution into Eqs. (2.22 and 2.23), this work uses a Gaussian distribution for the asperity height distribution that is given as:

$$G(z) = (2\pi)^{-1/2}\left(\frac{\sigma}{\sigma_s}\right)\exp\left[-0.5\left(\frac{z}{\sigma_s}\right)^2\right] \tag{3.23}$$

where σ is the standard deviation of the surface heights, and σ_s is the standard deviation of the asperity heights. These values also describe the roughness of the surfaces. McCool (1986) relates these values by the following:

$$\sigma^2 = \sigma_s^2 + \frac{3.717\times10^{-4}}{\eta^2 R^2} \tag{3.24}$$

Greenwood and Williamson (1966) also define a plasticity index as:

$$\psi = \sqrt{\frac{\sigma_s}{\omega_c}} \tag{3.25}$$

The plasticity index relates the critical interference and the roughness of the surface to the plastic deformation of the surface. A higher plasticity index indicates a surface whose asperities are more likely to yield. Asperities are thus more likely to deform plastically on rougher surfaces with lower critical interference values. Greenwood and Williamson suggest that for real surfaces the plasticity index can range from ψ=0.1 to ψ=100. This range will be analyzed in this work by holding the surface roughness constant and varying the material yield strength, which differs from previous approaches that usually vary the surface roughness.

3.3.1 Limitations of the Statistical Model

The outlined statistical model is only valid when the individual asperity contact models are also valid. Most current asperity contact models assume that the deformations are relatively small and limited to the asperity tip. The largest deformations considered thus far are those in section 3.2, where even those are given only up to a/R=0.41. Thus, during the integrations of Eq.(2.22) and Eq.(2.23), a/R should remain smaller than that value.

From Eq. (2.4), the radius of contact can be written as:

$$a = \sqrt{D\omega R} \tag{3.26}$$

where

$$D = \begin{cases} 1 & 0 \le \omega / \omega_c \le 1.9 \\ \left(\dfrac{\omega}{1.9\omega_c} \right)^B & \omega / \omega_c \ge 1.9 \end{cases} \tag{3.27}$$

and B is found from Eq. (3.14). Thus the equation for a/R can be written as:

$$\frac{a}{R} = \frac{\sqrt{D\omega R}}{R} = \frac{\sqrt{D\omega}}{\sqrt{R}} \tag{3.28}$$

The normalized interference ($\omega^* = \omega/\sigma$) is then substituted into Eq. (3.28) yielding

$$\frac{a}{R} = \frac{\sqrt{D\omega^* \sigma}}{\sqrt{R}} \tag{3.29}$$

From this point forward, in this section units of length will be normalized by σ and designated by a star superscript. This analysis uses a minimal value $D=1$, which sets Eq. (3.29) equal to the Hertz elastic solution. Also, $\omega^*=1$ is used because at this value a large number of the asperities on the rough surface are clearly in contact. These values are conservative in that for most cases both D and ω^* are usually larger than one.

A sampling of the experimental values reported by Nuri and Halling (1975) and implemented by Chang et. al. (1987) and Zhao et. al. (2000), are presented in Table 3.4, along with the resulting values of R/σ and a/R, using D=1 and ω^*=1. The resulting values of a/R indicate that very large deformations are being modeled by those using the experimental values of Nuri and Harding (1975). Even for sample one, the contact radius is approximately 10% of the asperity radius (a/R=0.097). Assuming Nuri and Halling's data is realistic, these results put into question the validity of the statistical model used by Chang et. al. (1987), Zhao et. al. (2000), and even originally by Greenwood and

Williamson (1966). In reality, the values of *a/R* will be larger than those calculated in Table 3.4 because both *D* and ω^* can assume values (sometimes significantly) larger than one. The values in Table 3.4 also suggest that many real rough surfaces may undergo extreme deformations during asperity contact and that the bulk material below the asperities would likewise deform significantly (a condition that is not considered in any of the existing single asperity contact models).

Table 3.4: Experimental parameters (Nuri and Halling, 1975).

Sample	σ (μm)	R (μm)	σ/R	$(a/R)^1$
1	0.16	16.8	0.00952	0.097
2	1.35	7.14	0.189	0.43
3	3.25	6.12	0.531	0.72

1. Based on Eq. (3.29) and assuming *D=1,* and $\omega^* = 1$.

Table 3.5: Material and Surface Properties Implemented in Analysis.

E = 200 GPa
ν = 0.32
R = *2.0 μm*
σ = *9.0 nm*
$\eta = 100.0 \times 10^{11}\ m^{-2}$

Table 3.6: Plasticity indices and corresponding yield strengths.

ψ	0.5	1.0	2.0	10.0	40.0	70.0	100.0
ω_c^*	3.98×10^{0}	9.94×10^{-1}	2.49×10^{-1}	9.94×10^{-3}	6.21×10^{-4}	2.03×10^{-4}	9.94×10^{-5}
S_y (GPa)	11.6	5.79	2.89	0.579	0.145	0.0827	0.0579

It is clearly evident, that great care should be taken when using the statistical model first used by Greenwood and Williamson (1966), and all subsequent models. Otherwise, the models may be calculating the contact area and contact force for deformations outside of their intended range. These calculations could produce meaningless or misleading results. The R and σ values used in the current analysis produce acceptable values for a/R that are less than the maximum value of 0.41.

3.4.2 Results and Discussion

This analysis uses the surface and material properties found in Table 3.5 to solve Eqs. 2.22 and 2.23 . Note the dependence between the plasticity index, ψ, and the yield strength, S_y, through Eqs. (3.1) and (3.25). In this case, the plasticity index is varied over the range shown in Table 3.6. The critical interference, ω_c^*, is then calculated for each ψ by using Eqs. (3.24, 3.25). Then the corresponding yield strength, S_y, is calculated from the critical interferences using Eq. (3.1). That value of S_y is now used in Eqs. (3.12-3.21*)*. Equations (2.22) and (2.23) are then numerically integrated using each of the asperity

contact models outlined above for $\overline{P}$ and $\overline{A}$. The integrals are evaluated using Gauss-Legendre quadrature.

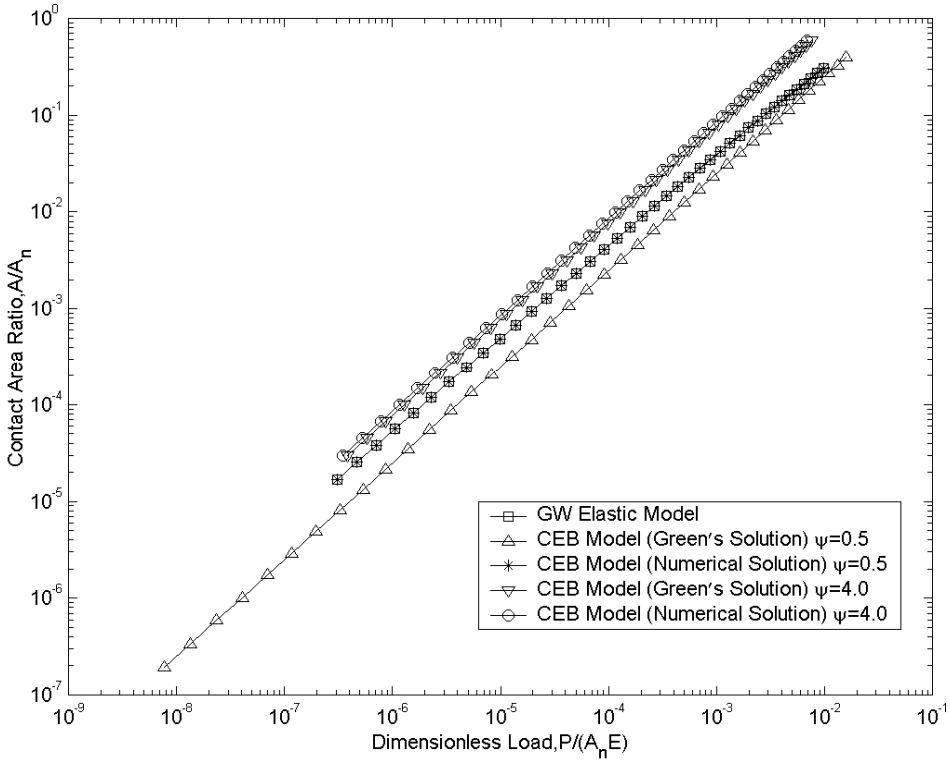

Figure 3.11: Comparison of numerically and analytically produced results for the CEB model.

The numerically evaluated CEB model is compared to the analytical solution of the CEB model provided by Green (2003) in Fig. 3.11. For each solution, the contact area ratio (A/A_n) is plotted as a function of the dimensionless load ($P/(E \cdot A_n)$). First, this plot verifies that the numerically evaluated integrals produce nearly identical results as Green's solution for large plasticity indices (ψ=4.0). Second, there is a significant amount of error between Green's solution and the numerical results at small plasticity indices (ψ=0.5). Thus, when the Hertz elastic solution is dominant, numerical techniques

should be used to solve the CEB model (by definition this solution is identical to the GW model as shown in Fig. 3.11). Although when Eq. (2.10) and Eq. (2.11) are dominant, Green's solution provides accurate values. This makes sense because Green solves exactly the integrals (Eq. (2.22) and Eq. (2.23)) of elasto-plastic portion of the CEB model (Eq. (2.10) and Eq. (2.11)) and only approximates the elastic portion (Eq. (2.4) and Eq. (2.5)).

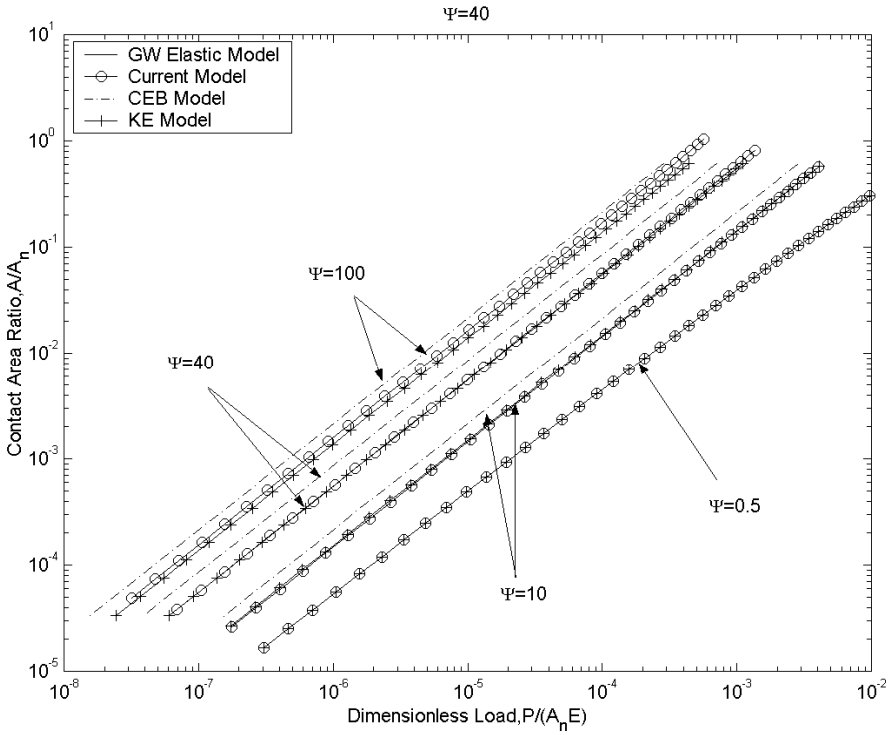

Figure 3.12: Contact area versus load for various values of the plasticity index.

Figure 3.12 shows the resulting contact area ratios (A/A_n) versus the dimensionless load ($P/(E \cdot A_n)$) for different plasticity indices. As expected, the contact area increases with the load. The plot also indicates that an increase in the plasticity index results in larger contact areas at the same loads. When ψ=0.5, all the models

converge to the GW model and are dominated by the Hertz elastic solution. As the plasticity index increases, so do the differences between the models. At ψ=10 the CEB differs largely from the GW model, while the KE and current model still differ relatively little. For higher plasticity indices the CEB model always has a larger contact area than the other models. Once ψ=40 is reached, slight differences appear between the KE and current model. Finally at ψ=100 it is clear that at the same load the contact area predicted by the current model is larger than the KE model. This is because the KE model's contact area is limited by Abbott and Firestone's truncation model (1933) at large interferences.

Next, the contact area ratio for each model is plotted as a function of the plasticity index, while h^* is held constant at a value of 1.0 (see Fig. 3.13). At low ψ, all the models follow the GW model, before any significant plastic deformation occurs. The CEB model clearly increases too quickly with ψ. Once again, the KE and CEB models are clearly limited by assuming Abbott and Firestone's truncation model (1933) at large plasticity indices. However, the current model and KE model follow closely initially, but then the current model continues past both the CEB and KE models. As reported in the previous section, the truncation model is invalid, and that is clearly evident in Fig. 3.13.

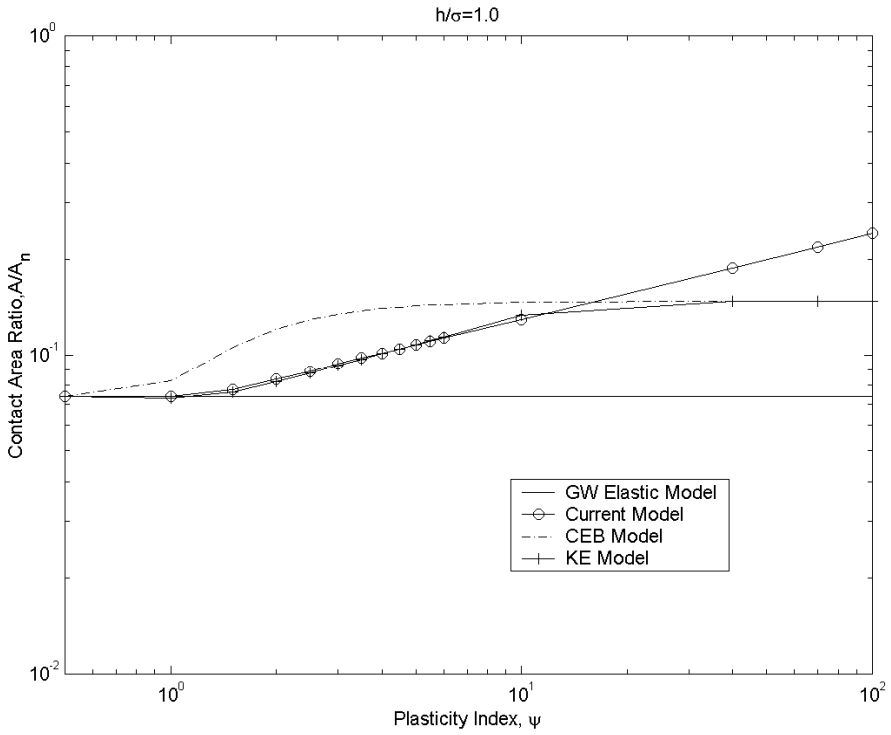

Figure 3.13: Comparison of predicted contact areas.

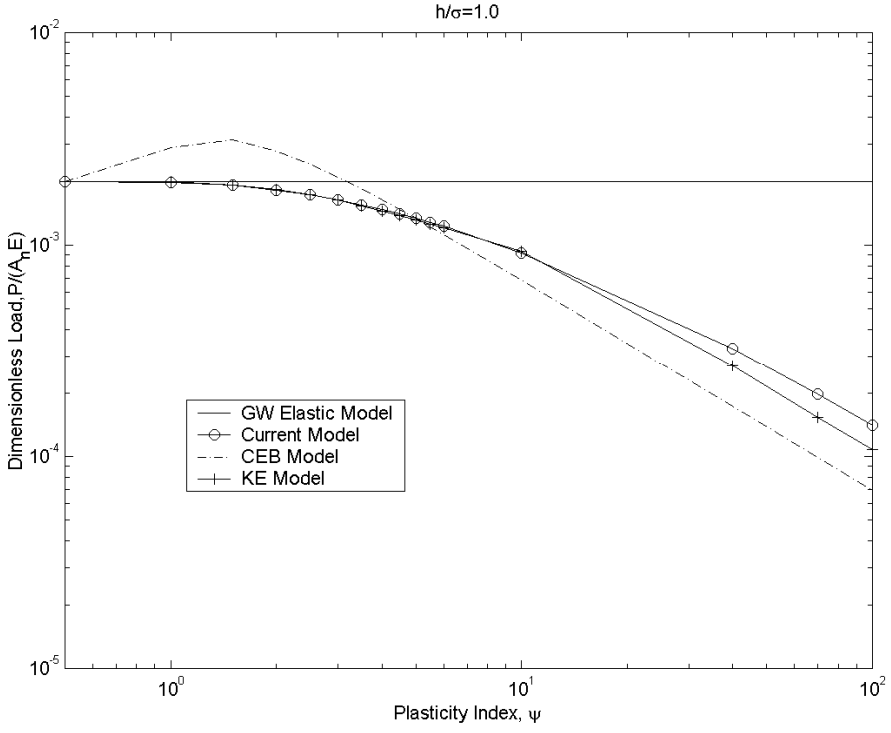

Figure 3.14: Comparison of predicted contact loads.

The dimensionless load is also plotted as a function of the plasticity index in Fig. 3.14. All the models again begin at the GW model when ψ=0.5. However, the CEB immediately increases past the GW model. This is physically not possible since the GW model is elastic and is thus the limiting case. Both the KE and the current model slowly decrease from the GW model as the plasticity index is increased. At $\psi=10$ the KE and current model differ by only 1.7%, but at $\psi=100$ this difference increases to 23%.

Overall though, and especially at plasticity indices less than ten, the two models agree very well due to an averaging effect of the integrals in Eq. (2.22) and Eq. (2.23). Thus, even though the individual asperity contact results of the KE and current model differ at some interferences, the integration averages out these differences.

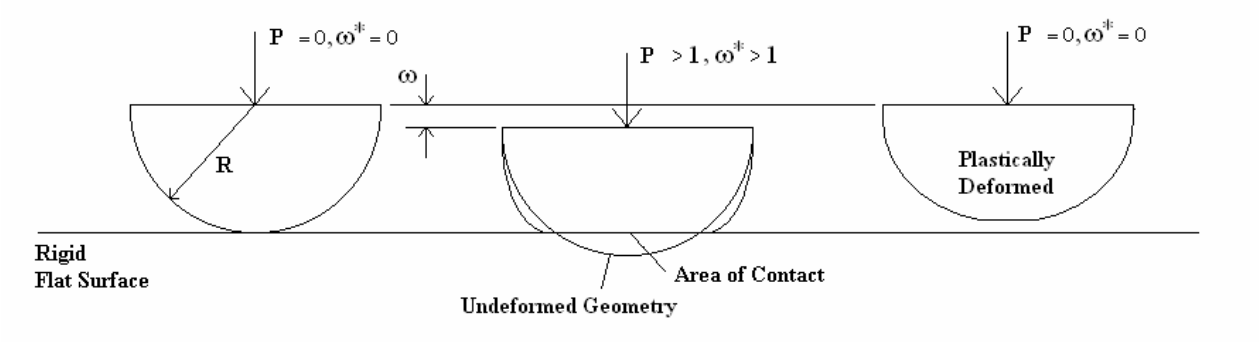

(a) (b) (c)

Figure 3.15: Diagram of loaded (b) and unloaded (c) contact of deforming elasto-plastic hemispheres and a rigid flat.

3.4 Residual Stresses and Deformation of Elasto-Plastic Spherical Contact

The case of an elasto-plastic hemispherical contact with a rigid plane has important engineering applications in both the macro and micro scale. The current model is normalized to be valid in both scales. Although the results of this section are not used in the numerical model outlined in Chapter 4, the asperities on the surface of the washer bearings will come in and out of contact and thus have permanent deformation and residual stresses. It has been well established that asperities will deform plastically during the contact of rough surfaces. It is also clear that in many applications the load will periodically be removed or cycled. This action makes it desirable to know the effect the contact has had on the surface material and the geometry through plastic deformations and residual stresses. Such information is useful in analyzing the friction, wear and deformation of contacts, as for example, in micro-switches, boundary lubrication, rolling element bearings, metal forming, fretting, and shot peening.

3.4.1 Background

The previously described elasto-plastic hemispherical contact model in section 3.2 is published and so any reference to Jackson and Green (2003) can be found in section 3.2. Jackson and Green (2003), Kogut and Etsion (2003), and Mesarovic and Fleck (2000) provide results for the loaded condition case. As a continuation of these previous results, the current work is focused on the residual stress and deformation, which remain after the interference has been removed (see Fig. 3.15). The model by Jackson and Green is regenerated to simulate the loaded condition and the unloaded condition for the first time. The von Mises yield criteria is used to indicate whether the hemisphere material is deformed elastically or plastically. The material is assumed to act elastic perfectly-plastic, so that there is no strain hardening effect.

Experimentally, Johnson (1968) observed the contact of bronze and steel spheres pressed against a steel flat. In order to make measurements of the deformation, he also unloaded the hemispheres. Once unloaded, he observed permanent indentation of both the hemisphere and the flat surface, along with a pileup or crown of raised material around the contact area. These findings match those found through FEM simulation in this work. Tabor (1951, pp.14-15) also recognizes the need to consider these effects when measuring the hardness of a surface using an indentation test.

Kral et al. (1993, 1995a, 1995b) modeled the inverse case of a repeated elasto-plastic contact of the rigid hemisphere against a non-layered and layered half-space using FEM. Although based on a different case, their model produces qualitatively similar

results to the one presented here. While Kral et. al. applies a load up to 300 times the initial load to cause yielding (critical load), the current work more than doubles this value by modeling a load of 750 times the critical load. Ye and Komvopoulos (2003) also simulate the contact in a layered deforming half space and a rigid sphere, although they manually apply a hydrostatic residual stress prior to contact. These applied residual stresses model surface treatments such as shot peening. They then attempt to quantify the effect of the applied residual stresses on the contact deformation and stresses. In addition, they also investigate the effect of sliding on the resulting stresses. Despite these works and other previous works, there is currently no in depth analysis of the residual stresses and deformations of an unloaded elasto-plastic spherical contact against a rigid flat.

In section 3.2, the hemispherical contact model was simulated under the loaded conditions for many interferences and five steel materials, during which the hemisphere deforms in the elastic, elasto-plastic, and fully plastic regimes. The following definitions are given for the regimes: 1) the elastic regime considers deformation absent of plasticity, 2) the elasto-plastic regime contains plastically deformed material but the contact area still contains an elastic region, and 3) the fully plastic regime defines the case of a contact whose area of normal pressure yields entirely. The measurement of hardness requires that the contact reaches the fully plastic regime, where the average contact pressure has traditionally been regarded as the hardness. However, the hardness should not be implemented as a material property, as it also varies with deformation, geometry, and material properties such as yield strength, Poisson's ratio and the elastic modulus (see section 3.2.4).

This section defines the interference depth, ω, as the distance the original hemisphere shape is pressed into the rigid flat (see Fig. 3.15). In this section a star superscript refers to a normalization by the terms critical value at the initial point of yield.

From Eqs. 2.4 and 3.1 the critical contact radius is

$$a_c = \sqrt{\omega_c R} \tag{3.30}$$

For residual stresses and strains to remain once the hemisphere is unloaded, a ω^* greater than one must be applied (see diagram in Fig. 3.15). The critical contact radius, a_c, defines the radius of the area of contact at an interference depth of ω_c. From this point forward residual stress and residual displacement will refer to stress and displacement that remain in the elasto-plastic hemisphere after the load is completely removed.

Table 3.7: The material properties and critical interferences for Aluminum and Steel

Material	**Young's Modulus (E)**	**Poisson Ratio (ν)**	**Yield Strength (S_y)**	**Critical Interference (ω_c/R)**	γ_c/ω_c **(R=1)**
Aluminum	70 GPa	0.33	0.310 GPa	0.000103	0.00169
Steel	200 GPa	0.32	1.619 GPa	0.000350	0.00312

This section uses a finite element procedure very similar to that used in Section 3.3. As shown in Figure 3.16 constraints in the x and y directions were applied to the nodes on the base, while a radial constraint is applied to the symmetric axis. The rigid

contact is constrained in the radial direction, while the interference, ω, is applied as a displacement in the axial direction.

A large range of interferences are applied to the FEM model and then the contact force, stress tensor, von Mises stresses and the displacement in both the radial and axial directions are recorded. After the loaded condition has been simulated (giving the same results as in section 3.2) the solution is then restarted and unloaded completely to simulate the residual stresses and the displacements. Since the problem is nonlinear, small load steps are used to increment toward a solution in both loading and unloading.

3.4.2 Results and Discussion

The results are presented for a range of normalized interferences, ω^*, from 0.571 to 171. The material properties used are for a steel material (extracted from [10]) and presented in Table 3.7. These material properties allow for effective modeling of all the elasto-plastic contact regimes. The computation time is about an hour for small interferences and two to three hours for large interferences on a 3.2 GHz PC.

As an additional check of the model's validity, the contact forces during the unloaded conditions are calculated. Based on the force balance solution, once the contact is completely unloaded the reaction force should be identically zero. This trivial condition is consistently satisfied with an eight-node FEM model which computes the reaction force to be about ten orders of magnitude smaller than the load originally applied to the hemisphere.

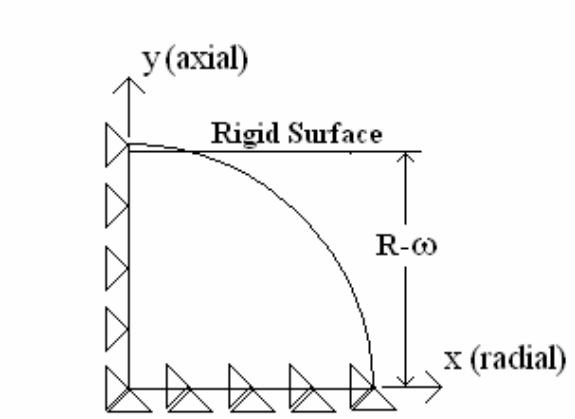

Figure 3.16: Schematic of the coordinate system and boundary conditions used in the FEM.

Displacement

The axial and radial surface displacements of the nodes on the hemisphere surface are monitored in order to investigate the deformation of the hemisphere. As shown in Figure 3.16 the axial and radial directions correspond to the *y*-axis and *x*-axis, respectively. While ω_c effectively normalized the axial displacement, U_y, it is ineffective in normalizing the radial displacement, U_x. It is found (see Appendix B) that U_x is effectively normalized by $\gamma_c = \frac{1}{6}\frac{(\omega_c)^{\frac{3}{2}}}{\sqrt{R}}$ which is the relative radial displacement of the critical contact radius before and after loading. In this section plots of the normalized axial and radial displacements, U_x/γ_c and U_y/ω_c, with respect to the normalized radial distance, r/a_c, are presented for both the loaded and unloaded conditions (see Figs. 3.17-3.20). Note that *r* is the radial distance from the axis of symmetry (*y*-axis) to a point on the surface. Thus, *r* is analogous to the *x*-coordinate of a location on the hemisphere surface. The displacements are presented relative to the hemisphere surface, such that

curvature is mitigated. Although the main focus of this work is the unloaded case, the surface displacements for the loaded case are also presented since they have not been included in a previous work.

Loaded Displacement

Figures 3.17 and 3.18 show the surface displacement in both the axial (U_y/ω_c) and radial (U_x/γ_c) direction for the loaded hemisphere. These plots show the evolution of hemisphere surface deformation with increasing interferences.

As expected, the displacements increase with the normalized interference depth. The boundary between the contact region and the free boundary of the hemisphere can be clearly seen through the sharp changes of the slope in the radial displacement plot (see Fig. 3.17). In the low interferences, the surface displaces radially in mostly the negative direction. This is because at the small normalized interferences most of the material in the hemisphere is deforming elastically and allowed to compress. As the interference significantly increases past the critical interference, the hemisphere increasingly deforms plastically and the material in the contact region increasingly displaces outward into the positive *x* direction. This bulging occurs because as the deformation increases, yielded material flows plastically, and is assumed incompressible abiding by a Poisson's ratio effectively equal to 0.5.

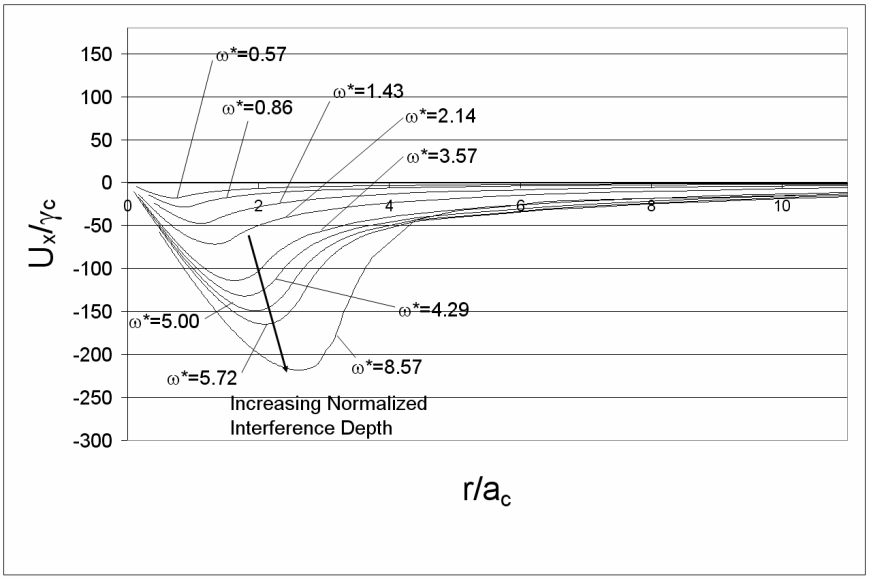

(a) small normalized loaded interferences, ω^*

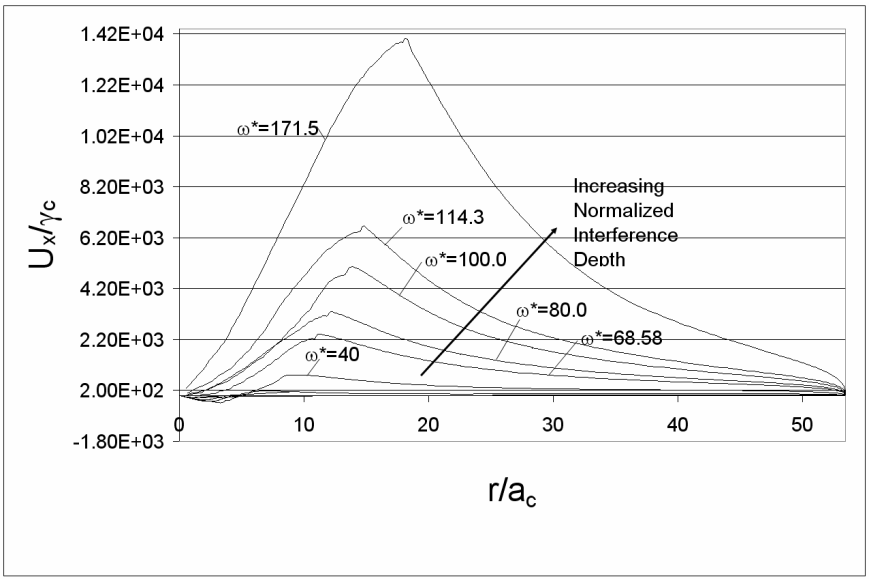

(b) large normalized loaded interferences, ω^*

Figure 3.17: The normalized radial surface displacement versus the normalized radial distance in the loaded condition for (a) small, and (b) large normalized interference depths.

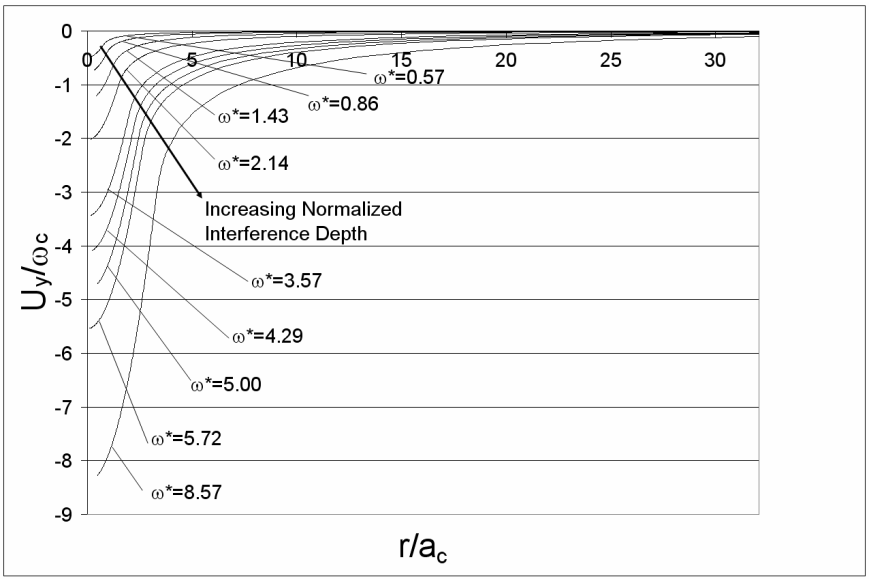

(a) small normalized loaded interferences, ω^*

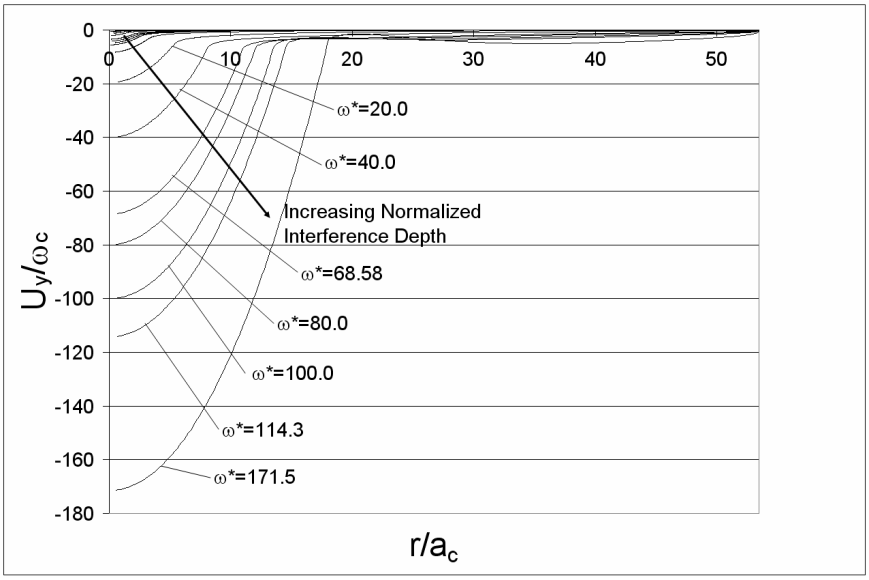

(b) large normalized loaded interferences, ω^*

Figure 3.18: The normalized axial displacement versus the normalized radial distance in the loaded condition for (a) small, and (b) large normalized interference depths.

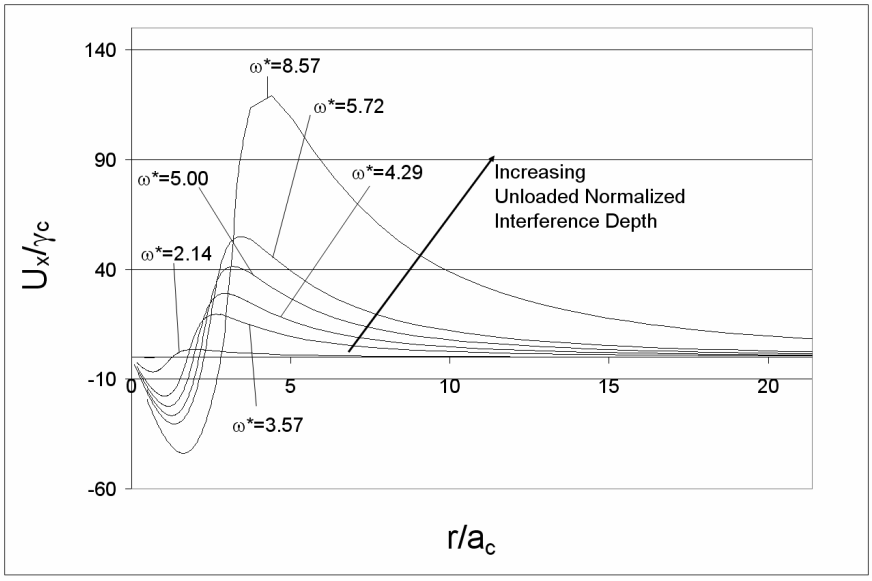

(a) small normalized unloaded interferences, ω^*

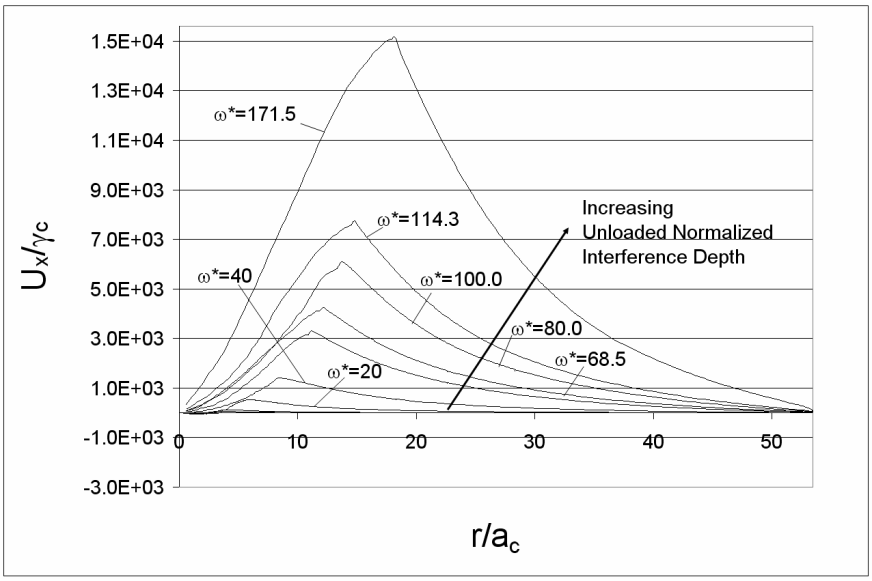

(b) large normalized unloaded interferences, ω^*

Figure 3.19: The normalized radial residual displacement versus the normalized radial distance of the hemisphere unloaded from (a) small, and (b) large normalized interference depths.

Unloaded Displacement

In this section the unloaded or residual displacement along both the radial and axial direction (U_x/γ_c and U_y/ω_c) of the hemisphere are monitored with respect to the normalized radial distance, r/a_c (see Figs. 3.19 and 3.20). The residual displacement is defined here as the displacement on the surface which remains after the hemisphere is completely unloaded from a normalized penetration depth, ω^*. The residual displacements occur when the hemisphere has plastically deformed and does not fully recover to its original shape (see schematic in Fig. 3.14). The displacements are also labeled for each normalized penetration depth, ω^*, from which the hemisphere is unloaded.

As seen from the normalized residual displacement plots (Figs. 3.19 and 3.20), once the hemisphere is loaded to $\omega^*>1$ (which marks the transition from the elastic to elasto-plastic regime) and then unloaded, the residual displacements tend to increase with the magnitude of the removed load (see Fig. 3.19). Comparing Figs. 3.16(a) and 3.19(a), at small normalized interferences the trends between the loaded and unloaded cases are very different. After a small normalized interference is removed, the hemisphere is still mostly elastic, with only a small region of plastic deformation. Most of the hemisphere material then tries to restore its original shape, while only a small portion resists. In the radial and axial direction this results in regions of negative and positive deformation when the hemisphere is unloaded. The negative deformation occurs above the plastic core, while the positive deformation occurs mostly outside of this region. This phenomenon is known as a residual pile-up, which is further enhanced for larger

deformations. The curvature of the hemisphere has the effect of negating the material pile-up so that the unloaded hemisphere is essentially flattened, resulting in "out-of-roundness" for the hemisphere. A dimple or indentation will form on a surface with little curvature.

After large interferences are removed, the plastic regions dominate, and the material remains more in the plastically deformed geometry (see Figs. 3.19(b) and 3.20(b)). In contrast to smaller residual deformations (Figs. 3.19(a) and 3.20(a)), the residual surface displacements after large loads mimic the deformations of the loaded hemisphere (see Figs 3.17(b) and 3.18(b)). However, there are some regions which still remain elastic and tend to return to their original shape when unloaded. Therefore, the overall magnitude of the residual displacements are less than that of the loaded conditions. Also, the residual displacements in the axial direction tend to change direction when unloaded and cause a crown of material to rise around the unloaded contact region (see Fig. 3.20). This occurs near the edge of the contact area and is referred to as the previously mentioned residual pile-up. The peaks of deformation in both the x and y direction are located at the same r/a_c and correspond to the residual pile-up. As the load that the hemisphere is unloaded from increases, the pile-up acquires a sharper edge.

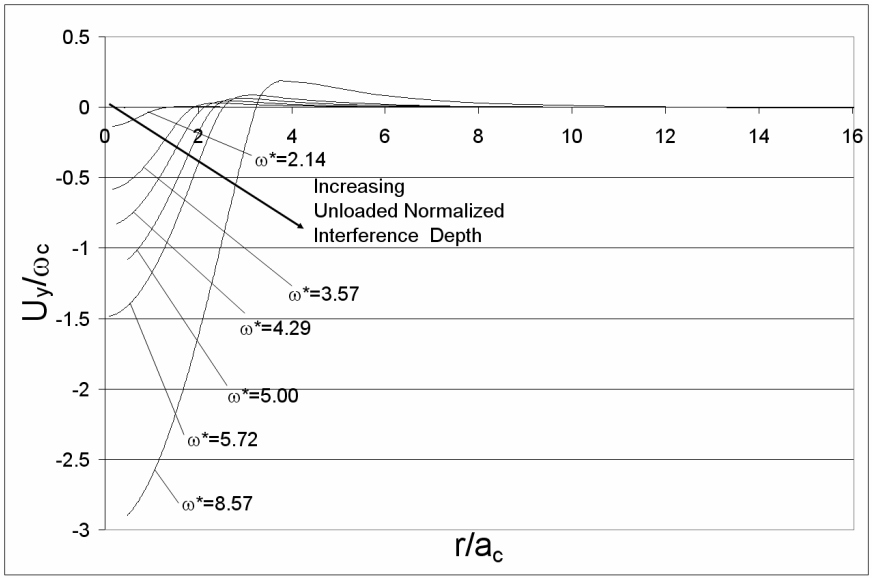

(a) small normalized unloaded interferences, ω^*

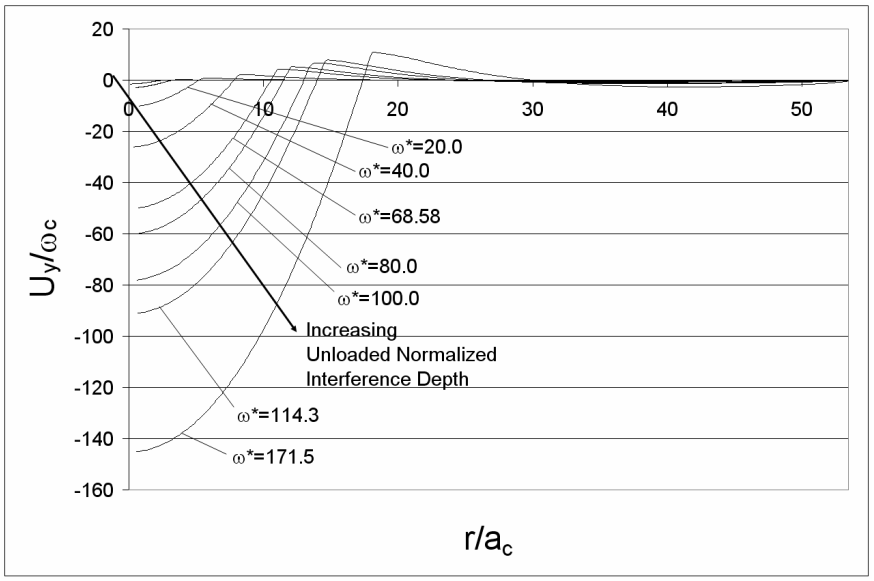

(b) large normalized unloaded interferences, ω^*

Figure 3.20: The normalized axial displacement versus the normalized radial distance of the hemisphere unloaded from (a) small, and (b) large normalized interference depths.

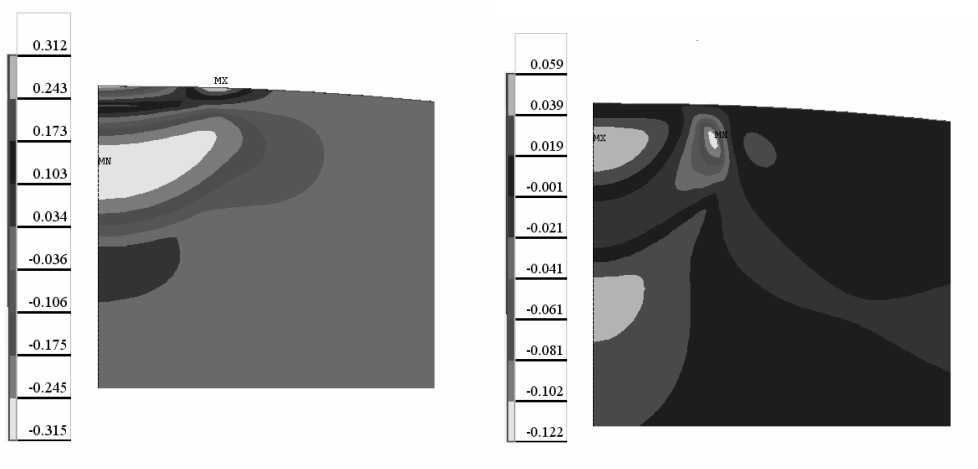

(a) radial stress, σ_x/S_y (b) axial stress, σ_y/S_y

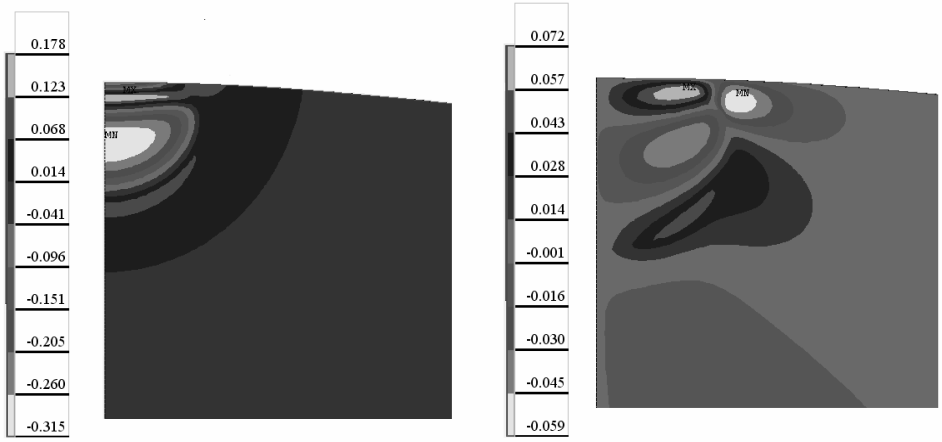

(c) hoop stress, σ_z/S_y (d) shear stress, τ_{xy}/S_y

Figure 3.21: Contour plots of the complete stress tensor for a hemispherical contact unloaded from ω^*=3.92.

The residual pile-up marks the sharp transition from the contact region to the free boundary and it also increases in magnitude with the normalized interferences from which the hemisphere is unloaded. Kral et al. (1993, 1995a, 1995b) and Ye and Komvopoulos (2003) also confirm the occurrence of pile-up during the FEM analysis of the repeated indentation of a half-space by a rigid sphere. Johnson (1968) also experimentally confirms the existence of a residual pile-up. Residual pile-up readily occurs during indentation type hardness tests after unloading, and must be accounted for when making hardness measurements (Tabor, 1951).

These deformations change the surface profile of the hemisphere. Also, the contact of the asperities on rough surfaces is commonly modeled by hemispherical contact. This indicates that the surface topographies of heavily loaded rough surfaces will also change after the load is removed. The current analysis suggests that after a rough surface is unloaded from plastic deformation, the surface asperities will be flattened and have a pile-up region around each contact. If the asperity has a large radius of curvature in relation to the contact radius, the pile-up may also cause an indentation in the surface. These changes in topography are important in such cases as boundary lubrication and sliding friction. The changes in the surface profile will also affect heavily loaded ball bearings. For ball bearings to operate properly, the balls must be as close as possible to spherical in shape. This work shows that after unloading from heavy loads, the balls may lose their original spherical shape and have the potential to cause bearing failure.

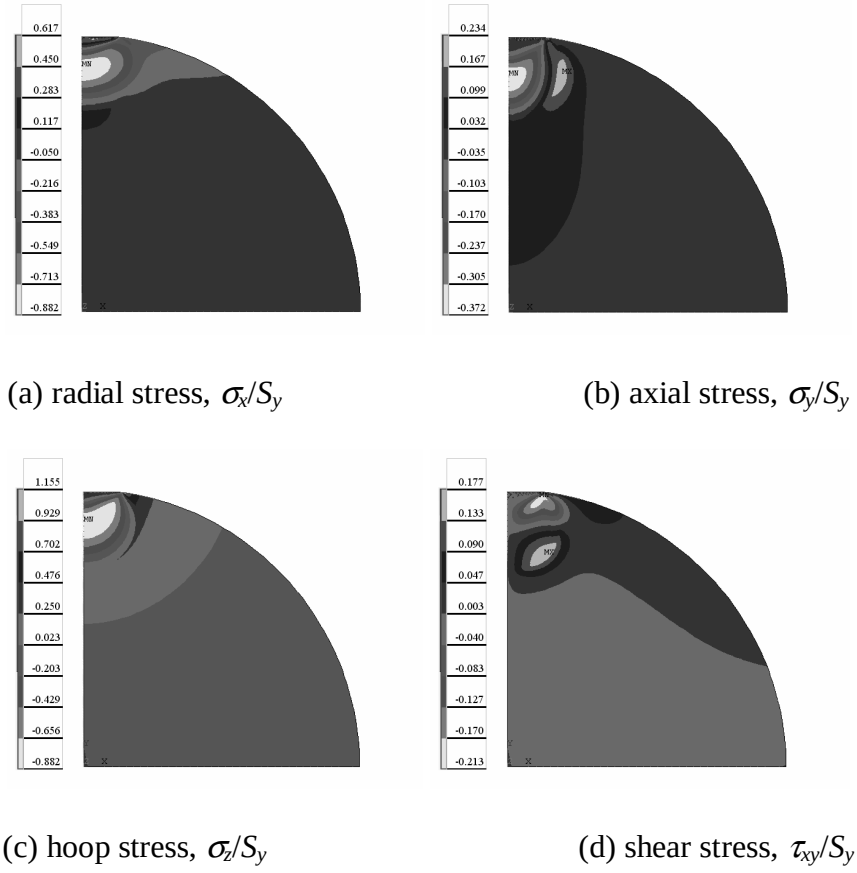

(a) radial stress, σ_x/S_y (b) axial stress, σ_y/S_y

(c) hoop stress, σ_z/S_y (d) shear stress, τ_{xy}/S_y

Figure 3.22: Contour plots of the complete stress tensor for a hemispherical contact unloaded from ω^*=35.0.

Residual Stress Formation

The value of the von Mises stress is used in this analysis to predict yielding of the hemisphere material. However, by calculating the von Mises stress some information about the material stress tensor is lost. The von Mises stress shows how 'intense' the stress state is relative to the yield strength; However, as a positive quantity it does not reveal if the material is in tension, compression, or under shear etc. In the study of crack initiation and propagation it is important to know the orientation of stress in relation to a

crack and if stress is tensile or compressive (Dowling, 1993). Thus it is important to first understand the distribution of the complete stress tensor throughout the hemisphere.

When the plastically deformed hemisphere is unloaded, the elastic material attempts to restore its original shape. However, the plastically deformed regions inhibit this since the material 'memory' or 'state' has changed. This results in regions of tension and compression, even though the overall force applied to the system sums to zero. The plots of the 3-D stress tensor (σ_x, σ_y, σ_z, τ_{xy}) for a hemisphere unloaded from ω^*=3.92 show clearly these regions of tension and compression (see Fig. 3.21). Since the problem is axisymmetric the shear stresses τ_{xz} and τ_{yz} are identically zero. These results are also given for a hemisphere unloaded from ω^*=35 in Fig. 3.22.

The distribution of σ_x shows compressive and tensile radial stress regions. Figure 3.21(b) shows the interesting distribution of stresses in the *y* direction. Near the plastic core σ_y is tensile and σ_x is compressive. For σ_y there is a band of compressive stresses below the edge of contact and also along the axis of symmetry but closer to the center of the hemisphere. The differing stress distributions of σ_x and σ_y will contribute to larger von Mises stresses in certain regions. For instance, a region will have higher von Mises stresses and be closer to yielding if orthogonal normal stresses differ in sign or magnitude.

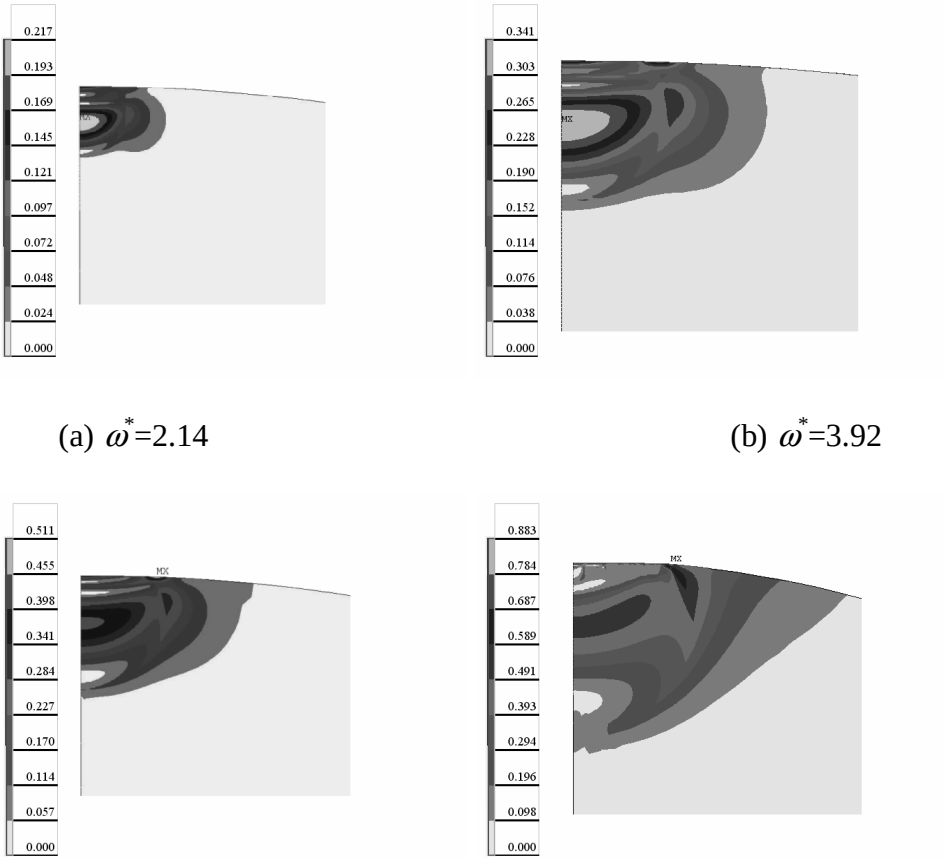

(a) ω^*=2.14 (b) ω^*=3.92

(c) ω^*=5.71 (d) ω^*=15.00

Figure 3.23: Contour plot of the normalized elastic residual von Mises stress (σ_{vm}/S_y) at various unloaded normalized interferences.

Figure 3.21(c) depicts stress contours for the residual hoop stress, σ_z. If the stress values are followed along the axis of symmetry, it is apparent that it switches between tension and compression several times. As mentioned, this results in complex formation of the von Mises stress.

The contour plot of the residual shear stress (τ_{xy}) in Fig. 3.21(d), for a hemisphere unloaded from ω^*=3.92, shows an interesting distribution. Near the edge of unloaded contact, there is a region of positive shear stress close to the axis of symmetry that lies next to a region of negative shear stress. The shear stress seems to peak at points away

from the axis of symmetry, thus forming hoops of high shear stress around the circumference of the hemisphere. This shear stress amplifies the von Mises stresses within the hemisphere.

The various stress contours which map the complete stress tensor throughout the unloaded hemisphere are also presented for a hemisphere unloaded from a larger interference depth of ω^*=35.0 in Fig. 3.22. In comparison to Fig. 3.21, these contour plots show how the residual stresses evolve and spread through the hemisphere with increasing plastic deformation. Clearly, the stress distributions can change significantly as load and plastic deformation are increased. Although the residual stresses still exhibit similar regions of tension and compression as shown for ω^*=3.92 in Fig. 3.21.

Interestingly, in Figs. 3.22(a) and 3.22(c) there are regions of high tensile stresses in the *x* and *z* direction at a point near to the unloaded edge of contact. These stresses correspond to the location of the residual pile-up identified earlier. It seems that when the hemisphere is unloaded, the yielded material, in conjunction with the elastic restoring effect, push the pile-up area upward in the *y*-direction. This action causes tensile stresses in the *x* and *z* directions.

Contour plots of the residual von Mises stress (Figs. 3.23-3.24) are also generated in order to monitor the intensity of the residual stress formation in the hemisphere. Figure 3.23 shows purely elastic residual von Mises stress distributions while Fig. 3.24 shows the onset and formation of plastic regions. The plots display the results for a hemisphere unloaded from a range of $2.14 \leq \omega^* \leq 100.0$. As the plastic deformation within the hemisphere increases due to larger interferences and then unloaded, the residual stresses increase and migrate. This migration causes the maximum von Mises stress to

move from one location to another. The maximum stress location then transitions from a point on the axis of symmetry to a point near the surface at the edge of the unloaded contact area. The maximum stress location after the shift corresponds to the location of the residual pile-up seen in Fig. 3.20. Table 3.8 shows the location of the maximum residual stress for hemispheres unloaded from various normalized interferences.

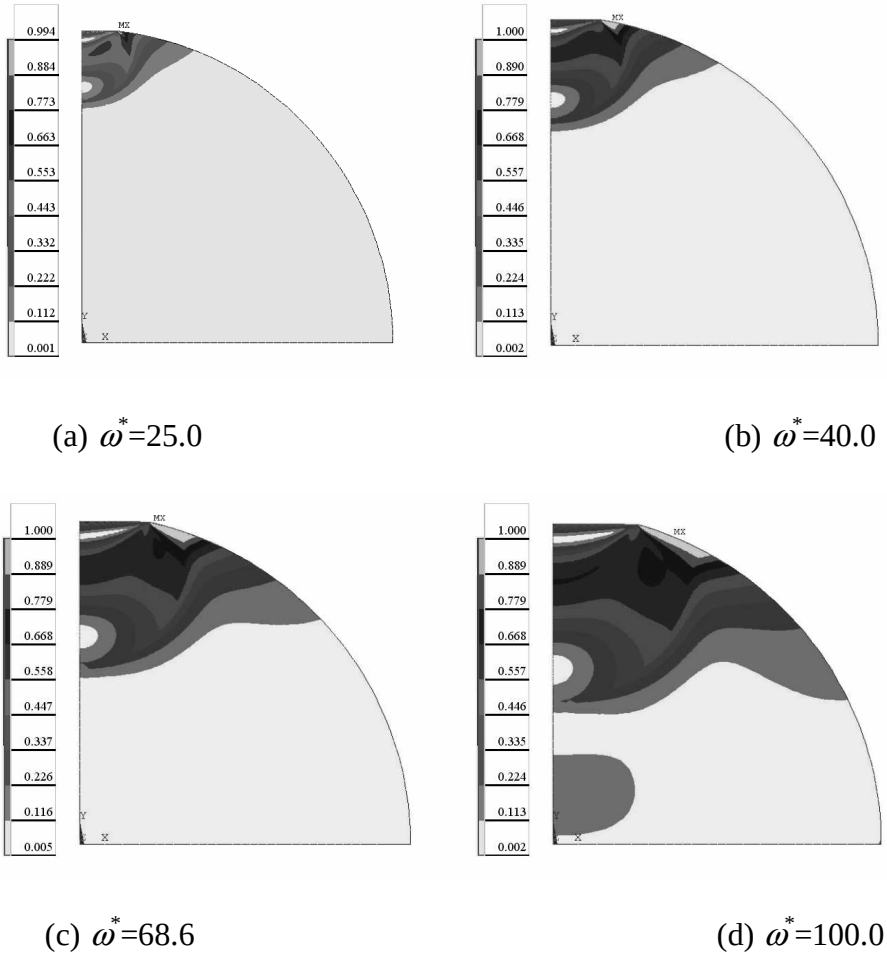

(a) ω^*=25.0 (b) ω^*=40.0

(c) ω^*=68.6 (d) ω^*=100.0

Figure 3.24: Contour plot of the normalized residual von Mises stress (σ_{vm}/S_y) at various unloaded normalized interferences at the onset and formation of plastic residual stresses.

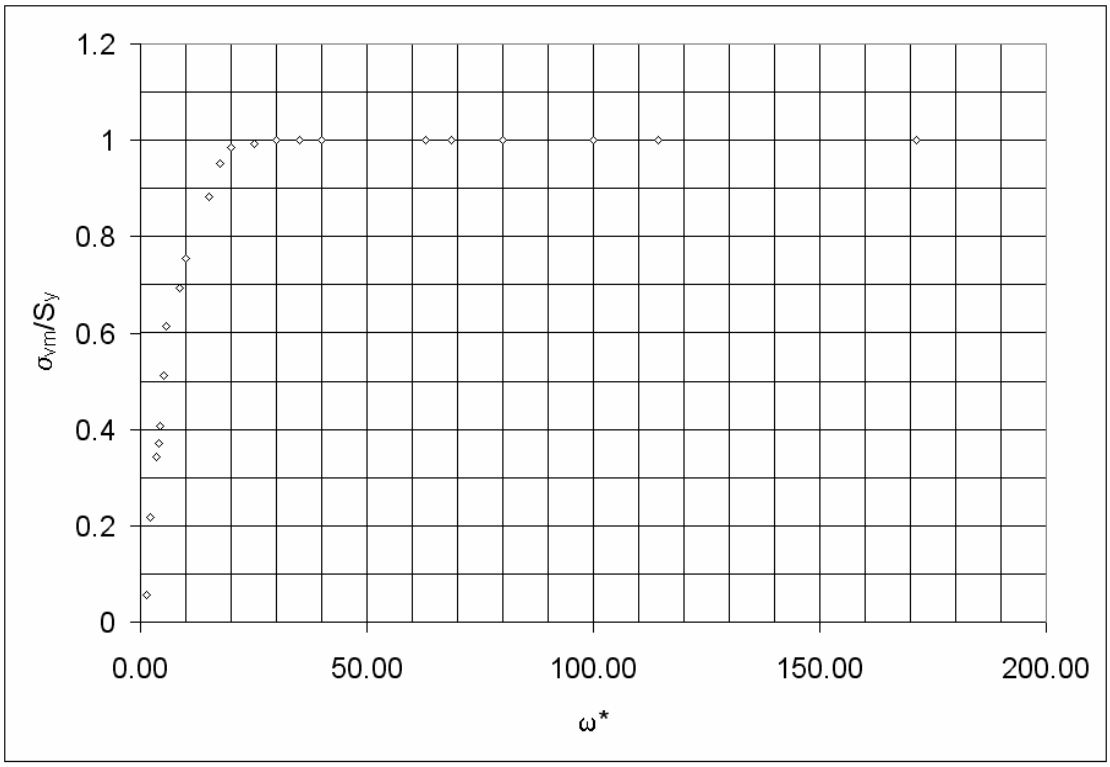

Figure 3.25: The normalized maximum von Mises residual stress of the unloaded hemisphere as a function of the unloaded ω^*.

Table 3.8: The location and value of the maximum von Mises residual stress for various normalized interference depths.

Normalized Interference Depth (ω^*)	**Maximum Unloaded von Mises Stress (σ_{vm}/S_y)**	r/a_c	$(R-y)/\omega_c$
1.43	0.057	0.00	34.18
2.14	0.217	0.00	43.44
3.57	0.344	0.00	61.64
3.92	0.371	1.90	1.81
4.29	0.408	2.02	2.07
5.00	0.511	2.29	2.61
5.72	0.615	2.46	3.03
8.57	0.693	3.24	5.26
10.00	0.754	3.73	6.97
15.00	0.883	4.70	11.05
17.50	0.952	5.11	13.11
20.00	0.986	5.59	15.65
25.00	0.994	6.38	20.46
30.00	1.000	7.25	33.57

Examining the values of $(R-y)/\omega_c$ in Table 3.8, the normalized location of the maximum von Mises stress shifts from the axis of symmetry to the surface for a hemisphere unloaded from normalized interferences between 3.57 and 3.92. This shift signifies the migration of the residual stresses from one location of the plastic core to the residual pile-up at the edge of unloaded contact. However, once the material remains plastic after unloading there is no single point of maximum von Mises stress since regions of plasticity are formed (see Fig. 3.24). The maximum von Mises stress normalized by the yield stress is plotted in Fig. 3.25 for hemispheres unloaded from increasing values of ω^*. This plot also shows how the maximum von Mises stress levels off to the yield strength for a hemisphere unloaded from a normalize interference within $25 \leq \omega^* \leq 30$. This value signifies a threshold that indicates residual plastic stresses. In other words, this value marks the minimum load that when removed, a region in the hemisphere has a high enough residual von Mises stress to remain plastic. Then the region of plastic residual stress grows at the edge of contact when the hemisphere is unloaded from increasing values of normalized penetration depth, ω^* (see Figure 3.24). The plastic residual stress appears to grow along the surface away from the unloaded area of contact. Since the unloaded hemisphere's location of maximum von Mises stress transitions to the surface, the location of plastic stress in the loaded and unloaded hemisphere do not always correspond.

Comparison between Aluminum and Steel

In order to measure the effect of the material properties on the hemisphere deformation, an aluminum hemisphere is also modeled for a hemisphere unloaded from a

ω^*=135. Table 3.7 shows the properties used for aluminum as taken from (Shigley, 1987). As previously, the radius, *R*, is held constant.

Figure 3.26 and 3.27 show the plot of the normalized axial and radial displacement as a function of the normalized radial distance, r/a_c, on both the loaded (Fig. 3.26) and unloaded (Fig. 3.27) condition and for both materials. An inset is provided for a plot of displacement normalized by the constant hemisphere radius, *R*. From the plots, the deformation of the aluminum and steel hemisphere tend to follow the same trend. However, the values of the displacements normalized by *R* (or by ω_c, which is not shown) are quantitatively very quite different. It appears that the normalizations (U_x/γ_c and U_y/ω_c) used are effective at generalizing the results for the two different materials (see Appendix B). As stated in the previous section, the deformation of the hemisphere also depends on the properties of the material as well as the interference. Even though loaded to the same normalized interference, the steel is compressed down with the real displacement of 4.7% of *R*, while the aluminum is compressed down with only 1.4% of *R*. Without normalization, the differences in the interference are significantly large, causing the differences in the displacements to also be large. The residual pile-up can still be spotted for both materials, as the contact was loaded to the fully plastic regime.

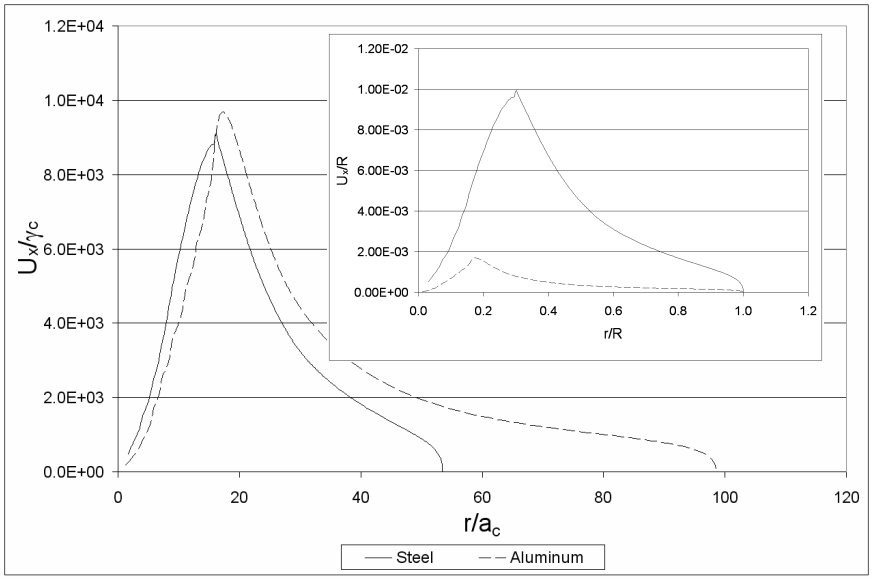

(a) Loaded Radial Displacement

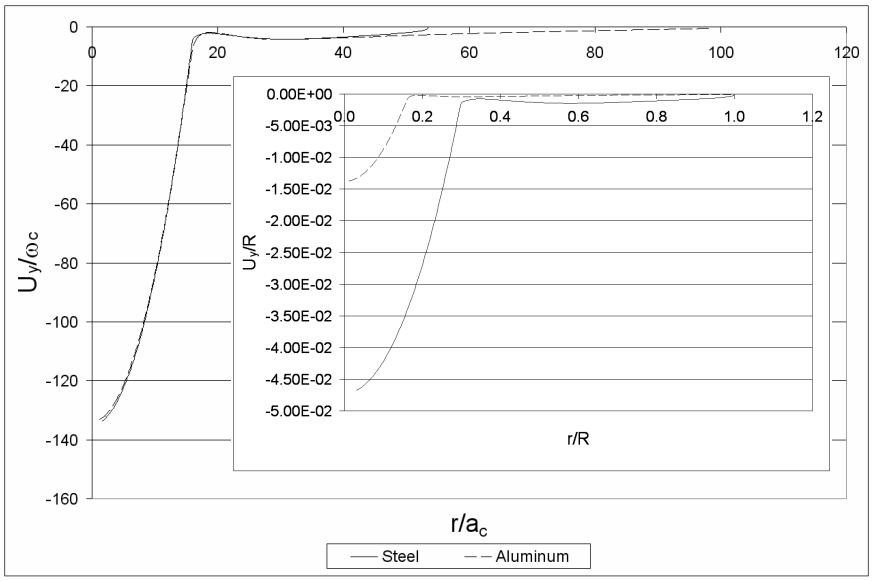

(b) Loaded Axial Displacement

Figure 3.26: The normalized surface displacement of aluminum and steel hemispheres loaded to ω^*=135 versus the normalized radial location.

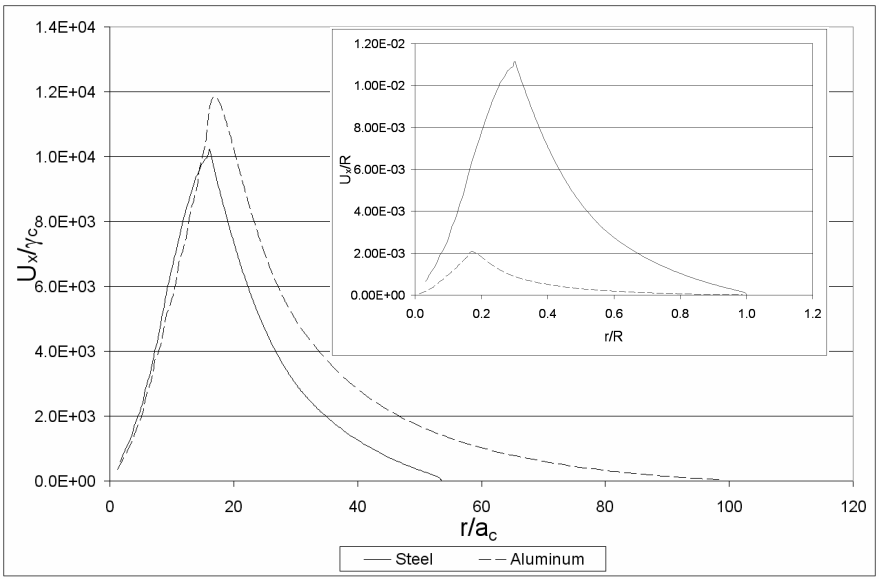

(a) Unloaded Radial Displacement

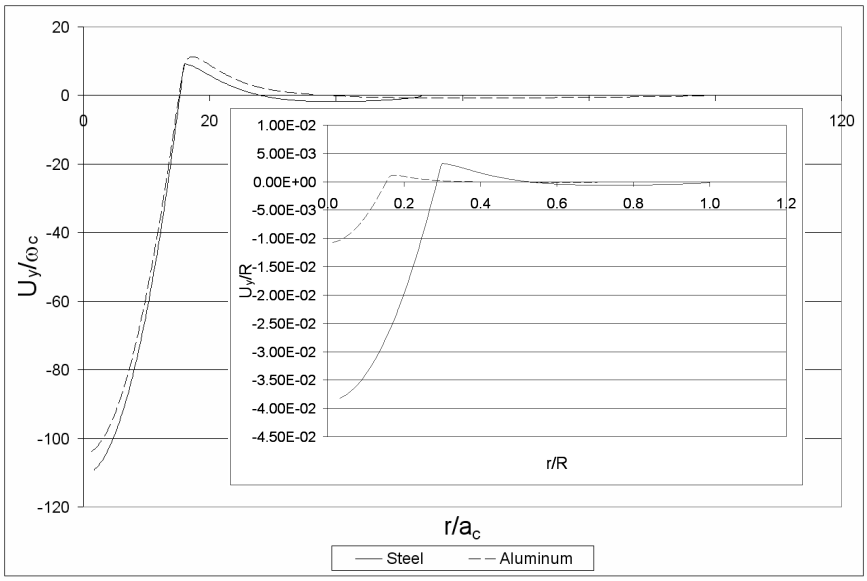

(b) Unloaded Axial Displacement

Figure 3.27: The normalized residual surface displacement of aluminum and steel hemispheres unloaded from ω^*=135 versus the normalized radial location.

Repeated Contact

As elastic perfectly-plastic theory suggests, when an identical repeated load is applied to the hemisphere after being unloaded from elastic perfectly-plastic deformation, the hemisphere returns to precisely the same loaded state as the initial loading. This occurs because the material undergoes no strain hardening, i.e. the load carrying capacity of the hemisphere material does not change with contact, even though it has plastically deformed. Introducing history dependant strain hardening is expected to alter these results. It should be noted, that in the contact of real rough surfaces in which the asperities do not align, bulk materials deform, and there is slip or sliding, the asperity contacts may not align and behave as described above.

3.6 Elasto-Plastic Spherical Contact Conclusions

This chapter presents a 2-D axisymmetric finite element model of an elastic-perfectly plastic hemisphere in contact with a rigid flat surface. A comparison is also made with other existing models. The material is modeled as elastic-perfectly plastic, and yielding occurs according to the von Mises criterion. A concise form is presented for the critical interference at which plastic deformation initiates within the hemisphere. It is derived from the Hertzian solution and the von Mises yield criterion. An a priori definition of the hardness is not needed.

The resulting plots indicate that the FEM results for the contact area agree closely at small interferences with the trends of the Hertzian solution. While at large interferences the FEM predicts contact areas that surpass Abbot and Firestone's fully plastic model (1933) (that is based upon truncation). The ZMC model is found to differ significantly from the FEM results, where the KE model (which is also based on FEM results) follows more closely, although still does not capture the varying hardness trend. An empirical formulation for the contact area is also fitted to the FEM data as a function of the material properties and interference.

The FEM results of the contact force predict a lower load carrying capacity than the AF model for most materials and values of ω^*. This is because the AF model assumes that the average pressure distribution is simply the hardness, which is approximated by $3 \cdot S_y$. It is found, however, that the fully plastic average contact pressure or hardness is not constant as is widely accepted.

Rather, the limiting value of the fully plastic average pressure varies with the deformed contact geometry, which in turn is coupled to the material yield strength. This is accounted for in an empirical formulation for the limiting average pressure to yield strength ratio, H_G/S_y. A formulation using H_G/S_y is then fit to the FEM contact force data.

A comparison is also made with the experimental results provided by Johnson (1968). The current model compares very well, and predicts the sparse experimental results significantly better than the KE model, particularly in the fully plastic regime. The experimental results also show that the hardness trend at large deformation is a very real phenomenon that can effect practical engineering applications.

This work reveals large differences between approximate analytical models and other numerical solutions. More importantly, the contact area, force, and pressure that are found to be particularly dependent upon the deformed geometry in all regimes and effectively dependent upon the material properties (e.g., strength) in the elasto-plastic and plastic regimes. The fit-them-all equations that solely depend upon deformation, which are found in previous works, are imprecise when compared to current FEM results. For example, the average contact pressure to yield strength ratio in all previous work is shown to increase monotonically with deformation, and is assumed to terminate (or truncate) at the hardness. In this work it is shown that such a truncation is not warranted. Particularly, it is shown that the truncation model of Abbott and Firestone (1933) cannot be justified. This work discovered significant geometrical and material nonlinearities, and that the hardness depends not just upon strength but also upon the modulus of elasticity,

Poisson's ratio, and most importantly upon the deformation itself (i.e., hardness is not a unique or fixed material property as indicated by Tabor (1951), and assumed by others after him). The results are based on the finest and adaptive mesh yet (over 11,000 four- and eight node elements for a single hemispherical asperity in contact with a rigid flat, and 100 contact elements) that is necessary for finite element convergence. The results were obtained by using ANSYS^{TM} and then independently confirmed by using ABAQUS^{TM}. The results have also been confirmed for material properties other than the five used in section 3.2.

The FEM elasto-plastic spherical contact model is then used to model a single asperity in a statistical model of contacting rough surfaces. This statistical model of contacting elasto-plastic rough surfaces is incorporated into the thrust washer bearing numerical simulation formulated in Chapter 4. The model is used in Chapter 4 to calculate the average asperity contact pressures on the surfaces of the bearing components. The KE model and the current model are found to be interchangeable at plasticity indices less than ten. However, on a single asperity scale, it has been proven in Section 3.2 that the current model is a more complete model. This is especially true when the models are used to predict large deformations. The CEB model is also proven invalid since at some surface separations it predicts a higher load carrying capacity for surfaces deforming elasto-plastically than for those deforming only elastically (GW model). The contact area predicted by the KE and CEB models are also limited by the Abbot and Firestone (1933) truncation model, which this chapter have proven to be unfounded.

It is also shown that the statistical models originally used by Greenwood and Williamson and subsequently used by Chang et. al. (1987), and Zhao et. al. (2000), among others, may not be valid for certain sets of surface parameters as indicated by Eq. (3.29). Great care should thus be taken when implementing Eq. (2.22) and Eq. (2.23) for surfaces having large value for σ/R. This also suggests that the contact of rough surfaces will likely result in a large number of asperities plastically deforming at their tip and into the bulk material.

Section 3.4 presents a finite element model (FEM) of the residual stresses and strains that are formed after an elasto-plastic hemispherical contact is unloaded. These results are presented but not used in any other portion of this thesis. The material is modeled as elastic perfectly-plastic and follows the von Mises yield criterion. A 2-D axisymmetric finite element model of an elastic perfectly-plastic hemisphere in contact with a rigid flat surface is used to calculate the residual stresses and deformations. At even light loads the residual stresses and deformations change the surface geometry of the hemisphere significantly and must be accounted for in cases such as in indentation tests, and rolling element bearings. This affect can also be applied to the repeated contact of rough surfaces when the alignment between them changes between load cycles.

The FEM produces contours for the axial and radial displacements as functions of the removed normalized interference depth and location on the surface of the hemisphere. The displacements are given relative to the surface. The displacements show how the deformation changes from elastic to elasto-plastic as the hemisphere begins to bulge outward instead of compress. A material pile-up can clearly be seen in Figure 6b of the residual axial displacement of the hemisphere after it is unloaded. This occurrence is also

verified experimentally by Johnson (1968) and also by the FEM analysis of Kral et al. (1993, 1995a, 1995b) on the repeated indentation of a half- space by a rigid hemisphere. Still, Kral et al. simulates the contact for about half the range of the current work.

Contour plots of the stress tensor components and the von Mises stress show the development of the residual stress distribution with increasing plastic deformation. This development results in a high stress residual pile-up appearing near the edge of the unloaded contact area. The approximate value for the minimum normalized interference, that when removed, a region of the residual stresses in the hemisphere remains plastic is found to be between $25 \leq \omega^* \leq 30$. This work also defines an normalized interference of about $3.57 \leq \omega^* \leq 3.92$ at which the maximum residual stress transitions from a location below the contact region and along the axis of symmetry to one near to the surface at the edge of the unloaded contact radius (within the pile-up).

Finally, this work analyzes the effect of material properties on the surface displacements. The deformation of the hemisphere is dependent on the properties of the material and the interferences. With a difference in Young's modulus, Poisson's ratio, and yield strength, the aluminum tends to deform differently from steel at the same normalized penetration depth. It appears that the normalization used for the displacements is effective at generalizing the results for both materials.

CHAPTER 4

NUMERICAL MODEL

This chapter outlines the formulation and individual components used in a thrust washer bearing model and then presents the results of the model. The physical mechanisms included in the model are elasto-plastic asperity contact, heat generation and balance, boundary and full-film lubrication, macro-scale thermoelastic deformation, and a force and moment balance. The force and moment balance couples all the effects together through the contact and hydrodynamic pressures. This coupled set of modeled mechanisms effectively results in a group of nonlinear equations which is solved numerically. Section 4.10 describes this procedure in greater detail. The following sections describe each physical mechanism and the modeling technique used for each.

Assumptions

The numerical simulation makes several assumptions which may result in differences between the results of the numerical and experimental portions of this investigation. The models of each physical phenomena also make assumptions, but they will not all be listed here. The major assumptions that the model makes are:

1. In the absence of wear models for lubricated conditions, wear of the component surfaces is not modeled anywhere in the simulation. Thus such effects as wearing in of the bearing surfaces and dampening of the thermoelastic instabilities is not captured.
2. Imperfections in the bearing components such as waviness or large scratches and burrs are not considered.
3. The model is quasi-steady state so that no time dependant effects such as vibrations and squeeze film effects are considered.
4. The effects of surface and lubricant chemistry at the component interfaces such as oxidation are not considered.
5. The gear is held at a constant tilt.
6. The relative speed is prescribed to occur between only two of the thrust washer bearing surfaces.
7. Convection is neglected because it is believed to be very small in comparison to the amount of heat conducted away from the bearing.

A schematic of the modeled problem for two washers is shown in Figs. 4.1 and 4.2. Figure 4.1 depicts the two washer bearing assembly looking straight into the y-axis. Figure 4.2 is the same assembly but viewed looking straight into the x-axis. The gear in the assembly is tilted about the y-axis an angle, γ_{tilt}. This tilt is held constant and the gear is only allowed to translate along the z-axis (as is indicated by assumption #5). Each washer is allowed to tilt (or rotate) about both the x and y axis and translate along the z-axis. All of the components will either be in contact, have fluid pressures separating

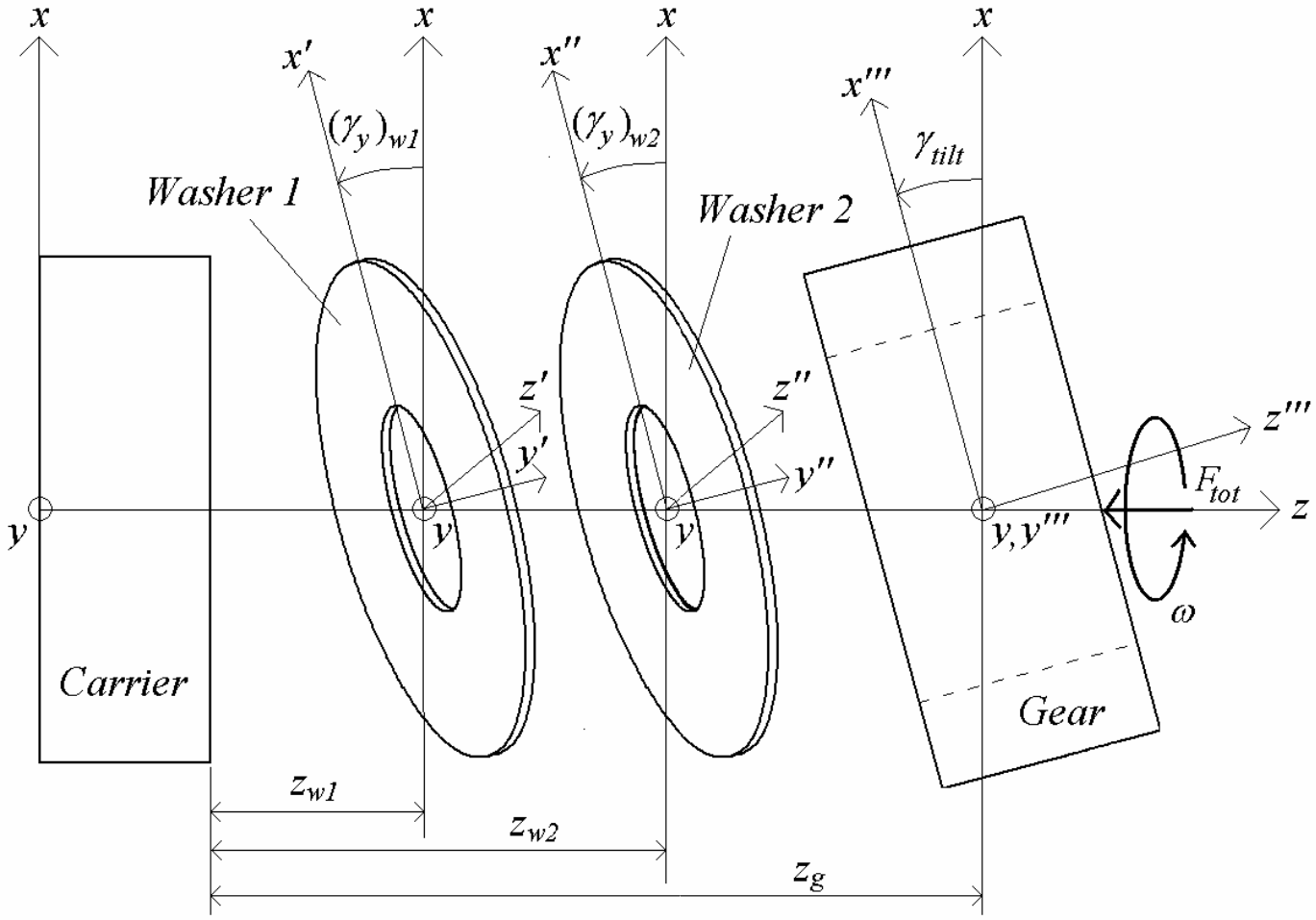

Figure 4.1: Schematic of two washer bearing system (view into y-axis).

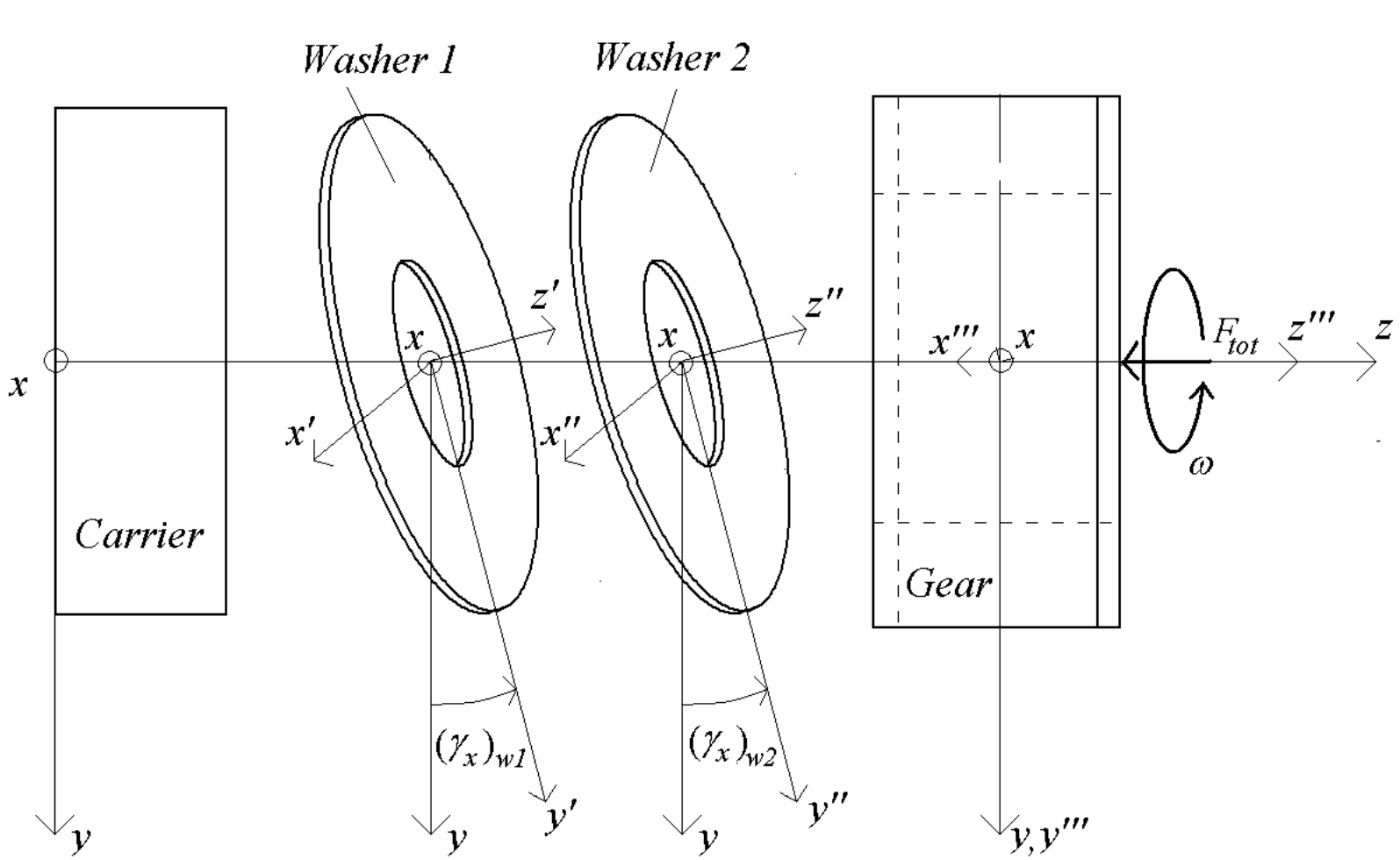

Figure 4.2: Schematic of two washer bearing system (view into x-axis).

them, or have a combination of both. The location and orientation of each component is determined by solving the set of nonlinear equations resulting from the coupled problem of physical mechanisms outlined in the following sections.

4.1 Boundary Lubrication

In regions in or near contact where asperities between surfaces come in close proximity, the asperities can influence the lubrication flow. Here the lubrication regime is known as boundary lubrication, in other words there is only a thin film of lubricant separating the surfaces, and the micro-topography of the surfaces greatly affect the flow of the lubricant. This work models a thin fluid film between the carrier, washer 1, washer 2, and the gear, as shown in Fig. 4.1 and 4.2.

Patir and Cheng (1978,1979) were the first to formulate these asperity flow effects between two three-dimensional surfaces. These flow effects were taken into account in the form of flow factors which were incorporated into a modified form of the Reynolds Equation given by

$$\frac{\partial}{\partial \mathrm{x}}\left(\phi_x \frac{h^3}{12\mu}\frac{\partial p}{\partial x}\right)+\frac{\partial}{\partial y}\left(\phi_y \frac{h^3}{12\mu}\frac{\partial p}{\partial y}\right)=\frac{U_1+U_2}{2}\frac{\partial \bar{h}_T}{\partial x}+\frac{U_1-U_2}{2}\sigma\frac{\partial \phi_s}{\partial x}+\frac{\partial \bar{h}_T}{\partial t} \qquad (4.1)$$

where ϕ_x, ϕ_y, and ϕ_s are flow factors which describe the affect the asperities have on the lubricant flow in different directions. Patir and Cheng give formulations for the flow factors as functions of surface roughness, asperity orientation (longitudinal or transverse) and film height. In this work it is assumed that the roughness is isotropic and thus

independent of direction. Patir and Cheng's formulations for the flow factors when the roughness is isotropic are:

$$\phi_x = \phi_y = 1 - .90e^{-.56(h/\sigma)} \tag{4.1a}$$

$$\phi_s = \left[\left(\frac{\sigma_1}{\sigma}\right)^2 - \left(\frac{\sigma_2}{\sigma}\right)^2\right]\Phi_s \tag{4.1b}$$

where

$$\Phi_s = 1.899 * \left(h/\sigma\right)^{0.98} e^{-0.92h/\sigma + 0.05h/\sigma} \qquad \text{for } h/\sigma \le 5 \tag{4.1c}$$

$$\Phi_s = 1.126e^{-0.25h/\sigma} \qquad \text{for } h/\sigma > 5 \tag{4.1d}$$

where σ_1 and σ_2 are the RMS roughness of each surface and $\sigma = \sqrt{\sigma_1^{\,2} + \sigma_2^{\,2}}$. Also $\overline{h}_T$ is known as the average gap and is defined as

$$\overline{h}_T = \int_{-h}^{\infty} (h + \delta) G(\delta) d\delta \tag{4.1e}$$

where δ is the combined roughness of the two surfaces given by $\delta = \delta_1 + \delta_2$ and G is the Gaussion height distribution of the surface given by Eq. (3.23).

In regions where the surfaces are out of the realm of asperity contact (h/σ>6) the lubrication model will be solved as a full film automatically by the modified Reynolds equation. This is because that as h/σ increases ϕ_x and ϕ_y approach the value of one and ϕ_s approaches zero so that Eq. (4.1) reduces to the unmodified version of the Reynolds Equation.

The fluid pressure between the bearing components is solved for from the modified Reynolds Equation (Eq. 4.1). Equation 4.1 is discretized using a finite difference scheme. The bearing surfaces are meshed by a cylindrical coordinate system. The mesh has 7 nodes in the radial direction and 50 nodes in the circumferential direction. A corresponding film thickness, h, is calculated at each node. At the inner and outer radius of the bearing, the boundary condition $p=0$ is applied to simulate ambient pressure. Around the circumference of the bearing surface the pressure follows the cyclic boundary condition. To model cavitation of the fluid, the Reynolds boundary condition is assumed. For each iteration, this condition assigns p=0 for any fluid pressures, p, which is less than zero. The Guass-Seidel over-relaxation method is used to iteratively solve the resulting set of equations. The fluid pressure, p, is solved for at each nodal location on the bearing.

Sections of the numerical model require the fluid force at the nodes on the surface of the bearing rather than values for the average fluid pressure. Linear interpolation is used to predict the pressure distribution between the nodes using the scheme outlined on pages 308-311 of Reddy (1993). Then the pressure over the areas surrounding each node are integrated to calculate the force at each node i, giving

$$F^i_{fluid} = \int_{A_i} p dA_i \tag{4.2}$$

4.2 Elasto-plastic Asperity Contact

In section 3.3, a model is derived to take into account elasto-plastic asperity contact. This model assumes that the individual asperity contact between rough surfaces can be approximated by hemispherical contact with a rigid flat. Then statistical relationships are used to model an entire surface of asperities with a range of heights described by a Gaussian distribution. The resulting model is given by substituting Eqs. (3.20, 3.21 and 3.23) into Eq. (2.23). Equation (2.23) is then integrated using Gauss-Legendre quadrature. Equation (2.23) provides an average contact force, P, as a function of surface separation or film thickness, h. In the numerical code, this relationship is used to predict the contact forces between the components of the thrust washer bearing. In the following sections the average contact force at a node i is assigned the notation F_{cont}^{i} such that $F_{cont}^{i} = P$.

4.3 Temperature/Viscosity Model

Within the transmission the lubricant is applied by small holes in the shaft at the center of the planetary gear set. Centrifugal forces cause the fluid in these holes to travel toward the outer radius of the assembly. The fluid thus may interact with gears, rotating components and other bearings before supplying any washer bearing in the assembly. Thus the lubricant may aerate or gather bubbles within it that are not expelled before it is used to lubricate a washer bearing. These bubbles will affect the behavior and load carrying capacity of the bearing. Because of the large scope of possibilities already incorporated in this work, the effect of bubbly lubrication will not be considered

The lubricant viscosity is predicted by the Roeland's equation (1966), which models empirically the effects of temperature on viscosity. The pressure independent form of Roeland's equation is given as

$$log(log\mu + 1.2) = -S_o log(1 + \frac{T_m}{135}) + log(G_o) \tag{4.3}$$

and solving for the viscosity, μ, yields

$$\mu = \mu_\infty 10^{G_o(1+T_m/135)^{-So}} \tag{4.4}$$

where μ_∞=6.31 x 10^{-5} N·s/m^2 and the rest of the variables can be found by fitting the formula to experimentally obtained viscosity values with respect to changing temperatures. This formula has been regressed to the measured viscosity of transmission fluid samples and found to be a good fit. For the transmission fluid used in this investigation G_o=3.545 and S_o=1.053.

4.4 Macro-scale Elastic and Thermal Deformation (FEM)

The finite element method (FEM) is used to model the elastic deformation of the bearing components on a macro-scale that is much larger than the asperities. Originally, the macro-scale deformations were to be calculated using the boundary element method (BEM). It was found that because the thinness of the washers, the BEM requires a mesh much finer than the FEM mesh. This discounts the advantage of using the BEM method. Thus the commercial FEM package ANSYS™ was used to calculate the deformations.

These deformations are coupled with the other models through the thermal and mechanical boundary conditions.

The finite element method provides a way to model an object and its governing equation (elasticity, energy, etc.) by breaking it up into a finite number of elements. The elements individually approximate the modeled equation within each element and satisfy its local boundary conditions, whether from adjacent elements or an external load. The finite element method is robust and can provide a solution to many engineering problems.

The system of equations which must be solved for the FEM, based on a given geometry and prescribed material properties is written as

$$[\mathbf{K}]\{\mathbf{u}\}=\{\mathbf{F}\} \tag{4.5}$$

where [**K**] is the resulting stiffness matrix, {**u**} is a vector of the displacements on the surface of the modeled domain and {**F**} is a vector of the traction forces on the surface of the modeled domain. A detailed derivation can be found in many textbooks, such as the book by Reddy (1993).

The finite element method is used in the current analysis to calculate the deformations of the washers due to thermal and mechanical loads. These loads are the sum of the fluid pressure, asperity contact pressure, and thermal loads due to surface temperature.

4.5 Half-Space Deformation

To improve computation time the gear and carrier on each side of the washer bearing are modeled as half spaces (see Fig. 4.3). These equations are found on page 54 and 382 of Johnson (1985). The nomenclature for this section is different than for other sections since area of interest is localized on the surface of the bearing as shown in Figure 4.3. For thermal deformations, the model uses specifically the analytical solutions to a half-space with a circular region of uniform heating:

$$\left(u_z\right)_{therm} = \begin{Bmatrix} -(cQ/4\pi)\left[2\ln(r_o/r) + (1-r^2/a^2)^{1/2}\right], r \le a \\ -(cQ/4\pi)\left[2\ln(r_o/r)\right], r > a \end{Bmatrix} \tag{4.6}$$

where $(u_z)_{therm}$ is the normal displacement due to thermal expansion, c is the specific heat capacitance, Q is the uniform heat across the circular region, r is the distance from the center of the circle, a is the radius of the circle, and r_o is the distance to a point where the $u_z = 0$.

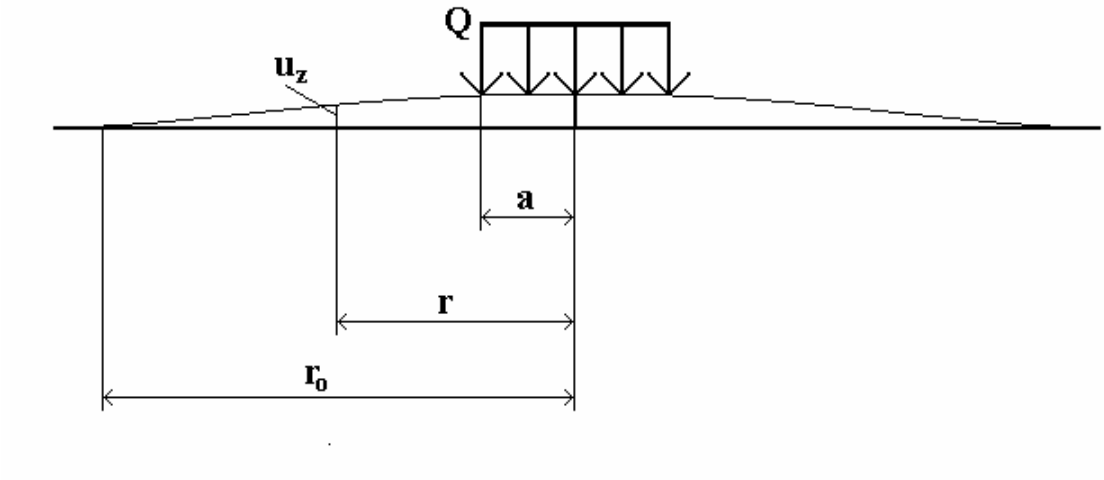

(a)

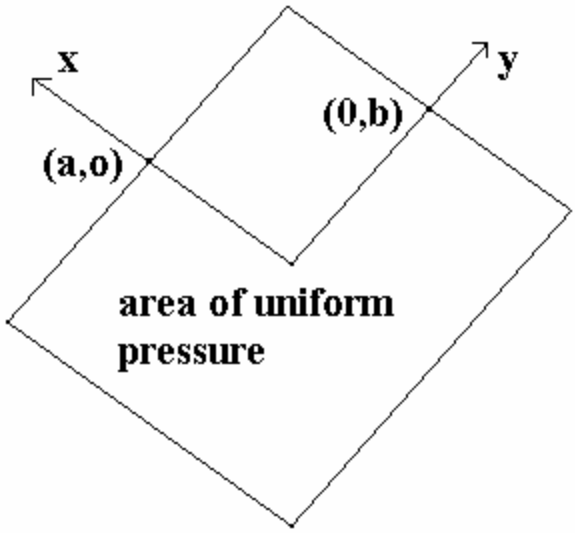

(b)

Figure 4.3: Schematic of local coordinate systems for half-space solutions of (a) uniform heat generation of a circular section and (b) uniform pressure over a rectangular section.

For the deformations resulting from mechanical pressures the solution for a uniform pressure on a rectangular region (see Fig. 4.3b) is used:

$$\frac{\pi E}{1-\nu^2}\frac{(u_z)_{mech}}{p_{tot}} = (x+a)\ln\left[\frac{(y+b)+\{(y+b)^2+(x+a)^2\}^{1/2}}{(y-b)+\{(y-b)^2+(x+a)^2\}^{1/2}}\right] + (y+b)\ln\left[\frac{(x+a)+\{(y+b)^2+(x+a)^2\}^{1/2}}{(x-a)+\{(y-b)^2+(x-a)^2\}^{1/2}}\right] + (x-a)\ln\left[\frac{(y-b)+\{(y-b)^2+(x-a)^2\}^{1/2}}{(y+b)+\{(y+b)^2+(x-a)^2\}^{1/2}}\right] + (y-b)\ln\left[\frac{(x-a)+\{(y-b)^2+(x-a)^2\}^{1/2}}{(x+a)+\{(y-b)^2+(x+a)^2\}^{1/2}}\right] \tag{4.7}$$

where p_{tot} is the sum of the average contact and fluid pressure in the polygonal region ($p_{tot} = p + F_{cont} / A_i$), a and b are the width and height of the region, and x and y are the location on the surface in relation to the center point of the polygonal region. $(u_z)_{mech}$ is the surface deformation due to the mechanical pressure.

The total surface displacement, u_z, is calculated as $u_z = (u_z)_{mech} + (u_z)_{therm}$. Then by using superposition, the surface deformation for the entire half-space due to an arbitrary heat and load distribution is approximated for the carrier and gear surfaces shown in Figs. 4.1 and 4.2.

4.6 Dry Friction Model

Locally, at the asperity contact a simple friction model is used to calculate the sliding friction force caused by asperity contact. The test rig was run at low speeds under dry conditions to predict the friction coefficient for the dry contact. Certain conditions

and materials behave in accordance to Amonton's law of friction, $F_{frict} = f \cdot F_{cont}$. For the bronze on steel bearings the friction coefficient was experimentally found to be, $f = 0.188$. Although other materials do not follow this 'law', as the friction coefficient, *f*, may vary significantly with load. There are various fundamentally derived models of friction that also suggest this same phenomena, such as the work by Chang et. al. (1988), Etsion and Amit (1993), Roy Chowdhury et. al. (1994), and Kogut and Etsion (2003). These works theorize that the plastic yielding of the contacting surface asperities can limit the COF between them.

Dry or unlubricated test runs resulted in the following coefficients of friction for the steel bearings at various loads given in Table 4.1. These values were obtained by running the bearing without any lubrication. It is interesting to also note that the COF decreases in relation to load. The resulting equation used to the friction of steel on steel contact is:

$$f = 0.48 - 0.05 \ln(F_{cont}) \tag{4.8}$$

Equation (4.8) may not be valid outside the range of the experimentally applied loads ($260.5N \le F_{cont} \le 1725.6N$).

Table 4.1: Dry effective COF values for various axial loads.

Normalized Load (F_{cont})	Experimental Coefficient of Friction (f)	Empirical Eq. (4.7) Coefficient of Friction (f)
260.5	0.274	0.276
504.7	0.207	0.243
748.9	0.201	0.224
1237.3	0.196	0.199
1725.6	0.186	0.182

4.7 Frictional Heating

The friction will be modeled at each point according to the asperity contact model and the fluid shear model. The entire friction force will be assumed to be transferred to heat at the contact point according to the equation at node *i*

$$q^i_{friction} = F_i V_i \tag{4.9}$$

where F_i is the average friction force and V_i is the relative sliding speed at the node. The average friction force will be calculated from the asperity contact model. The viscous shearing of the lubricant will also generate heat at the node. The equation for the viscous heating at an element *e* can be written as

$$q^i_{viscous} = \int_e \left(\mu \frac{V^2}{h} \right) dA_e \tag{4.10}$$

where μ is the effective viscosity, V is the relative speed between the surfaces, h is the film thickness and A_e is the area of a given element *e*.

If the relative speed between the two surfaces is large enough, each point on the surface will essentially see an average heat generation of all nodes that are the same

distance from the axis of rotation. This is because heat propagation is a time dependant process that is relatively slow in comparison to the rotational speed of most mechanical devices. Essentially, the temperature profile of washers that are rotating relative to neighboring components will be approximately axisymmetric. However, certain components may be stationary, like the carriers or washers that stick to neighboring components due to friction. The above approximation is then no longer valid, but the heat generation then becomes stationary and so can be easily applied as nodal boundary conditions.

4.8 Heat Balance

The finite difference technique is used to solve the steady-state heat conduction problem. Each component is modeled as a 2-D annulus with heat conduction and generation occurring between their contacting points. The two-dimensional steady-state heat transfer equation using cylindrical coordinates r and θ is:

$$\frac{\partial^2 T}{\partial r^2}+\frac{1}{r}\frac{\partial T}{\partial r}+\frac{1}{r^2}\frac{\partial^2 T}{\partial \theta^2}+\frac{1}{k}Q(r,\theta) \tag{4.11}$$

where $Q(r,\theta)$ is volumetric heat generation, T is the periodic temperature distribution around the circumference and

$$r=\sqrt{x^2+y^2} \tag{4.12}$$

$$\theta=\tan^{-1}\left(\frac{y}{x}\right) \tag{4.13}$$

Heat transfer is thus considered through the x and y plane of each component. Each component is meshed using a uniform cylindrical coordinate system and Eq. (4.11) is then discritized using the finite difference method. The finite difference discritized heat transfer equations in cylindrical coordinates on pgs. 469-471 of Ozisik (1993) are used.

The same mesh used to discritize the modified Reynolds equation (Eq. 4.1) is also used to discritize Eq (4.12). This mesh consists of 7 nodes in the radial direction and 50 nodes in the circumferential direction. At each nodal location the volumetric heat is the sum of the heat conducted to or from adjacent points on the bearing components (q_{cond}) and the heat generated due to friction (Eq. 4.9) and viscous shearing (Eq. 4.10):

$$Q(r,\theta) = (q_{cond} + q_{friction} + q_{viscous})_i / t_i \tag{4.14}$$

where t_i is the thickness of the component at node i. The heat transferred through to each node from adjacent components (q_{cond}) is modeled as a one-dimensional conduction problem as described in the following paragraphs. At the inner and outer radius the boundary condition of a zero heat flux is assumed. Thus heat convection is not considered because it is assumed to be small in comparison to the heat conduction.

The heat flowing away from the surfaces of the carrier and the gear are assumed to occur due only to one-dimensional conduction along the z-axis toward an ambient temperature set within the components. The ambient temperature is set to an approximate room temperature of 24°C. The heat transfer between the components is

modeled as one dimensional conduction in the *z*-direction (see Fig. 4.4). Thus conduction between the components (not within each component) is considered only between nodes at the same radial and circumferential location. Using the equivalent thermal resistance between each component at each nodal location, a prediction for the path of the heat conducted between the components is made.

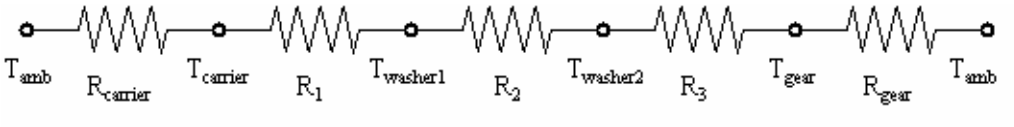

Figure 4.4: Schematic of heat transfer between components.

The thermal resistance between the components are calculated by

$$R_{carrier} = \frac{t_{carrier}}{K_{carrier}} \tag{4.15}$$

$$R_1 = R_{fluid} + \frac{R_{washer1}}{2} = \frac{h}{K_{atf}} + \frac{t_{washer1}}{2K_{washer1}} \tag{4.16}$$

$$R_2 = R_{fluid} + \frac{R_{washer1}}{2} + \frac{R_{washer2}}{2} = \frac{h}{K_{atf}} + \frac{t_{washer1}}{2K_{washer1}} + \frac{t_{washer2}}{2K_{washer2}} \tag{4.17}$$

$$R_3 = R_{fluid} + \frac{R_{washer2}}{2} = \frac{h}{K_{atf}} + \frac{t_{washer2}}{2K_{washer2}} \tag{4.18}$$

$$R_{carrier} = \frac{t_{gear}}{K_{gear}} \tag{4.19}$$

where t is the thickness of the component in subscript and K is the thermal conductivity. Then the one-dimensional heat conduction from a point a on one component to a point b on an adjacent component along the z-axis are calculated as

$$q_{cond} = \frac{(T_a - T_b)}{R_{a \to b}} \tag{4.20}$$

Equation (4.20) is substituted into Eq. (4.14) for the to calculate the total volumetric heat at a node. The Gauss-Seidel Method is used to solve for the temperature from the finite difference discritized Eq. (4.12). The temperatures and heat generation at each location on the component are then used to solve for the thermal deformations using FEM and the solution to a loaded half space (section 4.4 and 4.5). The temperature of two adjacent nodes on two sliding surfaces is also averaged to approximate the fluid temperature, T_m. T_m is then substituted into Eq. (4.4) to calculate the fluid viscosity at that node.

4.9 Force and Moment Calculations

The force balance of the individual components of the washer bearing (washers, carrier, gear) will each be solved individually using their specified boundary conditions. The elasto-plastic asperity contact model outlined in Chapter 3 calculates the average contact force, F^i_{cont}, at each node on the surfaces between the components. The solution of the Reynolds equation outlined in section 4.1 solves for the fluid pressures which are integrated to provide the fluid force at each node, F^i_{fluid} using Eq. (4.2). At each surface node i the total force is calculated as:

$$F_i = \left(F^i_{cont} + F^i_{fluid} \right) \tag{4.21}$$

A force and moment balance is performed by summing the contact forces and fluid forces of each component. Between each component there will be forces due to contact, fluid pressures or an externally applied load. For a bearing consisting of two washers there are six surfaces (see Fig 4.1 anf 4.2). On each surface the axial load and moments are calculated as:

$$\left(F_{tot} \right)_n = \sum\nolimits_n F^i \tag{4.22}$$

$$\left(M_x \right)_n = \sum\nolimits_n F^i \cdot y \tag{4.23}$$

$$\left(M_y \right)_n = -\sum\nolimits_n F^i \cdot x \tag{4.24}$$

where n is the surface number (the surfaces are numbered from 1 to 6 from left to right in Fig. 4.1 so that the surface of the carrier is surface 1 and the surface of the gear is surface 6). Figure 4.5 shows the resulting free body diagram of washer one.

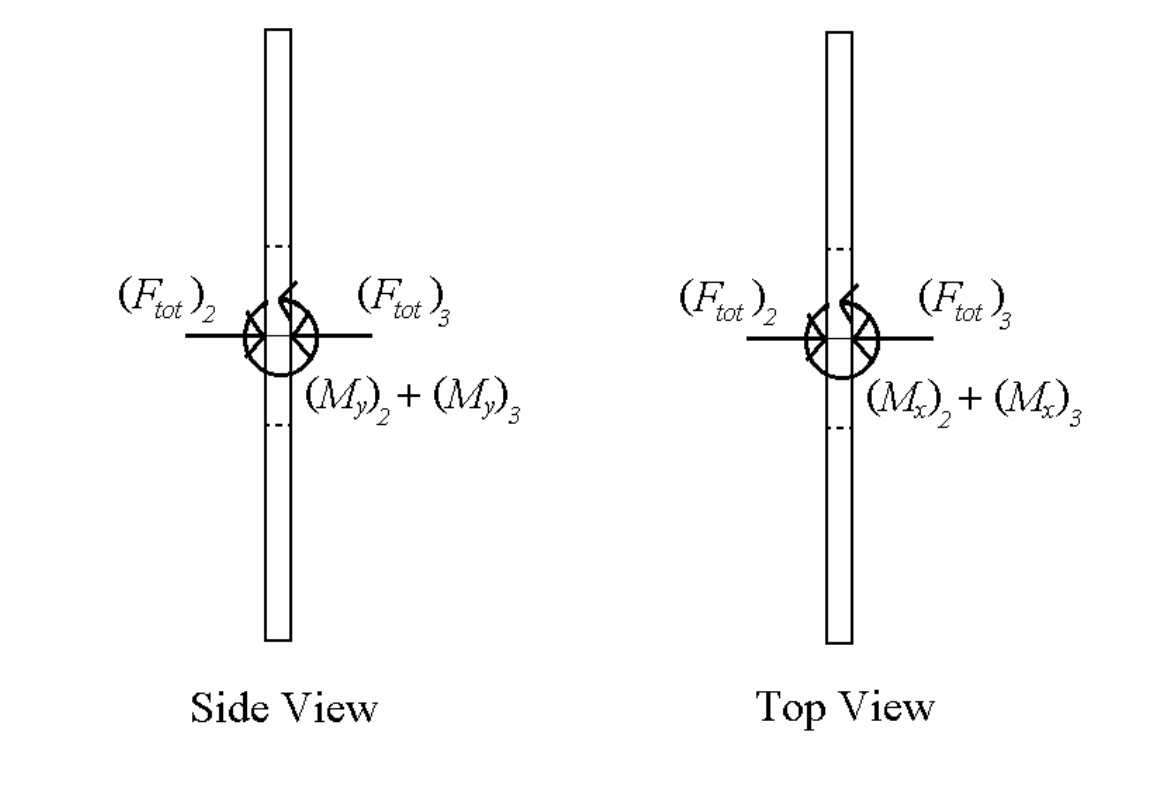

Figure 4.5: Free body diagram of washer one.

As is represented in Fig. 4.5, for washer one, the total force and moment balance are given by:

$$\left(F_{tot}\right)_2 + \left(F_{tot}\right)_3 = 0 \tag{4.25}$$

$$\left(M_x\right)_2 + \left(M_x\right)_3 = 0 \tag{4.26}$$

$$\left(M_y\right)_2 + \left(M_y\right)_3 = 0 \tag{4.27}$$

Similarly, Figure 4.6 shows the resulting free body diagram of washer two.

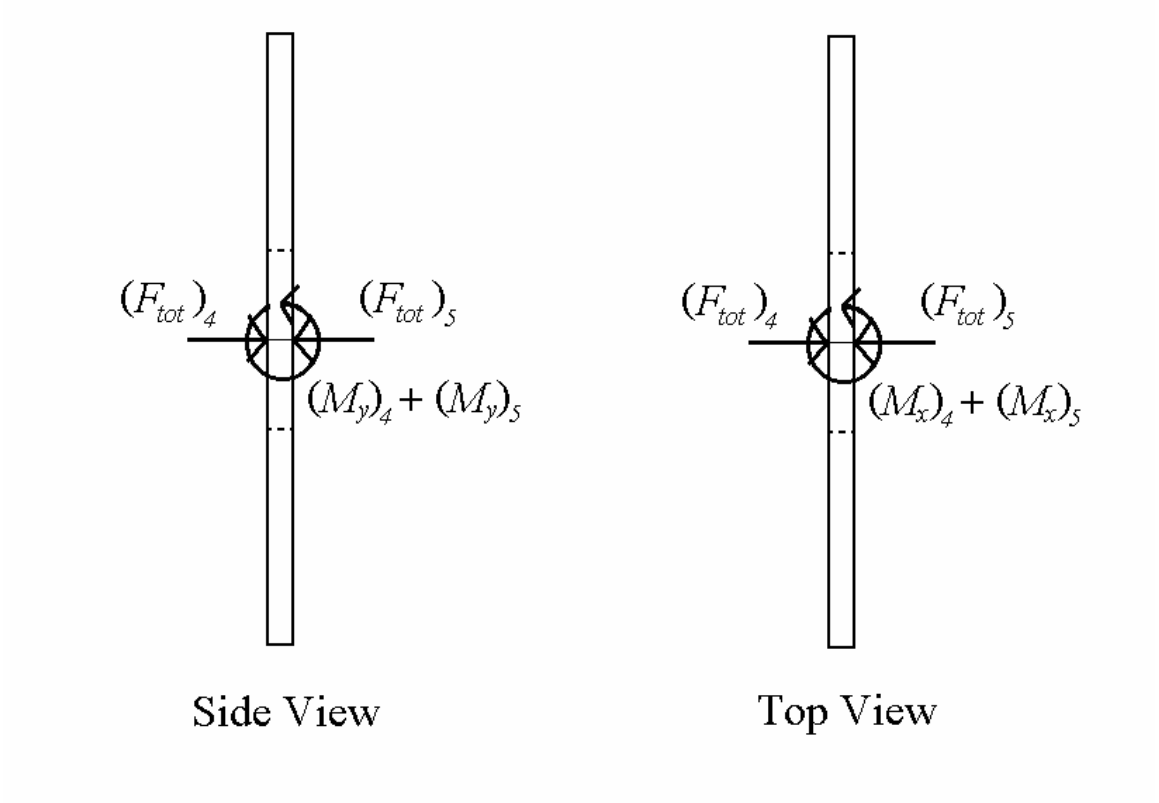

Figure 4.6: Free body diagram of washer two.

As is represented in Fig. 4.6, for washer two, the total force and moment balance are given by the three equations:

$$\left(F_{tot}\right)_4 + \left(F_{tot}\right)_5 = 0 \tag{4.28}$$

$$\left(M_x\right)_4 + \left(M_x\right)_5 = 0 \tag{4.29}$$

$$\left(M_y\right)_4 + \left(M_y\right)_5 = 0 \tag{4.30}$$

For the gear, the moments are not shown because the gear is not free to rotate and so only the axial load must be balanced. The free body diagram for the gear is shown in Fig. 4.7.

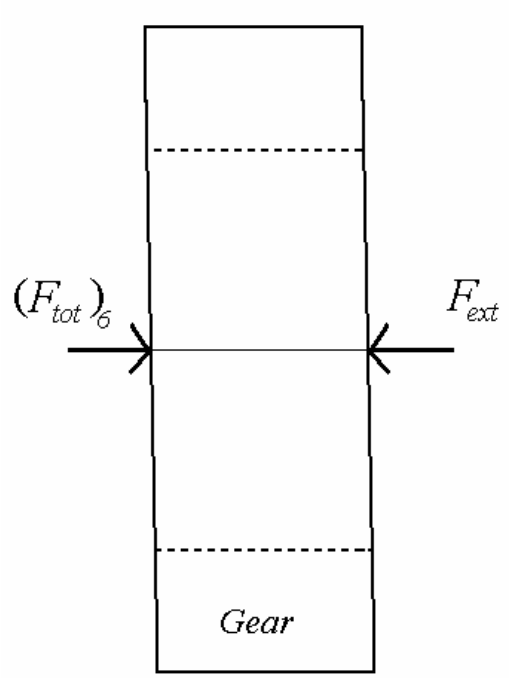

Figure 4.7: Free body diagram of gear.

As is represented in Fig. 4.7, for the gear, the total force balance is given by the equation:

$$\left(F_{tot}\right)_6 + F_{ext} = 0 \tag{4.31}$$

The force and moment balance depend ultimately on the location and orientation of the washers and gear. Thus the problem is formulated as a nonlinear set of 7 equations (Eqs. 4.25-4.31) with 7 unknowns. These equations are dependant on the governing physical equations of the thrust washer bearing and consider thermo-elastic deformation, asperity contact, boundary and full-film lubrication, and heat generation and balance. The unknowns are the axial location of each component, z, and the tilt of each component about the x and y-axis, γ_x and γ_y (see Fig. 4.1 and 4.2). For example, a thrust

washer bearing consisting of two washers, a carrier and a gear, there will be seven unknowns, or seven degrees of freedom. The gear is able to translate in the z direction, but has a fixed tilt, γ_{tilt}, about the y-axis and so accounts for one degree of freedom. The tilt of the gear is applied about the y-axis. Each washer is able to tilt about the x and y axis and also move along the z-axis and so has three degrees of freedom. The seven unknowns are explicitly z_{w1}, z_{w2}, z_g, $(\gamma_x)_{w1}$, $(\gamma_y)_{w1}$, $(\gamma_x)_{w2}$, and $(\gamma_y)_{w2}$.

4.10 Integrated Numerical Scheme and Convergence

The above methods are coupled through their boundary conditions and so must be satisfied simultaneously. This will be done by use of an iterative process. During each iteration, the above models are solved to satisfy their own boundary conditions. The Newton-Raphson method solves the set of nonlinear equations (Eq. 4.25-4.31) resulting from the coupled thrust washer bearing model. Since the derivatives of these nonlinear equations cannot be solved for analytically, the centered finite-difference method is used to approximate them.

$$f'(x_i) = \frac{-f(x_{i+2}) + 8f(x_{i+1}) - 8f(x_{i-1}) + f(x_{i-2})}{12\Delta x} \tag{4.33}$$

where f is one of unbalanced sums of the force and moment balances (Eqs. 4.25-4.31) and x is the one of the seven unknown variables (z_{w1}, z_{w2}, z_g, $(\gamma_x)_{w1}$, $(\gamma_y)_{w1}$, $(\gamma_x)_{w2}$, or $(\gamma_y)_{w2}$). Since the coupled problem is nonlinear (due to coupled effects of contact, lubrication and deformations), the Newton –Raphson method is further optimized toward convergence. This optimized Newton-Raphson method is written as:

$$f_{n+1} = f_n + c\left(f_n'\right) \tag{4.34}$$

where c is optimized using the golden rule method and f is again one of unbalanced sums of the force and moment balances (Eqs. 4.26-4.32). In addition, variable under-relaxation is used to further enhance convergence. The film height is under-relaxed by the following equation:

$$h_i = \lambda \cdot h_i + \left(1 - \lambda\right) \cdot h_{i-1} \tag{4.35}$$

where i is the current iteration number and λ is the current relaxation factor. Initially, when the solution is not near convergence and unstable, the film thickness values are relaxed, or softened by a low relaxation factor so erratic changes do not have a large effect. As the solution nears convergence and becomes more stable this value is increased to decrease the number of iterations needed and thus decreasing computational time.

The flow chart shown in Figure 4.8, depicts the overall iterative procedure and how the solution is checked for convergence. The interfacial conditions are the conditions between the components, such as fluid pressure and contact force, and will be adjusted until they converge to the final solution. Initially, a guess is made for the interfacial conditions. Initially the contact forces and fluid pressures are set to zero. The bearing components are initially evenly spaced and the minimum film thickness between them is set to h_{min}/σ=3. The initial temperature throughout the bearing is set to the

ambient temperature. The overall boundary conditions are also set at the same time (at the inner and outer radius, p=0). The flow chart also indicates that once the model converges that output values such as frictional torque and hydrodynamic load support are calculated (see following sections).

Frictional Torque

The frictional torque is calculated about the z-axis by summing the torques resulting from each frictional force at each node, i, on the surface of the bearing. The resulting equation for frictional torque on surface n is

$$\left(T_{frict}\right)_n = \sum_n \left[\left(F^i_{frict} + F^i_{viscous}\right)\cdot r\right]_i \tag{4.32}$$

where $F_{viscous}$ is the force due to viscous shearing on the bearing surface and is given by

$$F^i_{viscous} = \int_i \left(\mu \frac{V}{h}\right) dA_i \tag{4.33}$$

where V is the relative speed between the surfaces, and A_i is the area surrounding node i. The lowest total frictional torque between the six bearing surfaces is assumed to be the overall frictional torque which is transferred through the bearing.

Hydrodynamic Load Support

The total load carried by hydrodynamic lift is calculated by summing the nodal fluid forces on surface *n*:

$$\left(F_{fluid}\right)_n = \sum_n F^i_{fluid} \tag{4.34}$$

where F^i_{fluid} is given by Eq. (4.2). The total load carried by asperity contact is also calculated by

$$\left(F_{cont}\right)_n = \sum_n F^i_{cont} \tag{4.35}$$

where F^i_{cont} is calculated from Eq. (2.23).

Stop Criteria

Due to the phenomena of thermo-elastic instability and thermo-viscous distress, as described in the literature review in Chapter 2, the computer simulation is also capable of diverging, stalling or running in an infinite loop if not tracked properly. For this reason a few criterion are used to abort a load step prior to any numerical problems occurring. The criterion are:

1. If the bearing reaches an average temperature 200°C greater than ambient temperature.
2. If the temperature gradient continues to increase after a set number of iterations

These criterion represent real distress of the bearing due to thermo-elastic instability and thermo-viscous distress (see Chapter 2 for details of these phenomena).

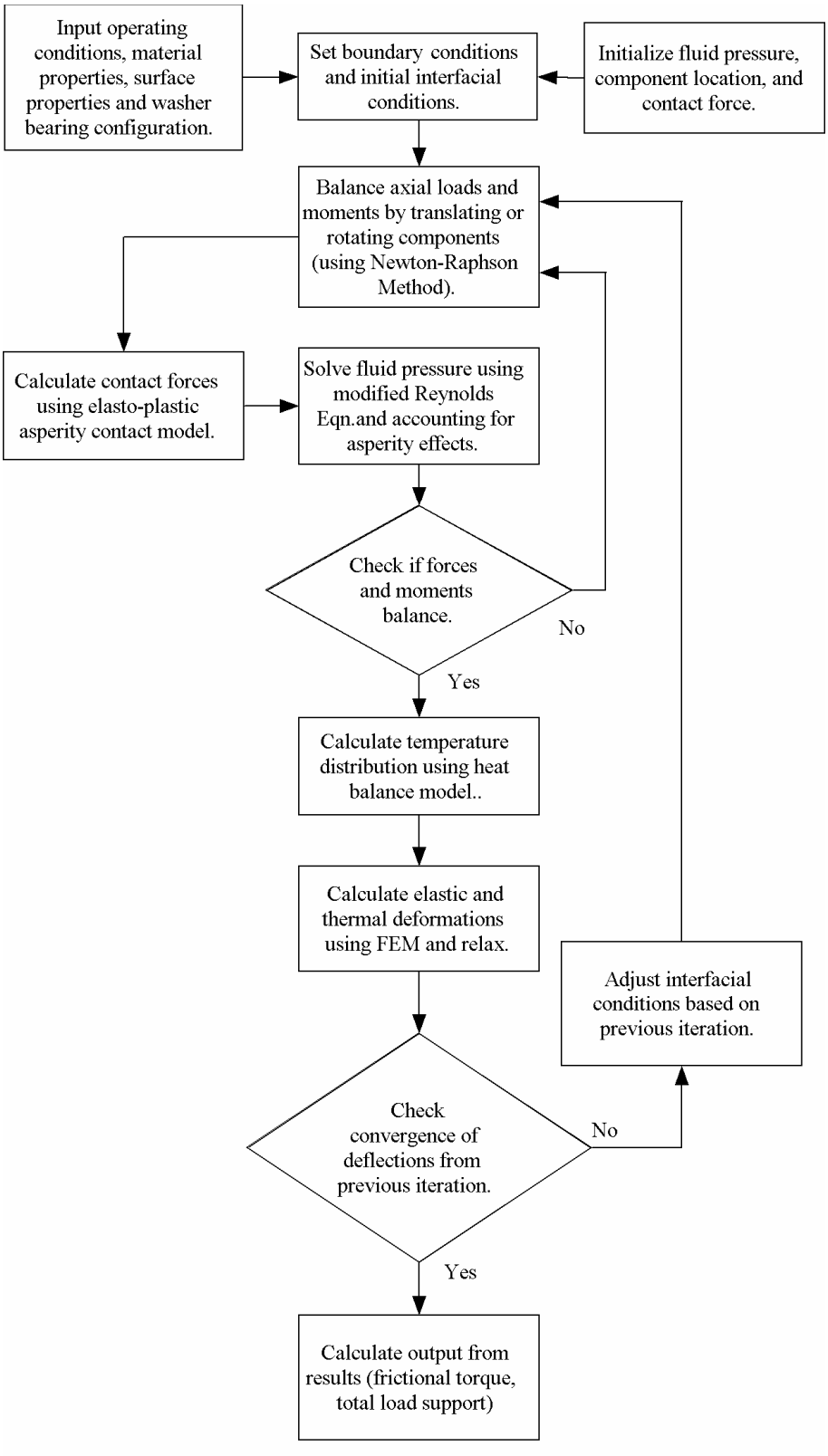

Figure 4.8: Flow-chart representation of algorithm to model a thrust washer bearing

4.11 Numerical Results

The numerical thrust washer bearing simulation is used to map and quantify the effect of various parameters on washer bearing performance. The case of a single round steel washer is used as reference with which to compare all results. The numerical program takes about six hours to run an initial load step on a 1.8Ghz PC. Once the initial load step is reached it takes considerably less time to converge to a new load step (about two hours). If the macro-scale deformations are neglected the computational time decreases drastically to about half an hour or less.

A tilt of γ_{tilt} is imposed on the gear to simulate the loading conditions in the transmission, although not exactly since in the transmission a moment causes the gear to tilt. The tilt is applied to simplify the problem and allow for a faster time until convergence. For the case of a single steel washer, the geometry and material properties found in table 4.2 are used. The relative velocity is applied between the washer and the gear.

The average spherical radius, *R*, at the tip of the asperities and the asperity surface desnsity, η, are needed to model asperity contact using Eq. (2.23). These values are approximated using profilometer measurements δ and σ and the methods outlined in McCool (1986). McCool finds that the equations for these variables are:

$$R = 0.375(\pi / m_4)^{1/2} \tag{4.36}$$

$$\eta = (m_4 / m_2) / 6\pi\sqrt{3} \tag{4.37}$$

where m_2 and m_4 are the second and fourth spectral moments of the surface profile. Once *R* and η are approximated, σ_s is then calculated using Eq. (3.24).

Table 4.2: Geometry and Material Property Inputs

:	Oil	Carrier	Washer	Gear
I.D.	-	-	0.0111 m	0.0156 m
O.D.	-	-	0.0227 m	0.0227 m
Thickness (t)	-	0.01 m	6.35E-4 m	0.01 m
γ_{tilt}	-	0 rad	-	0.006 rad
δ		4.50E-07 m	4.50E-07 m	4.50E-07 m
σ	-	5.15E-07 m	5.15E-07 m	5.15E-07 m
E	-	201 GPa	201 GPa	201 GPa
S_y	-	0.993 GPa	0.993 GPa	0.993 GPa
ν	-	0.296	0.296	0.296
α	-	1.2E-05/ °C	1.2E-05/ °C	1.2E-05/ °C
K	0.145 W/m·K	60.5 W/m·K	60.5 W/m·K	60.5 W/m·K
S_o	1.053	-	-	-
G_o	3.545	-	-	-

4.11.1 Results Neglecting Macro-Scale Deformations

When the macro-scale deformations neglected, the components behave rigidly, but pressures due elasto-plastic asperity contact are still produced. The contacts will thus be very concentrated and the contact pressures very high. This also results in a small contact area which increases the thermal resistance between components, thus increasing temperatures in the bearing. Certain mechanisms that control bearing behavior are still present and their effect on bearing performance can be quantified. The neglect of macro-scale contact also removes the phenomena of thermo-elastic instability. However this results in phenomena of thermo-viscous distress being the dominate feature in these results.

Figures 4.9 and 4.10 show the rigid bearing results for the effective coefficient of friction as a function of load and speed. The Appendix C contains a short derivation of the formula used in calculating the effective coefficient of friction from the frictional

torque. This formula is for a surface that is loaded by an even axi-symmetric pressure distribution, even though this is not the tested condition. The formula is given below:

$$f_{eff} = \frac{3}{2} \cdot \frac{T_{frict}(r_o^2 - r_i^2)}{F_a(r_o^3 - r_i^3)} \tag{4.38}$$

Where f_{eff} – effective coefficient of friction

F_a – axial load, [N]

T_{frict} – frictional torque (from Eq. 4.33), [N·m]

r_i – inner diameter of washer, [m]

r_o – outer diameter of washer, [m]

For a tilt of γ_{tilt}=0.006 rad the bearing only survives at the lowest load steps at speeds above 136 rad/s. Also, at the most speeds the washer is in the boundary lubrication regime and the effective coefficient of friction is very high. These conditions are similar to what is seen in the test rig, although to better observe the trends of the bearing behavior for γ_{tilt}=0.002 rad are used instead (see Fig. 4.10). At γ_{tilt}=0.002 rad the bearing performance more gradually changes than at γ_{tilt}=0.006 rad, although the overall trends are the same. From Figs. 4.9 and 4.10 it is clear however that the tilt applied to the gear has a significant effect on the predicted bearing performance.

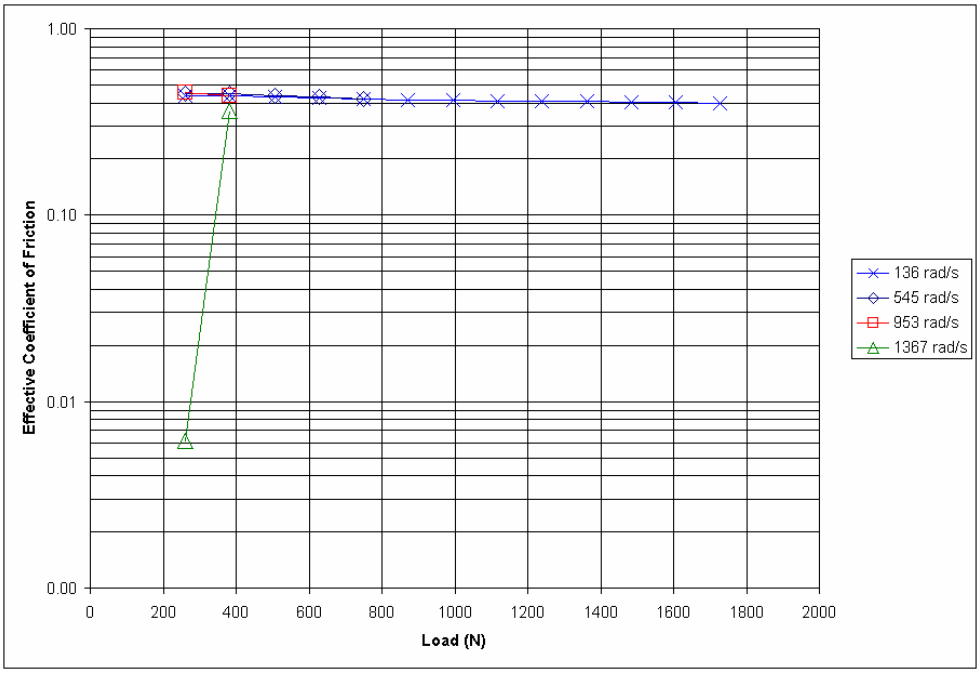

Figure 4.9: The effective coefficient of friction plotted as a function of load and speed (γ_{tilt}=0.006 rad).

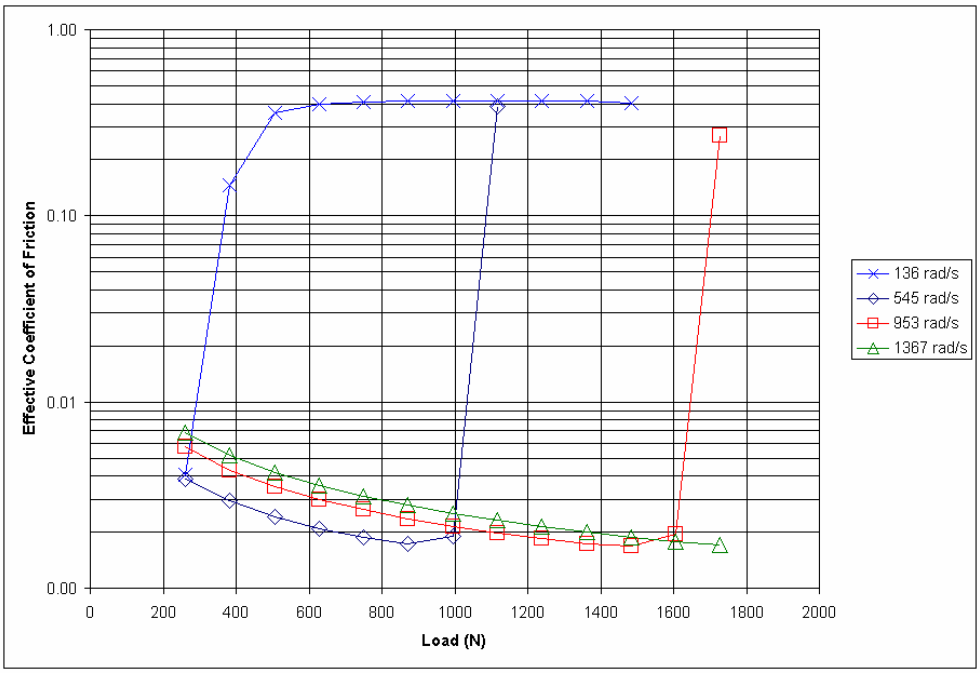

Figure 4.10: The effective coefficient of friction plotted as a function of load and speed (γ_{tilt}=0.002 rad).

At the lowest speed of 136 rad/s the bearing does not produce enough hydrodynamic lift to separate the components, and the resulting effective coefficient of friction is in the range of asperity contact. At the higher speeds, the effective coefficient of friction is much lower and in the typical range of full-film lubrication. Even at these higher speeds, eventually higher loads will overcome the hydrodynamic lift and thermo-viscous distress (TVD) occurs (see Chapter 2). The points of distress are marked by sharp increases in the effective coefficient of friction. This sudden distress is a real phenomena which also occurs during the experimental portion of this investigation. Missing here is the elastic deformation which will allow for thermo-elastic instability to occur and decrease the effective performance of the bearings.

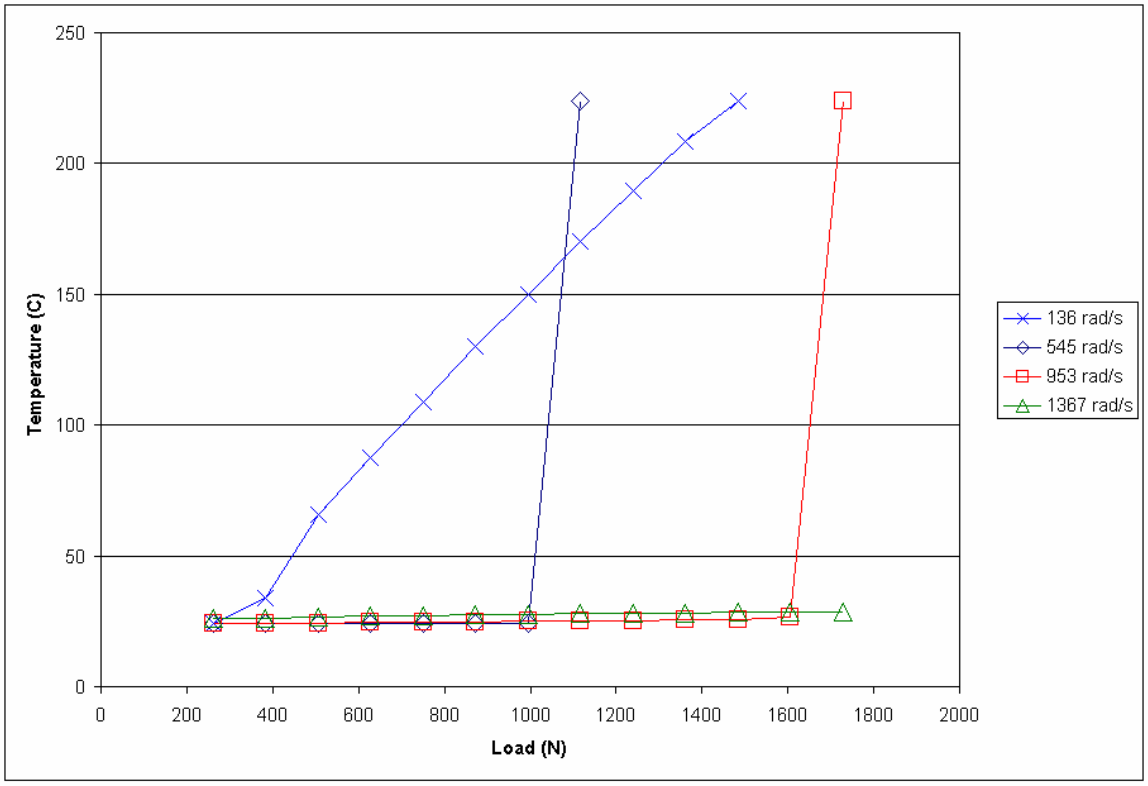

Figure 4.11: The average bearing temperature plotted as a function of load and speed.

Figure 4.11 shows that the average bearing temperature remains near the ambient temperature while a full film lubrication is maintained. However, once the load overcomes the hydrodynamic lift, the temperature increases drastically due to thermo-viscous distress. At the lowest speeds it appears that TVD does not occur immediately, rather, the temperature gradually increases with load as the hydrodynamic lift is slowly overcome. These sharp and drastic increases in temperature also occur in the experimental results and can be used to mark bearing distress (in the experimental work, a test is cutoff if the average temperature exceeds 91°C).

The minimum film thickness, h_{min}, decreases with load for all speeds (see Fig. 4.12). The magnitude of the film thickness gradient also decreases with load indicating an increasing effective stiffness of the asperity contact and fluid film. This trend is broken when bearing distress occurs and the film thickness decreases drastically for 545 rad/s at 1117 N and for 953 rad/s at 1728 N. This decrease in film thickness is also due to thermo-viscous distress.

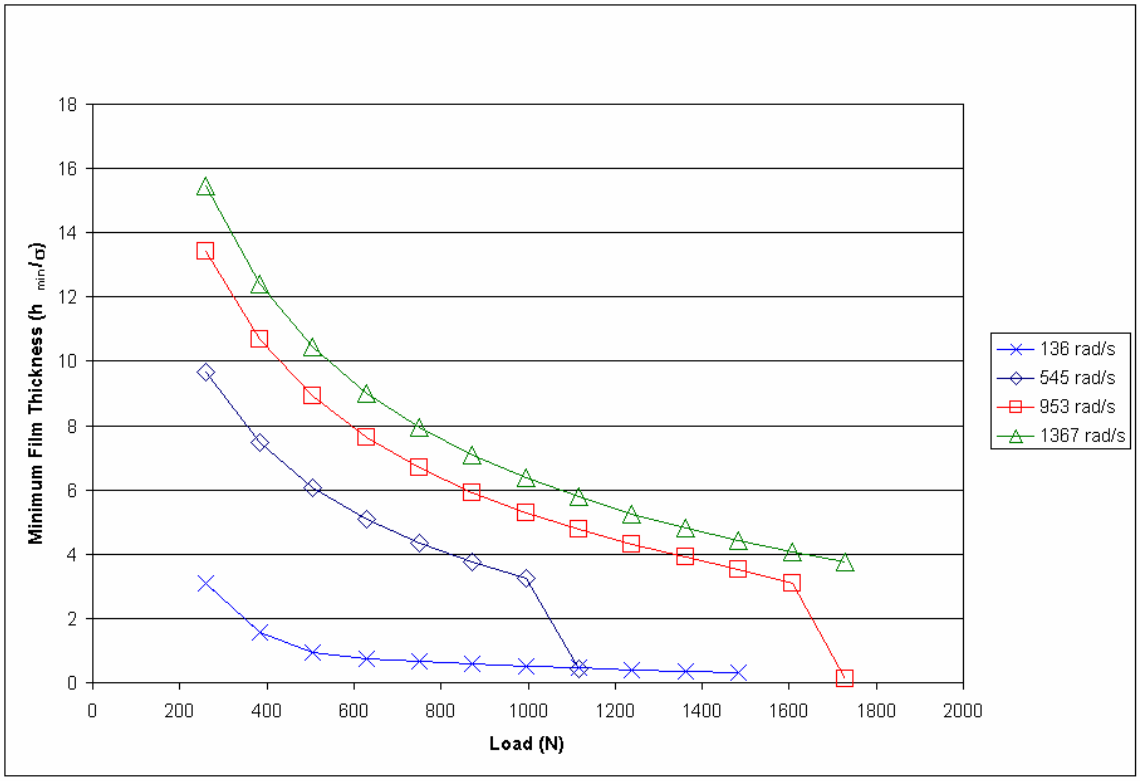

Figure 4.12: The normalized minimum film thickness plotted as a function of load and speed.

Since the hydrodynamics moment is out of phase with the tilt imposed on the gear about the y-axis, it causes the washer to tilt about the x-axis (see Fig. 4.13). At low speed, where the hydrodynamic lift cannot separate the components, γ_x/γ_{tilt} approaches the static case of zero with increasing load. For rotational speeds 545 rad/s, 953 rad/s, and 1367 rad/s the hydrodynamic lift increases to match the increasing load, and γ_x/γ_{tilt} also increases. When the hydrodynamic lift is overcome by the applied load, the magnitude of γ_x/γ_{tilt} decreases drastically.

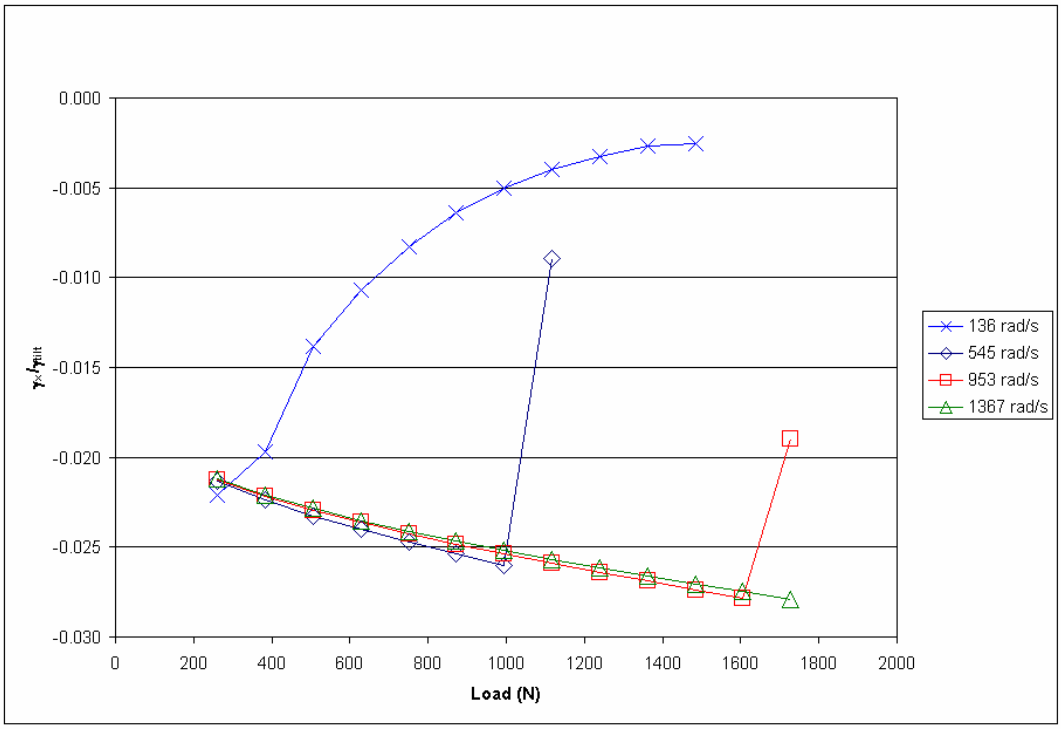

Figure 4.13: The normalized washer tilt about the x-axis plotted as a function of load and speed.

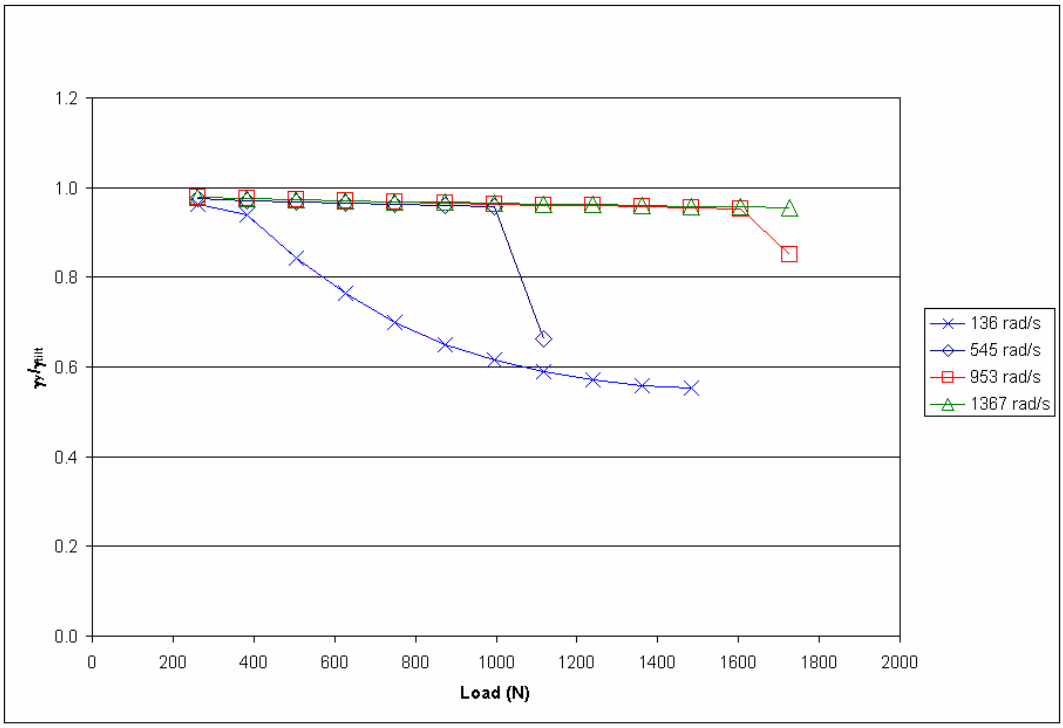

Figure 4.14: The normalized washer tilt about the y-axis plotted as a function of load and speed.

When sufficient, the hydrodynamic lift pushes the washer against the tilted gear (see Fig. 4.14). Thus for high speeds and load loads, γ_y/γ_{tilt} approaches the value of one. Once the applied load begins to overcome the hydrodynamic lift, γ_y/γ_{tilt} decreases toward a value of 0.5 which corresponds to the static position of the washer. This is the static position of the washer because for the moments to balance the contact pressure distribution on both sides of the washer must be a mirror image of each other. For the speeds shown above 136 rad/s, γ_y/γ_{tilt} drastically changes due to the fluid film succumbing to thermo-viscous distress. While for the slowest speed of 136 rad/s the shift in the γ_y/γ_{tilt} is a gradual one.

Since the tilts about the *x* and *y* axis are very small, an equivalent nutation tilt, γ_n, vector can be found which results in the same washer orientation. In vector form this relationship is:

$$\vec{\gamma}_n = \vec{\gamma}_x + \vec{\gamma}_y \tag{4.39}$$

Thus the magnitude of $\vec{\gamma}_n$ is calculated as

$$\gamma_n = \sqrt{\gamma_x^2 + \gamma_y^2} \tag{4.40}$$

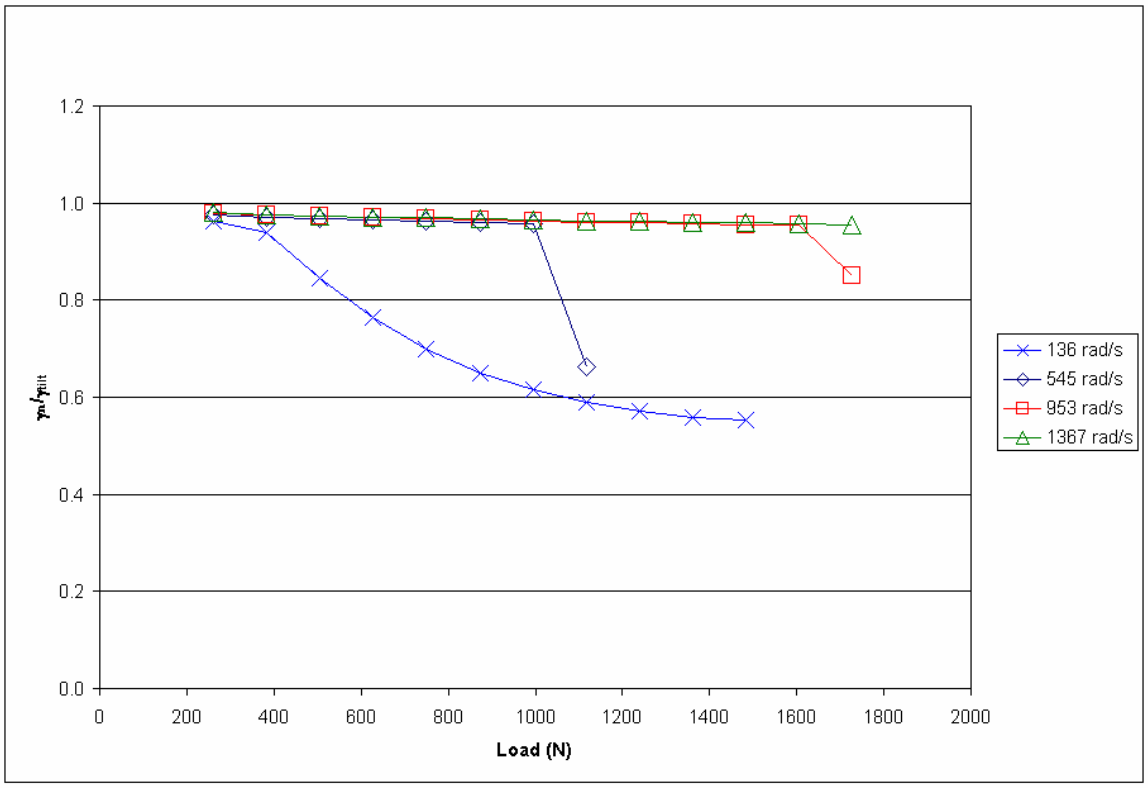

Figure 4.15: Normalized nutation angle of the washer plotted as a function of speed and load.

The value γ_n/γ_{tilt} is plotted in Fig. 4.15 as a function of load and speed. Fig. 4.15 is almost identical to Fig. 4.14 because γ_n/γ_{tilt} is dominated by γ_y/γ_{tilt} because it is much larger in magnitude than the γ_x/γ_{tilt}. Although some tilt does occur about the x-axis due to hydrodynamic lift, most of the tilt of the washers occurs about the y-axis, about which the tilt on the gear is applied. It appears that the presence of hydrodynamic lift will slightly increase the overall tilt of the washer. This could have a positive effect in that a larger tilt may increase hydrodynamic lift, and a negative effect because the concentrated area of contact is smaller (resulting in higher contact pressure and heat generation).

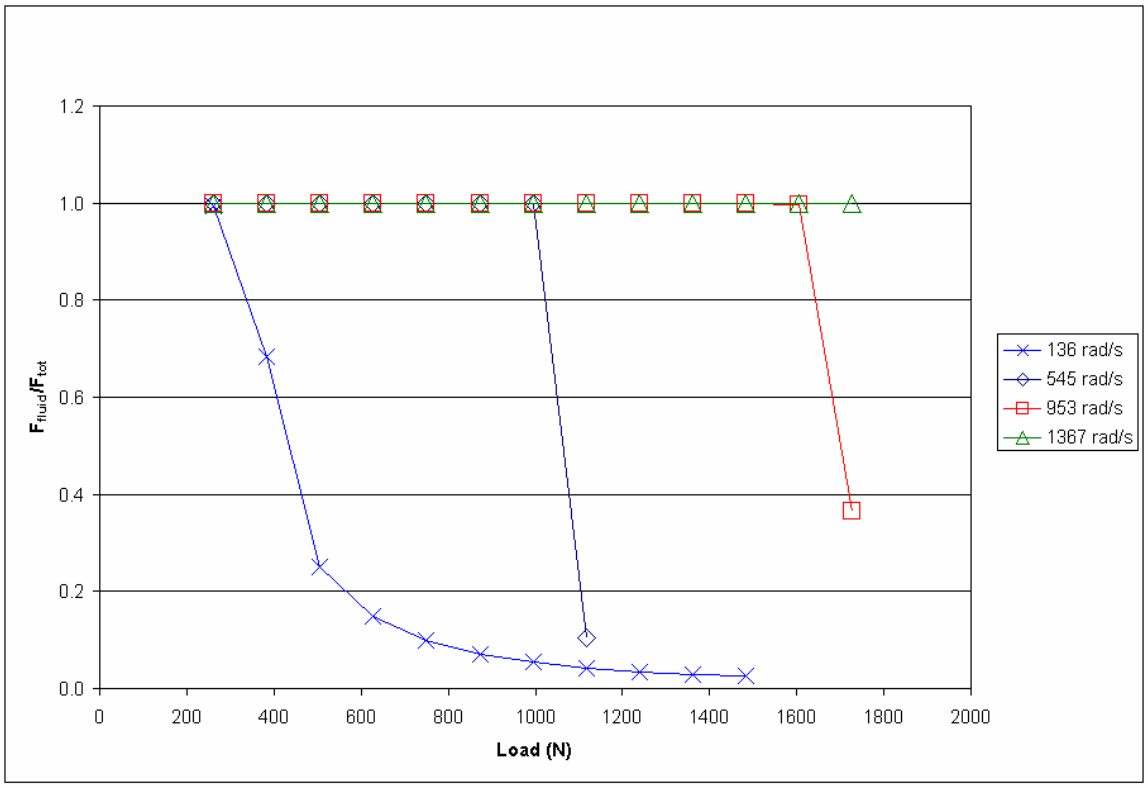

Figure 4.16: The normalized hydrodynamic lift about the x-axis plotted as a function of load and speed.

In Figure 4.16 the normalized hydrodynamic lift, F_{fluid}/F_{tot}, is plotted versus load and speed. At the lowest speed of 136 rad/s sufficient hydrodynamic lift is not generated and the total applied load is carried by both asperity contact and hydrodynamic lift. As load is increased at 136 rad/s, proportionally more of the load is carried by asperity contact as described in Chapter 2. At 1361 N and 136 rad/s, approximately 2% of load is being carried by hydrodynamic lift. For 545 rad/s, 953 rad/s, and 1367 rad/s the hydrodynamic lift carries the entire load until a thermo-viscous distress point is reached at which the hydrodynamic lift drops dramatically.

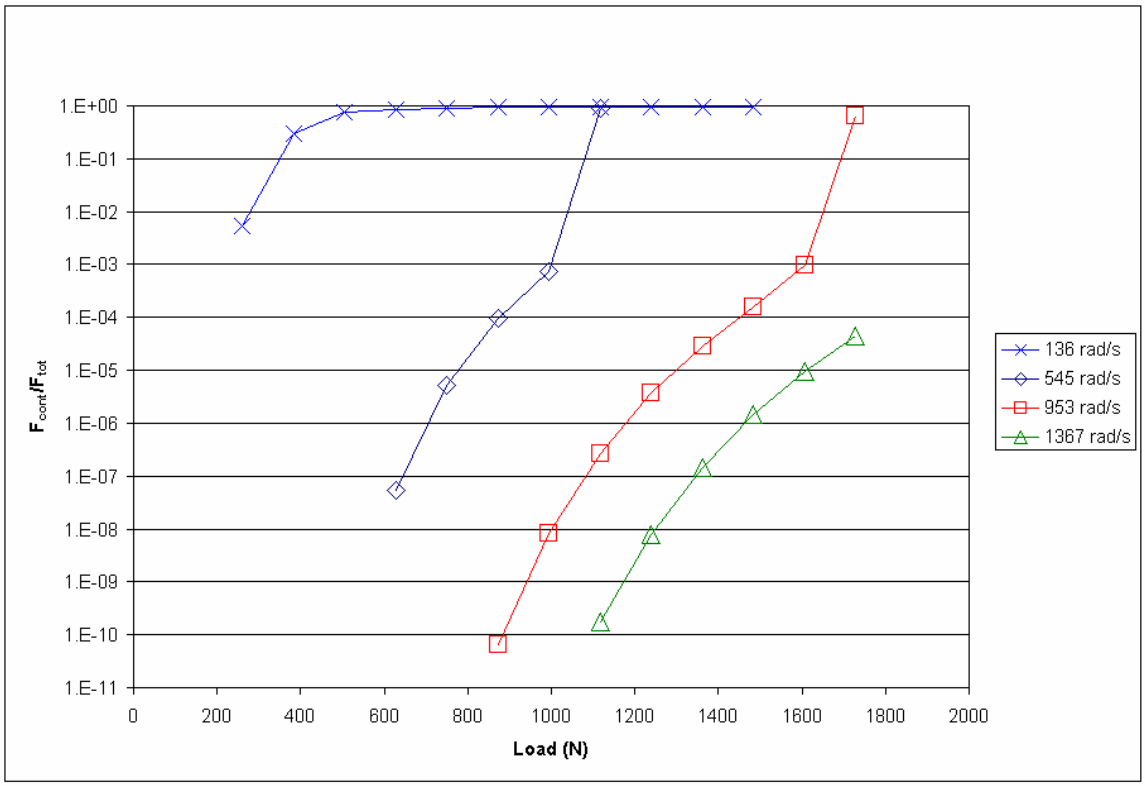

Figure 4.17: The normalized contact load as a function of applied load and speed.

The asperity contact force is plotted logarithmically with respect to load and speed in Fig. 4.17. Even at apparently fully hydrodynamic lift there is slight asperity contact, although the load carried by the asperities can be many orders of magnitude smaller than the hydrodynamic lift. This suggest though that even when a nearly full-film of lubrication separates the bearings, very small amounts of contact can occur. This is especially true in actual industrial conditions because vibrations and other dynamic events may cause momentary increases in load. As load is increased, the load carried by asperity contact increases until a distress point causes the hydrodynamic lift to effectively disappear, leaving the asperities to carry the entire load.

Figure 4.18 shows the normalized contact load, F_{cont}/F_{tot}, plotted as a function of the normalized minimum film height, h_{min}/σ and speed. It is clear that the contact force increases sharply as the minimum film height decreases. At $h_{\min}/\sigma \approx 3$, commonly used to mark the threshold of significant asperity contact, F_{cont}/F_{tot} jumps quickly to points near F_{cont}/F_{tot}=1. This represents the collapse of the fluid film thickness due to thermo-viscous distress. Washer bearings designed to operate at high speeds should be designed to generate enough lift to sustain $h_{\min}/\sigma > 3$. It should be noted though, that even though the numerical simulation predicts when asperity contact will become significant, wear is not modeled.

At the lowest speed of 136 rpm it appears the thermo-viscous distress is not as severe, probably since less kinetic energy is available to dissipate in the form of frictional heat (see Fig. 4.18). This illustrates that the at low speeds the bearing operates in the boundary lubrication region and at high speeds in the full film lubrication region unless the load is great enough to cause thermo-viscous distress and collapse the film. It seems logical to also present these results in the form of a Stribeck curve as described in Chapter 2.

Figure 4.19 shows a plot of the numerically generated data in the form of a Stribeck curve. The different regimes of bearing lubrication are clearly represented here. For higher Stribeck numbers the bearing operates in the full film region (to the right a the 'knee'). Moving to the left, the friction coefficient decreases until the bearings point of optimal efficiency is reached at a *ZN/P* value of about 2.0E-6. In the experimental results this value is about 1.0E-6. Then as the Stribeck value is further decreased the bearing enters the mixed lubrication regime. At this point high speeds will cause the bearing to

heat quickly and experience thermo-viscous distress. With distress the fluid film collapses and the friction coefficient rises dramatically. However at low speeds the process is more gradual and the film does not collapse immediately.

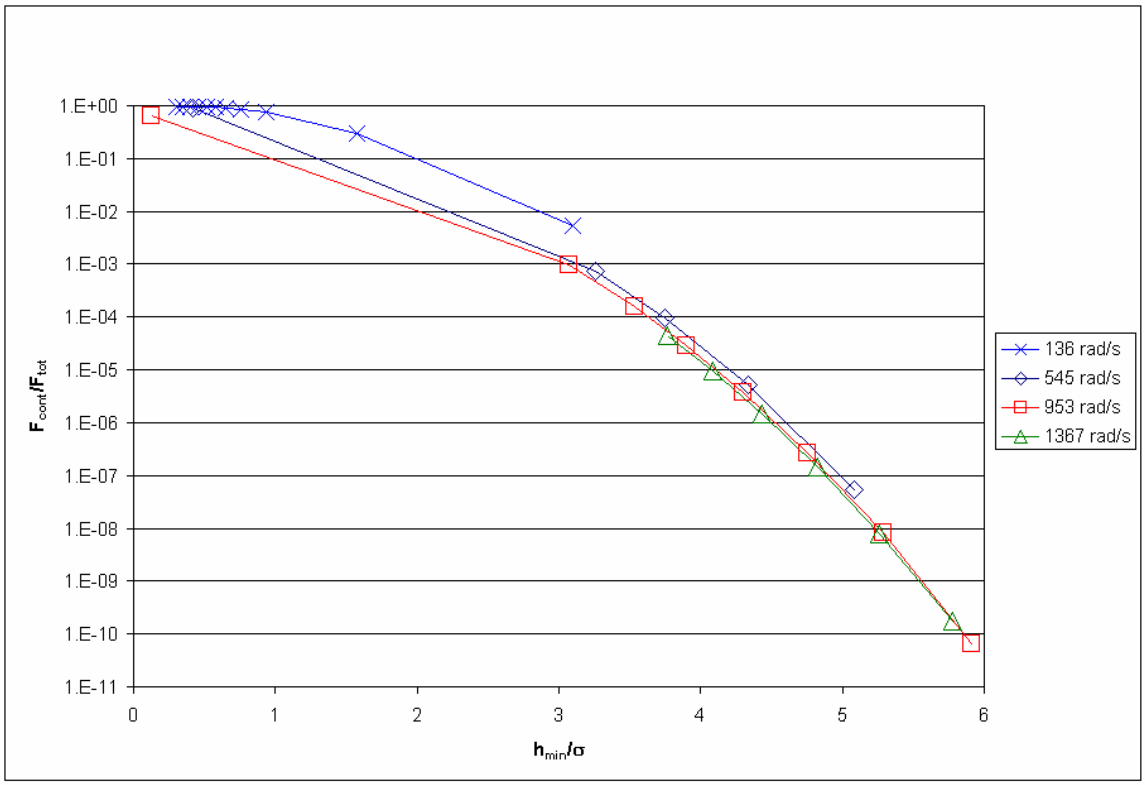

Figure 4.18: Plot of normalized contact load as a function of the normalized minimum film height.

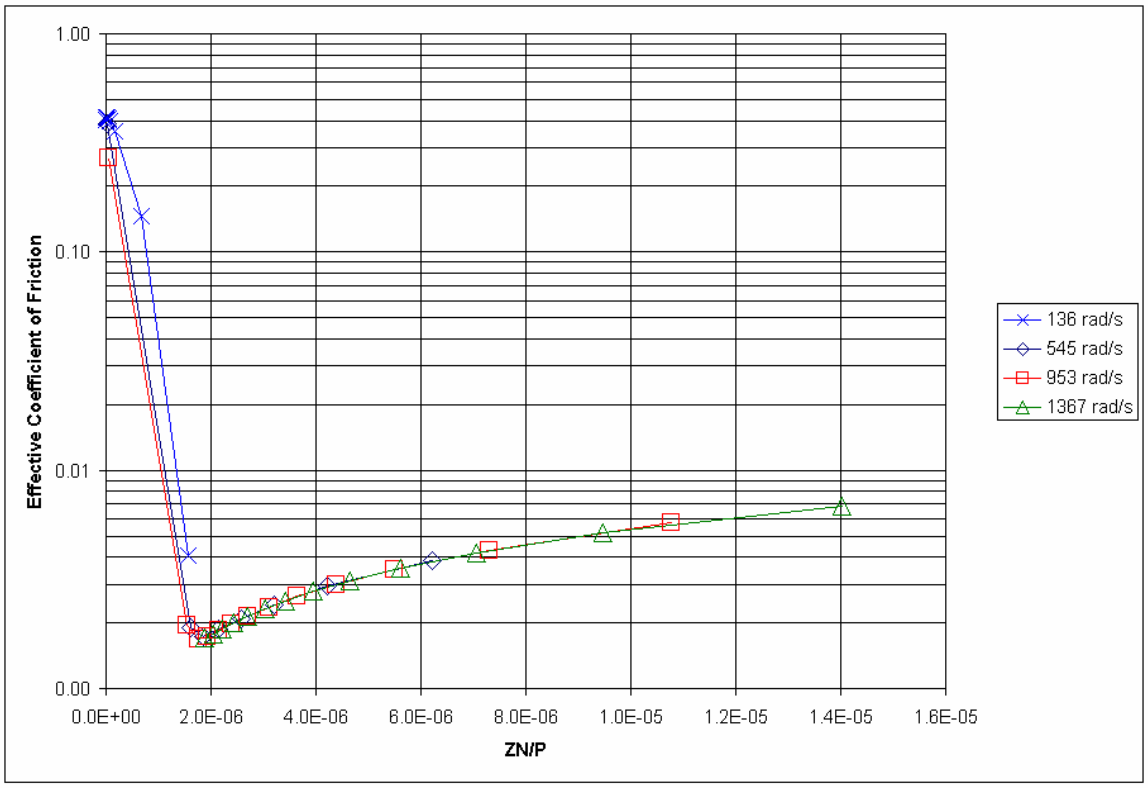

Figure 4.19: Stribeck curve generated from numerical results.

4.11.2 Component Rotational Speed

The round thrust washers in the transmission and test rig are allowed to rotate about the shaft and the axis of symmetry. The steady state rotational speed of each washer will thus depend on initial conditions, and the dynamics which occur during start-up before steady-state is reached. However, in the numerical code the rotational speed of each component is assigned manually and held constant. This work assumes that the washer speeds will adjust to the optimal configuration resulting in the minimal amount of frictional loss. What will most likely result is that the washers will stick to either the gear or carrier and the entire relative speed will be carried between only two components. Once this situation occurs the washers are essentially 'stuck' because the friction between

the sliding surfaces is usually much less than the static surfaces due to hydrodynamic lift. In other words, the frictional torque of the sliding surfaces cannot overcome the static frictional torque to 'free' the washer from the component it is stuck to. Experimental observations confirm that most of the relative speed is carried between two components.

In this section, three possible steady state rotational speed configurations for a thrust washer bearing consisting of two round steel washers between the carrier and the gear rotating at a speed ω (see Fig. 4.1 and 4.2). To save computation time, the macro deformations are again ignored. Also the tilt is set to γ_{tilt}=0.002 rad, although the tilt in the test rig is γ_{tilt}=0.006 rad. Nevertheless, the resulting trends are the same. There are actually four steady state rotational speed configurations which could occur. The cases are:

Case 1: Washer 1, washer 2 and the gear are rotating together such that the relative speed is taken between the carrier and washer 1. This does not mean that the washers are required to 'stick' together though, as there may still be a gap between them.

Case 2: Washer 1 is stationary while washer 2 and the gear are rotating together such that the relative speed is taken between the washer 1 and washer 2.

Case 3: Washer 1 and washer 2 are stationary and the gear is rotating such that the relative speed is taken between the washer 2 and the gear. Again, there may be a gap between the washers.

Case 4: The washers adjust to intermediate speeds between the carrier and the gear resulting in equal frictional torques on all surfaces. This case is unstable and will move toward one of the previous cases with any disturbance. Since this case is not likely to occur, it is not considered.

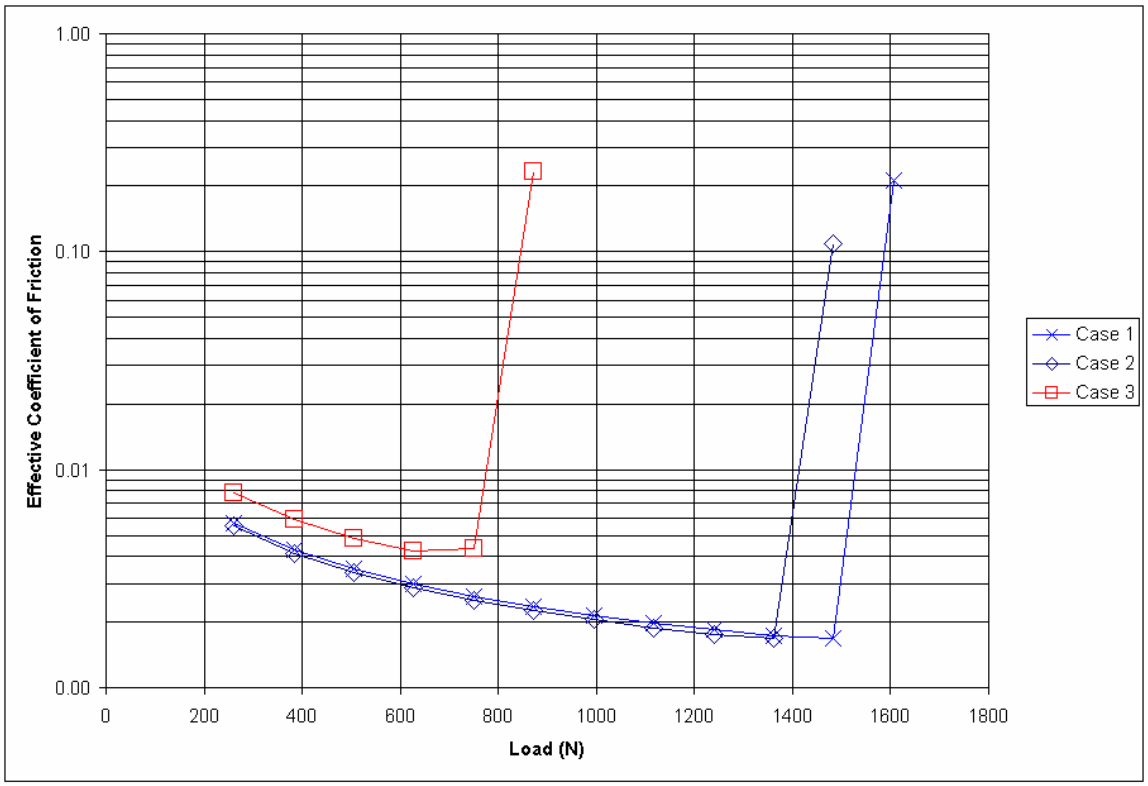

Figure 4.20: The effective coefficient of friction for a rigid thrust washer bearing at a ω=953 rad/s (9100 rpm).

Results are generated for a varying load and constant rotational speed, ω, of 953 rad/s (9100 rpm). Figure 4.20 shows that cases 1 and 2 perform with a lower coefficient of friction and can sustain higher loads before fluid film collapse than case 3. The reason case 3 performs at a higher effective friction coefficient than case 1 and 2 is geometry. The inner diameter of the gear is 36% larger than the washers and reduces the bearing surface area by 31%. This results in less area for load carrying hydrodynamic pressure, contact pressure, and also heat conduction. As evident in Figures 4.20-4.21, this significantly reduces the load carrying capacity of the washer. When the bearing is run at case 3 the load at which thermo-viscous distress and thermo-elastic instability can occur

is lower than Cases 1 and 2. Case 1 performs slightly better than Case 2 and for this reason for all numerical tests the washers will be assumed to rotate with the gear (Case 1).

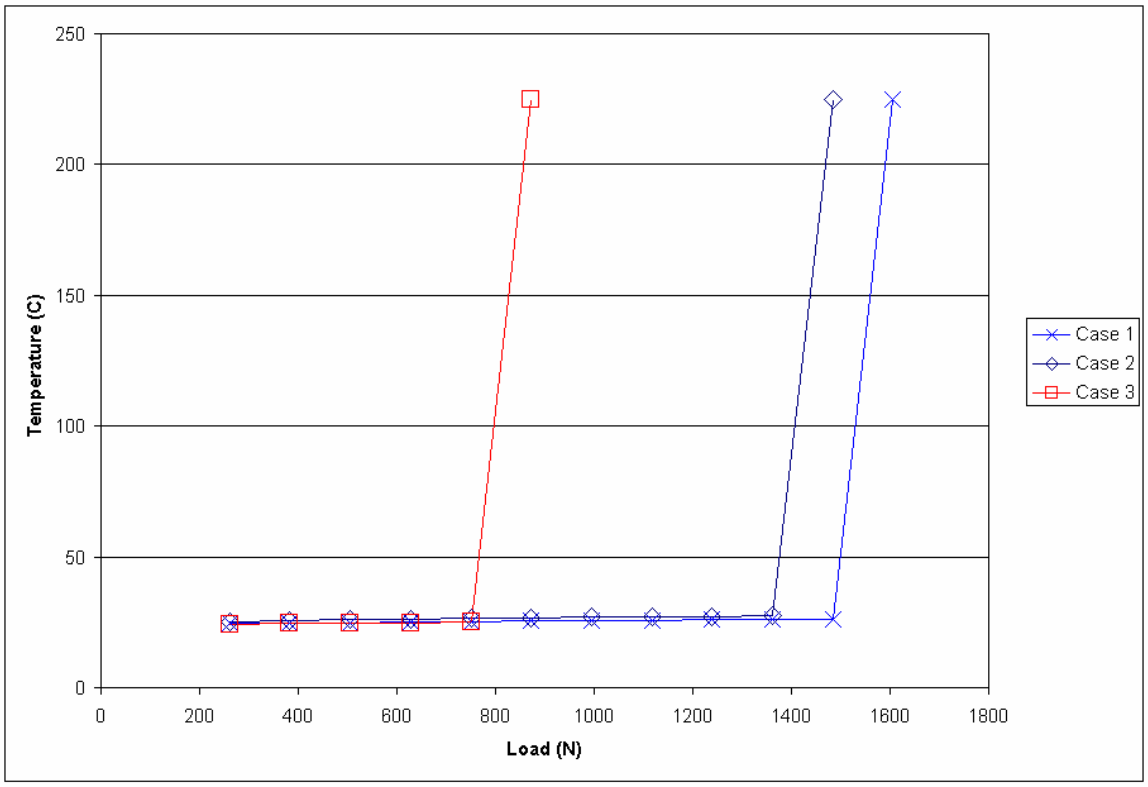

Figure 4.21: The average bearing temperature for a rigid thrust washer bearing at a ω=953 rad/s (9100 rpm).

The numerical code predicts that the average bearing temperature will only increase slightly at low loads (see Fig. 4.21). As the load is increased, eventually it overcomes the hydrodynamic lift, causing thermo-viscous distress and the film collapses. The temperature then increases sharply. From Figure 4.21 it appears that the Case 1 and 2 maintain a low average bearing temperature for higher loads than Case 3. As described previously, this is due to the gear face providing less bearing surface area than the thrust

washers and carrier. The reduced face area not only provides less load support, but provides less surface area for the generated heat to transfer through, away from the washer.

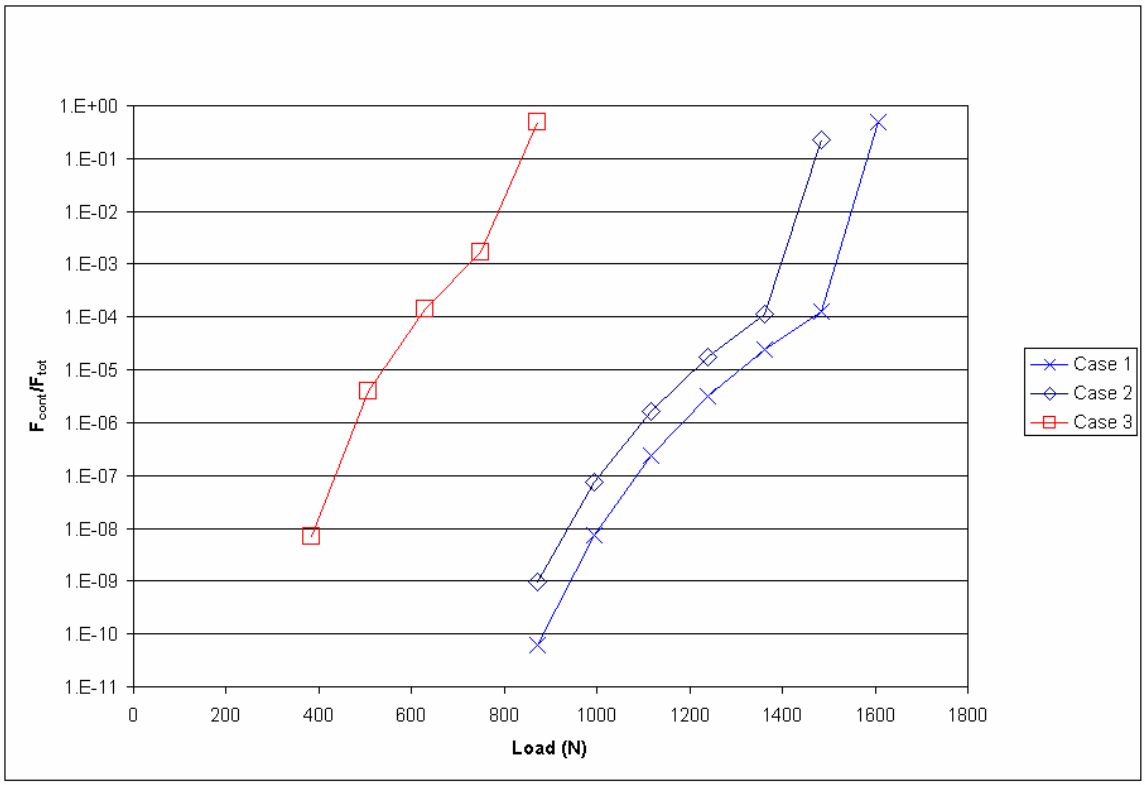

Figure 4.22: The normalized contact force for a rigid thrust washer bearing at a ω=953 rad/s (9100 rpm).

Figure 4.22 reaffirms that the hydrodynamic lift provided by case 3 is much less and relies more on asperity contact to carry the load. The asperity contact force for case 3 becomes significant at much lower loads than the other cases. However, in all three cases the asperity load eventually jumps as the fluid film collapses and thermo-viscous distress occurs.

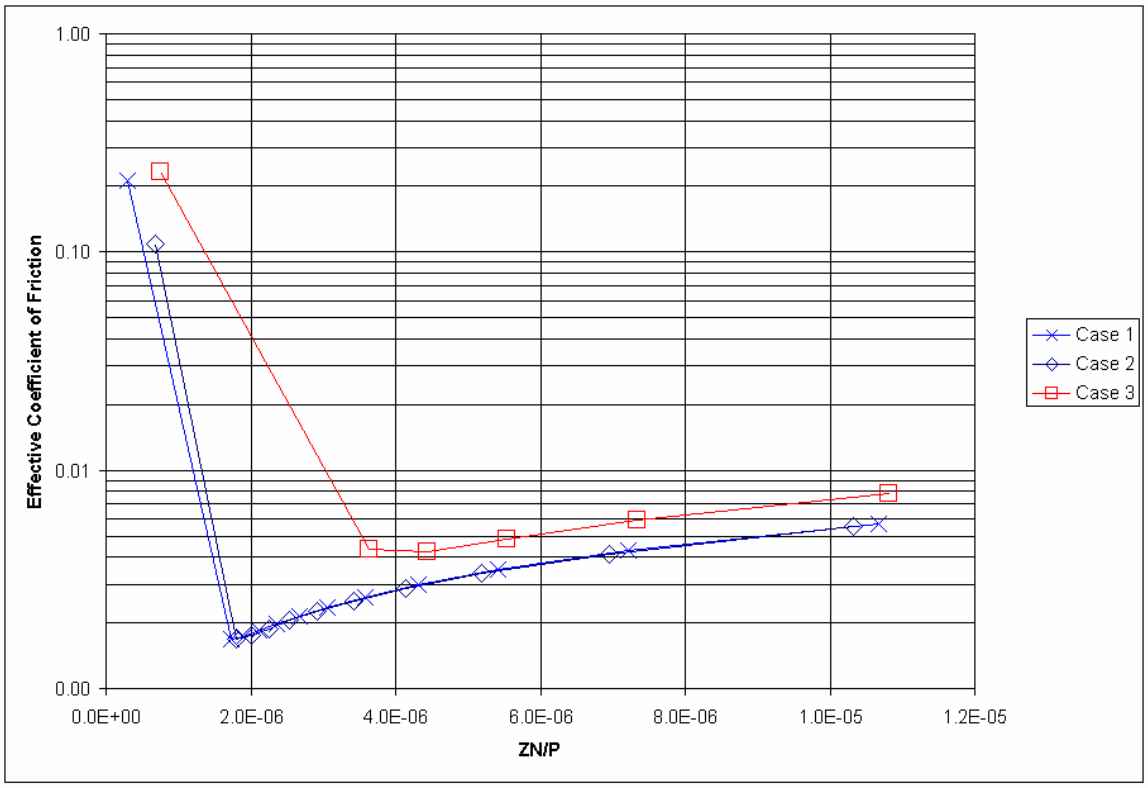

Figure 4.23: Stribeck curve plotted for rigid thrust washer bearing at a ω=953 rad/s (9100 rpm).

A Stribeck curve generated from the numerical results also indicate that the case 3 performs worse than case 1 and 2 (see Fig. 4.23). For all locations on the Stribeck curve, even in the full-film region on the right, the coefficient of friction is significantly higher for case 3 than case 1 and 2. The Stribeck curves for case 1 and 2 are almost identical, except that the curve for case 2 peaks out at a slightly lower Stribeck value. This indicates that case 1 is able stay in the fully film regime for slightly less ideal conditions for hydrodynamic bearings (i.e. lower viscosity, lower speed, higher load). As stated before, for the remaining tests case 1 is assumed. Also for the one washer configuration, the equivalent case of the washer attaching to the gear is assumed.

4.11.3 Effect of Dry Friction Coefficient

The dry friction coefficient, *f*, is varied to show the effect it has on bearing performance and distress. The role the dry friction plays in the thrust washer bearing model is described in section 4.6. For this case the macro deformations are neglected. Reducing the dry coefficient of friction not only decreases the effective coefficient of friction for the bearing, but also decreases the frictional heat generated. These effects are documented in Figs. 4.24-4.27.

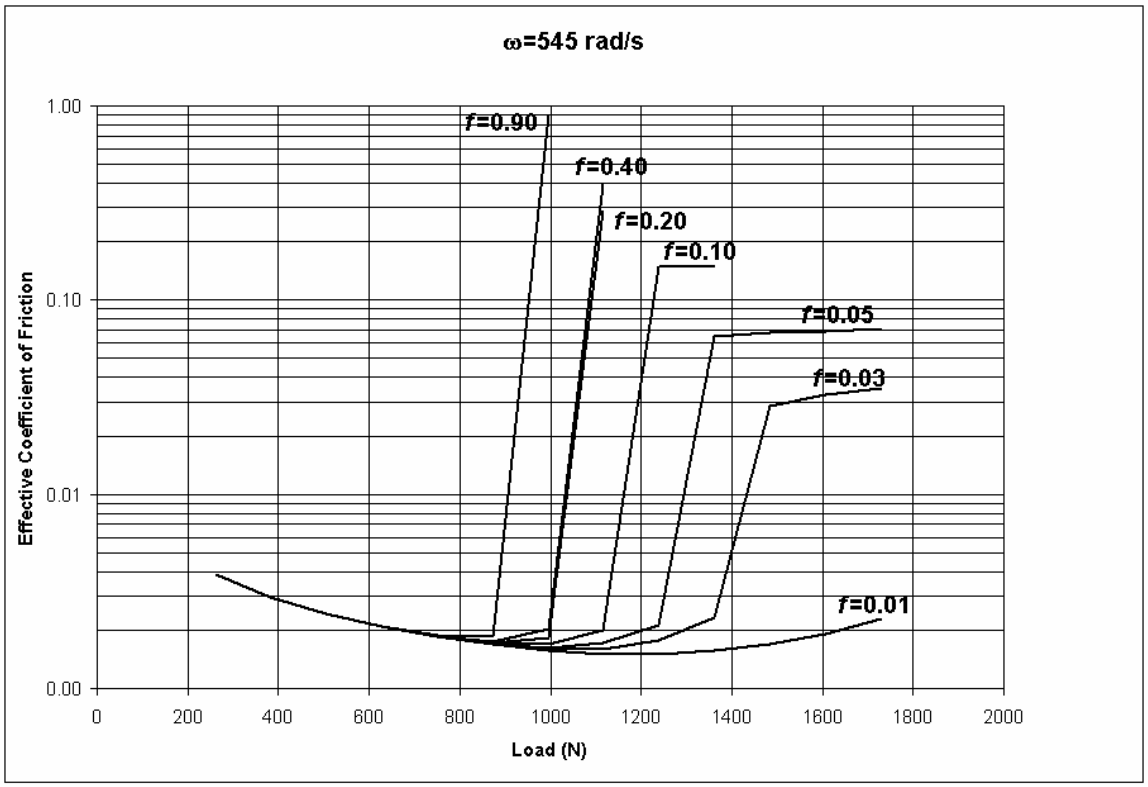

Figure 4.24: The effect of dry friction coefficient on the effective coefficient of friction for various loads.

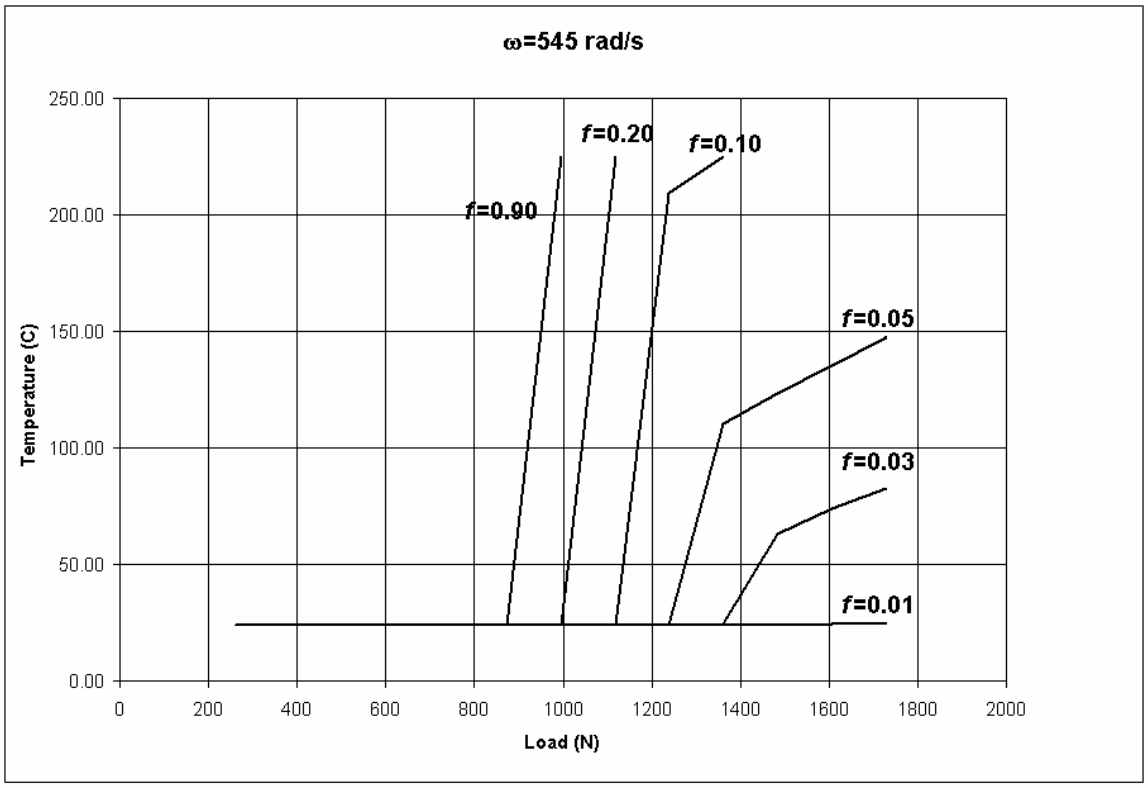

Figure 4.25: Average bearing temperature plotted as a function of load and dry friction coefficient.

As shown in Fig. 4.25, sudden increases in the effective coefficient of friction mark the point that the hydrodynamic lift is overcome by the load and the film collapses due to thermo-viscous distress (see Chapter 2). It is also evident that increasing the friction shifts the point of thermo-viscous distress to lower loads. As must be the case, the dry friction coefficient does not alter the effective coefficient of friction while the bearing is operating with a full film of lubrication separating the surfaces. At a load of 800 N significant asperity contact begins to occur and cause the effective coefficient of friction curve to separate for each dry coefficient of friction. Even though the film may collapse at certain loads, the bearing may still operate without reaching the defined the

defined cut-off temperature of 200°C. This results in sharp breaks at the top of some of the curves.

While operating in the full film regime the bearing temperature increases very little with applied load (see Fig. 4.25). However, at points of thermo-viscous distress there are sudden increases in the temperature. The magnitude of the temperature increases at points of distress increase with the dry friction coefficient. Increasing the dry friction coefficient also causes the point of distress to occur at lower applied loads. For friction coefficients below 0.2, the film collapses but the bearing does not meet the temperature distress criterion immediately. This results in the sharp elbows at some of the high contact forces.

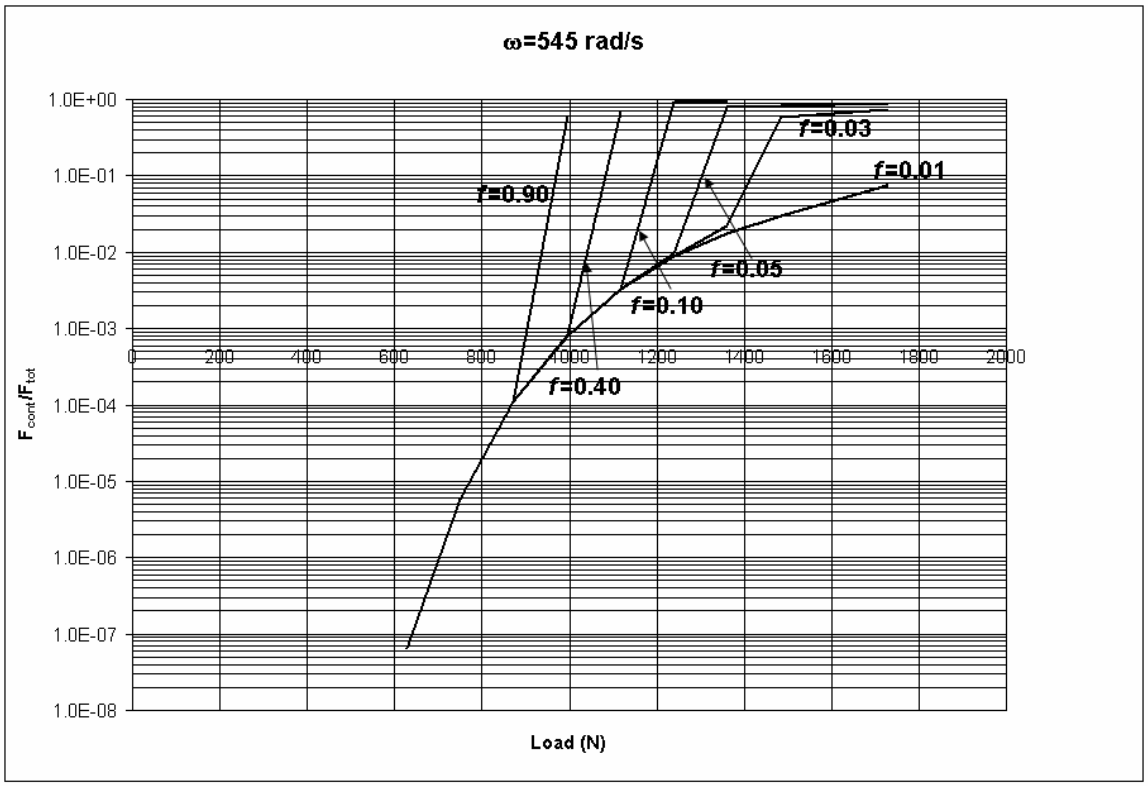

Figure 4.26: The normalized asperity contact load plotted as a function of the dry friction coefficient and load.

The contact force is plotted as a function the dry friction coefficient and load in Fig. 4.26. The normalized asperity contact force increases gradually with load until thermo-viscous distress causes a sudden fluid film collapse and for surface asperities to bear most of the load. Again, the load at which this occurs is decreasing as the dry friction coefficient of friction.

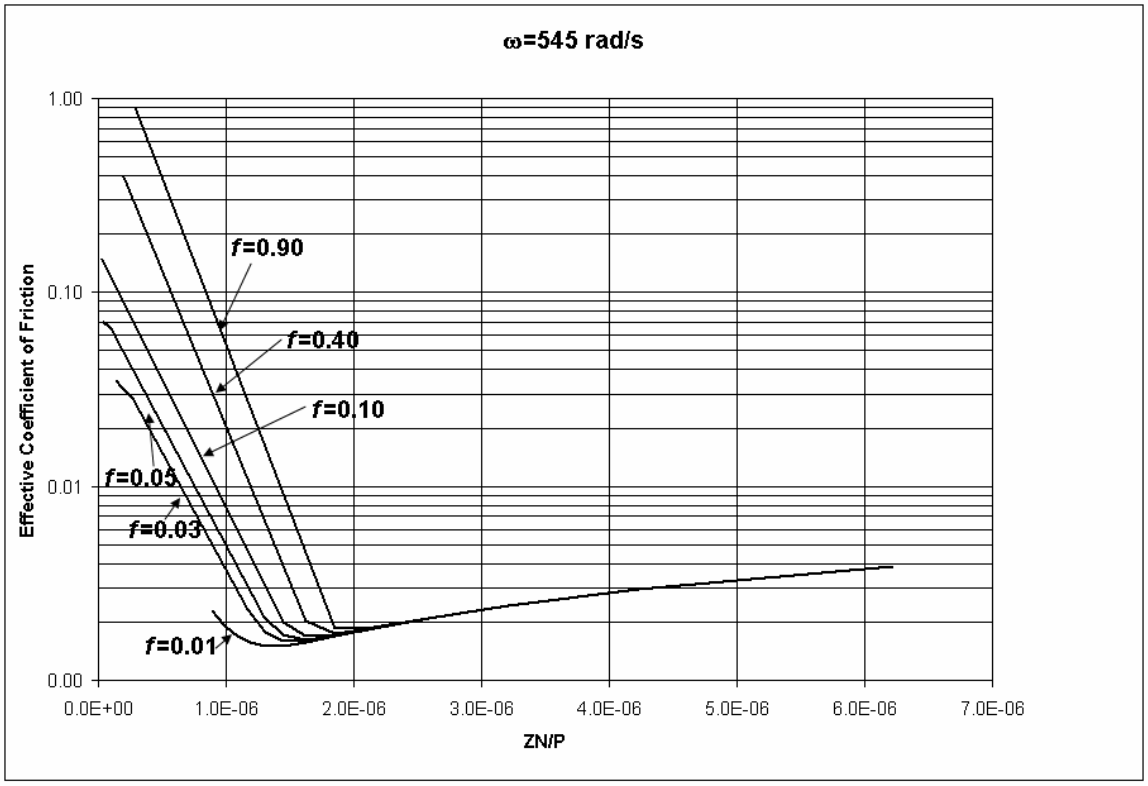

Figure 4.27: The numerically generated Stribeck plot for varying dry friction coefficients.

As expected, changes in the dry friction coefficient only affect the left side of the numerically generated Stribeck curve (see Fig. 4.27). The dry coefficient of friction merely shifts the initiation of boundary lubrication (the valley in the curve) to larger Stribeck values (farther to the right). Thus, increasing the dry coefficient of friction

reduces the range of operational conditions that the bearing can operate with a full film of lubrication.

The findings of this section suggest that lower dry friction coefficients between thrust washer bearing components will improve bearing performance. This is also confirmed by the results of the washers coated with low friction PTFE in Chapter 2.

4.11.4 Effect of Number of Washers

As will be seen, the effect of the number of washers is uncertain in the experimental results. However, the numerical results indicate otherwise. The numerical model does make some simplifications and so may not give a complete picture of the benefits that using one or two washers provide. For instance, in an actual two washer configuration there are three free surfaces. If one of these surfaces distresses and locks together, there are still two other free surfaces which can rotate. For one washer there are only two free surfaces and with no washers there is only one free surface. In other words, each extra free surfaces essentially gives the washer extra chances at performing. This mechanism is not considered in the numerical model since the rotational velocities of the components are held constant. Nonetheless, a comparison using the numerical model is still made between bearing configurations consisting two, one, and no steel washers.

When numerically modeling the thrust washer bearing it becomes clear that there are competing effects which govern the bearing performance. Research shows that more thin disks (i.e. more washers) will decrease stability of a thermo-elastic bearing (see Chapter 2 and Yi et al.(2000)). Washers have some positive effects though, such as they

can enhance hydrodynamic lift through deformation and increasing the surface area of the bearing face.

When elastic deformations are considered, the two washer configuration performed very poorly in the numerical model. This seems to be due to thermo-elastic instability and the resulting convergence problems. The two washer configuration distressed at the lowest load.

4.11.5 Consideration of Thermoelastic Deformations

When thermoelastic deformations are considered, the thrust washer bearing becomes susceptible to thermo-elastic instability. This physical phenomena, effectively reduces the performance of the bearing. Fig. 4.28 plots a numerically generated Stribeck curve for a single round steel washer configuration. The size of the load steps were refined for this plot to capture the behavior of the bearing better. It is clear that the bearing still follows the Stribeck curve and distresses near the left side of the curve. On the right side of the curve it is apparent that the bearing can operate within full film of lubrication. However, there are only a few points at the lowest considered loads that the numerical simulation predicts this for. Once the fluid film collapses and the bearing operates on the left side of the Stribeck curve, thermoelastic instability immediately occurs and the numerical code is stopped. In actual operation, wear will dampen the TEI and the bearing may perform better than indicated by the simulation. The simulation also neglects convection, which may in reality be sufficient in helping to remove heat from the bearing components. To confirm that it is indeed thermoelastic effects which

drive the numerical model to be unstable, a hypothetical case of a very conductive material is modeled in the next section.

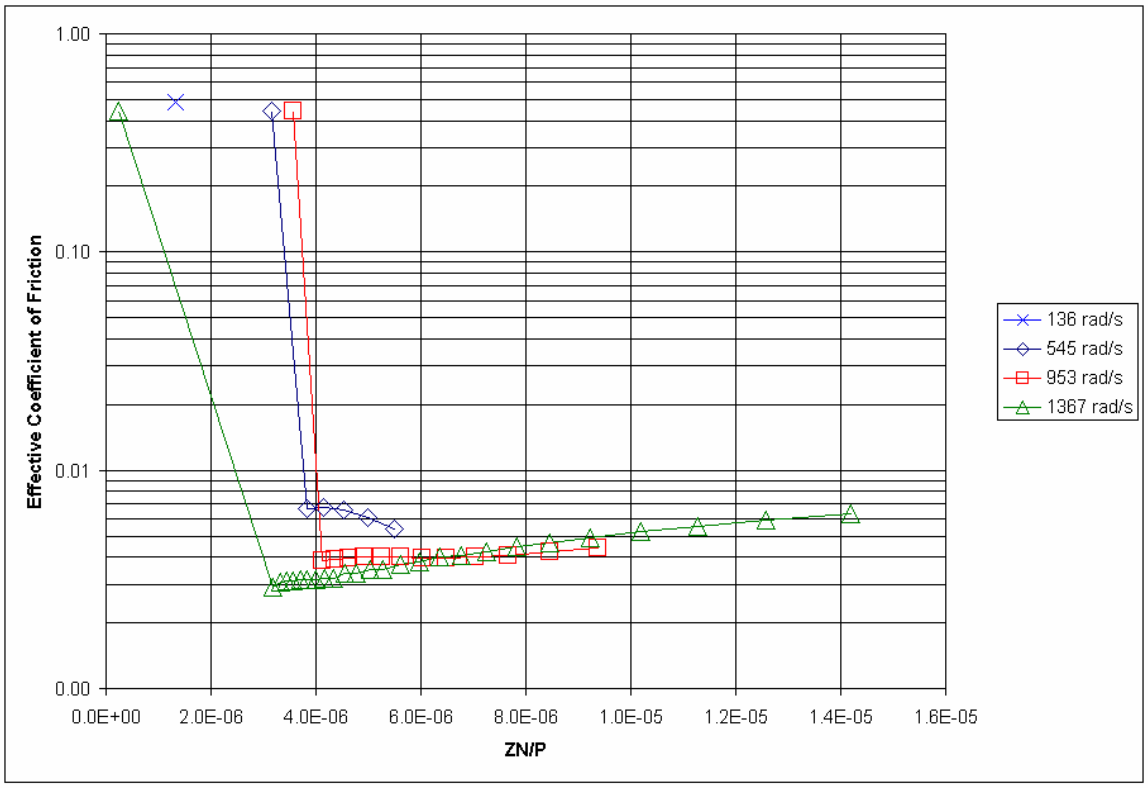

Figure 4.28: Stribeck curve for single round steel washer configuration.

4.11.6 Hypothetical Case of High Conductivity

The mechanisms of thermo-elastic instability and thermo-viscous distress seem to account for bearing distress both experimentally and numerically. In the numerical simulation these effects can cause divergence of the non-linear solution or very long computation times. To help confirm the effect these mechanisms have, a hypothetical case of a very conductive model is formed. The thermal conductivities, *K*, for the

lubricant and component materials in Table 4.2 are multiplied by a factor of 1000. All other material properties and geometries are held constant. This hypothetical situation effectively causes the material to conduct the frictional heat away. This brings the temperatures of the component very near to the ambient temperature. The resulting lower temperatures and temperature gradients reduce the thermo-elastic expansion and viscosity reduction by several orders of magnitude.

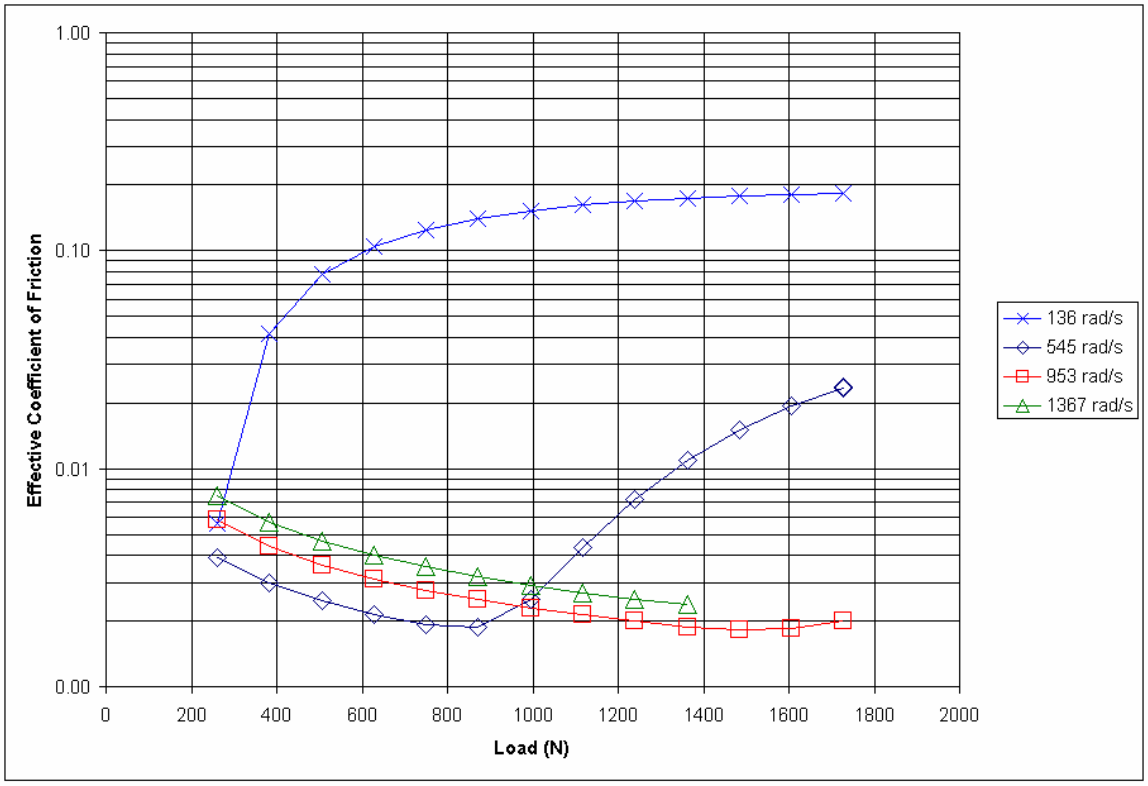

Figure 4.29: Effective coefficient of friction plotted as a function of applied load and speed.

Without thermal heating due to friction and viscous shearing, the effective coefficient of friction changes gradually with load and speed (see Fig. 4.29). There are no sudden points of distress where the fluid film is loss and the effective coefficient of

friction increases sharply as in the reference case (see Figs. 4.10 and 4.28). At high speeds of 953 rad/s and 1367 rad/s, with no significant change in viscosity due to heating, the bearing maintains a full film of lubrication at all loads. At a speed of 545 rad/s the bearing begins in the full film regime and at low friction, but as load is increased the effective coefficient of friction slowly increases. The bearing at the lowest plotted speed of 136 rad/s has a high coefficient of friction for most of the loads shown, indicating asperity contact is carrying a significant amount of the load.

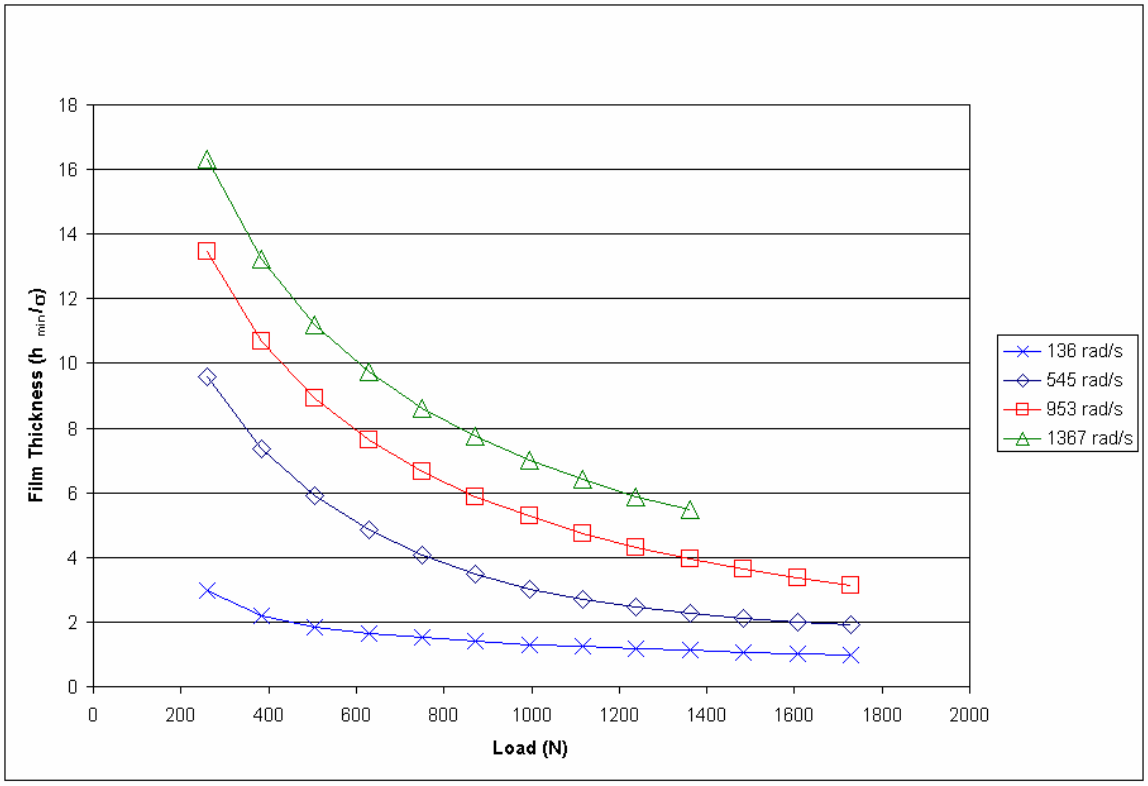

Figure 4.30: Normalized film thickness plotted as a function of load and speed.

For this case, there are no sudden changes in the normalized film thickness with increasing load (see Fig. 4.30). Even though, $h_{\min}/\sigma$ still decreases gradually with

increasing applied load. As expected, when temperature rise and the resulting decreases in viscosity is not a factor, the higher speeds also provide additional hydrodynamic lift.

In Fig. 4.31, there are also no sudden increases in the load carried by asperity contact. As speed increases the asperity contact decreases. The hydrodynamic lift at higher speeds is unhindered by decreases in viscosity due to thermal heating. The change from load carried by fluid to asperity contact is a gradual one when the thermal effects are not present to cause bearing distress.

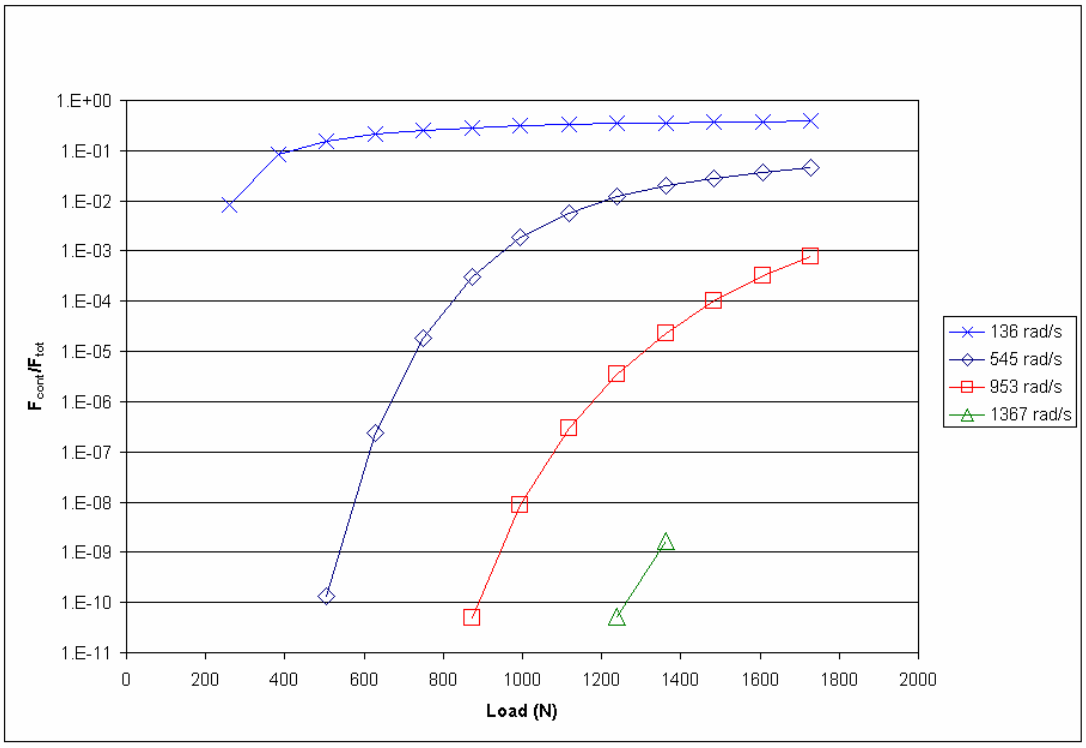

Figure 4.31: Normalized asperity contact force plotted as a function of load and speed.

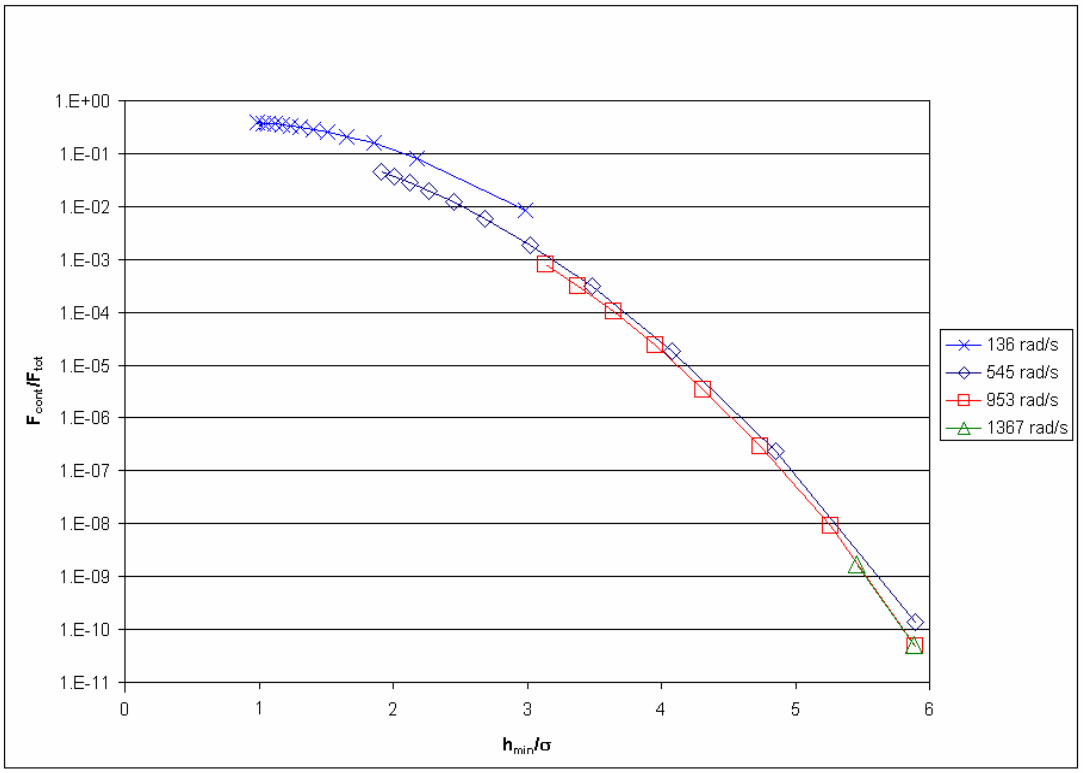

Figure 4.32: The asperity contact force normalized by the minimum film thickness plotted as a function of load and speed.

When normalized by the minimum film thickness, the asperity contact force for all speeds follows nearly the same paths (see Fig.4.32). As with Fig. 4.18, a logarithmic scaling is used on the asperity load axis. The slight differences between speeds can be attributed to the hydrodynamic lift changing the position of the washer. With increasing speed the hydrodynamic lift will 'press' the washer more against the gear. Comparing Fig. 4.18 to Fig. 4.32, it is apparent that by negating the thermal effects the bearing film does not collapse suddenly at $h_{\min}/\sigma \approx 3$. In Fig. 4.32, the asperity contact force still increases inverse to the minimum film thickness as statistically, more and more asperities come into contact.

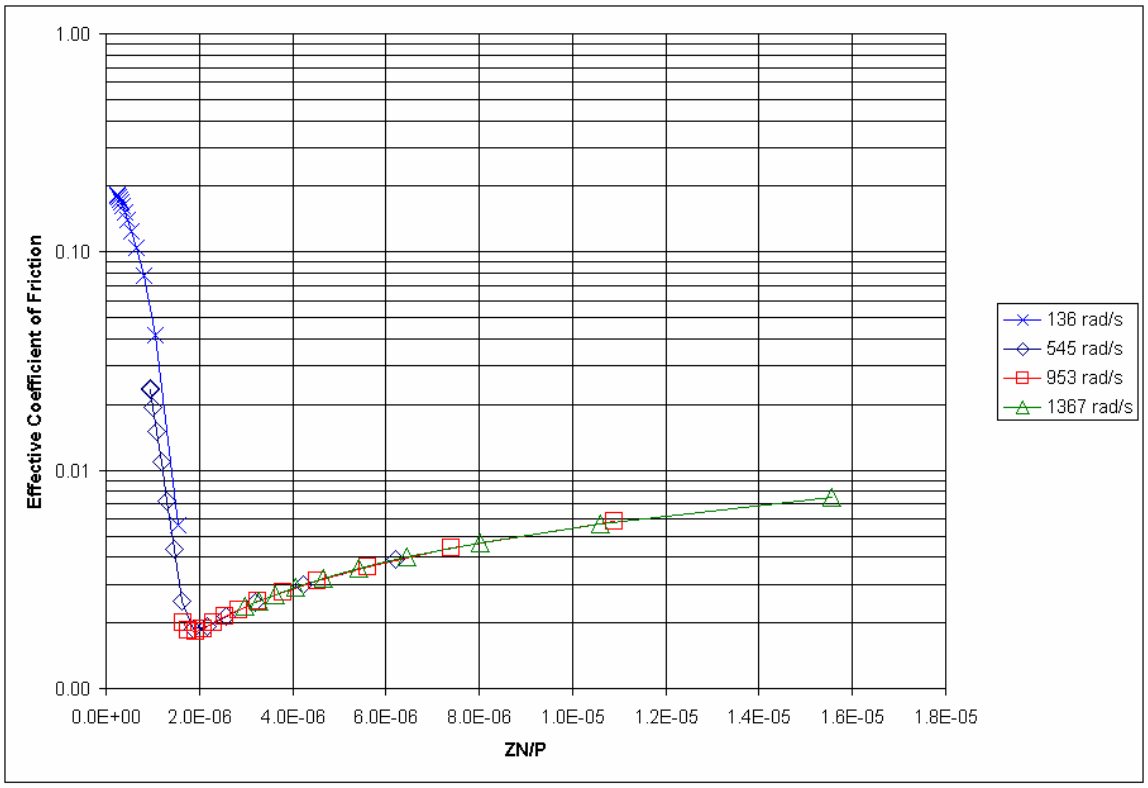

Figure 4.33: The Stribeck curve plotted using generated numerical data.

By effectively removing the thermal heating effects from the numerical model, the bearing does not suddenly distress at the minimum point on the generated Stribeck curve (see Fig. 4.33). Instead, the mixed lubrication region of the plot is populated by data points as the applied load slowly overcomes the hydrodynamic lift.

The results of Figs. 4.29-4.33 show that since there are no sudden distress events that the negated thermal effects appear to be responsible for these events. These events are due to essentially the two mechanisms thermo-viscous distress and thermo-elastic instability. In application it is thus advantageous to decrease the magnitude of such effects as thermal expansion and decreases in viscosity. This can be accomplished by decreasing frictional heat generation and increasing heat dissipation (as was done in this section). The effect of the friction coefficient on bearing performance is investigated in

section 4.11.3. The results show that that low friction coatings may be an effective at improving bearing performance by increasing the bearings resistance to thermoelastic instability.

4.12 Conclusions

By considering heat generation and thermoelastic deformation the numerical solution captures the physical mechanisms of thermoelastic instability and thermoviscous distress. These two mechanisms are believed to be the root cause of severe and sudden distress in the bearing during operation. When thermo-elastic deformation is considered, the numerical code predicts that the washers distress at very low loads. The case of a highly conductive material was also investigated and it was found than that the bearing operates at all speeds and loads without the occurrence of any sudden distresses. This again confirms that the distress of the bearing is due thermal effects which cause the bearing to distress quickly and severely.

The results of the numerical model also generate the traditional trends of the Stribeck curve when plotted. The numerical model thus predicts that the washer can operate in all the regions of the Stribeck curve (full-film lubrication, mixed lubrication, and boundary lubrication). However, once asperity contact occurs in the mixed and boundary lubrication regimes the friction increases significantly and the bearing becomes much more likely to distress due to thermo-elastic instability.

The dry friction coefficient was varied to investigate the effect it has on bearing behavior. Decreasing the friction coefficient significantly improves the range of effective

bearing behavior. By decreasing the dry friction the frictional heat generation also decreases significantly. This is effective at expanding the loads and speeds that the bearing can operate at without thermoelastic instability or thermoviscous distress occurring.

Next the experimental methodology is outlined and the results are presented for a number of different washer configurations and loads. Many of the trends predicted by the numerical code are confirmed in the experimental results. In Chapter 7 the experimental and numerical results are compared and correlated as much as possible. Although in many cases the numerical and experimental results do not quantitatively agree, it is most important that they predict some of the same qualitative trends in bearing behavior.

CHAPTER 5

EXPERIMENTAL SIMULATION

It is the goal of this portion of the research to experimentally quantify and map the behavior of various thrust washer configurations under various conditions. A bearing life test in which major bearing behavior influences such as load and speed are held at prescribed amounts for a governed period of time has been created. The test allows the bearing to be tested over an acceptable length of time (up to 14 hrs) so that multiple tests can be performed. In addition, the results for a smaller set of variable load and speed tests are presented.

5.1 *Test Rig Description*

To improve the understanding of the thrust washer bearing behavior, a test rig, shown in Fig. 5.1, was designed to provide a physical model. The test rig was designed to simulate as accurately as possible the conditions of the bearing within the transmission, and also to allow variation in the operational parameters, governing the tribological behavior of the washer. For this reason actual gears and bearings from the transmission where used in the test rig. All components of the test rig are designed to safety, except for a shear pin transferring the torque from the motor to the rig. The pin is designed to protect the test rig from sudden stresses that may arise from a bearing failure. It does this by shearing before the maximum limit of any of the test rig components is reached.

The test rig allows controlled variation of the operational parameters governing the tribological behavior of the bearing. The parameters that most affect the life of the bearing and its tribological behavior are believed to be thrust or axial load, rotational speed, lubrication supply, lubrication properties, and the geometry of the bearing. The test rig also records pertinent real-time data from the bearing, namely, the frictional torque transferred through the bearing and the temperature near the bearing and of the fluid exiting the bearing.

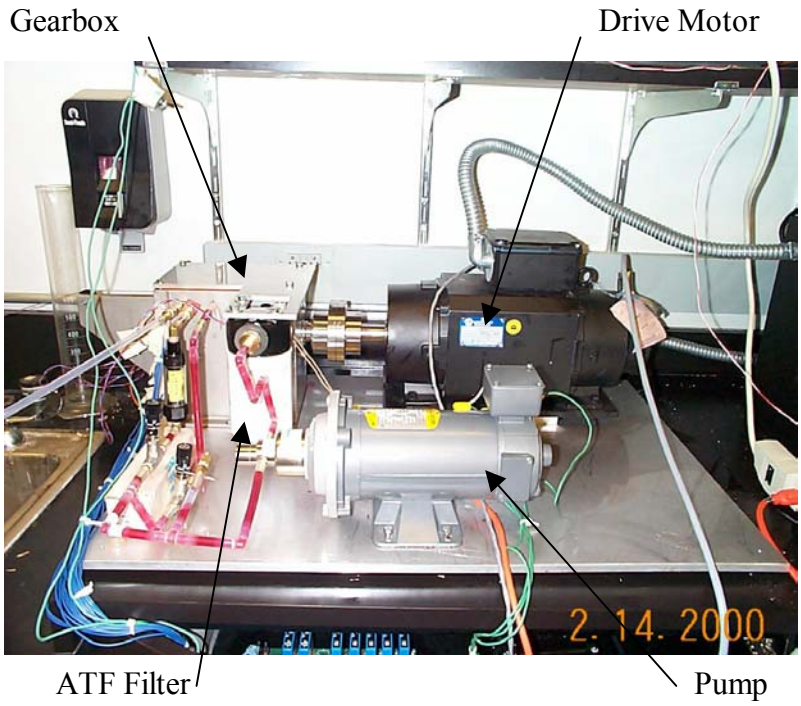

Figure 5.1: Photograph of assembled test rig from side.

The torque transferred through the bearing is directly related to the effective coefficient of friction, since friction is the mechanism that transfers torque from the bearing to the carrier. The recorded torque is thus seen as a very important aspect of the bearing, because the efficiency and performance of the bearing can be directly related to

the effective coefficient of friction of the bearing. As with most bearings, it is desired that the coefficient of friction be as small as possible to minimize the loss of mechanical energy. The friction does not only contribute to energy loss, but it can also be related to wear, because when a bearing wears its friction will be higher since energy is lost in removing material from the bearing. All the energy lost through friction is convected away by the lubricant and whatever components the bearing is in contact with, in this case these components are the carrier, the shaft, and the gear. The temperature of these components will rise in direct relation to how much frictional energy is dissipated.

A torque sensor using strain gauges was originally implemented in the test rig. It was found, however, that the power output of the motor provides a more reliable reading. At a constant load and speed (with no acceleration) the power output of the motor is theoretically proportional to the frictional loss of the bearing. This power output was calibrated to the frictional torque and is now used to measure it.

Thermocouples measure the temperature near the bearing. Four thermocouples are embedded in the stationary carrier next to the bearing. Another thermocouple placed at the bottom of a plate positioned directly below the bearing gathers the exiting lubrication and reads its temperature.

All the sensors are wired into a data acquisition system, which amplifies and filters the signals before they are acquired by a data acquisition board installed in a PC. Professional software is used to record and plot the data in real-time. See Appendix D for a listing of the data acquisition parameters of the system.

An electric motor is used to drive a shaft, which drives the larger gear, which in turn drives the smaller gear. The pinion and bearings are loaded by a press attached to a

lever, which is loaded by a cable that exits the rig and follows a series of pulleys to a hanger. The hanger can be loaded with an assortment of weights and thus impose various axial loads on the bearing. The lever that loads the bearing magnifies the force by a factor of 3.6. The thrust washer bearing system can thus be loaded from 16.0 N (3.6lbf) to 2419.7 N (544lbf), or even more if desired. The hanger can be loaded with an assortment of weights and thus impose various axial loads on the bearing. The pinion rides on a series of needles (forming a needle bearing) placed between the shaft and boring. A steel gearbox encloses the gears, loading system, and lubricant.

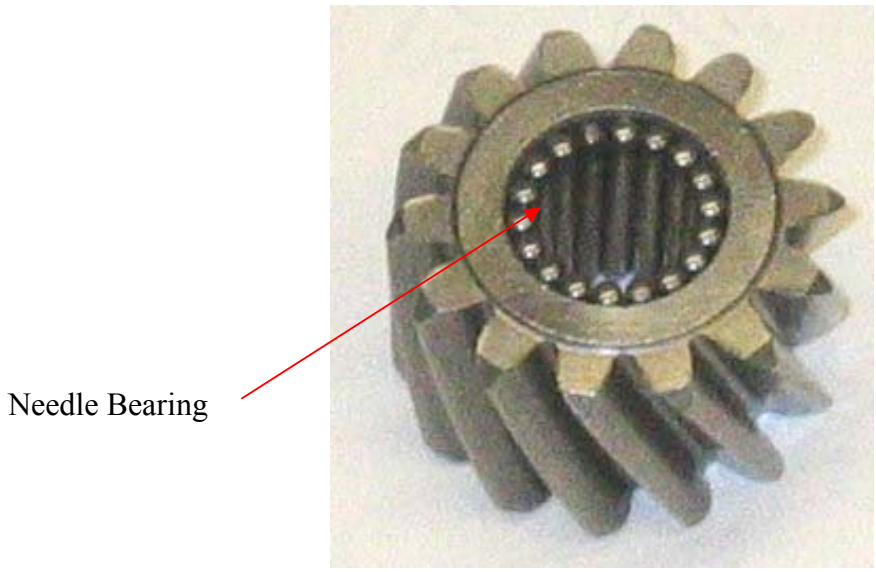

Figure 5.2: Picture of pinion gear and the needle bearing which carries the radial load between it and the shaft.

A thrust roller bearing is used at the side of the pinion where the load is applied in order to reduce the friction between the force applicator and the gear. All the purely functional bearings and components in the rig are rated for speeds and loads in excess of what the test rig can produce. Even the needle bearing upon which the gear rides is under

very little radial load, a load that is much less then it receives in the transmission (see force analysis in Chapter 1). Thus, the only bearing failure which should occur is that of the thrust washer bearing.

The pinion (planet gear) and sun gear are the production gears used in the automatic transmission. These gears are used to provide the most realistic simulation of the actual transmission. The gear ratio of 1.86:1 between the sun gear and pinion also magnifies the rotational speed provided by the motor. The gears and loading system are enclosed in a steel gearbox that contains the lubricant. The driving shaft is supported by two high precision ball bearings at the two ends of the test rig. The ball bearings are sealed on the side facing out of the gearbox to prevent leakage.

The pinion can be rotated at a maximum rotational speed of 13,000 rpm. The three-phase electric motor driving the system has a maximum rating of 11 horsepower at the maximum speed of 7000 rpm. The gear ratio from the sun gear to the planet gear provides the needed magnification of rotational speed to 13,000 rpm. The motor is controlled by an inverter unit, which is digitally programmed by a PC.

A simple lubrication system is also provided to lubricate the tested bearing and also the other bearings used in the mechanism. Figure xx shows a side view of the test rig in which the lubrication system can be seen by the red transmission fluid within the tubing. A flow meter is also installed; it measures the fluid flow to the bearing and is located in the center of the picture. A gear pump is used to pressurize the fluid, thus causing it flow into lubrication applicators within the gearbox. A filter is placed ahead of the pump to remove any significant debris that might affect the gear pump and the thrust bearing performance. The inside of the gearbox is used as an oil sump from which the

lubrication is cycled. The sump also provides lubrication to the ball bearings carrying the driving shaft. The lubrication used is standard factory fill automatic transmission fluid used by the industrial sponsor.

The applicators expel lubrication to the thrust washer bearing from above. The applicator consists of a pressurized cylinder through which lubrication enters from the outside of the gearbox; The lubricant then exits through a small hole of the same size as the supplying holes in the transmission. In the test rig the lubrication system can supply lubrication at flow rates from 0 to 0.416 l/min. This same system also lubricates the rolling element thrust bearing on the loading side of the gear.

In the test rig a majority of the axial load is induced by a lever pressing from one side of the gear and bearing assembly (see Fig. 5.3). In practice, the bearings are loaded by the axial forces of the meshing of helical gear teeth and the skewing of the needle bearing upon which the gear rides. In the test rig the axial load is applied using a tapered face to cause a tilt of the pinion to simulate the actual non-axisymmetric loading conditions. It is believed, however, that on a qualitative and comparative basis the results from this test rig can be useful in determining the distressing conditions seen in practice.

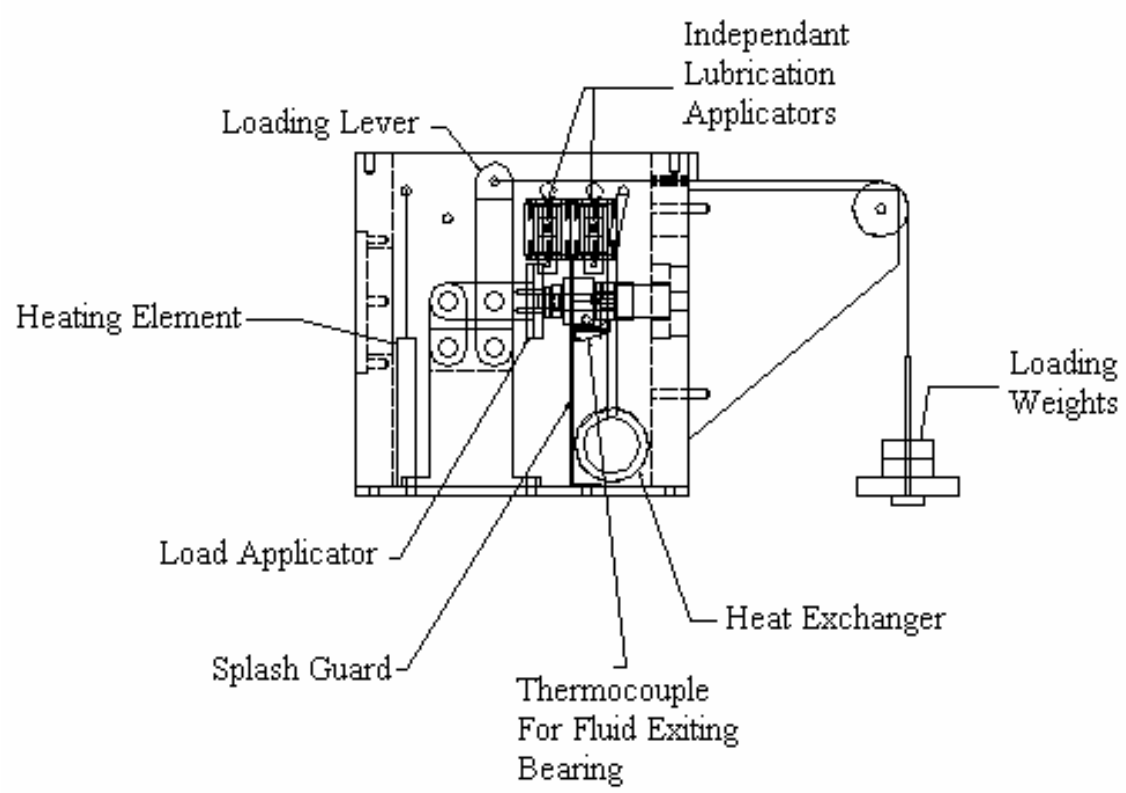

Figure 5.3: Diagram of test rig from side.

Since the gears used are helical in the test rig, an additional load is also applied to the bearing. The force is directly related to the torque. This force is very small in comparison to the manually applied axial load and so is not taken into account. Since no significant load causes the needles between the gear and shaft to skew, the load induced by the skewing is ignored.

Little or no wear caused by these tests would indicate sufficient hydrodynamic lubrication. Theoretically, the life of a fluid film bearing is infinite when there is no contact; thus, the length of bearing life during these tests could also indicate if bearing behavior is indeed hydrodynamic. The tests will also indicate whether failure induced over long periods is sudden or gradual (wear or lubricant film breakdown).

5.2 Variable Speed and Variable Load Tests

During the following tests the operating conditions were varied incrementally. The resulting data provide predictions for the thrust washer operation at a number of various load and speed conditions. Only a round steel and round bronze washer combination were tested. Many other washer combinations will be tested in Section 5.3. These tests produced a large amount of scatter in the data and so the testing methodology was changed to constant operating condition tests for Section 5.3. The variable speed and load tests do set a criterion for the observed distress of the thrust washer bearing, which is then implemented in the constant load and speed tests.

During these tests a slightly different experimental setup was used. The frictional torque during these tests was measured by using a set of strain gages mounted on a cantilever beam as shown in Fig. 5.4. During the constant load and speed tests the frictional torques were made from the power output of the motor driving the gears and thrust washer bearing. The problem with the cantilever setup was that the strain gages delaminated due to contact with the ATF fluid in the rig.

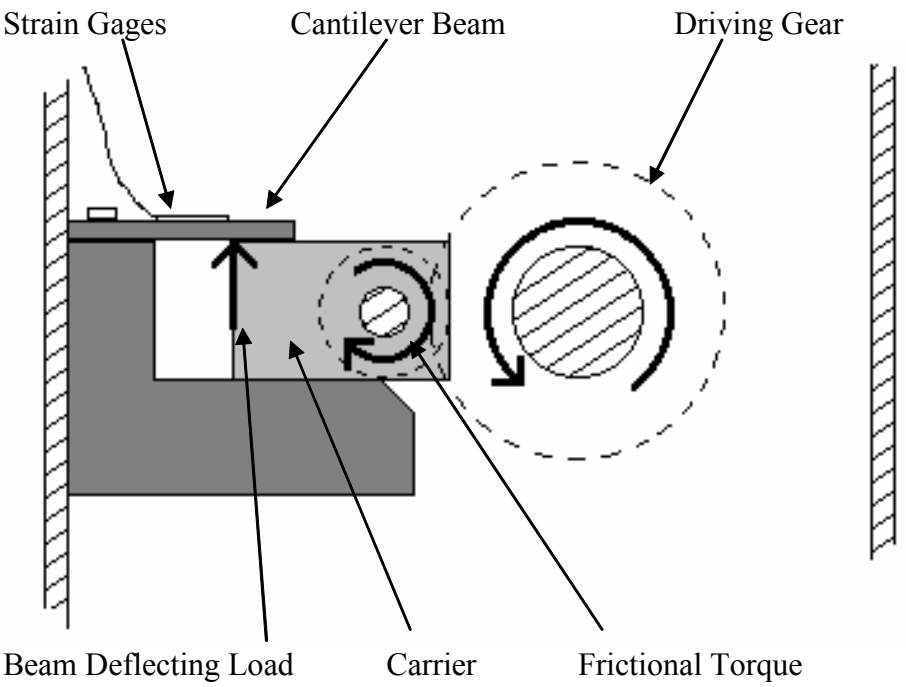

Figure 5.4: Diagram of the test rig at the thrust washer-bearing interface.

5.2.1 Experimental Methodology

All values have been non-dimensionalized for generality. For each loading condition a normalized PV (pressure·velocity product) value is calculated using the following equation:

$$PV = \frac{N \cdot F_a}{N_{\max} \cdot F_{\max}} \tag{5.1}$$

Where N – rotational speed, [rpm]

F_a – axial load, [N]

N_{max} – maximum tested rotational speed, [rpm]

F_{max} – maximum tested axial load, [N]

The PV value is meant to represent the total tribological "stress" the bearing is under. In other words, the effectiveness of the bearing can be quantified by how high a PV value the bearing can sustain without distress or significant friction. Distress is defined as a point when the temperature or frictional torque rises suddenly. This sudden rise in temperature is linked to thermoelastic instability and thermoviscous distress (see Chapter 2 & 4).

An experimental model of the bearing at different loads, speeds, or different PV values is desired. The experimental model here is obtained by varying the speed and load with time. During these tests the lubrication flow rate is kept constant at the maximum rate. Three types of tests are thus used to obtain data:

1. The rotational speed is kept constant while the axial load is increased in steps until distress is achieved (see Table 5.1).
2. The axial load is kept constant while the rotational speed is increased in steps until distress is achieved (see Table 5.2).
3. Both the axial load and rotational speed are increased simultaneously until distress is achieved (see Table 5.3).

Each step is incrementally increased at the same intervals for each test type. These intervals were obtained from previous tests by observing how long it took the bearing to reach a near steady-state condition. The time increments were then made to be longer. Three tests were conducted for each type of test, using the same sequence of load steps, except that the lowest load of 80 N was skipped after test 1A. The load steps which were taken for each test are listed in Tables 5.1-5.3.

Table 5.1: Constant speed and varying load (type 1 test, all time listed in seconds).

Load Step	Speed (rpm)	Load (N)	Time (Test 1A)	Time (Test 1B)	Time (Test 1C)
1	13000	80.06	0		
2	13000	240.19	448	0	0
3	13000	400.32	820	303	129
4	13000	480.38	1141	495	205
5	13000	640.51	1523	619	455
6	13000	800.64	1867	786	594
7	13000	880.7	2328		

Table 5.2: Constant load and varying speed (type 2 test, all time listed in seconds).

Load Step	Speed (rpm)	Load (N)	Time (Test 2A)	Time (Test 2B)	Time (Test 2C)
1	650	880.7	0	0	0
2	1300	880.7	331	313	334
3	1950	880.7	792	481	795
4	2600	880.7	963	652	965
5	3250	880.7	1197	811	1198
6	3900	880.7	1391	972	1393
7	4550	880.7	1620	1249	1621
8	5200	880.7	1852	1412	1798
9	5850	880.7	2050	1577	1996
10	6500	880.7	2249	1909	2195
11	7150	880.7	2547	2082	
12	7800	880.7	2744	2239	
13	8450	880.7	2977	2568	
14	9100	880.7	3180	2724	
15	9750	880.7	3306		
16	10400	880.7	3440		
17	11050	880.7	3602		
18	11700	880.7			
19	12350	880.7			

Table 5.3: Simultaneously varying load and speed (type 3 test**,** all time listed in seconds).

Load Step	Speed (rpm)	Load (N)	Time (Test 3A)	Time (Test 3B)	Time (Test 3C)
1	1950	240.19	0	0	0
2	3250	320.26	423	122	208
3	4550	400.32	903	291	603
4	5850	480.38	1399	452	1003
5	7150	560.45	1802	701	1550
6	8450	640.51	2188		
7	9750	720.58	2568		

5.2.2 Experimental Results and Discussion

The variable speed and load experiments described previously were performed, and all real-time data recorded. See Figure 5.5 for a sample of data recorded from the test rig. The load in this test is held constant at 880.7 N. In this plot each quantity is non-dimensionalized by a value so that all the data can be represented on the same scale. The temperature is non-dimensionalized by a value of 100°C. The rotational speed is non-dimensionalized by the maximum test rig speed of 13000 rpm and the viscosity was non-dimensionalized by the viscosity of the automatic transmission fluid at 0°C or 0.221 $N \cdot s/m^2$. To show how the viscosity is a function of temperature, the viscosity in the plot is calculated using Roeland's equation (Eq. 4.3) and the measured fluid temperature.

In these tests the load steps are clearly represented, as is the frictional torque and temperature. A sudden rise in bearing temperature and frictional torque also indicates a clear distress point (as shown to the far right in Fig. 5.5). In the sample plot it should also be noted that the changes in the friction coefficient usually precede the changes in viscosity. In other words, the viscosity changes do not seem to be causing the changes in the friction; rather the heat dissipated by the friction seems to change the viscosity. At

higher speeds more energy must be dissipated by friction even if the friction coefficient is lower, so the temperature often rises even though the friction coefficient is lower.

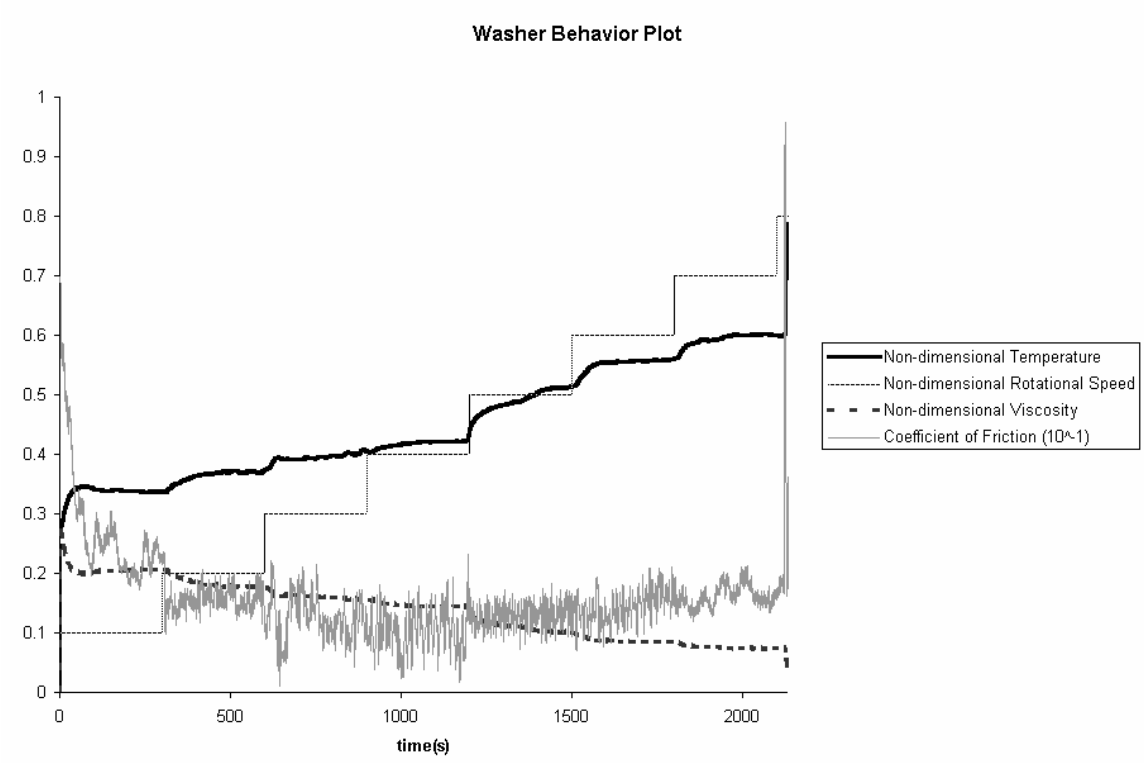

Figure 5.5: Sample plot of test rig data. Velocity is incremented from low to high speeds. The load is held constant.

There is a definite variation in the distress point and behavior within like tests. These variations could be due to manufactured differences in the surface roughness or composition of the bearings. This may also be due to the wearing of those parts used in the test rig that are not replaced between tests or to some variation in the testing procedure that may have affected the bearing behavior. In addition, the same lubricant was used through all the tests and so the lubricant properties may have been altered during testing and thus affected the bearing behavior; Although, a simple analysis of the

lubricant viscosity has been performed to demonstrate that the viscosity does not change significantly for the number of tests performed.

Steady-State Values

Using the steady-state data from the recorded data sets, the effective coefficient of friction and the fluid temperature versus PV are plotted in Figures 5.6. These plots use the steady-state values at the end of each load step for each value of PV induced during each test. To calculate the torque, a time average value is used over the last data points taken for each step of PV. This plot is created in an attempt to find some correlation between the PV value and the bearing behavior. This correlation could then be applied to future tests, especially if accelerated testing is implemented.

As seen in the plot in Figure 5.6, the bearing temperatures generally rise with PV. This rise in temperature is expected, since the load induced on the bearing increases, and thus the frictional energy dissipated increases as well. An increase in speed should also increase the temperature since more energy must be dissipated by the bearing.

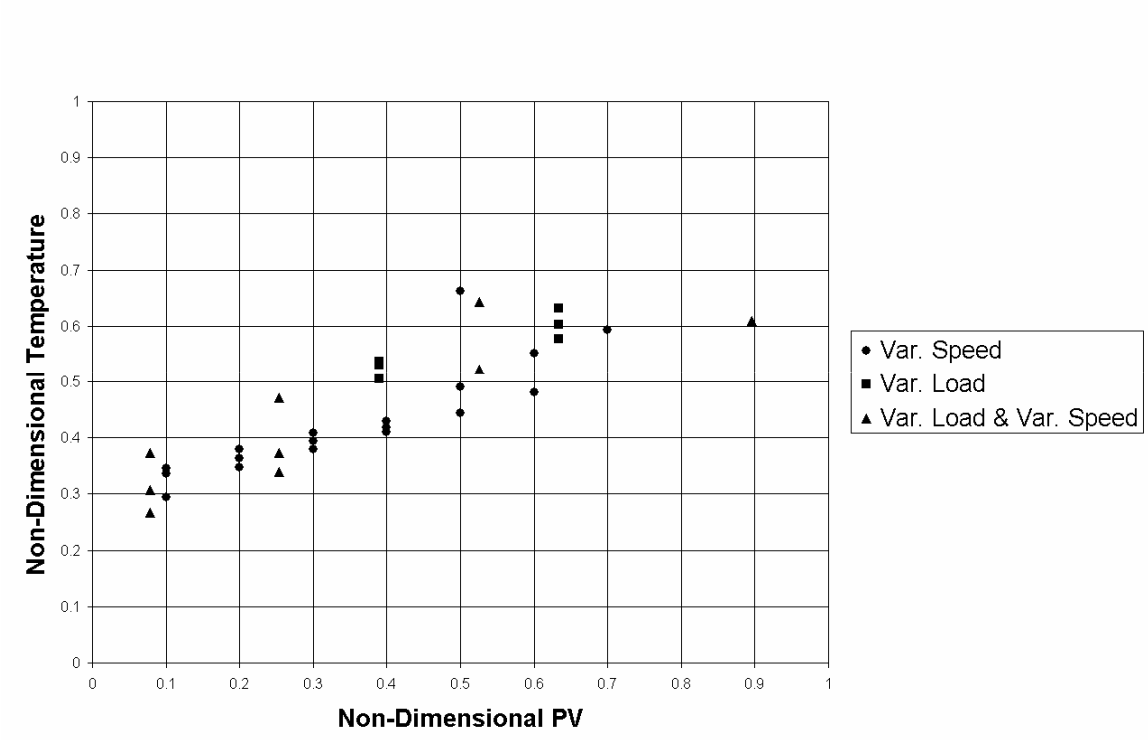

Figure 5.6: Plot of temperature data from all tests versus pressure-velocity value.

Effective Coefficient of Friction

Next, the steady-state torque is used to calculate the effective coefficient of friction (COF) for the bearing at the various loaded values of PV (see Figures 5.7-5.8). The Appendix C contains a short derivation of the formula used in calculating the effective coefficient of friction. This formula is for a surface that is loaded by an even axi-symmetric pressure distribution, even though this is not the tested condition. The formula is given below:

$$f_{eff} = \frac{3}{2} \cdot \frac{T_{frict}(r_o^2 - r_i^2)}{F_a(r_o^3 - r_i^3)} \tag{5.2}$$

Where f_{eff} – effective coefficient of friction

F_a – axial load, [N]

T_{frict} – frictional torque, [N·m]

r_i – inner diameter of washer, [m]

r_o – outer diameter of washer, [m]

During operation, the COF varies between 0.004 and 0.13. While the bearing seems to be operating with some indication of hydrodynamic effects, in boundary layer form, mixed lubrication form or full fluid film form, the COF is between 0.004 and 0.036. At the distress points, the COF rises to be between 0.06 and 0.13.

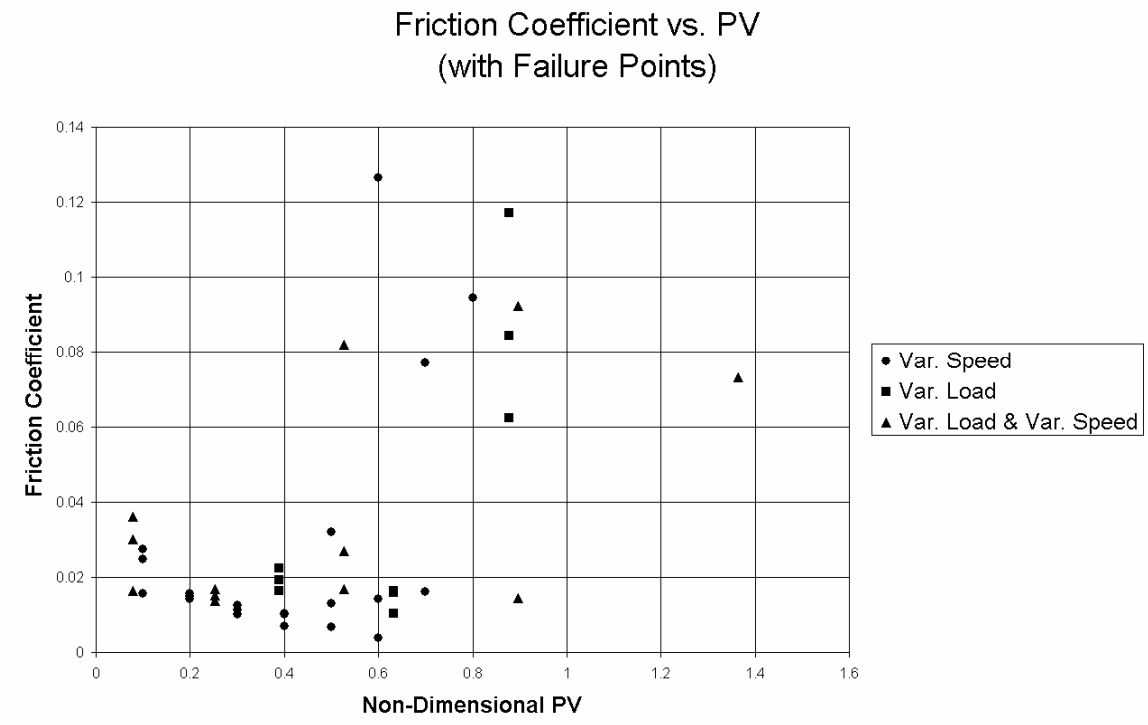

Figure 5.7: Plot of steady state effective coefficient of friction versus pressure-velocity value.

Each calculated COF was plotted versus PV. This plot is presented in Figure 5.7. Note that the PV value does not seem to represent the data well, because there does not seem to be a strong trend or pattern.

Although there is some variation in the values of the COF at each PV value (due to various ratios of speed to load), the general trend is that the COF decreases with increasing PV values. Hydrodynamic effects that increase proportionally with the rotational speed or decreasing fluid viscosity probably cause this trend.

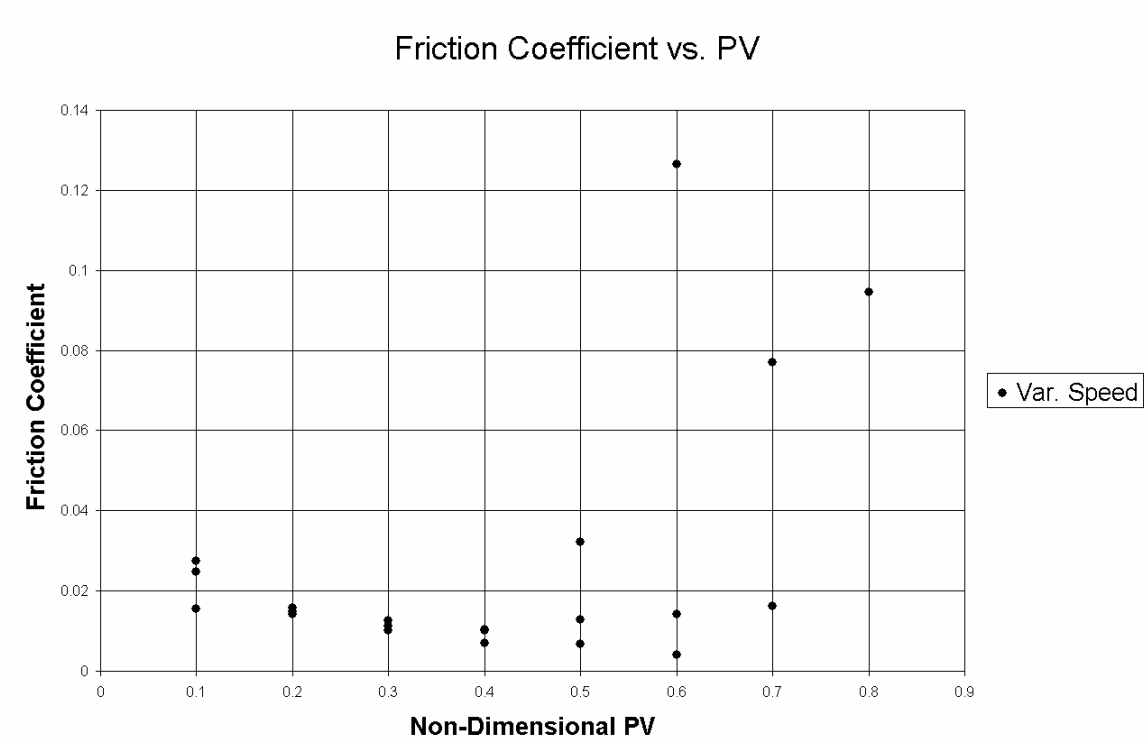

Figure 5.8: Plot of steady state effective coefficient of friction for data from test type 2 (varying speed and constant load).

If the values for the varied speed (Test Type 2) tests are presented alone the possibility of hydrodynamic lubrication becomes more apparent. Figure 5.8 shows the varied speed tests plotted alone against PV. Since load does not change, this graph is the same as a plot of the COF versus speed. These results contain some of the highest

relative COF seen during these tests at the beginning load steps. This is because at these load steps the rotational speed is low and thus unable to produce any hydrodynamic effects. As the speed is increased though, the COF lowers until bearing distress is reached. Distress at high speeds could be the result of centrifugal effects reaching significance (Pinkus et al., 1981), but most likely it is due to thermoelastic instability or thermoviscous distress as discussed in Chapter 2.

The COF does vary between each individual test of the same conditions for unknown reasons. Perhaps manufacturing inconsistencies in the surface topology or material composition cause these variations. For all three tests though, the COF rises significantly at the distress point, which would suggest dry contact or loss of hydrodynamic effects.

Stribeck Curve

Since the Pressure-Velocity (PV) value did not produce strong trends when it is plotted versus the steady state coefficient of friction, a different approach is taken. In Fig. 5.9 the experimental data is plotted as a Stribeck curve as outlined in Chapter 2. The data seems to roughly represent the two sides of the Stribeck curve. On the left side of the curve the coefficient of friction is decreasing as the Stribeck value increases. The plot suggests that the bearing behavior here is boundary lubrication or on the verge of full film hydrodynamic lubrications. Here hydrodynamic effects cause less friction with increasing speed. On the right side of the curve, the coefficient of friction begins to increase with increasing Stribeck values. Thus the hydrodynamic effect here seems to already be near the full film regime at these speeds.

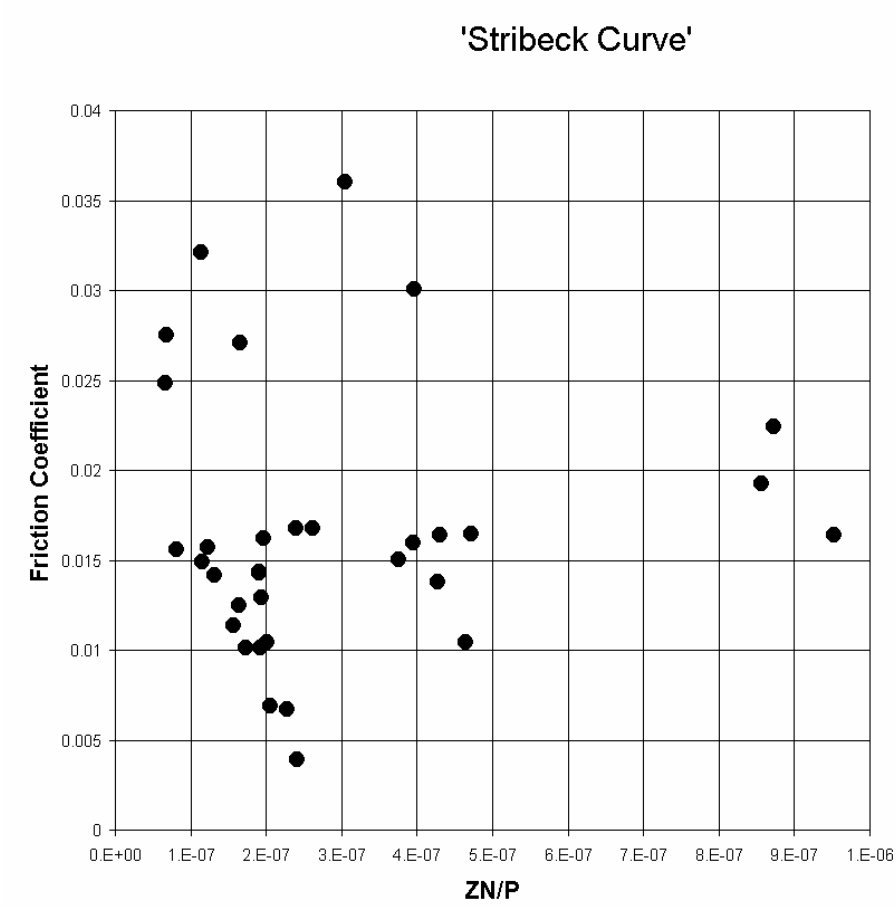

Figure 5.9: Plot of calculated effective coefficient of friction using the Stribeck value.

5.2.3 Variable Load and Variable Speed Conclusions

Distress of the bearing is linked to load and speed. Both temperature and torque seem to be good indicators of failure, since both increase noticeably at a distress point, although temperature seems to be the better indicator.

The data sets also indicate the possible presence of hydrodynamic effects produced by the bearing at certain combinations of rotational speed and axial load. This is indicated by a decrease in friction with speed, while the temperature and viscosity remain momentarily unchanged (Figs. 5.5, 5.8). When the coefficient of friction is

plotted versus the Stribeck value, a trend similar to the Stribeck Curve is produced. This would suggest that the bearing might be behaving under the influence of boundary layer, elasto-hydrodynamic and hydrodynamic effects.

Due to the coefficient of friction values and the geometry of the bearing, it is believed that these effects are caused by a thin boundary layer at the contact point and possibly a full film at higher speeds. It has been shown in past works that the coefficient of friction indicates various lubrication conditions (Hamrock, 1994). Thus the COF indicates the bearing behavior as it traverses between the most desirable hydrodynamic lubrication through elasto-hydrodynamic, boundary and also unlubricated contact, although all conditions may not be represented. At a distress point seen in all the tests, however, the COF increases sharply and is believed to represent a loss of fluid film and thermo-elastic instability. Chapter 2 discusses in detail thermo-elastic instability, thermo-viscous distress as the causes of bearing distress.

5.3 Constant Load and Constant Speed Tests

To decrease the amount of scatter that occurred in the variable load and speed tests, the test methodology was changed to a constant load and speed methodology. Thus the washer behavior would no longer be affected by its load and speed history.

A time of two hours for tests at 9100 rpm was chosen. At 9100 rpm, a two-hour test produces 1,092,000 cycles, in which one cycle is one revolution. For other tests to be comparable, they must be run for the same number of cycles. To produce the same number of cycles for each speed the tests must be run for the amounts of time indicated in Table 5.4.

Table 5.4: Maximum test duration at each gear speed.

Speed (rpm)	1300	5200	9100	13,000
Time (hr)	14	3.5	2	1.4

5.3.1 Procedure

Based on tests previously conducted it was found that at a certain load and speed the effective friction coefficient of the bearing rises suddenly from a value less than 0.04 to a value at or above 0.06. The coefficients may sometimes elevate for only a brief moment as if the bearing is able to dynamically correct itself and return to a more desirable state. The temperature at these elevated coefficients rises quickly and may cause damage to the test rig. It was found that the local temperature might rise above the boiling point of the lubricant in about 30 seconds. This boiling point causes lubricant in a gaseous or vapor form to exit the bearing and also the test rig. This occurrence is extremely undesirable since it drastically decreases the effectiveness of the lubricant.

Thus, an average friction coefficient of 0.06 over a time period of 30 seconds is considered the distress point or failure criteria for these tests. The tests, however, may not be interrupted if this criterion is met.

Under certain conditions, the friction coefficient may be high, but the bearing temperature may not rise significantly. In these cases, the test will not be interrupted until the temperature rises above a critical temperature, which may cause damage to the rig and its components. This critical temperature is set at 91°C. It should be noted, that this is the temperature behind the bearing in the carrier, and that the temperatures in the actual bearing may be significantly higher. It is uncertain which of the two, temperature or frictional torque is a better indicator of wear or distress of the bearing. These tests will help determine that indicator.

The minimum time for a test is set at 1 minute at speeds of 9100 rpm. Just as the maximum duration of tests were set to time periods that produce the same number of cycles, the minimum test period will also be set to produce the same number of cycles, according to the speed of the test. The minimum test periods at different speeds is given in Table 5.5.

Table 5.5: Minimum test duration at each gear speed.

Speed (rpm)	1300	5200	9100	13,000
Time (min.)	7	1.75	1.0	0.7

A few different loading conditions will be used to obtain a statistical representation of the bearing behavior and life. The initial goal is to obtain a good understanding of the failure mechanism of the bearing, than other bearing designs will be tested using this standard. These tests are within a range of speeds and loads, which are

comparable to what the bearing carries in the transmission. The 16 different load and speed combinations vary widely over the capable loads and speeds of the test rig (see Table 5.6). Initially, two tests will be performed at each load to bring the number of data points to 32. Then, if there is a large variation at certain loads and speeds, additional tests will be performed. Also, load combinations not included in the mesh may be tested by refining the mesh in those desired regions.

A new set of washers are used for each test and the carrier and gears are resurfaced or exchanged for new parts at regular intervals to prevent wear from affecting the tests. This interval has been determined by measuring the surface properties (roughness) after each test using a profilometer (see Wear Tests and Analysis).

Table 5.6: Axial loads and rotational speeds of life tests to be performed. Intersecting locations give PV (average pressure × average linear velocity) values for each combination.

Load → Speed ↓	260.9 N (58.67 lbf)	749.8 N (168.7 lbf)	1239.0 N (278.7 lbf)	1728.1 N (388.7 lbf)
1300 rpm	0.972 MPa·m/s	2.794 MPa·m/s	4.617 MPa·m/s	6.439 MPa·m/s
5200 rpm	3.889 MPa·m/s	11.18 MPa·m/s	18.47 MPa·m/s	25.76 MPa·m/s
9100 rpm	6.806 MPa·m/s	19.56 MPa·m/s	32.32 MPa·m/s	45.08 MPa·m/s
13000 rpm	9.722 MPa·m/s	27.94 MPa·m/s	46.17 MPa·m/s	64.40 MPa·m/s

5.3.2 Washer Bearing Configurations

A number of washer bearing configurations are tested using the above testing methods. These configurations are compared with each other and to the results of the numerical simulation (Chapter 7). The coated bearings were added to the original scope

of the investigation and so are not as thoroughly compared to the numerical results. The following is a list of the configurations that will be tested. During a test, the washer configuration is placed between the gear and the carrier attachment (see Fig. 5.10). The list of tested washer configurations is:

1. One round steel washer, one round bronze washer (Bronze washer is adjacent to carrier, as depicted in Figure 1)
2. Two round steel washers
3. One round steel washer
4. One round bronze washer
5. One stationary steel washer (Discontinued)
6. One stationary bronze washer (Discontinued)
7. One stationary bronze washer and one round steel washer
8. One stationary PTFE coated washer, one round steel washer (stationary washer is adjacent to carrier)
9. One stationary nibron (nickel boron) coated, one round steel washer

Due to the possibility of long-term wear and run-in within the test rig, the tests performed are cycled through the different washer combinations. Four tests are performed using one combination and then the combination is switched. The load and speed combinations are also cycled, such that every load and speed combination will have the same number of tests performed (the matrix will be complete) before a new matrix is begun. This cycle is continued until all the tests are performed. Certain washer

combinations were discontinued if the testing suggests that the results will not provide useful information. Also, during initial testing, the regions of high loads and speeds are found to fail severely and to be very destructive to the test rig. Due to these concerns, once a load and speed combination results in a failure for a certain washer combination, the higher load and speed tests for that matrix is not performed.

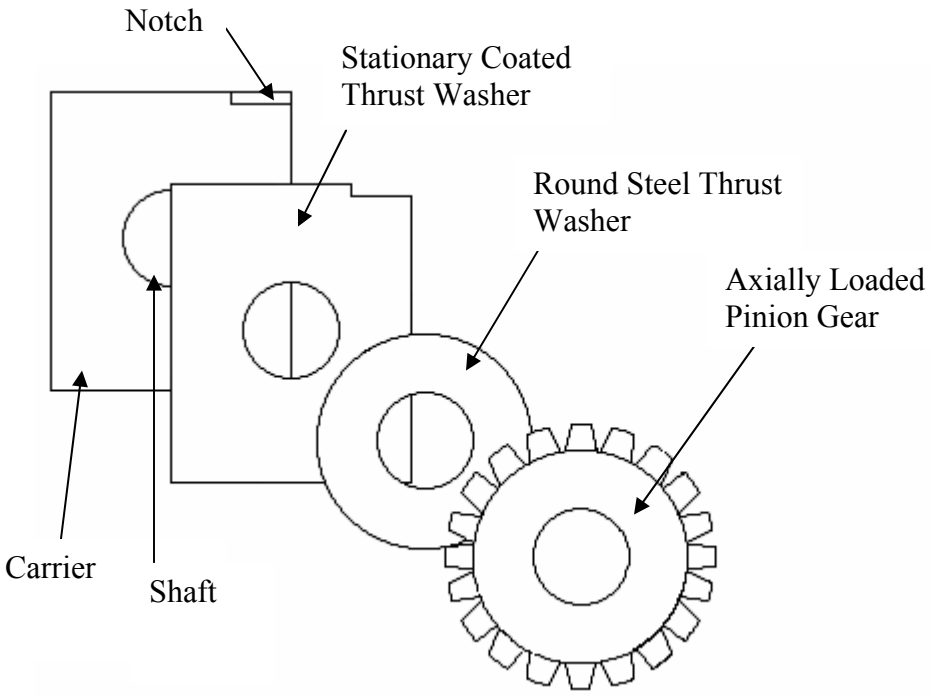

Figure 5.10: Typical coated washer bearing configuration.

The one stationary steel washer and one stationary bronze washer tests were discontinued due to severe failure at the lowest loads and speeds. This indicates that in comparison to the other tested configurations, these are not suitable for use. Since these combinations correspond to no round or free rotating washers, their sub par performance indicates that round washers do enhance washer bearing performance.

5.3.3 Experimental Results and Discussion

For each load and speed test, the average values for the COF and average temperature are calculated. The test duration and maximum temperature are also calculated for each load and speed test. The resulting values are then plotted versus load and speed in Figures 5.11-5.14.

The standard deviation between tests at the same conditions for temperature is 6.88°C and for the COF 0.0472, although if the tests which distressed are not considered, these values reduce to 5.86 °C and 0.0176. The standard deviation reduces significantly probably because when the bearing does distress, scuffing and excessive wear occurs, and the COF becomes less predictable. If the bearing operates at a point on the threshold of distress, due to slight differences in the tests the bearings may or may not distress. This will also increase the scatter for these loads and speeds which are on the threshold of distress.

Single Round Steel Washer Results

As expected for load and speed the test duration decreases (see Fig. 5.11). However, at the lowest load of 261 N, the washer operates for the full test duration for all speeds. This is probably due to sufficient hydrodynamic lubrication separating the parts and decreasing the friction and heat generation. For all except two tests the bearing either lasts the entire duration or distresses immediately. This indicates that the washer does not distress due to fatigue or other cyclic phenomena during these tests. Rather, the distress is attributed to a severe and immediate distress condition that is believed to be

caused by thermo-elastic instability, thermo-viscous distress and scuffing (Section 2.2 and 2.4). These general trends are present in most of the tested bearings, except in the coated bearings, which reduce the friction and provide resistance to these thermally induced physical phenomena.

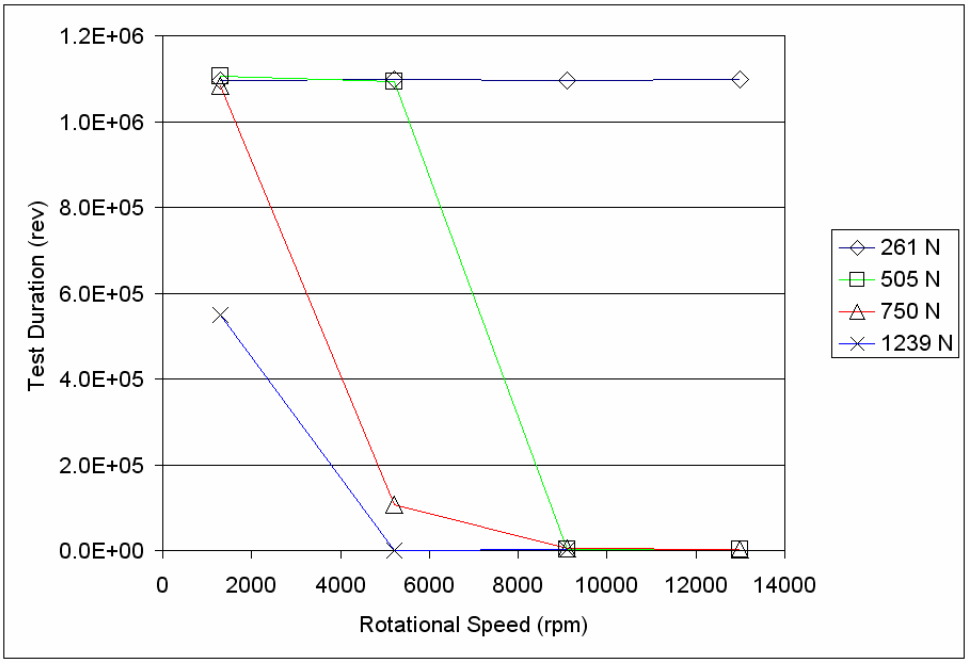

Figure 5.11: Plot of test duration for single round steel washers as a function of load and speed.

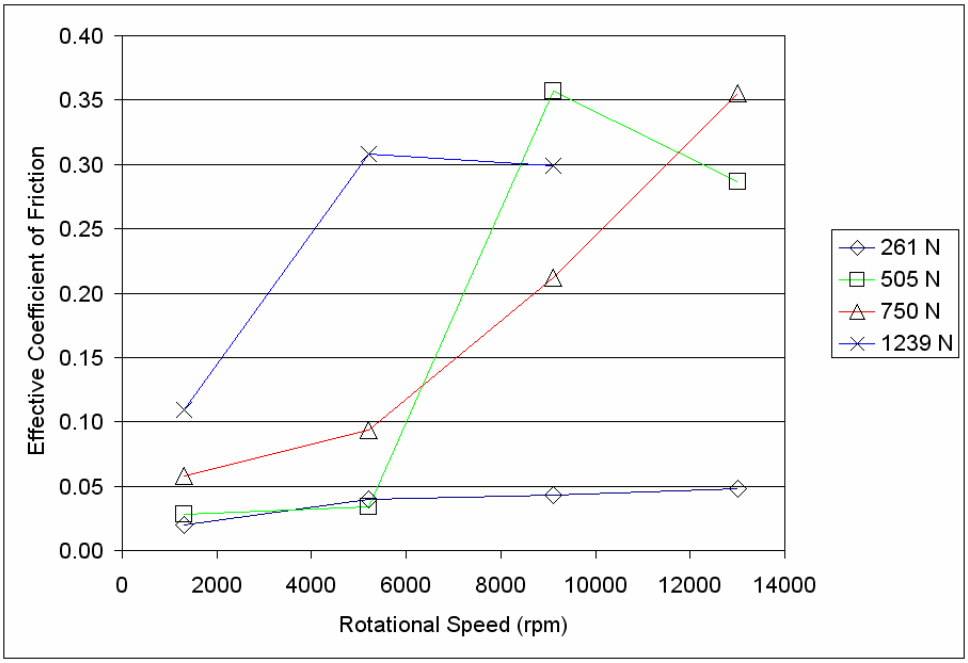

Figure 5.12: Plot of average effective coefficient of friction for single round steel washers as a function of load and speed.

The average effective coefficient of friction (COF) increases with load and speed as shown in Fig. 5.12. At the lowest load of 261 N, the COF appears to be low enough to suggest that the bearing is operating in a full hydrodynamic film between two of the bearing surfaces. As speed increases at 261 N and the film thickness increases (and the shear force of the lubricant), the COF also increases. For higher loads however, the film thickness cannot be sustained and the surface asperities contact. This contact causes the traction between the surfaces and the effective COF to increase. At the highest loads and speeds the high COFs are due to scuffing occurring between the surfaces (for a definition of scuffing see section.2.2).

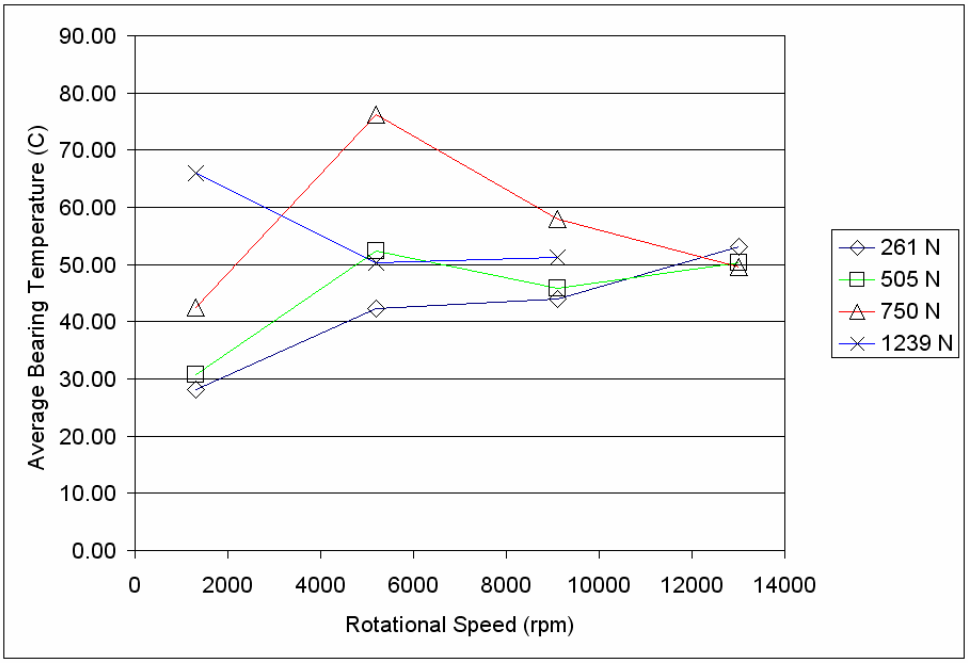

Figure 5.13: Plot of average bearing temperature for single round steel washers as a function of load and speed.

There is no clear trend for the average bearing temperature shown in Fig. 5.13. When the bearing distresses, the temperature increases quickly until the test is stopped because the test interruption criteria is met. When this occurs, the maximum temperature (see Fig. 5.14) is much higher than the average. For this reason the maximum temperature is much more reflective upon the state of the bearing at a certain load and speed. From this point forward the average temperature will not be plotted for each washer configuration.

The maximum bearing temperature increases with both load and speed (see Fig. 5.14). The maximum temperature is for some loads and speeds greater than the test interruption temperature because the temperature often continues to climb after the test is cutoff. This is due to the delayed propagation of heat from the surface of the bearing to the thermocouples.

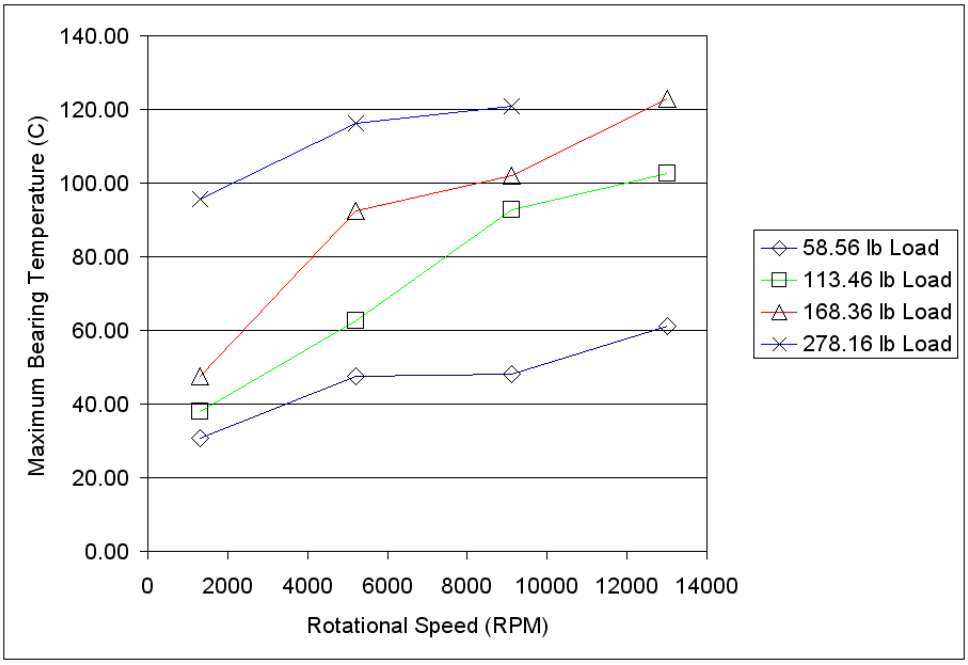

Figure 5.14: Plot of maximum bearing temperature for single round steel washers as a function of load and speed.

A Stribeck curve is also generated from the experimental results and shown in Fig. 5.15. The experimentally generated Stribeck curve follows the very closely the trends that are expected for a Stribeck curve operating in both the full film and boundary lubrication regimes. Fig 5.15 shows that at a Stribeck value of about 1.0E-6 that the bearing begins operating in the mixed lubrication regime. At that point the effective coefficient of friction increases sharply due to fluid film collapse and the resulting asperity contact. Also, looking back at the Stribeck curve generated from the variable loads and speed tests (Fig. 5.9), it appears that those tests were run more in the region of the elbow at the bottom left of the curve. This is where the bearing transitions from full film lubrication to mixed and boundary lubrication.

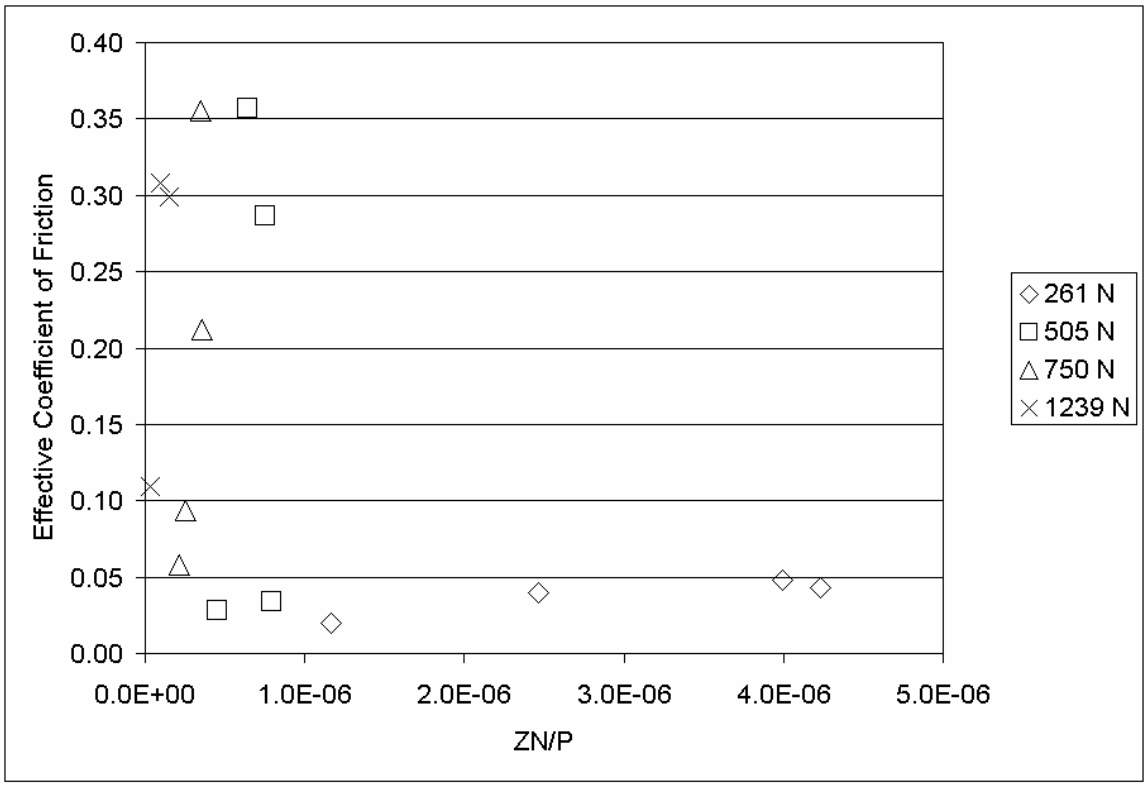

Figure 5.15: Experimentally generated Stribeck plot for a single round steel washer.

Comparative Results

From this point forward the results of the single steel washer will used as a reference with which to compare the other washer combinations. The single round steel washer combination is chosen because it is the simplest configuration that actually performs reasonably well. When coated washers were tested it was also with a single round steel washer and a stationary coated washer.

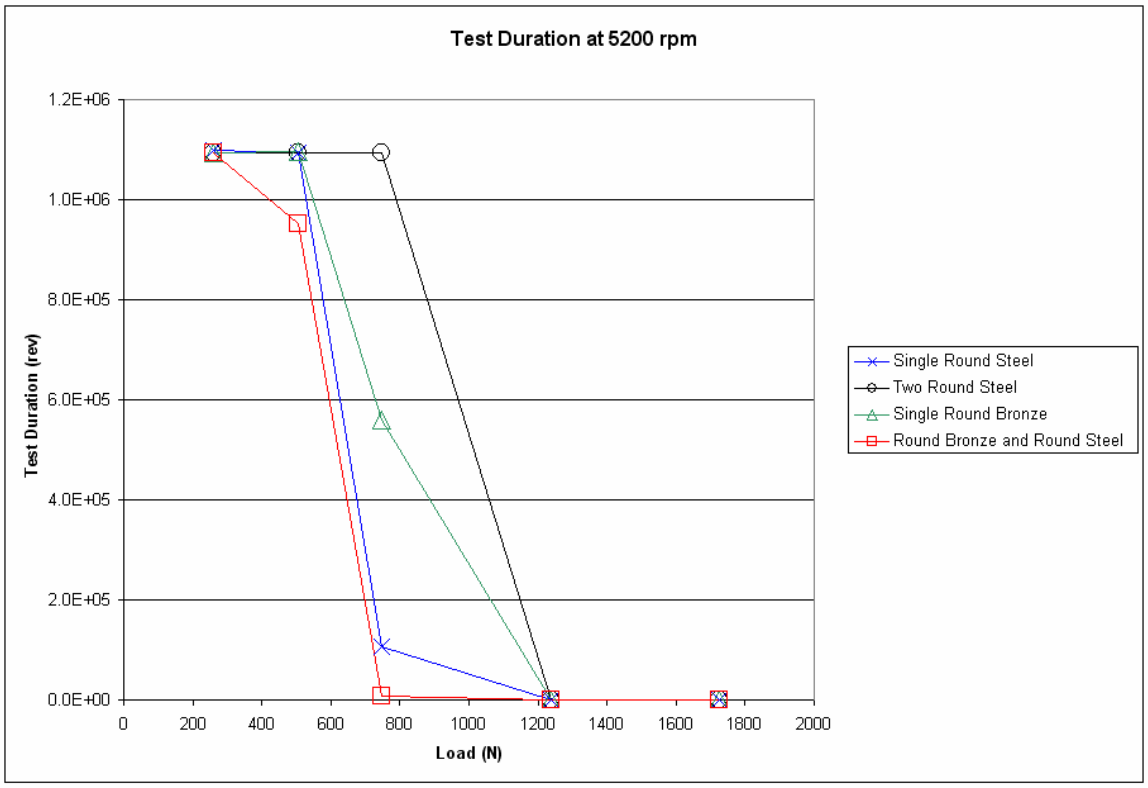

Figure 5.16: Test duration plotted as a function of load and washer type.

The test duration for various loads and washer configurations at a rotational speed of 5200 rpm is plotted in Fig. 5.16. The two round steel performs better than the single steel, but the round steel and bronze perform worse than the single bronze. It is thus unclear if the number of washers used in the bearing increases or decreases performance. It appears that the use of more than one round washer provides no significant increase in performance in comparison to the single round washer configurations.

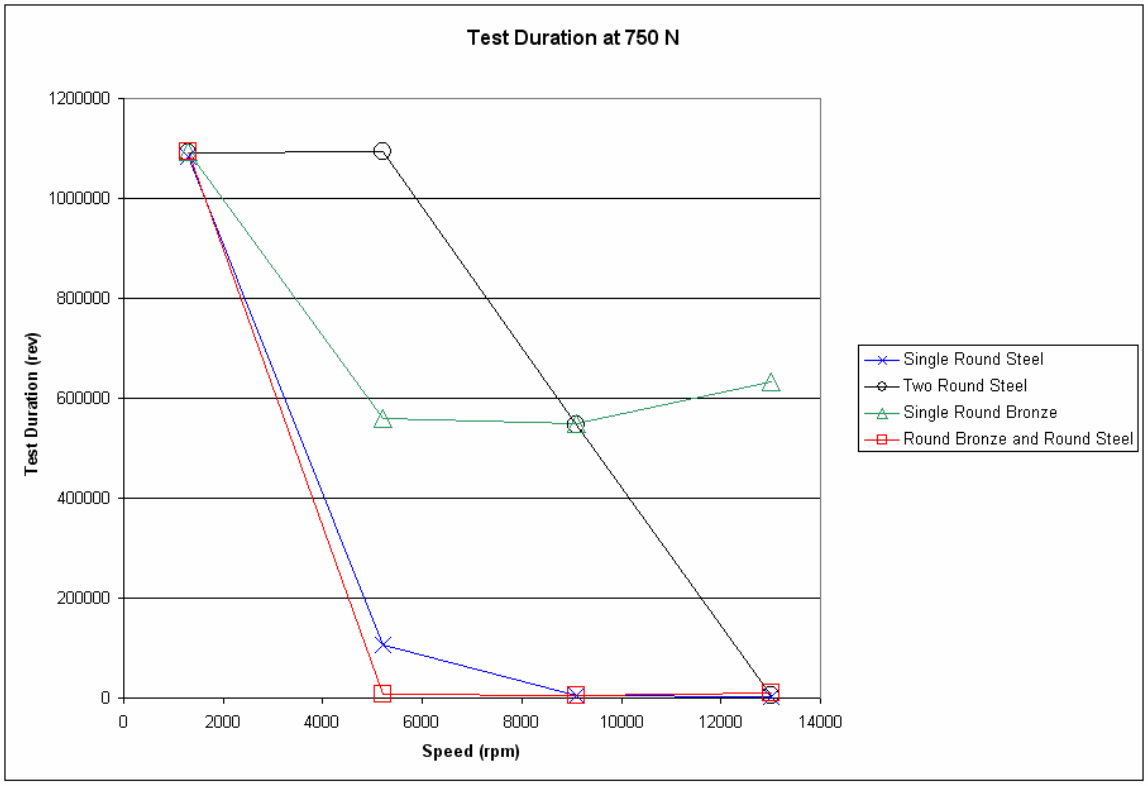

Figure 5.17: Test duration plotted as a function of speed and washer type.

It appears that the two round steel and single round bronze test washer bearing configurations perform better than the single round steel and round bronze steel configurations (see Figure 5.17). Again, even though certain washers seem to survive longer, the results show no advantage to using multiple round washers.

In Figure 5.18, the effective coefficient of friction follows similar trends for all the washer configurations, except at the highest load of 1139 N. At the highest load there are no representative bronze tests because they distressed at a lower load. However, the steel tests show a significant increase in friction at the highest load. At the highest load the steel washers appear to begin to scuff and adhere due to high temperatures (see Fig. 5.20). As will be more apparent in Fig. 5.19, the bronze washers provide some resistance to scuffing. This is because scuffing occurs more readily between two materials of similar structure which more easily bond.

It is apparent in Fig. 5.19, that at high loads the bronze washers significantly reduce the effective coefficient of friction. This is thought to be due to an increased resistance to scuffing. The material selection does seem to have an effect on bearing performance, although using additional round washers appears to provide no benefit. At some conditions the two washer configurations appear to perform best, while for other conditions the single washer configurations seems to do better.

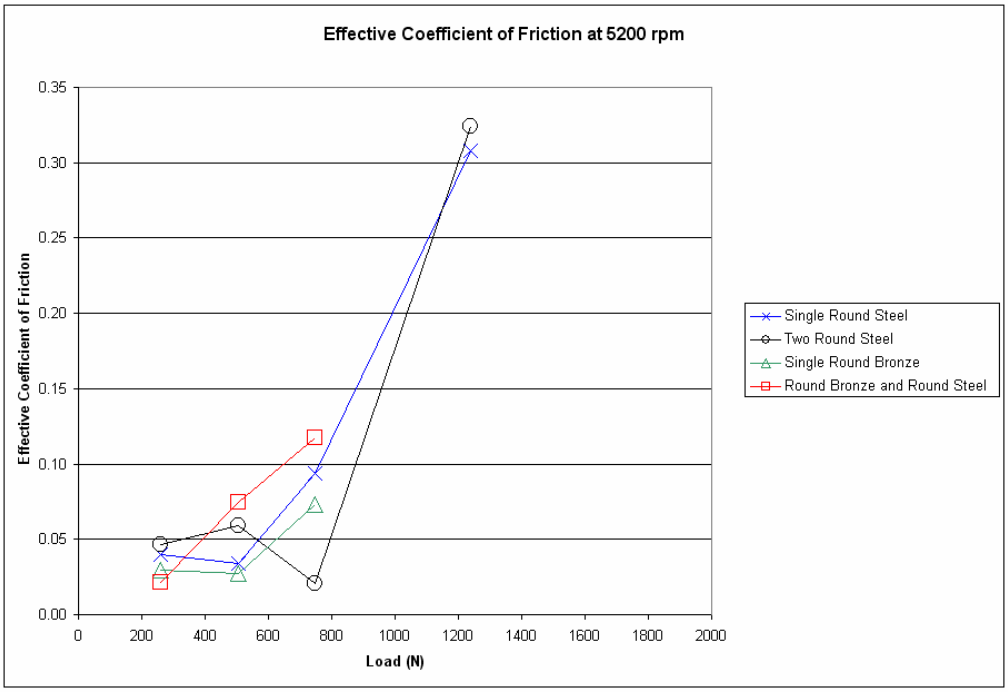

Figure 5.18: Effective coefficient of friction plotted as a function of load and washer type.

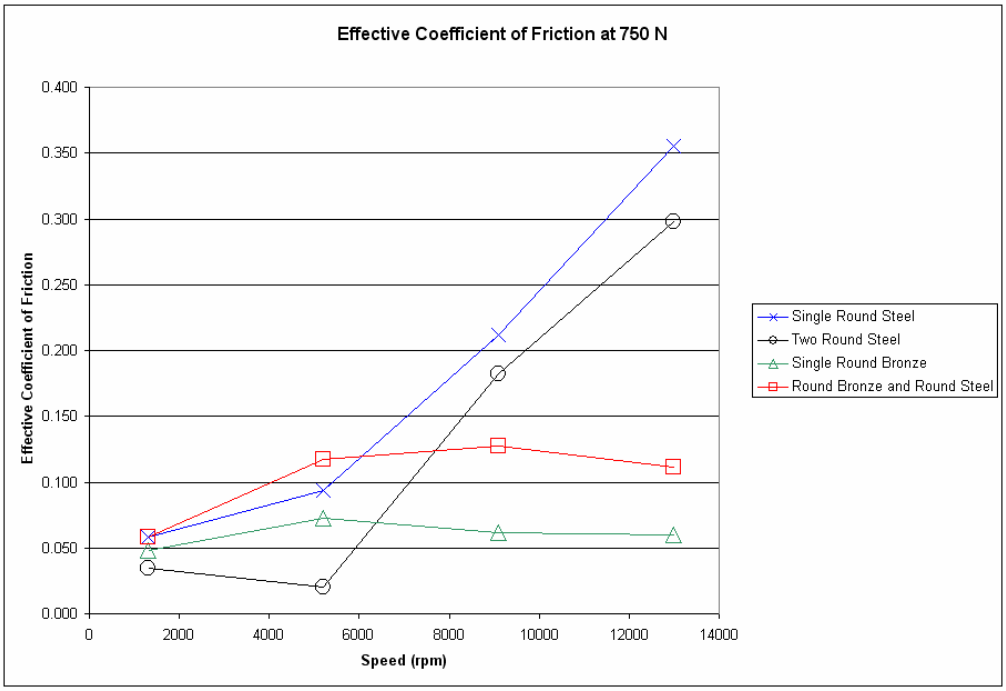

Figure 5.19: Effective coefficient of friction plotted as a function of load and washer type.

In Figure 5.20, the maximum temperature of all the bearing configurations appear similar, except for the two round steel washers at 750 N. Also, there is no comparison at the highest load since tests were not run for the bronze bearings at those loads. Again in Figure 5.21, when the speed is varied, there is no clear trend between number of washers, bearing material and maximum temperature. Although the bronze did improve bearing performance in Fig. 5.19, the bronze washers do not decrease significantly the overall temperature of the bearing. The bronze bearing just tends to scuff less once bearing distress has occurred. This does not mean that the bronze washer is more resistant to wear in general, because the bronze washer will still wear due to abrasive wear. The bronze will be less likely to cause the bearing weld together and cause lock up.

Based on the results presented in Figs. 5.16-5.21, it does appear that bronze washers provide a resistance to scuffing which could significantly reduce the possibility of the thrust washer bearings locking up when under distress. However, bronze washers also appear to distress at lower loads in some cases. There does not seem to be a significant benefit to adding additional round washers into the configuration.

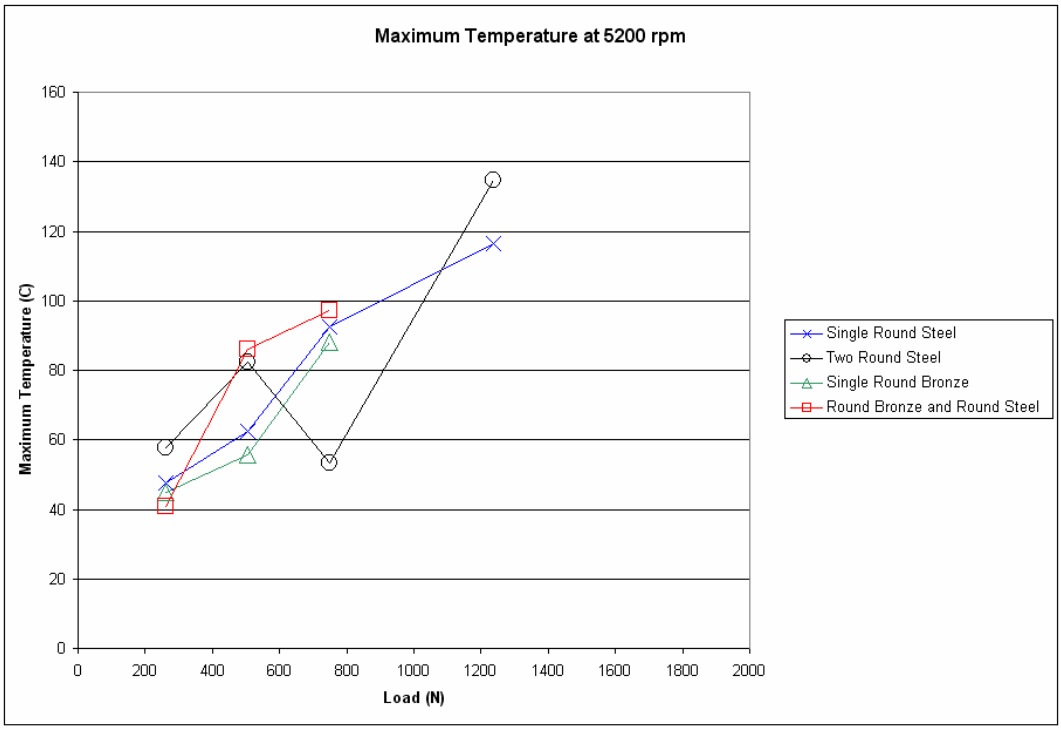

Figure 5.20: Maximum bearing temperature plotted as a function of load and washer type.

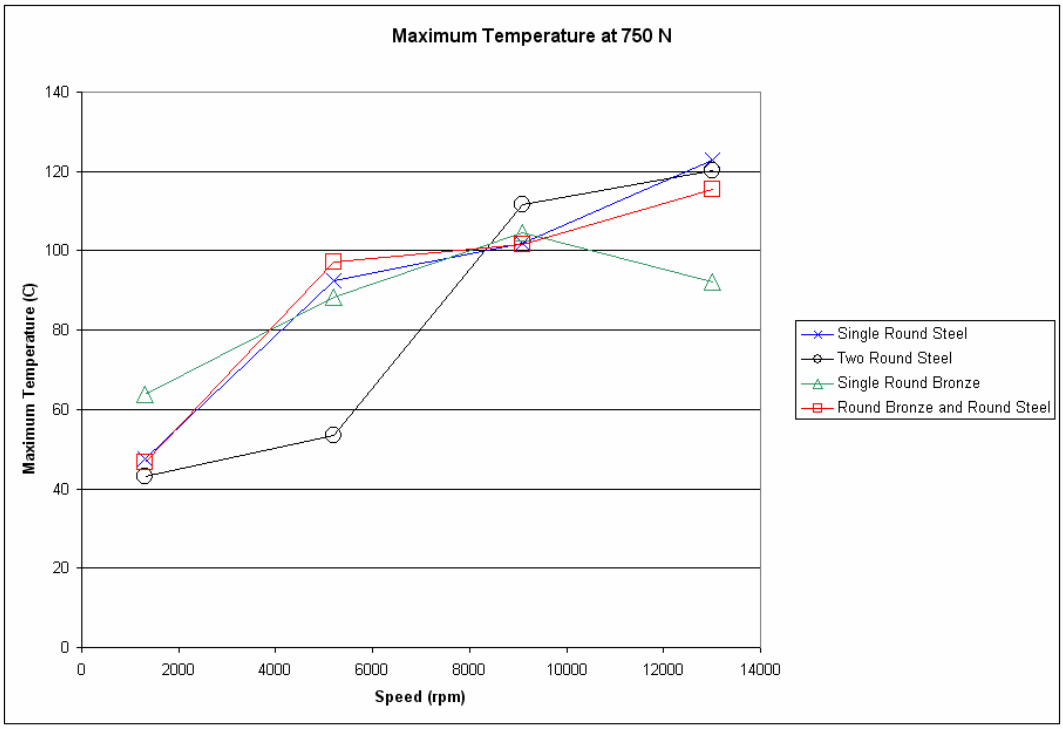

Figure 5.21: Maximum bearing temperature plotted as a function of speed and washer type.

The Effect of Coatings

The two coated (PTFE and nibron) stationary washers running with a single round steel washer are compared to the reference single round steel washers. The nibron coating consists of a nickel and boron plating which increases the hardness of the surface. A bronze stationary washer in place of the coated washers is also compared. The main effect the coatings have is to reduce friction. By simply reducing the friction other coupled effects will take place. Less frictional heat is generated and the coated bearing temperature will less than the uncoated bearing temperature. By decreasing the bearing temperature, scuffing and thermo-elastic instabilities are less likely to occur. The decrease in friction can also have the effect of decreasing wear and thus extending the life of the bearing.

As is shown in the following set of figures (5.23-5.29) coatings, especially PTFE, enhance bearing performance significantly. Nevertheless, coatings eventually wear away and leave the substrates below unprotected.

The nibron and PTFE coated washers appear to survive higher loads than the stationary bronze and the reference single round steel washer configurations (see Fig. 5.23). The stationary bronze washer does not seem to improve bearing performance significantly from the single round washer. Again in Fig. 5.24 the PTFE and Nibron coatings prove to enhance bearing performance. Actually, the PTFE coated bearings survived every load condition presented in the plot. It will be shown in subsequent plots (Figs. 5.25-.5.28) that the PTFE coated bearing performs superior to other bearing configurations for most criteria.

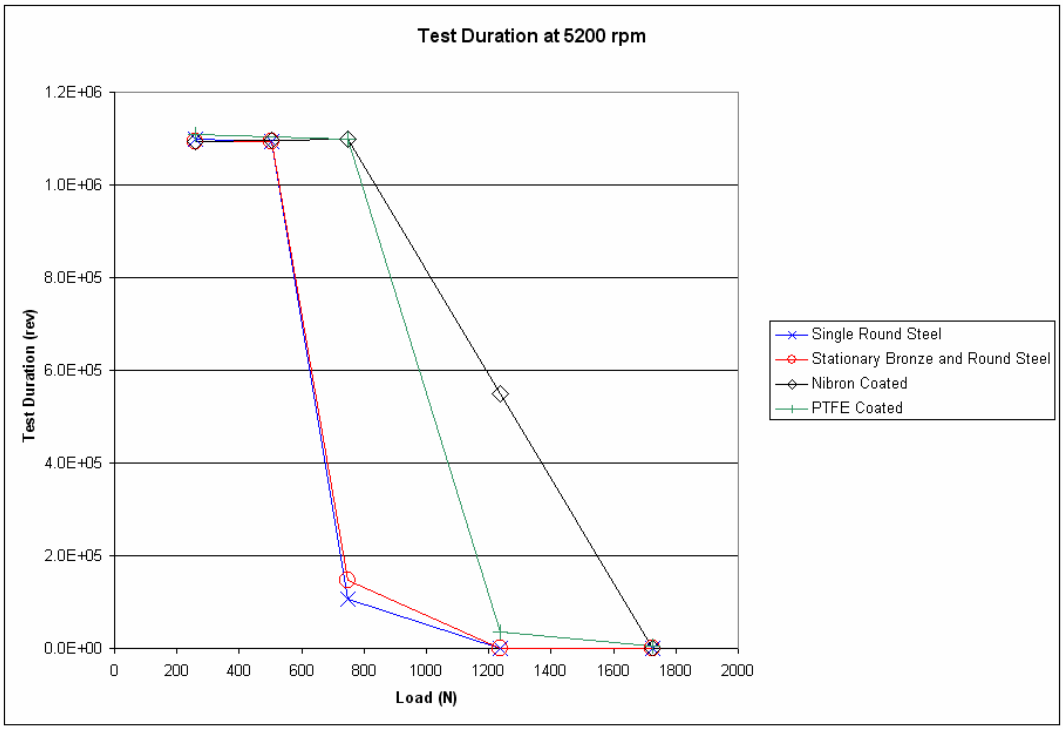

Figure 5.23: Test duration plotted as a function of load and washer type.

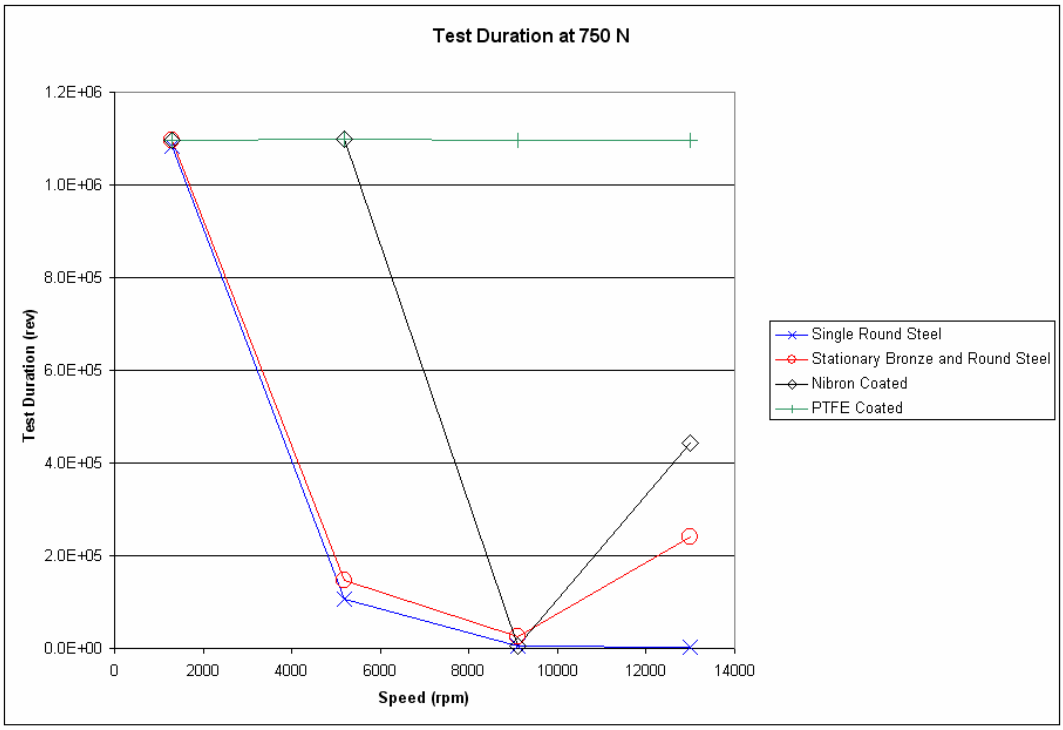

Figure 5.24: Test duration plotted as a function of speed and washer type.

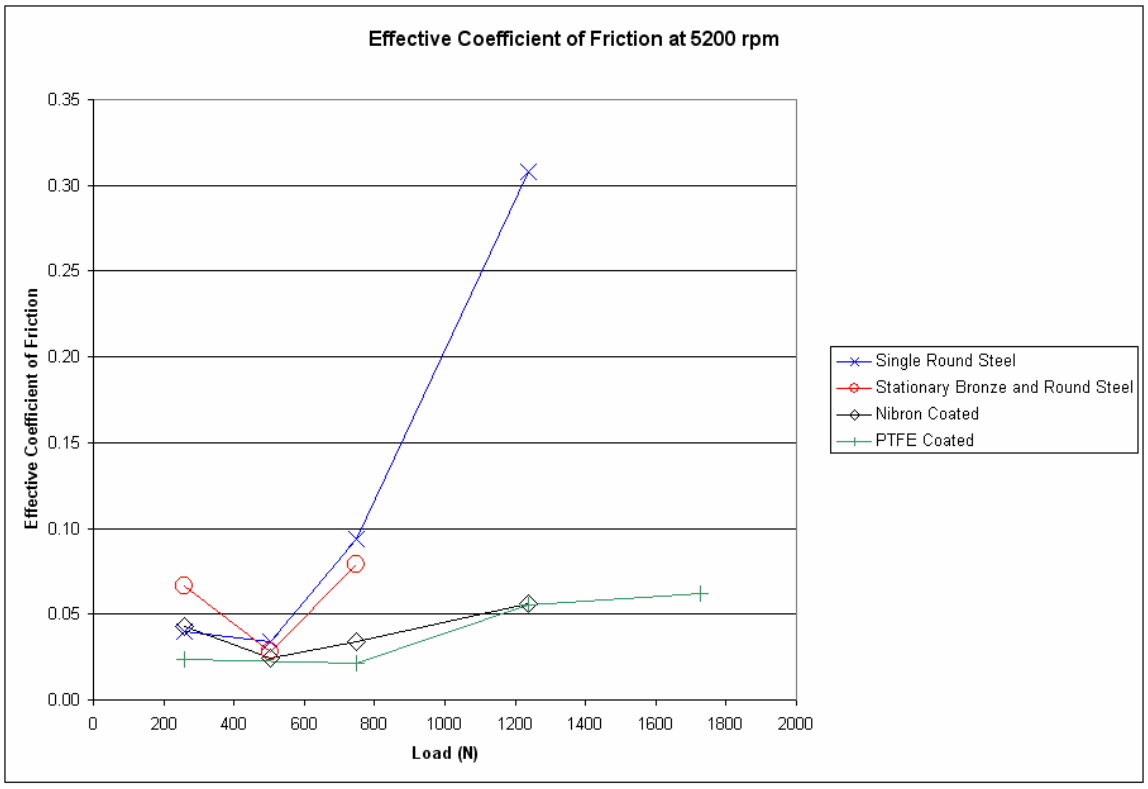

Figure 5.25: Effective coefficient of friction plotted as a function of load and washer type.

In Figure 5.25 the effective coefficient of friction for the reference single round steel washer configuration and various coated washers is plotted as a function load. The effective coefficient of friction (about 0.30) reached by the single round steel washer is due to scuffing of the bearing faces. It appears from this plot that the nibron and PTFE coatings significantly reduce the friction coefficient and the inhibit scuffing at high loads. Since the bronze stationary washer failed before the coated washer and the single round steel washer, it is not apparent if it has improved washer performance significantly.

Although for most loads, the effective coefficient of friction of the bronze stationary bearing is larger than both coated bearings.

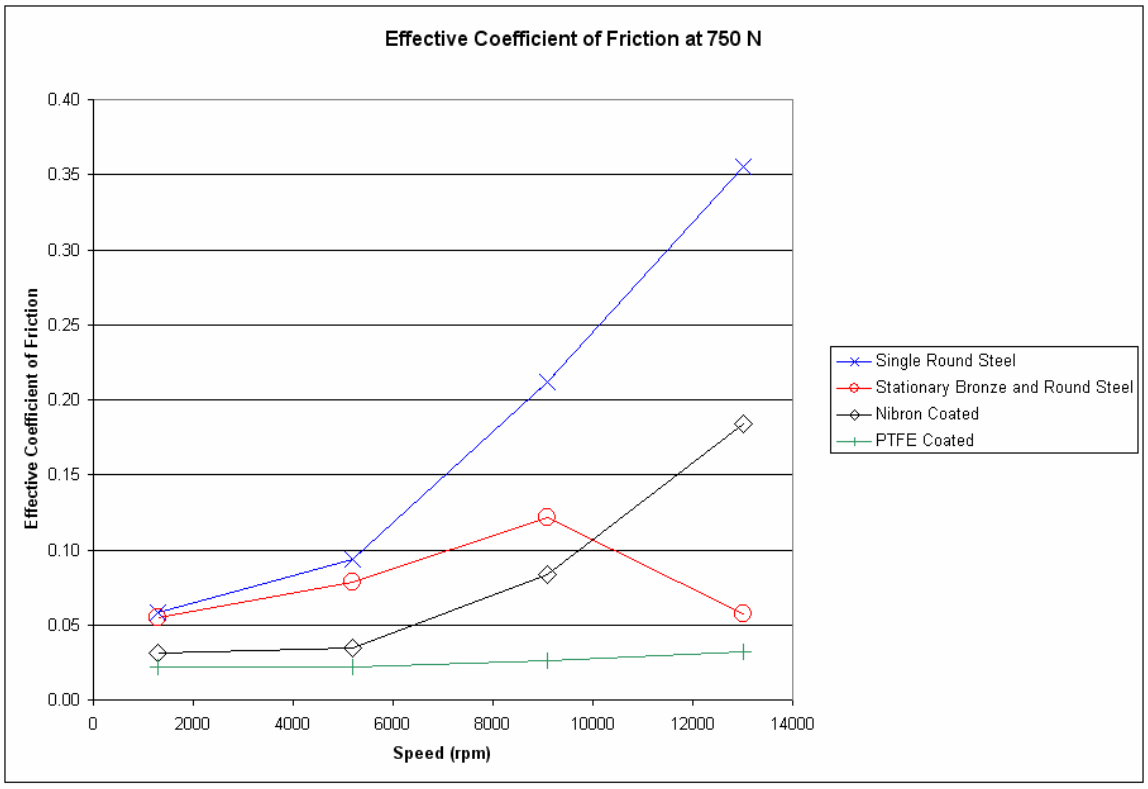

Figure 5.26: Effective coefficient of friction plotted as a function of speed and washer type.

In Figure 5.26, all the washer configurations show to have lower effective coefficients of friction than the reference single round steel washer. Again the PTFE out performs all other bearings at all speeds. At 13,000 rpm the stationary bronze performs better than the nibron coated bearing. The single round steel washer again appears to scuff at the highest speeds, whereas the bronze bearing and two coated bearings do not.

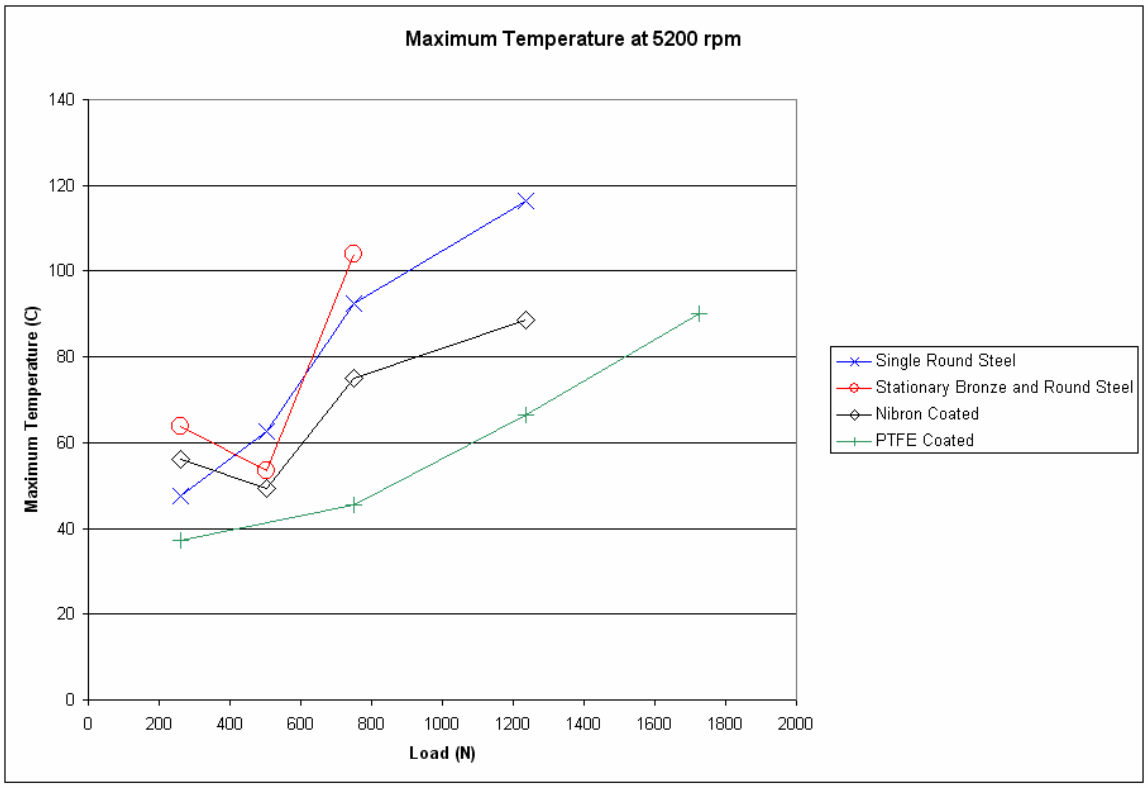

Figure 5.27: Maximum bearing temperature plotted as a function of load and washer type.

For the loads presented in Fig. 5.27 the PTFE coated bearing never reaches temperatures as high as the other bearings. Overall, the stationary bronze and single round steel produce the highest maximum temperatures. While the nibron coated bearing shows a slight improvement over the two uncoated bearings. For a varying speed instead of load in Fig. 5.28, the nibron coated bearing again only shows a slight improvement over the uncoated bearings. Again, the PTFE shows a much lower maximum temperature than the other bearings.

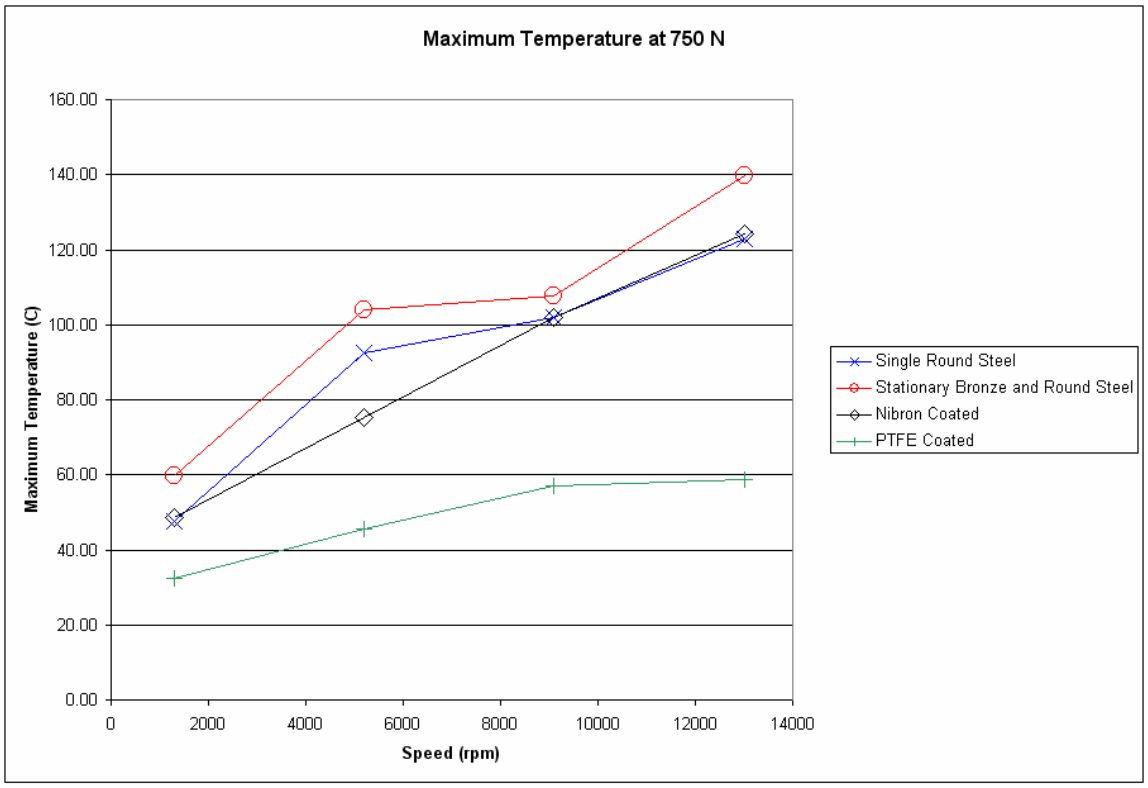

Figure 5.28: Maximum bearing temperature plotted as a function of speed and washer type.

Combined Results

For each washer configuration the average friction coefficient and average test duration are calculated (See Figs. 5.29 and 5.30). For loads and speeds that certain washer combinations were not tested at, a test duration of zero seconds was assigned. The washer combinations comprising of all steel components produced the largest average coefficients of friction. This is because like materials tend to bond at the asperity contacts and require larger shear forces to break apart. Adding bronze components decreased the average friction coefficient, and the single round bronze washer had the lowest. However, the coatings and especially the PTFE coating produced the lowest average coefficient of friction. Lower coefficients of friction to improve bearing

performance by generating less heat, although there are other factors involved as showed in Fig. 5.30 since the order of the washers changes.

Figure 5.30 plots the average test duration for each bearing configuration. In theory, bearings with longer average test durations should also have longer lives in the actual transmission. Clearly the PTFE coated washer performed much better than all washer combinations by having the longest average test duration. As with in Figure 5.29, the Nibron coated bearing performs second best behind the PTFE coated. From there on it appears that multiple washers have a slightly longer test duration than the other bearings. However, the differences between the two round steel, one round steel-one round bronze, and one round bronze appears to be insignificant.

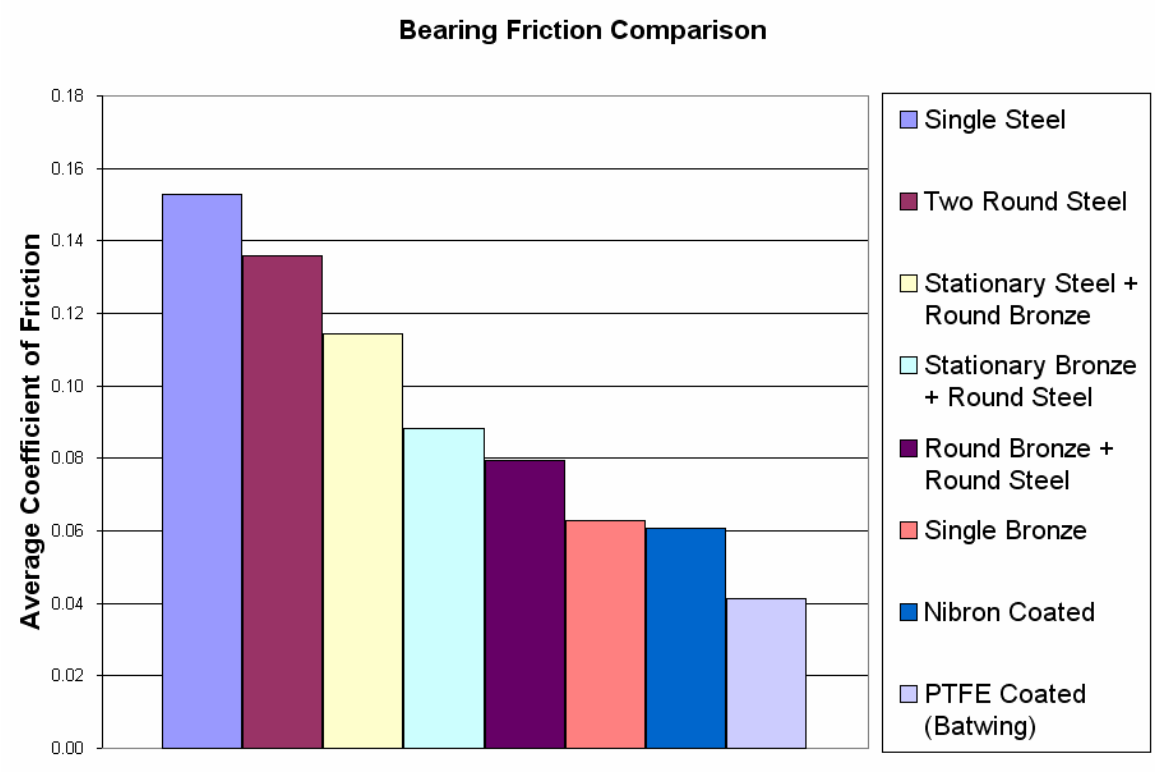

Figure 5.29: The average coefficient of friction for all tests conducted for each washer combination.

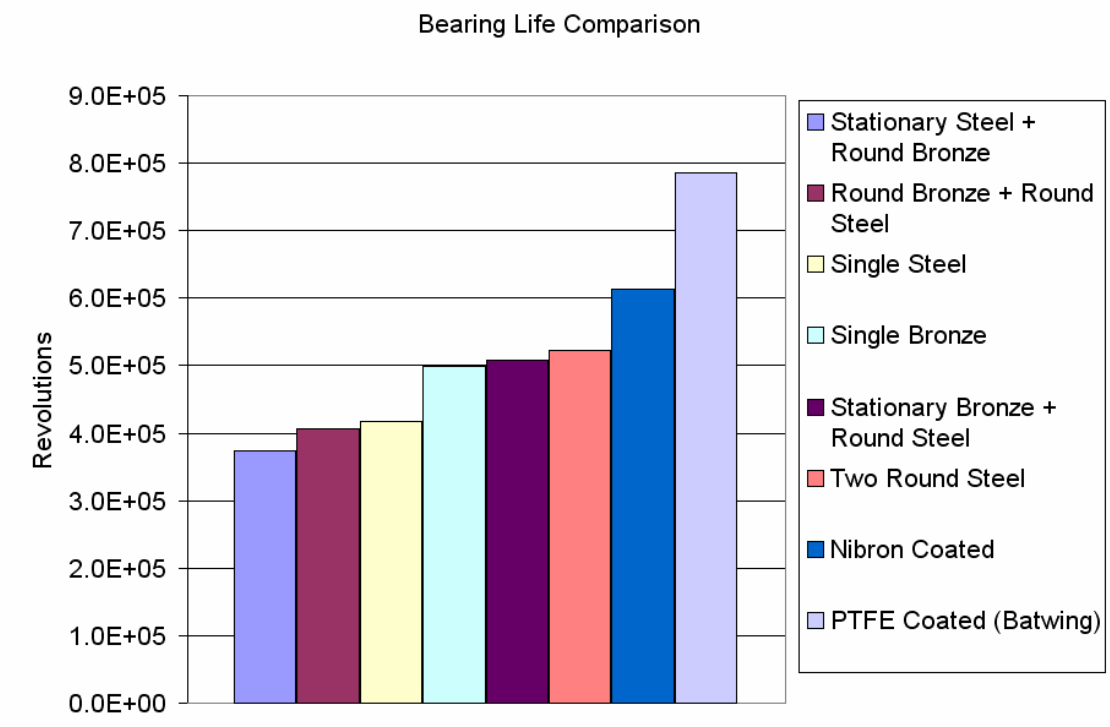

Figure 5.30: The average bearing test duration for each type of tested bearing configuration.

5.4 Conclusions

The experimental results show that at some loads and speeds the bearing operates with a near full hydrodynamic film. The bearing behavior can thus be characterized by the Stribeck curve. When the bearing is operating on the right side of the Stribeck curve the hydrodynamic lift is significant enough to separate the components with a fluid film. This decreases friction and extends the life of the bearing. If the bearing is operating on the left of the Stribeck curve, it has less hydrodynamic lift and is more likely to operate in the boundary lubrication regime. The bearing temperature increases with load and speed and will eventually cause the viscosity to decrease enough that the fluid film collapses (corresponding to the left side of the Stribeck curve). When the film collapses the

temperature and friction increase very quickly and cause the bearing to distress (thermoviscous distress). If the test is not stopped immediately, the bearing components may weld together and cause bearing lock-up. This sequence of events can be explained by thermoviscous distress and thermoelastic instability causing bearing distress and resulting in scuffing wear between the components. Besides the wear, these physical phenomena are captured in the numerical model (Chapter 4) and also result in the bearing distressing quickly and severely at certain loads and speeds.

The experimental results indicate that coatings can enhance overall bearing performance. It is believed that coatings enhance performance by decreasing friction and thus decreasing the heat generated. As discussed in previous chapters, by decreasing the generated heat, the physical mechanisms thermoelastic instability and thermoviscous distress are less likely to occur. Using bronze will decrease the friction between the bearings, although it may also decrease the life of the bearing. However, using multiple round washer configurations appears to not significantly benefit washer bearing performance. The best way to extend bearing life is by using a washer which has a very low friction coefficient with other components or by adding low friction coating.

Based on the numerical and experimental results, distress of the bearing is severe at certain loads and speeds due to what is believed to be a thermoelastic instability. To investigate the physical mechanism of thermoelastic instability in the bearing, Chapter 6 presents an analysis of experimental and analytical predictions to help confirm if the bearing operates in the range of thermoelastic instability.

In Chapter 7, the numerical and experimental results will be compared to see if the numerical model correctly captures the important trends. A correlation will be made

between the numerical and experimental results so that the numerical program may be applied to the design and testing of new thrust washer bearing configurations.

CHAPTER 6

THE THERMOELASTIC INSTABILITY OF THRUST WASHER BEARINGS

6.1 Introduction

The purpose of this chapter is to confirm that the physical phenomena of thermoelastic instability and thermoviscous distress occur in bearing operation. This is important because these phenomena are believed to be the root cause of bearing distress which can lead to severe wear and bearing lock-up. Thus, this chapter investigates the thermoelastic stability, thermoviscous distress and scuffing of thrust washer bearings using experimental data and existing analytical approximations. There is a considerable amount of work studying thermoelastic instabilities for various cases, although the thrust washer bearing case has been largely unaddressed until now. Before this work, the cause of severe distress in these bearings was unknown. Now it is believed to be caused by thermoelastic instabilities (TEI) and thermoviscous distress (TVD) in the bearing.

During the experimental tests, the thrust washer bearing often reaches a point of distress under certain loads and speeds (see Chapter 5). This point of distress is marked by a sudden increase in the effective coefficient of friction and the bearing temperature. While the bearing is in distress, material is often transferred between bearing surfaces and/or worn away. Under severe conditions the contacting surfaces can even weld together and cause the test rig to seize. Since this also occurs mostly at high speeds, it fits the definition of scuffing failure and wear as described in Williams (1998). At low

speeds wear does occur, but parts rarely weld together. Scuffing is the wear mode when the bearing is under distress, however, it is not the cause of distress. The fluid film protecting the surfaces must first collapse due to thermo-elastic instability and thermo-viscous distress for significant asperity contact and wear to occur.

Barber (1969) has documented the existence of TEI through the wear cycles it can induce. He states that the heat generation and expansion of a TEI is eventually slowed by the wear of material, allowing for other points of TEI to initiate, resulting in a new cycle to begin (see section 2.2 for a thorough discussion). Figure 6.1 shows samples of fluctuations in temperature due to what is believed to be thermoelastic wear cycles recorded from the current thrust washer bearing test rig. All of the plots in Fig. 6.1 are generated from test results from the single steel washer configuration. The results are for medium loads (505N-750N) and low to medium speeds (1300 rpm-5200rpm). These load ranges are on the 'edge' of bearing distress and maybe thermoelastically unstable, and only 'damped' by wear. Although other physical phenomena may cause the disturbances, because of the long cycles the cause is likely attributed to a thermoelastic wear cycle. Heat transfer and wear are typically much slower processes than other mechanisms. For instance, mechanical vibrations will most likely be at a much higher frequency than the cycles shown in Fig. 6.1. Significant amounts of wear were also observed to occur at these loads and speeds.

The plots in Fig. 6.1 are very similar to those that Barber recorded from a different test rig and a different geometry. It should also be observed that the amplitudes and periods of the thermoelastic wear cycles repeat very steadily. The period of the wear cycles in the current thrust washer bearing seem to be on the order of a few minutes. Fig

6.1(d) is for the highest load and speed shown of 505N and 5200rpm and also eventually distresses (as is suggested by the increasing temperature with each cycle).

The wear will cause the temperature to reduce and initiate thermoelastic wear cycles. However, at higher loads and speeds the instability may not recover, and temperature, friction and wear may continue to increase, bounded only by seizure of the contact. This description of distress correlates to that which occurs in the tested thrust washer bearings.

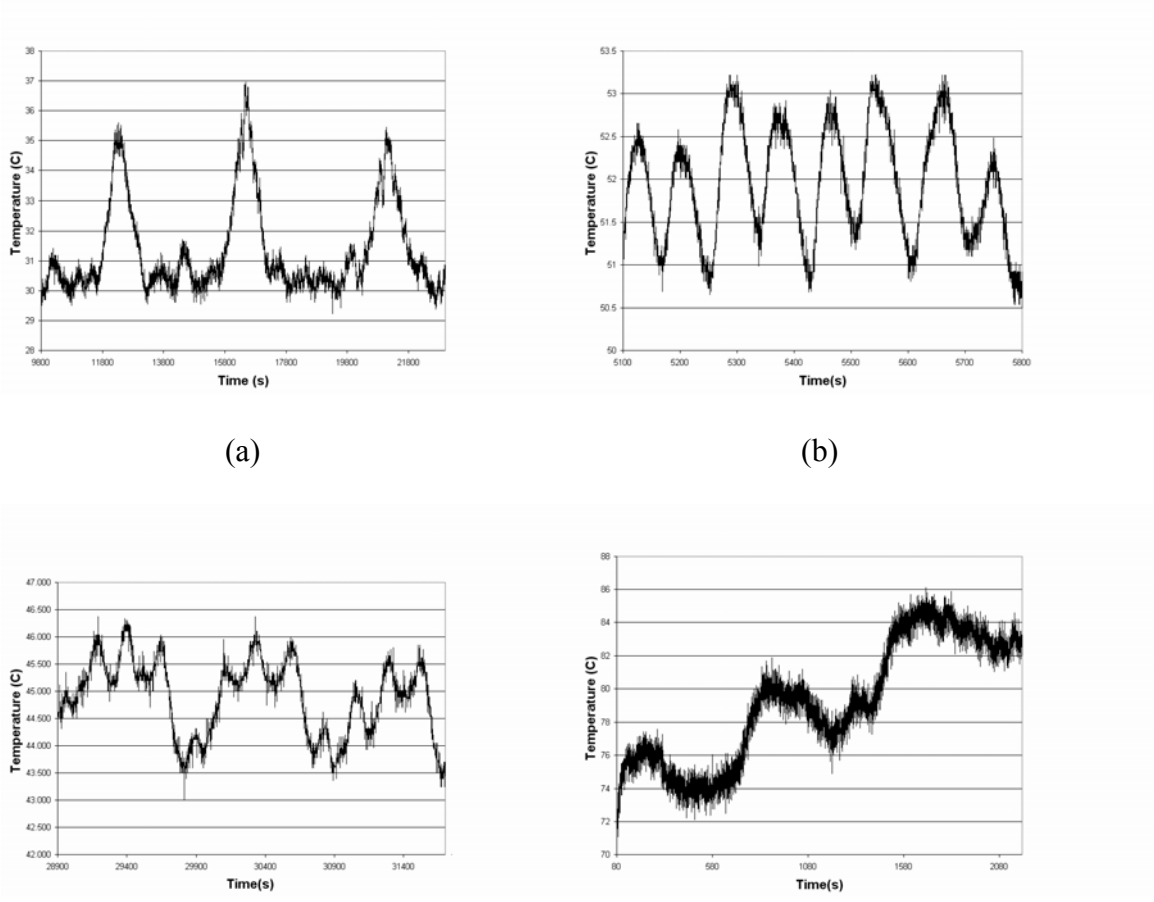

(a) (b)

(c) (d)

Figure 6.1: Examples of temperature fluctuations due to thermoelastic wear cycles for single steel washer bearing at (a) 505N, 1300 rpm (b) 505N, 5200 rpm (c) 750N, 1300 rpm and (d) 750N, 5300 rpm.

6.2 Modeling

There are many simple models which can calculate a threshold of thermoelastic stability for a given situation. The models complicate quickly however as more details, such as roughness, geometry and wear, are accounted for.

Banerjee and Burton (1976) derived a critical speed which defined the threshold of TEI. They modeled the surfaces as a 'good' thermal conductor sliding on a 'good' insulator. Although this may be a reasonable assumption for clutches which usually have layers of metal and a paper-like friction material, it is not a good assumption for thrust washer bearings. Banerjee and Burton's equation for the critical speed that marks the threshold of TEI is

$$U_{crit} = \bar{h}\kappa\sqrt{\frac{K}{\mu\alpha}} \tag{6.1}$$

where $\bar{h}$ is the nominal thickness, κ is the disturbance wave number, K is the thermal conductivity of the 'good' conductor, μ is the fluid viscosity, and α is the thermal expansion coefficient of the 'good' conductor. To use this equation a disturbance wavelength for the instability must also be assumed when calculating the critical speed. The washer circumference and thickness are used as the wavelength to calculate wave-number 1 and 2, respectively. By using these wave-numbers and typical material values for a steel thrust washer (see Table 4.2), the critical speeds are calculated using Equation 6.1. The predicted critical speed as a function of the normalized film thickness is shown in Fig. 6.2. Clearly, these two possible wavelengths produce very different predictions for the critical speed that TEI will initiate in the bearing. The predictions made by wave-

number 1 underestimates the speed at which TEI will occur, while the predictions made by wave-number 2 appear to over estimate this value. This model does not consider the complete geometry of the washers in making a prediction and so is probably not very useful, although it does suggest that the washer bearing performs well in the range of TEI.

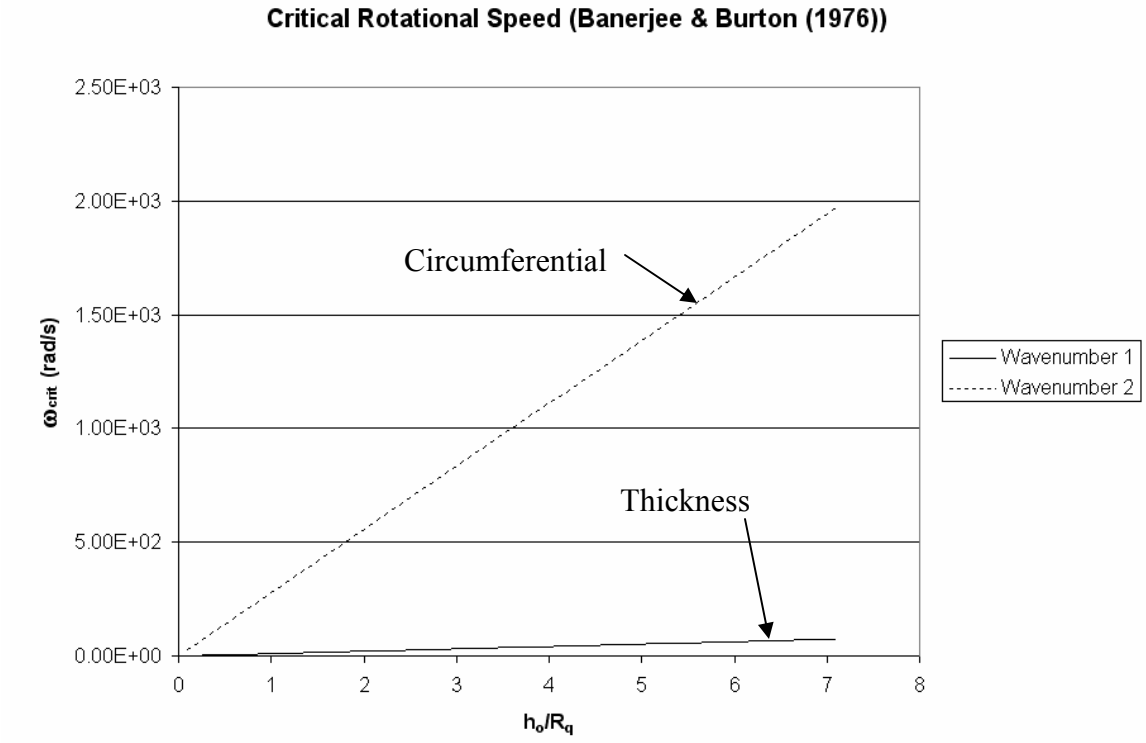

Figure 6.2: Prediction for the critical speed to case TEI in steel thrust washer bearings.

In 2002, Davis et al. (DKS) model TEI in thin disks and more specifically in mechanical clutches. The DKS model does not consider lubrication or the dampening effects of wear, although it does model a geometry that is very similar to thrust washer bearings. DKS deduce that the region of the thermoelastic instability is coupled between a critical bulk temperature (average bearing temperature) and operating speed (see Fig.

6.3). As the operating speed increases, the critical temperature required to cause the system to become unstable decreases. DKS also perform a parametric investigation into the effect of elastic modulus, thermal conductivity, and disk thickness, on the location of the thermoelastic stability threshold. Summarizing their results: Increases in elastic modulus, thermal conductivity, and disk thickness pushes the stability threshold to higher temperatures and speeds.

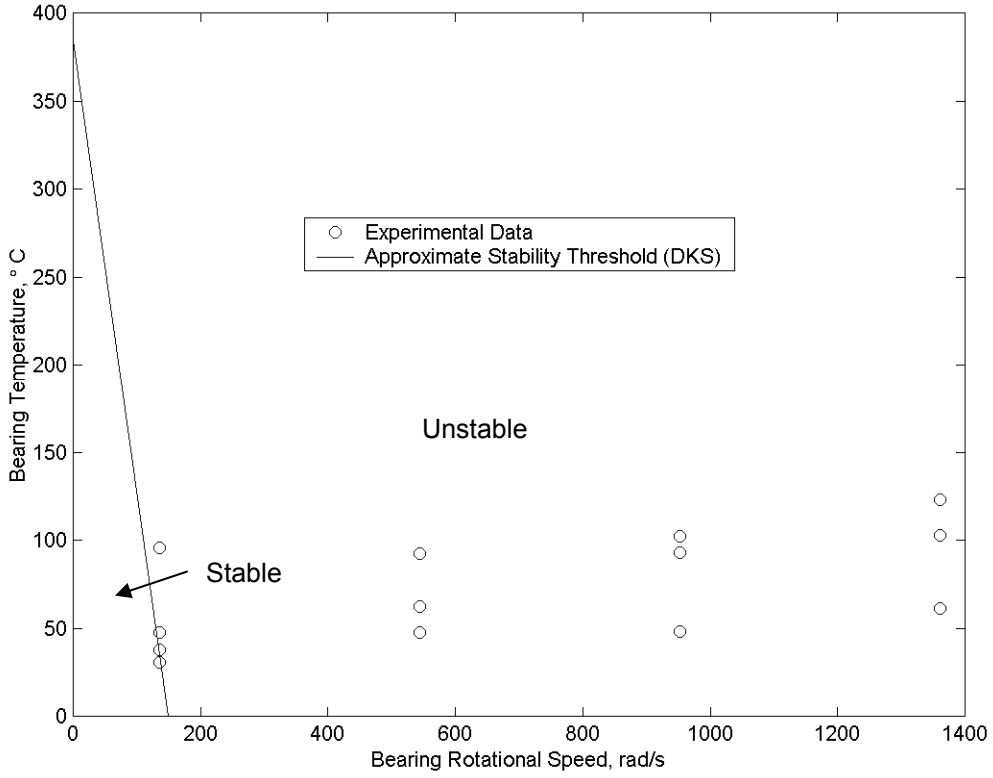

Figure 6.3: Comparison of DKS model predicted stability threshold and the location of the experimental data points for the average bearing temperature of a single steel washer combination.

In modeling the deformation of the disk, DKS make an analogy between thermal loading and mechanical loading. Axisymmetric temperature distributions are analogous to an axisymmetric axial load, while asymmetric temperatures are analogous to an

applied moment. The investigation considers these different loading conditions and thus different modes of thermal deflection. The important mode though is the mode which causes TEI at the lowest speed and temperature. Although created to model TEI in clutches, the results can also be used to simulate the similar geometry of thrust washer bearings. There are some differences between the DKS model and the current thrust washer bearing case: 1) DKS do not consider the effect of hydrodynamic lubrication, and 2) the effect of wear.

TEI threshold values for temperature and rotational speed were extracted from the DKS model for the current thrust washer bearing case. The critical bulk temperature at zero rotational speed, T_c, is approximated to be 360° C. The critical average bearing temperature is T_c plus the ambient temperature. The ambient temperature is taken to be 24° C. The critical operational speed at $T_c=0$ is approximated to be 149 rad/s. Using a straight line to connect these two boundary points results in the TEI threshold shown in Fig 6.3. Also plotted in Fig. 6.3 are sample data points for the average bearing temperature of a single round steel washer tested at loads ranging from 261N to1239N and the speeds shown in the plot. These are the same tests presented in Section 5.3.3. From this plot the conditions that the bearing was tested at seems very likely to be in the range of thermo-elastically instability. In reality, the thrust washer bearings probably have a higher stability threshold since wear and lubrication is not accounted for in this analysis.

Figure 6.4 shows the standard deviation of the experimentally recorded average bearing temperature for the same range of temperatures and speeds that are presented in Fig. 6.3. The progression of the bearing temperature standard deviation for the tests is

represented by the change from dark to light shading. A scale is given on the right to show how the shading quantifies the bearing temperature standard deviation. The standard deviation of the temperature increases as the bearing operates farther to the right of the plot (into the unstable region). This indicates that the instability is growing stronger and it is more difficult for wear to provide enough damping to contain the instability. At the high temperature standard deviations at the upper right of the graph, the bearing is distressing immediately, and the temperature increases suddenly.

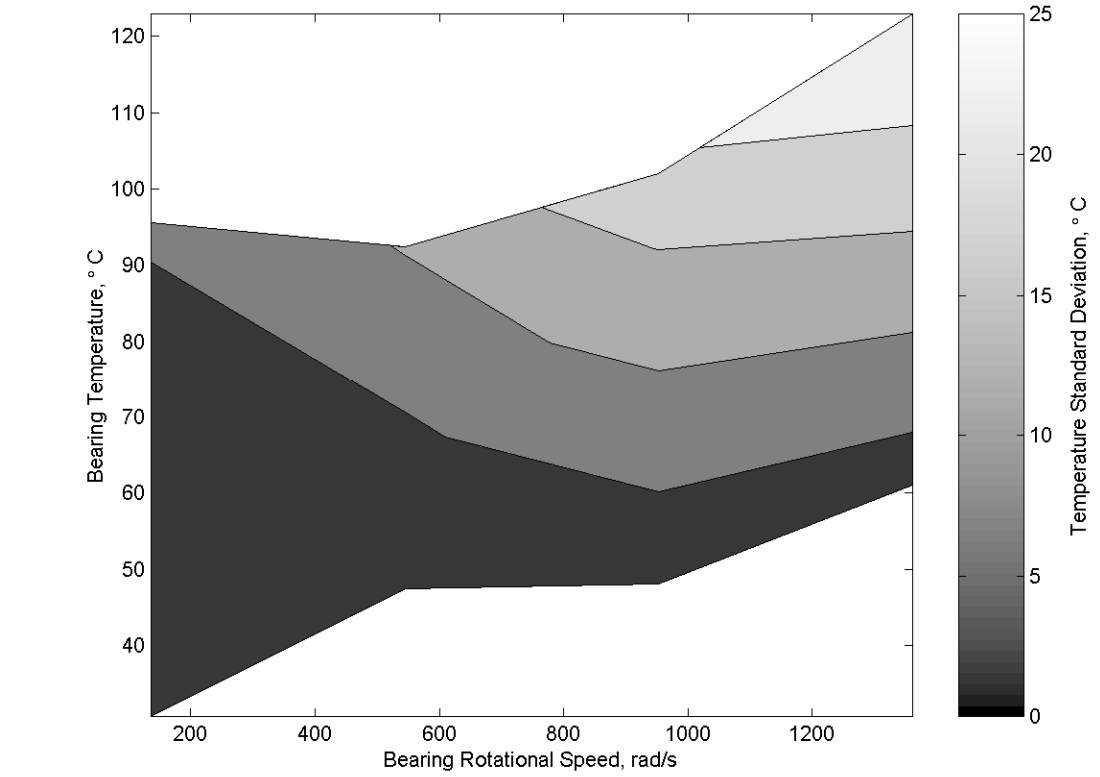

Figure 6.4: Standard deviation of bearing temperature in relation to rotational speed and average bearing temperature.

6.3 Scuffing Wear

The experimental results in Chapter 5 indicate that once the thrust washer bearing reaches a certain load and speed it will suddenly distress. These bearings, when under high loads and speeds, will sometimes effectively weld together. This suggests the occurrence of adhesive wear mechanisms, which is the cause of scuffing (Williams 1998). At these loads and speeds a vapor mist is often seen to exit the test rig, which encloses the bearing. This suggests that the local surface temperatures on the bearing surfaces are very high.

Bollani (1976) investigated the effect of lubricant additives, geometry, and speed on the occurrence of scuffing. Bollani found that scuffing was less likely to occur at low speeds. The same trends occur in the current thrust washer bearing investigation, as shown in the progression of washer distress in Figure 6.5. The washers shown are from the single round steel washer configuration constant load and speed tests described in section 5.3. By visual inspection of the washer wear progression shown in Fig. 6.5 it is seen that at high speeds the wear changes from an abrasive type of wear to scuffing. The scuffing depicted in Fig. 6.5 is so severe that the washer at the highest load and speed has adhered or welded to the contacting part behind it. While at a low load (260.9 N) and speed (1300 rpm) the washer wears very little, indicating that there is then probably a full film of lubrication separating the surfaces.

Load (N):	New	260.9	1239	1239
Speed (rpm):	New	1,300	1,300	13,000
Duration(cycles):	0	10^6	6,000	6,000

Figure 6.5: Visual comparison of thrust washer wear under different loading conditions.

In the work by Alzoubi et. al. (2001) and Section 5.5 the resistance of surfaces to scuffing can be increased by a low-friction coating, specifically amorphous carbon and PTFE. If thermal heating and the resulting thermal phenomena are the root cause of bearing distress, than it seems vary likely that a low-friction coating capable of decreasing the heat generated in dry sliding contact will improve bearing performance. By increasing resistance to thermoelastic instability and thermo-viscous distress, the coating is also increasing resistance to scuffing. The coating is also resistant to scuffing because it bonds less readily to the steel surface it rubs against. However, once the coating wears off, the washer is exposed to the same physical phenomena that distress uncoated washers.

6.4 Conclusions

Based on the experimental and numerical results, TEI appears to occur during the operation of thrust washer bearings at certain loads and speeds. Once a critical temperature is reached the thrust washer bearing may lose sufficient hydrodynamics lift due to TVD and increase susceptibility to TEI. Using the results the DKS model provides for a similar geometry of mechanical clutches, the thrust washer bearing appears

to operate well in the range of TEI. Once the film collapses due to TEI and TVD significant wear will occur due to scuffing between the surfaces. Experimental results show that by decreasing friction between the components, TEI and scuffing are less likely to occur. This can be accomplished by using a low friction coating on the bearing surfaces.

CHAPTER 7

COMPARATIVE ANALYSIS BETWEEN EXPERIMENTAL AND NUMERICAL RESULTS

To evaluate the effectiveness of the thrust washer bearing numerical model, a comparison is made between the experimental and the numerical results. Although the results are compared quantitatively and qualitatively, it is more important for the results to produce the same qualitative trends. Then, if the trends are similar they can be quantitatively adjusted from the numerical results to make predictions of actual bearing operation.

7.1 Single Round Steel Washer Results

First, the Stribeck curves generated numerically and experimentally for the case of a single round steel washer bearing configuration are compared in Fig. 7.1. This data is generated from loads ranging from 261N to1239N and speeds ranging from 1300 rpm to 13000 rpm. Qualitatively, the same traditional Stribeck curve is produced both numerical and experimentally. Quantitatively, the two curves are significantly different. In the hydrodynamic region on the right, the effective coefficient of friction predicted by the numerical simulation is much less than the experimental results. Also, the numerically and experimentally predicted critical points of the Stribeck curve, at the initiation of

mixed lubrication on the left side of the curve, are offset from each other. The numerical simulation makes a number of assumptions which may account for large differences between the numerical and experimental results. The most notable of these assumptions is that wear is not modeled or considered. In an actual bearing application wear will affect the performance in a number of different ways. Wear will alter the geometry and roughness of the bearing surfaces and dampen thermoelastic instabilities. Altering the geometry will affect the hydrodynamic lubrication and the friction between the surfaces, and thus has potential to cause large differences between the numerical and experimental results.

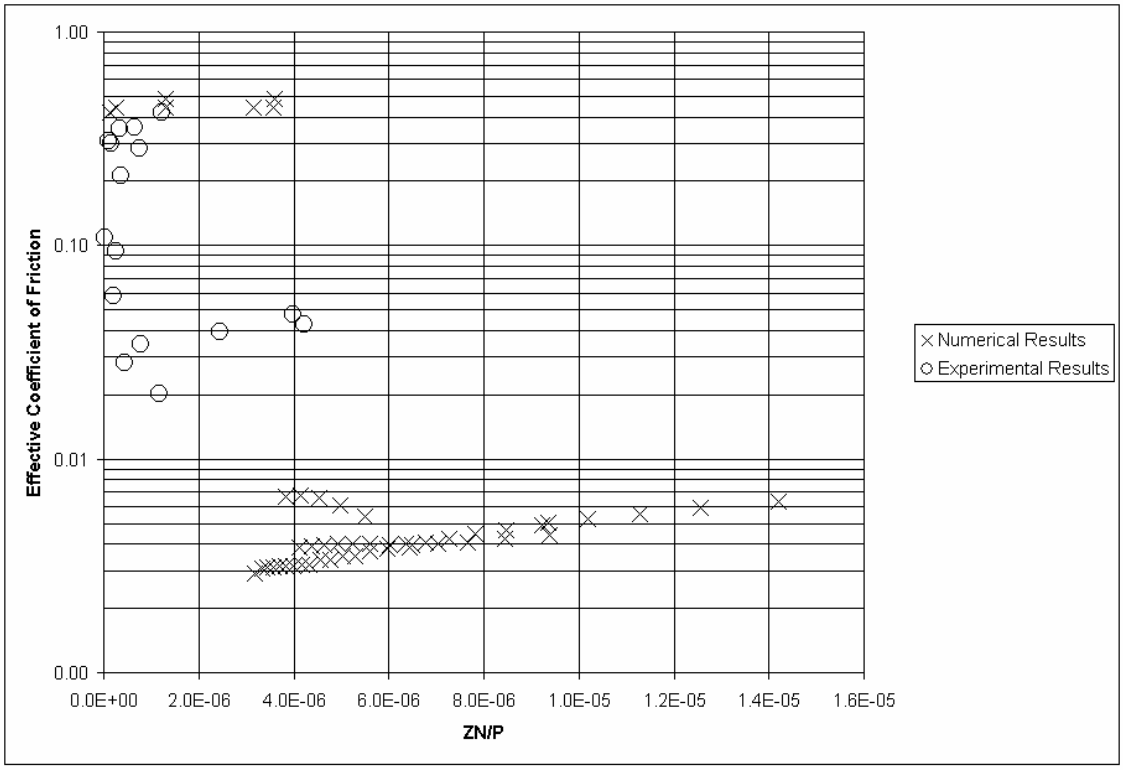

Figure 7.1: Numerically and experimentally generated Stribeck curves for a single steel washer bearing for loads ranging from 261N to1239N and speeds ranging from 1300rpm to 13000rpm.

Probably the most important prediction that can be made of bearing behavior is at what load and speed the bearing distresses. Due to the dramatic increase in friction and temperature when the bearing distresses it is fairly easy to use the numerical and experimental results to make predictions for bearing distress. Figure 7.2 presents the numerical and experimental predictions of this distress threshold for loads ranging from 261N to1728N and speeds ranging from 1300 rpm to 13000 rpm. The loads used in Figure 7.2 are the lowest loads predicted by the numerical and experimental results at which the bearing distresses as a function of rotational speed. The numerical and experimental predictions however will be different since the numerical code does not model certain mechanisms which affect washer bearing performance, such as chemical interactions at the surfaces, chemical breakdown of the lubricant, and wear. Since the numerical results do not consider this effect, the predicted threshold of distress should be lower for the numerical results than the experimental results.

The numerical simulation can also be run for cases without elastic deformation, during which thermo-elastic instabilities cannot occur. During these cases, thermo-viscous distress still occurs and can cause the fluid film to collapse. The results of this case should be similar to a hypothetical bearing that wears enough to dampen out any thermo-elastic instability. The neglected elastic deformation will also affect the hydrodynamic lift generated by the bearing, and in some cases enhance it [Cameron and Wood (1958), Brockwell, et. al. (1970), Heshmat (1987), Yu and Sadeghi (2001, 2002) and Kucinschi et. al. (2003)]. Since in reality wear of the bearing does occur, the actual distress of the bearing should occur at some point between the elastic and rigid case.

Figure 7.2 shows that as predicted the full numerical results predict distress to occur at loads much lower than the experimental results. However, when macro-deformation is neglected, the bearing can sustain much higher loads at the lowest speeds. This is because at the lowest speed the hydrodynamic pressures are not great enough to separate the films, but when the bearing is assumed rigid thermo-elastic instability does not occur and the heat generation alone is not enough to cause distress. This result is also seen experimentally because at low speeds the bearing often incurs significant amounts of wear and yet does not distress (see Fig. 6.5). In other words, at the low speeds wear is able to damp out the thermoelastic instability because the heat generated is not very large.

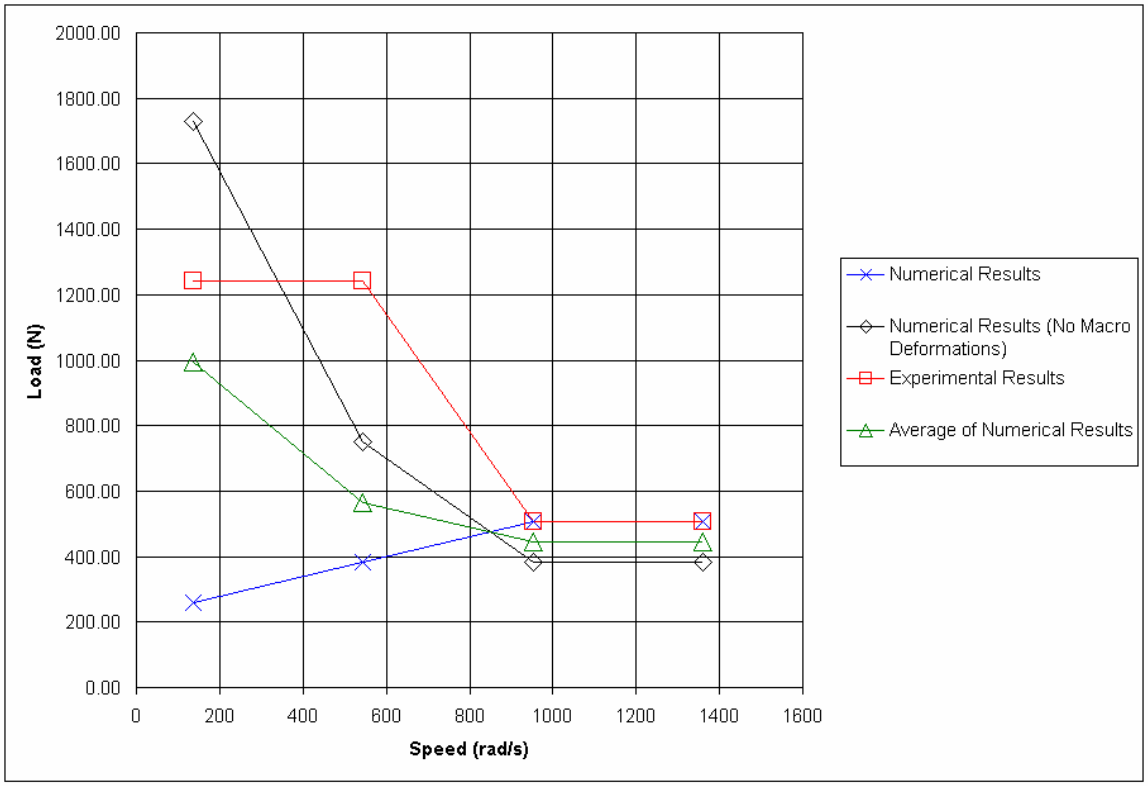

Figure 7.2: Comparison of predicted threshold of distress for a single round steel washer bearing by numerical and experimental methods as a function of load and speed.

Since the threshold of distress should occur somewhere between these two cases, the average of the two cases for each speed is calculated. This average of the numerical results is also plotted in Fig. 7.2. The average value appears to provide a conservative prediction of the threshold of bearing distress in comparison to the experimental results. At high speeds both numerical cases appear to converge on the experimental results. This is probably due to the distress initiating from thermo-viscous distress rather than thermo-elastic instability. At high speeds if significant asperity contact occurs thermo-elastic instability is very likely to initiate. Also, at high speeds the generated hydrodynamic lift is much greater and will separate the bearing components with a fluid film (and low friction). Thus, at high speeds the bearing will immediately distress when thermo-viscous distress occurs and the film collapses.

Not considered in the numerical simulation are imperfections in the washer geometry and material. The washers, gears and other bearing components will contain imperfections such as surface waviness, scratches, burrs, and material inconsistencies. It is difficult to predict what effect these imperfections will have on bearing performance, but by comparing the numerical and experimental results at least a prediction be made as to where the numerical model is most accurate and most deficient.

The results shown in Fig. 7.2 indicate that the numerical simulation can be cautiously used as a design tool for future thrust washer bearings and their implementation in mechanical devices such as transmissions. However, quantitatively the numerical results such as friction and temperature do not compare as well. This is evident in Fig. 7.3 which plots the effective coefficient of friction as predicted by the numerical and experimental results. The effective friction coefficient predicted by the

numerical results in the full film region is much lower than the experimental results. This is probably due to asperity contact which occurs in the experiment but not in the numerical simulation, possibly due to imperfections in the geometries of the bearing components. The discrepancies between the experimental and numerical predictions can be attributed to effects which the numerical simulation does not consider. The numerical simulation does not consider wear which will help dampen the thermo-viscous distress and thus the bearing distresses much earlier in the numerical simulation than in the experimental results. The numerical simulation neglects heat convection which may help dissipate heat from the bearing.

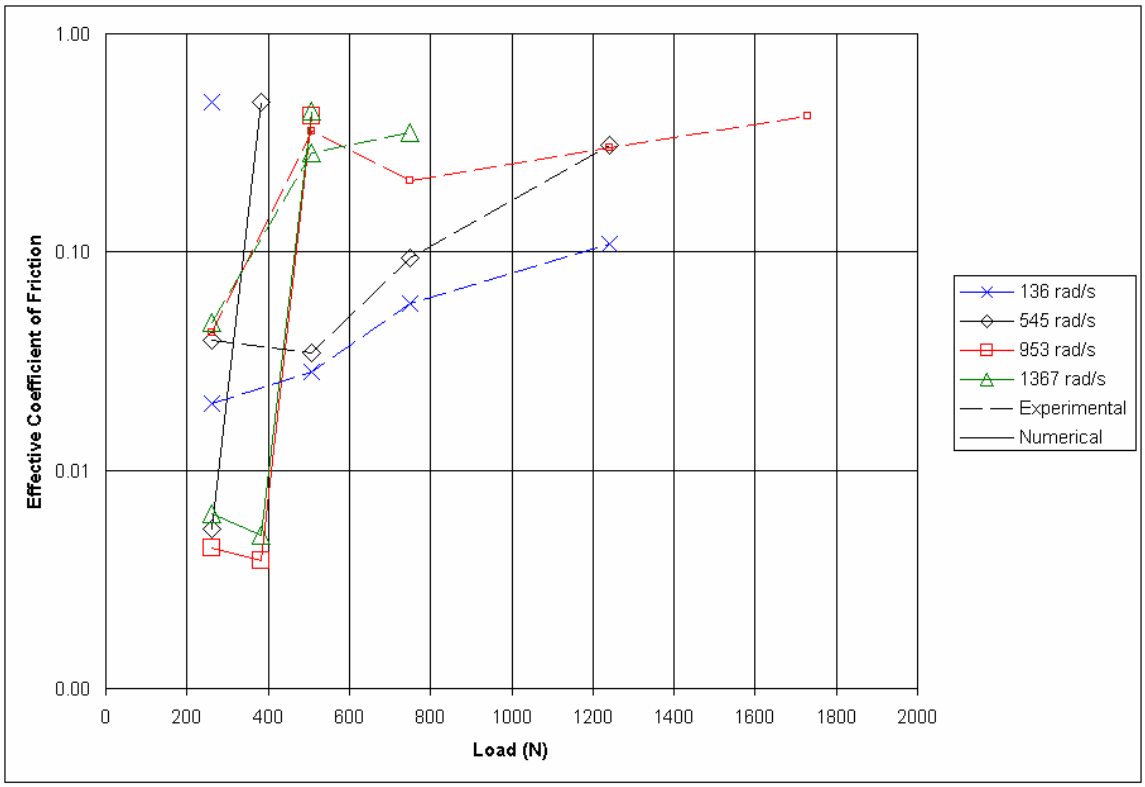

Figure 7.3: A comparison of the numerically and experimentally generated effective coefficient of friction as a function of load and speed.

7.2 Other Washer Configurations

The case of no washers was tested experimentally but discontinued due to severe distress occurring at the lowest tested loads and speeds. The numerical results also predict that the bearing without any washers will distress at loads and speeds much lower than bearings with round washers. As discussed in Section 4.11.2., the washers expand the bearing surface provided by the gear only. Thus the numerical and experimental results for the case of no washers, at least qualitatively, agree and will not be discussed further.

One Round Bronze Washer

The same comparison of the numerical and experimental predictions for the threshold of distress is made for the single round bronze washer bearing configuration (see Fig. 7.4). The numerical results considering and neglecting macro-scale deformation are again averaged to make a prediction which crudely accounts for wear. As with the single steel round washer the averaged numerical results make a fairly conservative approximation of the threshold of distress. However, there is a large difference in the predictions at the highest speed at which the numerical results would incorrectly predict an improvement in bearing performance. The numerical model predicts that at the high speed the hydrodynamic lift is great enough to allow the bearing to carry heavy loads. The difference between the experimental and numerical results may thus be due to the numerical model predicting more lift than occurs in the experiment. In the experiment, wear may occur at the beginning of a test when the speed is being ramped up. This wear

could alter the geometry enough to hinder the generation of hydrodynamic lift, which is not accounted for in the numerical model.

The numerical results also show an interesting trend because as speed increases the distress load increases then decreases and finally increases again. There are number of competing effects considered in the numerical code which can account for this trend. For instance, at some loads and speeds deformation of the washer may increase hydrodynamic lift, while for other conditions the deformation may cause the bearing to be thermoelastically unstable.

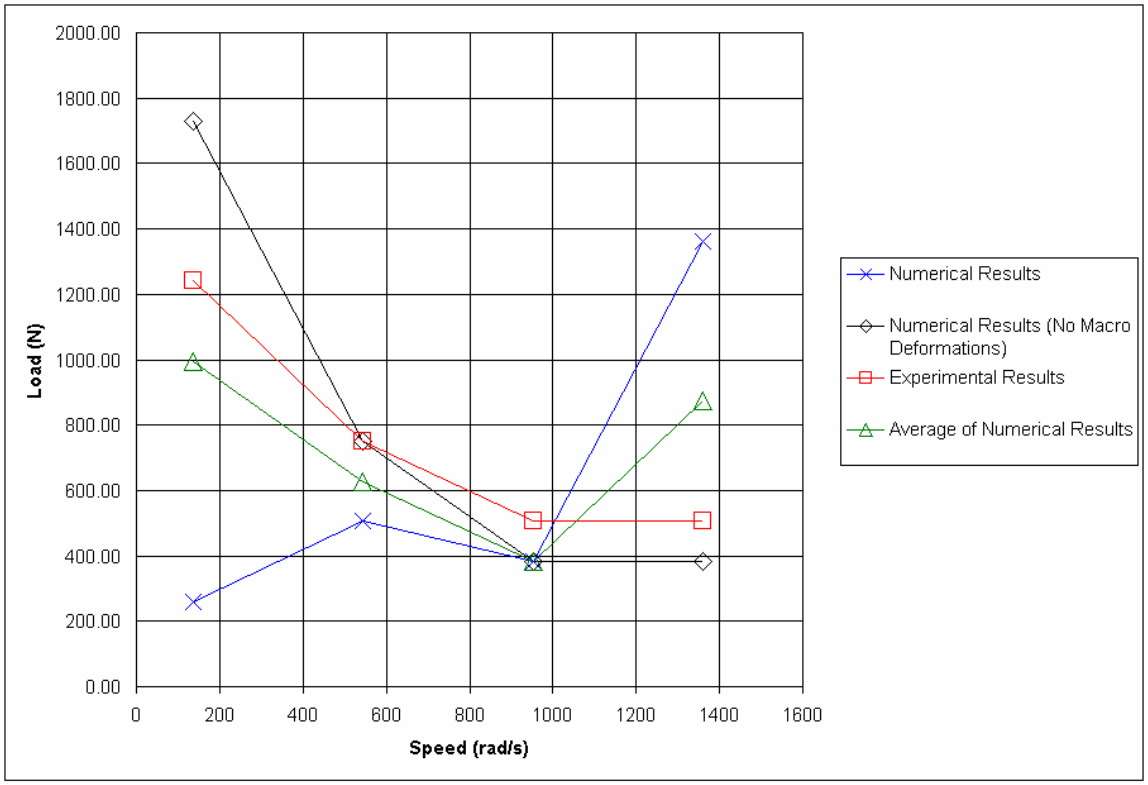

Figure 7.4: Comparison of predicted threshold of single round bronze washer bearing distress by numerical and experimental methods.

Two Round Steel Washers

For the case of two round steel washers the numerical results drastically underestimate the experimentally predicted threshold of bearing distress (see Fig. 7.5). This is most likely due to the numerical model making several assumptions which actually have a large effect on bearing performance. The numerical model predicts that thermoelastic instability will occur at very low loads for the double steel washer configuration when in the experimental results wear may for low loads and speeds effectively damp out the instability.

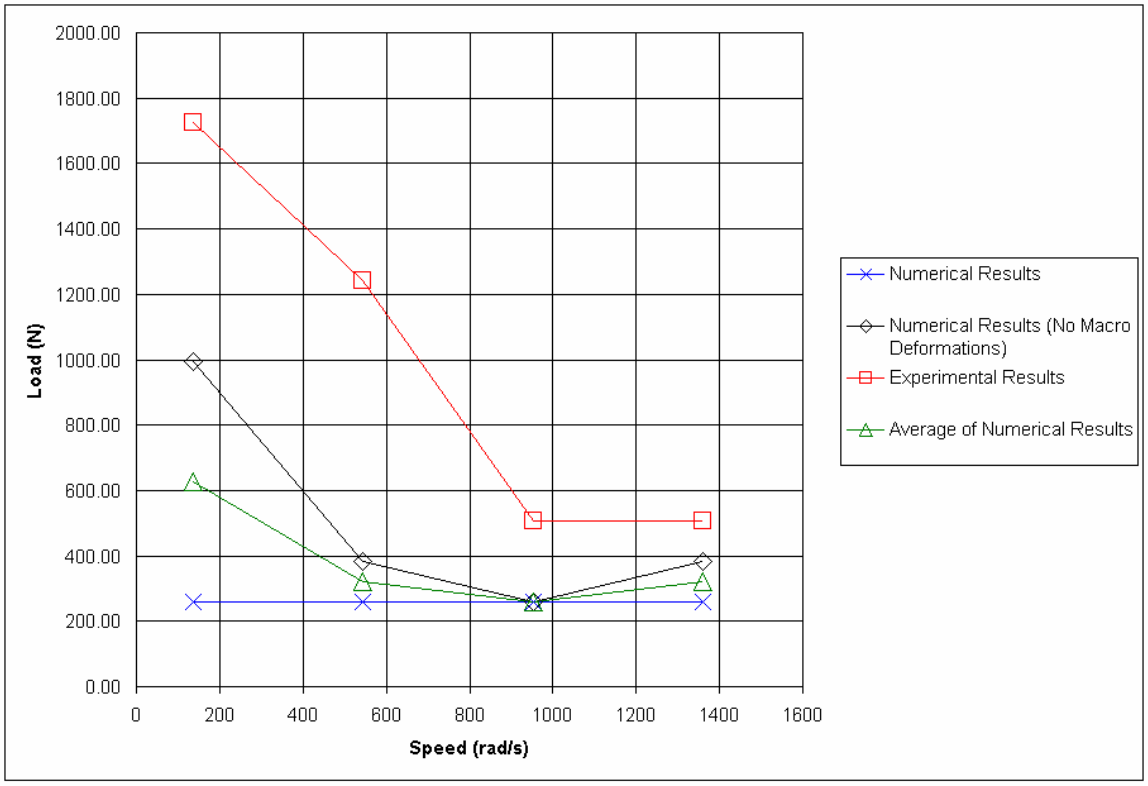

Figure 7.5: Comparison of predicted threshold of the double round steel washer bearing distress by numerical and experimental methods.

7.3 Comparison of Washer Rankings

The numerical and experimental results for the threshold of bearing distress are used to rank the performance of the different bearing configurations. The numerical and experimental predictions of the threshold load at which the bearing initially distresses is averaged for all speeds. These average values are then used to rank bearings according to the numerical and experimental results. Notably, the numerical predictions in the right column do not match the experimental results. However, it should be noted that both the numerical and experimental results picked the case of no washers to be the worst case and the low friction coated washers to be the best case. The disagreement is probably due to several of the assumptions which the numerical model makes. The most significant of these is that the numerical model neglects wear in its calculations. The assumption in the numerical model that the relative speed cannot transfer from one surface to another may also have an effect. Experimentally, if one surface of the washer bearing distresses and locks up, another surface can still function and essentially give the bearing a second chance. Due to this phenomena, adding more washers may actually increase the bearing life. This phenomena is not represented in the numerical code.

Table 7.1: Ranking of bearings based on Numerical and Experimental Results (Ranking given after value)

	Experimentally Determined Average Distress Load (N)	Numerically Determined Average Distress Load (N)
Single Round Steel	873 (2)	612 (3)
Single Round Bronze	750 (4)	719 (2)
Two Round Steel	994 (1)	383 (5)
Stationary Bronze and Round Steel	872 (3)	1040 (1)
Round Bronze and Round Steel	689 (5)	505 (4)

7.4 Conclusion

The numerical model does make conservative estimates of the threshold of bearing distress for most conditions. However, the numerical model does not consistently predict which bearings will perform best experimentally. The numerical model does agree with the experimental results and predict that the case of no washers performs the worst and that the low friction PTFE coated bearings perform the best. The discrepancies between the numerical and experimental results is most likely due to some of the assumptions that the numerical model makes, such as neglecting wear. Caution should thus be taken when using the numerical model as a design tool for future bearings. The numerical model does provide a strong foundation upon which to build improved models of thrust washer bearings and other similar tribological devices.

The numerical model does qualitatively predict some of the important physical mechanisms which govern bearing behavior. For instance, the numerical model predicts that the bearing will distress at a certain load and speed due to thermoelastic instability and thermoviscous distress. This is a significant achievement in itself, because it reveals what causes bearing distress and points toward solutions which can help solve the problem, such as using a low friction coating like PTFE.

The numerical model also predicts that the thrust washer bearing will follow the Stribeck curve. The numerical and experimental results both indicate that the bearing will operate in the full film regime for high Stribeck values, and in the mixed and boundary lubrication regime for lower values. An ideally designed thrust bearing will operate in the full film lubrication regime on the right of the Stribeck curve. If the bearing operates in the region it will have little wear and low friction.

Since there should be no wear and contact in the full film regime (on the right side of the Stribeck curve), then the numerical and experimental friction coefficient should be more likely to agree. However, this is not the case. The experimental results predict an effective friction coefficient that is higher on the right side of the Stribeck curve than the numerical results. There are a number of possibilities which may explain this: (1) Contact is occurring due to imperfections in the washer surface such as 'very high' asperity peaks that are not accounted for in the numerical model. (2) Waviness in the washers affects the lubrication and contact between the bearing surfaces. (3) Wear occurring during start-up (before the bearing reaches the full-film regime) changes the bearing geometry. (4) Vibrations in the test rig causes the bearing surfaces to contact periodically, despite sufficient hydrodynamic lift. It seems very likely that vibrations and

imperfections of the bearing geometry could cause contact to occur even when the hydrodynamic lift might be sufficient to provide a full-film of lubrication for ideal conditions. Ball bearing rotation, meshing of the gear teeth, and the excitation of the inherent natural frequencies of the system may account for such vibrations occurring in the test rig.

CHAPTER 8

CLOSURE

8.1 Conclusions

This thesis performs an experimental and numerical investigation of the physical phenomena that govern and distress thrust washer bearings. The numerical model incorporates the coupled physical effects of lubrication, heat generation, macro-scale deformation, and elasto-plastic asperity contact into a quasi steady-state prediction of thrust washer bearing operation. These coupled effects are solved simultaneously by using the Newton-Raphson technique to solve the set of non-linear equations they produce.

For use in the numerical investigation, an elasto-plastic asperity contact model is generated by considering the case of a single elastic-perfectly plastic hemisphere in contact with a rigid flat. A comparison is also made with other existing models. The results indicate that the FEM results for the contact area agree closely at small interferences with the trends of the elastic Hertzian solution. While at large interferences the FEM predicts contact areas that surpass Abbot and Firestone's fully plastic model (1933) (that is based upon truncation). The ZMC model is found to differ significantly from the FEM results, where the KE model (which is also based on FEM results) follows more closely, although it

still does not capture the varying hardness trend. An empirical formulation for the contact area is also fitted to the FEM data as a function of the material properties and interference. The new elasto-plastic hemispherical contact model is used in a statistical formulation to simulate contact between two rough surfaces with Gaussian height distributions. This asperity contact model is incorporated into the numerical model of the thrust washer bearing.

In both the numerical and experimental results some common trends emerge. Both the numerical and experimental results predict that the bearing follows the traditional Stribeck curve that is often used to describe the performance of hydrodynamic bearings at various combinations of load and speed. That the results fit the curve suggest that at high Stribeck values a full film of lubrication will form between the bearing faces and protect them from wear. However, at low Stribeck values the bearing will operate in a mixed lubrication or boundary lubrication regime, at which the load is carried by the fluid pressure and asperity contact. The occurrence of asperity contact between the surfaces results in a significant increase in wear and friction.

The numerical results indicate that maintaining a nearly full film of lubrication ($h_{min}/\sigma>3$) will significantly reduce the bearings susceptibility to thermo-elastic instability and thermo-viscous distress. This is because the effective coefficient of friction is much lower (and the heat generated much less) for surfaces separated by a fluid film than those with significant asperity contact. At a minimum film thickness, h_{min}, below three times the RMS roughness and at high speeds, significant amounts of heat are generated. The heat causes the temperature to rise. The rise in temperature can then cause the viscosity to decrease and initiate thermo-viscous distress. The increase in

temperature can then cause thermal expansion and result in thermo-elastic instability. These mechanisms result in a viscous cycle which causes the bearing fluid film to collapse. In the test rig this occurrence results in severe scuffing wear and often bearing lock-up.

Due to thermo-elastic instability and thermo-viscous distress the bearing can reach load and speed combinations which cause a sudden collapse of any generated hydrodynamic film and a drastic increase in temperature. In the numerical simulation the temperature can become unstable and increase without bounds, while in the experimental test rig, either the bearing will eventually wear enough to stabilize the temperature or it will seize. When the film collapses at high speeds, scuffing wear occurs which can cause the surfaces to weld together. The distress of the bearing can thus be severe, especially at high speeds.

Since the causes of bearing distress are predominately thermally generated, certain steps may be taken in the design process to decrease these effects. Numerical and experimental results show that a low friction coating such as PTFE is very effective at alleviating the problem. Having a similar, but less profound effect is using a bronze washer. The coefficient of friction between bronze and steel is less than steel on steel, yet bronze is softer than steel and wears away more easily. Numerical results also indicate that increasing thermal conductance away from the thrust washers will also improve performance.

Numerical results show that a single steel washer benefits bearing performance more than two washers or no washers. The single washer performs well because it increases the surface area of bearing face, thus increasing hydrodynamic lift and thermal

heat dissipation. However, the thin washers are also less thermo-elastically stable and tend to destabilize the system. For this reason the numerical simulation indicates that the use of two washers causes the system to be very unstable, and not add a significant amount of hydrodynamic load carrying capacity to overcome this. However, adding washers has another effect which may benefit actual bearing performance by adding 'extra' bearing surfaces which can activate when another bearing surface has distressed and locked-up. Such an affect is not considered in the numerical simulation. Also the dampening effect wear has on thermoelastic instabilities is not considered.

The numerical and experimental predictions for the load and speed which cause bearing distress are compared. Although the numerical simulation predicts a conservative estimate of the load which will cause bearing distress, it does not consistently predict which bearings perform best in the experimental results. These differences are probably due to the assumptions made in the numerical model. The most significant of these assumptions is believed to be the neglecting of wear. The numerical model is still very comprehensive compared to past models of similar tribological systems and thus provides a strong foundation for future models. A future version of the model will most likely be expanded upon to consider wear. At the current time there does not exist a robust wear model for such use.

8.2 Future Work

This work finds that the thrust washer bearing behavior is thermo-elastically unstable for certain cases. The thermoelastic instability is a time variant process and

should be modeled as such. For this reason a transient model of the thrust washer bearing may map better the effects of thermal mechanisms on bearing behavior. In addition, an in depth model of the instability threshold should be constructed. Such a model will help better define a clear distress criterion for thrust washer bearings. Perhaps eventually the dampening effects of wear could also be considered in the model.

Currently, additional coating and surface texturing technologies are being experimentally investigated. This work suggests that these approaches will lead to improved thrust washer bearing designs.

The characterization of friction and contact between rough surfaces, which was advanced by the elasto-plastic hemispherical contact results presented in Chapter 4, still requires extensive work. There is substantial room for work into such areas as the effect of asperity shape on contact, sliding contact, and the wear of contacting asperities. Probably the most significant advancement that could bring thrust washer bearing modeling closer to reality would be the inclusion of wear. Wear occurs often during washer bearing operation (and in the contact between most surfaces) and will alter the surface geometry and roughness of the surfaces. These changes then affect contact and lubrication between the surfaces. The current numerical model provides a good foundation upon which to build models of tribological systems which do consider wear and other mechanisms.

APPENDIX A

CRITICAL INTERFERENCE

The Hertz solution results in the following equations for stress within the deformed sphere along the axis of revolution, z (Johnson, [20]):

$$\sigma_1 = -p_o\left(1+\left(\frac{z}{a}\right)^2\right)^{-1} \tag{A1}$$

$$\sigma_{2,3} = p_o\left\{\left[2\left(1+\left(\frac{z}{a}\right)^2\right)\right]^{-1} - (1+\nu)\left[1-\frac{z}{a}\tan^{-1}\left(\frac{a}{z}\right)\right]\right\} \tag{A2}$$

where the origin of the z-axis lies at the point of initial contact between the hemisphere and the rigid flat, and p_o is the maximum contact pressure.

The von Mises yield criterion is given as:

$$S_y = \sqrt{\frac{1}{2}\left[(\sigma_1-\sigma_2)^2+(\sigma_2-\sigma_3)^2+(\sigma_3-\sigma_1)^2\right]} \tag{A3}$$

By substituting the principal stresses given in Eq. (A1) and Eq. (A2) into Eq. (A3) and then simplifying, the following equation for the von Mises yield criterion is obtained:

$$\frac{S_y}{p_o} = \frac{3}{2}\left(1+\left(\frac{z}{a}\right)^2\right)^{-1} - (1+\nu)\left[1-\frac{z}{a}\tan^{-1}\left(\frac{a}{z}\right)\right] \tag{A4}$$

The resulting Eq. (A4), which must be positive, dictates where within the hemisphere initial yielding occurs. This is obtained by setting the derivative with respect to z to zero. Hence,

$$\frac{d}{dz}\left(\frac{S_y}{p_o}\right) = -az\left[a^2(4+\nu)+(1+\nu)z^2\right]+(1+\nu)\left(a^2+z^2\right)^2\left[\tan^{-1}\left(\frac{a}{z}\right)\right]=0 \qquad \text{(A5)}$$

This equation is solved numerically for Poisson's ratios between 0.01 and 0.50 to find the locations, z, at initial yielding. These locations are then substituted in Eq. (A4) to find the applied maximum contact pressure to yield strength ratio, p_{oc}/S_y. This ratio, p_{oc}/S_y, is referred to as the yield strength coefficient and designated by the symbol C. An empirical function is fitted to the final numerical data, which is given by:

$$\frac{p_{oc}}{S_y} = C = 1.295\exp(0.736\nu) \qquad \text{(A6)}$$

Equation (A6) differs from the numerical solution by an average of 1.2% and by no more than 3.1%.

The interference, ω, is given as a function of p_o by the Hertz elastic solution in Johnson [20] as:

$$\omega = \left(\frac{\pi \cdot p_o}{2E'}\right)^2 R \qquad \text{(A7)}$$

Thus, to find the critical interference, or the interference at the initial point of yielding, the maximum pressure when yielding first occurs, p_{oc}, is substituted into Eq. (A7) for p_o. This maximum pressure is the pressure given by the maximum contact to yield strength ratio given in Eq. (A6). The equation $p_{oc}=CS_y$ is substituted into Eq. (A7), resulting in the Eq. (3.1).

A similar derivation is also given in Chang (1986). However, that derivation assumed a fixed value between strength and hardness, $S_y=0.35H$, which resulted in an equation for the hardness coefficient, $K = 0.454 + 0.41\,\nu$. Such an assumption is not made in this work (see discussion on H_G within).

APPENDIX B

NORMALIZATION OF DISPLACEMENT

It is important to find an effective method of normalization for the surface displacements so that the presented results may be applied to a general hemispherical contact with a radius R and material properties E, ν, and S_y. The vertical displacement U_y is effectively normalized by ω_c, which is the relative distance that the contact point at the centerline travels before and after loading is applied at the onset of plasticity (Figs. 12(b), 13(b)). A similar typical distance in the radial direction, γ_c, is sought for normalizing U_x. The quantity a_c identifies the radius of the contact at the onset of plasticity. To find out the distance that this point travels radially, its location before loading, a_{co}, is sought such that $\gamma_c = a_c - a_{co}$. Finding this quantity results in the normalization

$$\frac{U_x}{\gamma_c} = \frac{U_x}{a_c - a_{oc}} \tag{B1}$$

By assuming no slip occurs between the hemisphere and the rigid flat, a_{co} is easily approximated. As shown in Fig. B1 the hemisphere surface essentially wraps onto the rigid surface. This results in the arc $\overset{\frown}{AB}$ deforming into the segment $\overline{A'B'}$, such that $\overline{A'B'} = \overset{\frown}{AB}$. And since $\overline{A'B'} = a_c$, $\overset{\frown}{AB} = a_c$. The angle θ is then calculated as

$$\theta = \frac{\widehat{AB}}{R} = \frac{a_c}{R} \tag{B2}$$

Next, a_{co} is calculated to be

$$a_{co} = R\sin(\theta) = R\sin\left(\frac{a_c}{R}\right) \tag{B3}$$

Substituting Eq. (3.30) into Eq. (B3) and simplifying results in

$$a_{co} = R\sin\left(\frac{\sqrt{\omega_c R}}{R}\right) = R\sin\left(\sqrt{\frac{\omega_c}{R}}\right) \tag{B4}$$

Now γ_c is defined by

$$\begin{aligned} \gamma_c &= a_c - a_{co} = a_c - R\sin\left(\sqrt{\frac{\omega_c}{R}}\right) \\ \gamma_c &= \sqrt{\omega_c R} - R\sin\left(\sqrt{\frac{\omega_c}{R}}\right) \end{aligned} \tag{B5}$$

Then factoring out R from the right side of the Eq. (B5) gives

$$\gamma_c = R\left[\sqrt{\frac{\omega_c}{R}} - \sin\left(\sqrt{\frac{\omega_c}{R}}\right)\right] \tag{B6}$$

Letting $x = \sqrt{\frac{\omega_c}{R}}$ and using the approximation

$$\sin x = x - \frac{x^3}{3!} + \frac{x^5}{5!} - \frac{x^7}{7!} + \ldots \tag{B7}$$

results in

$$x - \sin x \approx \frac{x^3}{3!} \tag{B8}$$

after neglecting higher order terms. Then, Eq. (B6) is approximated using Eq. (B8).

$$\gamma_c \approx R\left[\frac{1}{6}\left(\frac{\omega_c}{R}\right)^{\frac{3}{2}}\right] = \frac{1}{6}\frac{(\omega_c)^{\frac{3}{2}}}{\sqrt{R}} \tag{B9}$$

Equation (B9) is tried as an effective normalization of U_x by γ_c. The results of steel and aluminum hemispheres loaded and unloaded from $\omega^* = 135$ are presented in Figs. 3.26 and 3.27. It appears from the plots that the normalizations derived are effective at generalizing the problem for the two different sets of material properties. The ratio of γ_c/ω_c is also presented in Table 3.7 for both materials. For both materials the value of γ_c is much smaller than ω_c.

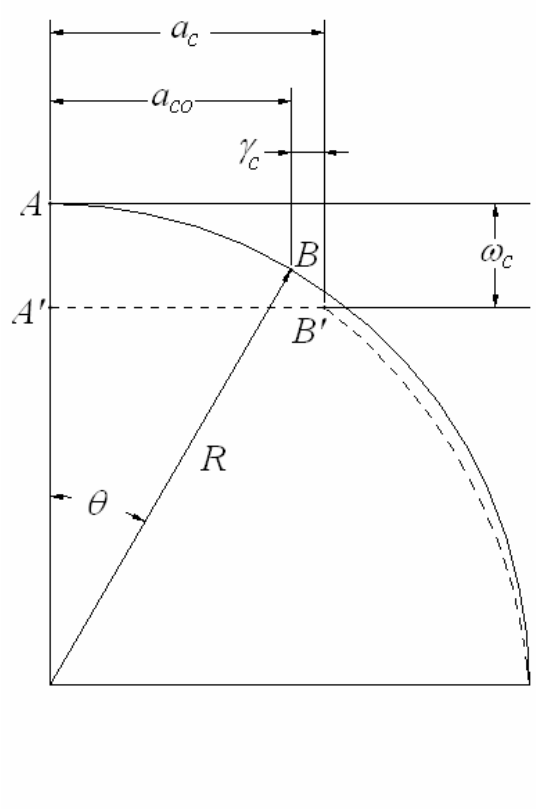

Figure B1: Schematic for the approximation of the location of the critical contact radius before loading (solid line) and after loading (dashed line).

APPENDIX C

DERIVATION OF THE COEFFICIENT OF FRICTION FOR AN AXISYMMETRIC GEOMETRY AND AN EVENLY DISTRIBUTED LOAD

For an annulus of inner radius, r_o, and outer radius, r_i, an infinitesimally small portion of the bearing surface has an area dA. The normal force on the surface is then given by the formula:

$$dN=PdA \tag{C1}$$

where P is the evenly distributed pressure and dN is the normal force. The friction force , dF, applied to the area is then given by

$$dF=f_{eff}dN \tag{C2}$$

where f_{eff} is the effective coefficient of friction. The frictional torque applied to the annulus at any point can then be calculated by the equation

$$dT_{fricf}=rdF \tag{C3}$$

where dT_{frict} is the frictional torque applied and r is the distance from the annulus rotational axis to any point. Then by substituting equations C1 and C2 and the relation $dA = drd\theta$ into Eq. C3 the following is obtained

$$dT_{frict} = rf_{eff}Prdrd\theta \tag{C4}$$

The pressure, P, is easily calculated by dividing the total load on the annulus by the area of the annulus or

$$P = F_a/[\pi(r_o^2 - r_i^2)] \tag{C5}$$

Next equation A4 is integrated to get T_{frict}, the frictional torque, as follows

$$T_{frict} = \int_{r_i}^{r_o}\int_{0}^{2\pi} r^2 f_{eff} P drd\theta = 2\pi f \cdot P(r_o^3 - r_i^3) \tag{C6}$$

Now substituting in equation C5 for P provides

$$T_{frict} = \frac{2}{3} f_{eff} F_a \frac{r_o^3 - r_i^3}{r_o^2 - r_i^2} \tag{C7}$$

Then solving for f_{eff}, Equation C8 is obtained

$$f_{eff} = \frac{3}{2} \cdot \frac{T_{frict}(r_o^2 - r_i^2)}{F_a(r_o^3 - r_i^3)} \tag{C8}$$

APPENDIX D

DATA ACQUISITION DEVICE PARAMETERS

Data Acquisition Board

Resolution: 16 bit

Thermocouple Module

Amplification Factor: 0.206211 V/mV

Zero: -3.378 mV

Thermocouples

Type: T

Sensitivity: 0.043 mV/°C

Range: -100 to 400°C

Error: +/-1.0°C

Frictional Torque Source (From Motor Power Output)

Accuracy: +/-0.4 Nm

References

Abbott, E. J., and Firestone, F. A., 1933, "Specifying Surface Quality-A Method Based on Accurate Measurement and Comparison," *Mech. Engr.*, 55, pp. 569-572.

Abdel-Latif, L. A., Safar, Z., Peeken, H., 1985, "Centrifugal Effects on the Thermohydrodynamic Peformance of Circular Pad Thrust Bearings," *Wear,* Vol.101, pp. 99-105.

Abdel-Latif, L. A., Peeken, H., Benner, J., 1985, "Thermohydrodynamic Analysis of Thrust-Bearing With Circular Pads Running on Bubbly Oil," *Journal of Tribology,* Vol.107, pp. 527-537.

Anderson, A. E., Knapp, R. A., 1990, "Hot Spotting in Automotive Friction Systems," *Wear*, 135, pp. 319-337.

Bair, S., Winer, W.O., 1989, "Tribological Characteristics of Needle Bearings," Proc. Leeds-Lyon Symposium.

Banerjee, B. N., Burton, R. A., 1976, "An Instability for Parallel Sliding of Solid Surfaces Separated by a Viscous Liquid Film," *ASME J. Lubr. Technol.*, 98, pp. 157-166.

Barber, J. R., 1967, "The Influence of Thermal Expansion on the Friction and Wear Process," *Wear*, 10, pp. 155-159.

Barber, J. R., 1969, "Thermoelastic instabilities in the sliding of conforming solids," *Proc. Roy. Soc. A.,* 312, pp. 381-394.

Barber, J. R., Ciavarella, M., 2000, "Contact Mechanics," *Int. J. Solids Struct*., 37, pp. 29-43.

Beer, G., 2001, *Programming the Boundary Element Method*, John Wiley and Sons, Inc., New York.

Bethlehem Steel Corporation, 1967, Modern Steels and Their Properties, Bethlehem Steel Corporation.

Bollani, G., 1976, "Failure Criteria in Thin Film Lubrication with Ep Additives," *Wear*, 36, pp. 19-23.

Burton, R. A., Nerlikar, V., Kilaparti, S. R., 1973, "Thermoelastic Instability in a Seal-like Configuration," *Wear*, 24, pp. 177 188.

Cameron, A., Wood, W. L., 1958, "Parallel Surface Thrust Bearing", *ASLE Trans*., 1, pp. 254-258.

Chang, W. R., 1986, "Contact, Adhesion, and Static Friction of Metallic Rough Surfaces," PhD Thesis, University of California, Berkeley, pp.18-23.

Chang, W. R., Etsion, I., and Bogy, D. B., 1987, "An Elastic-Plastic Model for the Contact of Rough Surfaces," *ASME J. Tribol.*, 109, pp.257-263.

Change, W. R., Etsion, I., Bogy, D., B., 1988, "Static Friction Coefficient Model for Metallic Rough Surfaces," *ASME J. Tribol.*, 110, pp. 57-63.

Czichos, H., 1976, "Failure Criteria in Thin Film Lubrication – Investigation of the Different Stages of Film Failure," *Wear*, 35, pp. 13-17.

Davis, C. L., Krousgrill, C. M., Sadeghi, F., 2002, "Effect of Temperature on Thermoelastic Instability in Thin Disks," *ASME J. Tribol.*, 124, pp.429-437.

Decuzzi, P., Ciaverella, M., Monno, G., 2001, "Frictionally Excited Thermoelastic Instability in Multi-Disk Clotches and Brakes," *ASME J. Tribol.*, 123, pp.865-871.

Dow, T. A., 1980, "Thermoelastic Effects In a Thin Sliding Seal- A Review," *Wear*, 59, pp. 31-52.

Dow, T. A., Burton, R. A., 1972, "Thermoelastic Instability of Sliding Contact in the Absence of Wear," *Wear*, 19, pp.315-328.

Dow, T. A., Burton, R. A., 1973, "The Role of Wear in the Initiation of Thermoelastic Instabilities of Rubbing Contact," *ASME J. Lub. Technol.*, 95, pp.71-75.

Dowling, N. E., 1993, Mechanical Behavior of Materials, Prentice-Hall, Inc., Englewood Cliffs, New Jersey.

Etsion, I., Amit, M., 1993, "The Effect of Small Normal Loads on the Static Friction Coefficient for Very Smooth Surfaces," *ASME J. Tribol.*, 115, pp. 406-410.

Etsion, I. and Front, I., 1994, "Model for Static Sealing Performances of End Face Seals," *Trib. Tr*ans., 37, 1, pp.111-119.

Faulkner, A., Arnell, R.D.,2000, "The Development of a Finite Element Model to Simulate the Sliding Interaction Between Two, Three-dimensional, Elasto-plastic, Hemispherical Asperities," *Wear*, 242, pp. 114-122.

Fohl, J., Uetz., H., 1976, "Failure Criteria in Thin Film Lubrication – Influence of Temperature on Seizing, Wear and Reaction Layer Formation," *Wear*, 36, pp. 25-32.

Francis, H. A., 1976, "Phenomenological Analysis of Plastic Spherical Indentation," *ASME J. Eng. Mater. Technol.*, 98, pp.272-281.

Front, I., 1990, “The Effects of Closing Force and Surface Roughness on Leakage in Radial Face Seals,” MS Thesis, Technion, Israel Institute of Technology.

Giannakopoulos, A. E., Larsson, P. L., Vestergaard, R., 1994, “Analysis of Vickers Indentation,” *Int. J. Solid. Struct.*, 31, pp. 2679-2708.

Goodier, J. N., Hodge, P. G., 1958, Elasticity and Plasticity, Wiley & Sons, Inc., New York.

Green, I., 2002, “A Transient Dynamic Analysis of Mechanical Seals Including Asperity Contact and Face Deformation,” *Trib. Trans*., 45, 3, pp.284-293.

Greenwood, J. A., Williamson, J. B. P. 1966, “Contact of Nominally Flat Surfaces,” *Proc. R. Soc. Lond. A*, 295, pp. 300-319.

Greenwood, J. A., Tripp, J. H., 1971, “The Contact of Two Nominally Flat Rough Surfaces,” *Proc. Instn. Mech. Engrs. 185*, pp. 625-633.

Hayward, A. T. J., 1961, “The Viscosity of Bubbly Oil,” National Engineering Laboratory, Glasgow, U.K., Fluids Report No. 99.

Hess, D. P. and Soom, A., 1992, “Normal and Angular Motions at Rough Planar Contacts During Sliding with Friction,” *ASME. J. Tribol.*, 114, 3, pp. 567-578.

Hess, D. P. and Soom, A., 1993, “Effects of Relative Angular Motions on Friction at Rough Planar Contacts,” *ASME. J. Tribol.*, 115, 3, pp. 96-101.

Jackson, R. L., Green, I., A Finite Element Study of Elasto-plastic Hemispherical Contact, *Proc. of the 2003 ASME/STLE International Tribology Conference, Preprint 2003-TRIB102*.

Jacq, C., Nelias, D., Lormand, G., Girodin, D., 2003, “Development of a Three-Dimensional Semi-Analytical Elastic-Plastic Contact Code,” *ASME J. Tribol.*, 125, pp.653-667.

Jang, J. Y., Khonsari, M. M., 1999, “Thermoelastic Instability Including Surface Roughness Effects,” *ASME J. Tribol*., 121, pp. 648-654.

Jang, J. Y., Khonsari, M. M., 2000, “Thermoelastic Instability With Consideration of Surface Roughness and Hydrodynamic Lubrication,” *ASME J. Tribol*., 122, pp. 725-732.

Jang, J. Y., Khonsari, M. M., 2002, “On the Formation of Hot Spots in Wet Clutch Systems,” *ASME J. Tribol*., 124, pp. 336-345.

Jang, J. Y., Khonsari, M. M., 2004, “On the Growth Rate of Thermoelastic Instability,” *ASME J. Tribol*., 126, pp. 50-55.

Johnson, K. L., 1968, “An Experimental Determination of the Contact Stresses Between Plastically Deformed Cylinders and Spheres,” Engineering Plasticity, Cambridge University Press, Cambridge, pp. 341-361

Johnson, K. L., 1985, Contact Mechanics, Cambridge University Press, Cambridge.

Johnson, R. R., Dow, T. A., Zhang Y. Y., 1988, “Thermoelastic Instability in Elliptic Contact Between Two Sliding Surfaces,” *ASME J. Tribol*., 110, pp. 80-86.

.

Kazama, T., Yamaguchi, A., 1993, “Application of a Mixed Lubrication Model for Hydrostatic Thrust Bearings of Hydraulic Equipment,” *ASME J. Tribol.*, 115, pp. 686-691.

Kennedy, F. E., Chuah, C. K., Brote, F. O. W., 1985, “Thermomechanical Contact Phenomena in Face Seals,” *Wear*, 102, pp. 127-140.

Kogut, L., & Etsion, I., 2002, “Elastic-Plastic Contact Analysis of a Sphere and a Rigid Flat,” *J. of Applied Mechanics, Trans. ASME*, 69(5), pp. 657-662.

Kogut, L., Etsion, I., 2003, “A Semi-Analytical Solution for the Sliding Inception of a Spherical Contact,” *ASME J. Tribol,* 125(3), pp. 499-506.

Kral, E. R., Komvopoulos, K., Bogy, D. B., 1993, “Elastic-Plastic Finite Element Analysis of Repeated Indentation of a Half-Space by a Rigid Sphere,” *ASME J. Appl. Mech.*, 60, pp. 829-841.

Kral, E. R., Komvopoulos, K., Bogy, D. B., 1995a, “Finite Element Analysis of Repeated Indentation of an Elastic-Plastic Layered Medium by a Rigid Sphere, Part I: Surface Results,” *ASME J. Appl. Mech.*, 62, pp. 20-28.

Kral, E. R., Komvopoulos, K., Bogy, D. B., 1995b, “Finite Element Analysis of Repeated Indentation of an Elastic-Plastic Layered Medium by a Rigid Sphere, Part II: Subsurface Results,” *ASME J. Appl. Mech.*, 62, pp. 29-42.

Kucinschi, B. R., DeWitt, K. J., and Pascovici, M. D., 2003, “Thermoelastohydrodynamic (TEHD) Analysis of a Grooved Thrust Washer,” *Proc. of the 2003 ASME/STLE International Tribology Conference, Preprint 2003-TRIB180*.

Lebeck, A. O., 1976, “Theory of Thermoelastic Instability of Rotating Rings in Sliding Contact with Wear,” *ASME J. Lubr*. Technol., 98, pp.277-285.

Lee, K., Barber, J. R., 1993, “Frictionally Excited Thermoelastic Instability in Automotive Disk Brakes,” *ASME J. Tribol*., 115, pp.607-614.

Lee, K., Barber, J. R., 1994, "An Experimental Investigation of Frictionally-Excited Thermoelastic Instability in Automotive Disk Brakes Under a Drag Brake Application," *ASME J. Tribol*., 116, pp.409-414.

Lee, S. C. and Cheng, H. S., 1992, "On the Relation of Load to Average Gap in the Contact Between Surfaces with Longitudinal Roughness," *Trib. Trans*., 35, 3, pp. 523-529.

Lee, S. C. and Ren, N., 1996, "Behavior of Elastic-Plastic Rough Surface Contacts as Affected by Surface Topography, Load, and Material Hardness*," Trib. Trans*., 39, 1, pp 67-74.

Liu, G., Wang, G. J., and Lin, C., 1999, "A Survey of Current Models for Simulating the Contact between Rough Surfaces," *Tribol. Trans.,* 42, pp.581-591.

Liu, Z., Neville, A. and Reuben, R. L., 2000, "Analytical Solution for Elastic and Elastic-plastic Contact Models," *Trib. Trans.,* 43, 4, pp. 627-634.

Maksimov, I. L., 1988, "Thermal Instability of Sliding and Oscillations Due to Frictional Heating Effect," *ASME J. Tribol*., 110, pp.69-72.

McClintock, R., 1974, "A Laboratory Study of Automatic Transmission Thrust Washer Wear," *SAE Prepr.*, paper 740050.

McCool, J. I., 1986, "Comparison of Models for the Contact of Rough Surfaces," *Wear*, Vol. 107, pp. 37-60.

Mesarovic, S. D. and Fleck, N. A., 2000, "Frictionless Indentation of Dissimilar Elastic-plastic Spheres," *Int. J. Solids and Structures*, 37, pp.7071-7091.

Nikolajsen, J. L., 1999a, "Viscosity and Density Models for Aerated Oil in Fluid-Film Bearings," *Trib. Trans*., 42, 1, pp. 186-191.

Nikolajsen, J. L., 1999b, "The Effect of Aerated Oil on the Load Capacity of a Plain Journal Bearing," *Trib. Trans*., 42, 1, pp. 58-62.

Nuri, K. A., and Halling, J., 1975, "The Normal Approach between Rough Flat Surfaces in Contact," *We*
Vol. 154, pp. 115-124.

Oliver, W. C., Pharr, G. M., 1992, "An improved technique for determining hardness and elastic modulus using load and displacement sensing indentation," *J. Mater. Res.,* Vol. 7, No.6, pp. 1564-1583.

Patir, N., Cheng, H. S., 1978, "An Average Flow Model for Determining Effects of Three-Dimensional Roughness on Partial Hydrodynamic Lubrication," *ASME J. Tribol*., 100, pp.12-17.

Patir, N., Cheng, H. S., 1979, "Application of Average Flow Model to Lubrication Between Rough Sliding Surfaces," *ASME J. Tribol*., 101, pp.220-230.

Polycarpou, A. A. and Etsion, I., 1999, "Analytical Approximations in Modeling Contacting Rough Surfaces," *ASME. J. Tribol.,* 121, 2, pp. 234-239.

Reddy, J. N., 1993, An Introduction to the Finite Element Method, 2nd Ed., Mcgraw-Hill, New York.

Ren, N. and Lee, S. C., 1993, "Contact Simulation of Three-Dimesnional Rough Surfaces Using Moving Grid Method," *ASME J. Tribol.,* 115, 4, pp. 597-601.

Ren, N. and Lee, S. C., 1994, "The Effects of Surface Roughness and Topography on the Contact Behaviors of Elastic Bodies," *ASME J. Tribol*., 116, 4, pp. 804-811.

Roy Chowdhury, S. K., Ghosh, P., 1994, "Adhesion and Adhesional Friction at the Contact Between Solids," *Wear,* 174, pp. 9-19.

Ruan, B., Salant, R., and Green, I., 1997, "A Mixed Lubrication Model of Liquid/Gas Mechanical Face Seals," STLE Tribology Transactions, Vol. 40, No. 4, pp. 647-657.

Salomon, G., 1976, "Failure Criteria in Thin Film Lubrication – The IRG Program," *Wear*, 36, pp. 1-6.

Shamim, A., Kettleborough, C. F., 1994, "Tribological Performance Evaluation of Oil Mist Lubrication," *Transactions of ASME,* Vol.116, pp.224-231.

Shigley, J. E., Mischke, C. R., 1989, Mechanical Engineering Design*,* 5th Edition, McGraw-Hill Inc., New York.

Streator, J. L., 2003, "Dynamic Contact of a Rigid Sphere With an Elastic Half-Space: A Numerical Simulation," *ASME J. Tribol.*, 125, pp.25-32.

Tabor, D., 1951, The Hardness of Materials, Clarendon Press, Oxford.

Taniguchi, S., Ettles, C., 1975, "A Thermo-Elastic Analysis of the Parallel Surface Thrust Washer," *ASLE Trans*., 18, 4, pp. 299-305.

Tian, H., Saka, N., 1991, "Finite element analysis of an elastic-plastic two-layer half-space: normal contact," Wear, 148, pp.47-68.

Timoshenko, S., and Goodier, J. N., 1951, Theory of Elasticity, New York, McGraw-Hill.

Ulezelski, J. C., Evans, D. G., Haka, R.J., Malloy, J. D., 1983, "Needle Bearing Axial

Thrust Study," *SAE Technical Paper Series*, 830568.

Vu-Quoc, L. Zhang, X., and Leesburg, L., 2000, "A Normal Force-Displacement Model for Contacting Spheres Accounting for Plastic Deformation: Force Driven Formulation, " *ASME J. Appl. Mech.*, 67, pp. 363-371.

Williams, J. A., 1994, Engineering Tribology, Oxford University Press, Oxford.

Ye, N., and Komvopoulos, K., 2003, "Effect of Residual Stress in Surface Layer on Contact Deformation of Elastic-Plastic Layered Media," *ASME J. Tribol*., 125, pp. 692-699.

Yi, Y., Barber, J. R., Zagrodski, P., 2000, "Eigenvalue solution of thermoelastic instability problems using Fourier reduction," *Proc. R. Soc. Lond*., A, 456, 2799-2821.

Yi, Y., Shauqin, D., Barber, J. R., Fash, J. W., 1999, "Effect of Geometry on Thermoelastic Instability in Disk Brakes and Clutches," *ASME J. Tribol*., 121, pp.661-666.

Yu, T., Sadeghi, F., 2001, "Groove Effects on Thrust Washer Lubrication," *ASME J. Tribol*., 123, 1, pp. 295-304.

Yu, T., Sadeghi, F., 2002, "Thermal Effects in Thrust Washer Lubrication," *ASME J. Tribol*., 123, 1, pp. 166-177.

Zagrodski, P., 1990, "Analysis of thermomechanical phenomena in multidisc clutches and brakes," *Wear*, 140, pp. 291-308.

Zhao, Y., Maletta, D. M., Chang, L., 2000, "An Asperity Microcontact Model Incorporating the Transition From Elastic Deformation to Fully Plastic Flow," *ASME J. Tribol*., 122, pp.86-93.

Zahavi, Eliahu., 1992, The Finite Element Method in Machine Design, Englewood Cliffs, NJ: Prentice Hall.